Guilherme Jorge Vernizzi Lopes

Contributions to the investigation of the nonlinear dynamics of immersed slender structures: Reduced-order model analysis and their advantages

São Paulo

2022

Guilherme Jorge Vernizzi Lopes

Contributions to the investigation of the nonlinear dynamics of immersed slender structures: Reduced-order model analysis and their advantages

Versão Corrigida

Tese apresentada à Escola Politécnica da Universidade de São Paulo para a obtenção do título de Doutor em Ciências.

Universidade de São Paulo – USP

Escola Politécnica

Área de Concentração: Engenharia de Estruturas

Orientador: Prof. Dr. Guilherme Rosa Franzini

São Paulo

2022

Este exemplar foi revisado e corrigido em relação à versão original, sob responsabilidade única do autor e com a anuência de seu orientador.

São Paulo, 10 de Novembro de 2022

Assinatura do autor: Guilherme Vernizzi

Assinatura do orientador: Guilherme R Franzini

Catalogação-na-publicação

Lopes, Guilherme Jorge Vernizzi
Contributions to the investigation of the nonlinear dynamics of immersed slender structures: Reduced-order model analysis and their advantages / G. J. V. Lopes -- versão corr. -- São Paulo, 2022.
274 p.

Tese (Doutorado) - Escola Politécnica da Universidade de São Paulo. Departamento de Engenharia de Estruturas e Geotécnica.

1.Dinâmica das Estruturas 2.Método de Galerkin 3.Métodos Assintóticos 4.Interação Fluido-Estrutura 5.Estruturas Offshore I.Universidade de São Paulo. Escola Politécnica. Departamento de Engenharia de Estruturas e Geotécnica II.t.

This thesis is dedicated to the teachers and professors of the world. The success of a scientist is their success.

Acknowledgements

First of all, I would like to thank the São Paulo Research Foundation (FAPESP) for the grants n. 2016/25457-1 and n. 2017/16578-2. This work would not be possible without the financial support provided. I would also like to thank all the team of workers of the Offshore Mechanics Laboratory (LMO) for all the help with administrative or infrastructure matters regarding the activities carried on. I would also like to thank the secretaries from the graduate course in civil engineering (PPGEC) for all the help given in times of need. Special thanks are dedicated to the secretary Wandréa Dantas and to professor Sérgio Ângulo to whom I am in great debt for the support given in the final steps of the PhD.

I would like to thank professors Carlos Eduardo Nigro Mazzilli, Celso Pupo Pesce and Guilherme Rosa Franzini (the best supervisor I could ask for) for the major contributions they gave to my formation along the years, as well as for being good friends and personal advisors during my journey as a PhD student. A kind thanks goes for professor Stefano Lenci, from Università Politecnica delle Marche, for accepting to supervise me during my internship in Italy, and for all the knowledge that greatly enhanced my activities as a researcher.

I am also thankful to professors Waldemar Hachich, Pedro Wellington and Claudius Barbosa, from the Structural and Geotechnical Engineering Department, for all the opportunities they gave me during my undergraduate formation and all the encouraging on the decision of starting the PhD. I am also grateful for the friendship, talks and encouragement received from professor Antonio Figueiredo from the Civil Construction Department.

For all the good moments and laughs at coffee breaks, special lunches, and in the laboratory corridors, I am thankful for the friendship of professors Clovis Martins, Rodrigo Provasi and Renato Orsino, as well as from the researchers Giovanni Aiosa, Wagner Defensor, Renato Finoteli, Fernando Toni, Fernanda Takafuji, Daniela Kawaguti, Heloisa Beraldo, Michel Freitas, Tatiana Ueno and Igor Mancilla.

A special thanks goes to Giulia Gomes and Daniel Pasetti, responsible for the necessary spark of hope when life seems dire. Also in this category is Vitor Maciel, for all the outstanding adventures and quests, and to whom I also remind, it is not about the gold, is about the glory, and a big mug of grog when we live to publish an article.

Most of all, I am thankful for the support of my family, specially to my mother, grandmother and two beloved sisters who need to stand me every day.

Finally, since no person can ever be its best without its mental stability in check, three people deserve a legendary hail. To Leticia Madi I am grateful for all the emotional support given in the daily life in the laboratory. I also thank her for being the best friend I could ever have. To Beatriz Ribeiro I leave my deepest lovely feelings for all the support and the company throughout my PhD, even when an entire ocean kept us apart. Completing the legendary triad, I am thankful to all the support, encouragement, and self-confidence that Bruna Szabo gave me since my stay in Italy. This thesis would definitely not exist without you all. Thanks for being much more than I would ever expect from anyone I ever met.

I let my special thanks to the Brazilian Air-Force (FAB) and my Atlas squadron, who made me the person I am today and want to be for the rest of my life, and teaching me that there is always someone needing our help, and we must do what we can to help them.

Closing, I am thankful for all the teachers and professors who taught me everything I know during my life. I certainly could write an entire new thesis only to describe how much I own to each of them.

"Less is more."
(Ludwig Mies van der Rohe)

Resumo

Em problemas de engenharia estrutural, existe a necessidade de criação de modelos matemáticos para representar o fenômeno desejado, seguido de sua solução. Essa última etapa pode ser realizada de diversas formas, por meio de soluções analíticas, ou via métodos numéricos de baixa ou alta hierarquia. No tocante aos modelos de baixa hierarquia, denominados modelos de ordem reduzida (MOR), as técnicas e ferramentas aplicadas para obtê-los a partir do modelo original são de suma importância. Embora diversos trabalhos na literatura utilizem MORs para a análise de diferentes problemas, poucos são dedicados a abordar aspectos qualitativos do processo de geração dos modelos, além de suas vantagens como ferramentas complementares para projetos. Tais aspectos são investigados nesta tese, utilizando problemas da engenharia *offshore* como exemplos aplicados e motivadores. As investigações se iniciam pelo caso de excitação paramétrica em barras retas e flexíveis imersas em água. Diferentes MORs são concebidos, utilizando diferentes funções para representar o campo de deslocamentos. Em seguida, são realizadas análises para investigar o efeito do uso de funções de projeção mais detalhadas sobre a qualidade dos modelos obtidos, bem como verificar qual base é capaz de produzir um modelo minimal, que, por sua vez, apresenta vantagens em termos de investigações analíticas e esforço computacional necessário para simulações. Algumas soluções analíticas obtidas diretamente sobre o modelo contínuo são desenvolvidas, sendo tais soluções uma forma de modelo de ordem reduzida no sentido em que o campo contínuo fica descrito em termos de poucas variáveis a determinar. Para este caso, uma solução polinomial simples é desenvolvida para uso em projeto. Dando sequência, o caso de cabos elásticos inicialmente curvos e imersos em água sob excitação de suporte é considerado. Novamente, diferentes MORs são concebidos e comparados a fim de se investigar a vantagem de cada um e se obter um modelo mínimo. Finalmente, estruturas flexíveis sob vibrações induzidas pela emissão de vórtices são também objeto de estudo. Com o uso de diferentes MORs, mostra-se como eles limitam a faixa de análise em termos dos valores de velocidade do fluido externo nos quais podem ser aplicados. Também é mostrado como eles podem filtrar a resposta, limitando a análise em casos de respostas multicromáticas. A fim de reduzir ainda mais a ordem dos modelos para este cenário, apresenta-se uma metodologia para obtenção dos modos normais não-lineares para o problema. Isto permite a uma maior redução no número de graus de liberdade a serem analisados, sem comprometer a qualidade dos resultados. Analisando o conjunto de resultados apresentados, mostra-se a importância da análise detalhada do procedimento de obtenção de MORs, principalmente no que diz respeito aos campos de deslocamento adotados. São também mostrados os ganhos ao se obter um modelo mínimo. Tais modelos são por fim transformados em ferramentas úteis para projetos.

Palavras-chave: *Dinâmica não-linear, Modelos de ordem reduzida, Técnicas analíticas,*

Excitação paramétrica, Vibrações induzidas por vórtices.

Abstract

In any problem of structural engineering, there is the need of creation of a mathematical model to represent the desired physical phenomenon, followed by its solution. The latter step may be done in various ways, being it through analytical solutions, or by means of low/high-order hierarchical numerical methods. In what concerns the low-hierarchy models, herein called reduced-order models, the technique and tools applied to extract them from the original model are of great importance. Although there are plenty of works in the literature using reduced-order models to analyse different problems, few works are focused solely on addressing qualitative aspects of the generation process of such models and their advantages as complementary design tools for engineering practice. Those aspects are investigated in this thesis, using the offshore engineering scenario as background for the applied examples and problem motivation. The investigations are started within the problem of parametric excitation of straight and flexible rods immersed in water. Different reduced-order models are conceived, using different functions to represent the displacement field. Analyses are then carried out to investigate the effect of using more detailed projection functions over the quality of the obtained models and which base is able to produce a minimal model, which presents great advantages in terms of analytical investigations and computational effort needed for simulations. Some analytical solutions directly obtained from the continuous model are also developed, being such solutions a form of reduced model themselves in the sense that they are able to describe the continuous field by solving a small number of defined variables. For this case, a simple yet effective polynomial solution is also developed for design use. Giving sequence, the case of initially curved elastic and immersed cables under support excitation is also considered. Again, different reduced-order models are conceived and compared in order to address the advantage of each model and to obtain a minimal one. Finally, flexible rods under vortex-induced vibrations are also an object of study. With the use of different reduced-order models it is shown how they limit the range of analysis in terms of the external fluid velocity range in which they can be applied. It is also shown how they may filter the response, limiting the analysis of cases where multi-frequency responses are present. In order to further reduce the order of the models for this scenario, a methodology to obtain the nonlinear normal modes for this problem is also presented. This allows the maximum possible reduction in the number of degrees of freedom to be analysed, without compromising the quality of the results. In the collection of results, it is shown the importance of detailed analysis in the procedure to obtain reduced-order models, specially in what concerns the displacement fields adopted for the solution. It is also shown the advantages in analysis of being able to obtain a minimal model, together with approaches to turn such models into useful design tools.
Keywords: *Nonlinear dynamics, Reduced-order models, Analytical techniques, Parametric*

excitation, Vortex-induced vibrations.

List of Figures

List of Tables

List of abbreviations and acronyms

CFD	Computational fluid dynamics
DOF	Degree of freedom
FAB	Força Aérea Brasileira (Brazilian Air Force)
FAPESP	Fundação de Amparo à Pesquisa do Estado de São Paulo (São Paulo Research Foundation)
FEM	Finite element method
FIV	Flow-induced vibration
FSI	Fluid-structure interaction
LMO	Laboratório de Mecânica Offshore (Offshore Mechanics Laboratory)
MMTS	Method of multiple time scales
MOR	Modelo de ordem reduzida (Reduced order model)
NNM	Nonlinear normal mode
ODE	Ordinary differential equation
PDE	Partial differential equation
PPGEC	Programa de Pós Graduação em Engenharia Civil (Graduate Program on Civil Engineering)
ROM	Reduced order model
TLP	Tension-leg platform
VIV	Vortex-induced vibration
VSIV	Vortex-self-induced vibration
WKB	Wentzel, Kramers and Brillouin method

List of symbols

$\alpha_i,\ \beta_i,\ \eta_i,\ \zeta_i$	Dimensionless reduced order model coefficients
δ	Dimensionless top motion amplitude
ϵ	Bookkeeping parameter
ε_ℓ	Linear strain measure
ε_q	Quadratic strain measure
ε_x	Van der Pol equation parameter in the in-line direction
ε_y	Van der Pol equation parameter in the crosswise direction
$\eta,\ \zeta,\ \xi$	Local frame coordinates or dummy variables for the corresponding directions
ϕ_i	Specified spatial function in the axial direction
γ	Dynamic angle variation for cables or apparent self-weight per unit length for straight structures
γ_s	Apparent self-weight per unit length for cables
κ	Dimensionless parameter for polynomial solutions in parametric excitation problems
Λ	Amplitude-frequency relation parameter
λ	Length scale parameter defined as needed
μ	Mass per unit length of a straight structure
μ_a	Potential added mass per unit length of a straight structure
ψ_i	Specified spatial function in the transversal direction
ρ	Specific mass of the surrounding fluid
σ	Detuning parameter
σ_i	Stress in a specified direction
θ	Angle of a curve with the horizontal direction
θ_i	Euler angle accordingly to specified directions

τ	Dimensionless time
Ω	Generic domain of a partial differential equation problem
ω_n	Natural frequency of specified mode n
ω_s	Strouhal frequency
$\mathcal{A}$	Generic linear differential operator
A	Cross section area
$A_i,\ B_i$	Temporal functions for reduced order models
a_i	Indexed parameter defined as needed
A_m	Steady-state motion amplitude
A_x	Wake oscillator inertial coupling parameter in the in-line direction
A_y	Wake oscillator inertial coupling parameter in the crosswise direction
B	Solution amplitude on the method of multiple time scales
$C_\eta,\ C_\zeta,\ C_\xi$	Generalized curvature according to the directions of the local frame
C_a	Potential added mass coefficient
C_i	Polinomial coefficient
C_D	Drag coefficient
$\overline{C}_D$	Mean drag coefficient
C_D^0	Fluctuation of the drag coefficient of a rigid cylinder
C_L	Lift coefficient
C_L^0	Fluctuation of the lift coefficient of a rigid cylinder
D	Diameter
D_i	Differential operator of a specified time scale
E	Young modulus
EA	Axial stiffness
EI_i	Flexural or torsional stiffness according to index
$\mathcal{F}$	Generic nonlinear forcing term differential operator

F_i	Force component in a specified direction
f	Generic function defined as needed]
G	Shear modulus
g	Gravity acceleration or a generic function if stated otherwise
H	Horizontal component of traction force at the bottom support of a cable
i	Imaginary constant unless stated otherwise
$i,\ j,\ k,\ l$	Counters for summation procedures
$\vec{i},\ \vec{j},\ \vec{k}$	Unit vectors of a Cartesian frame
I_i	Area moment of inertia accordingly to a specified direction
J_i	Mass moment of inertia accordingly to a specified direction
$\mathcal{L}_i$	Generic differential operator defined as needed
$L,\ \ell$	Structural length
m	Axial inertial constant per unit length of a cable
m_t	Transversal inertial constant per unit length of a cable
n	Dimensionless top motion frequency
p_e	External pressure acting over a cable
p_i	Polynomials
q_x	Wake variable in the in-line direction
q_y	Wake variable in the crosswise direction
R_i	Manifold representing a specified displacement
r_i	Master coordinate for displacements in nonlinear modes
s	Arclength coordinate
S_i	Manifold representing a specified velocity
s_i	Master coordinate for velocities in nonlinear modes
S_t	Strouhal number
$\mathcal{T}$	Kinetic energy

T_i	Component of the total traction force specified as needed
t	Time
t_i	Specified time scale
$\vec{t}$	Tangent vector of a curve
$U,\ V,\ W$	Cartesian components of displacements
u	Axial displacement
U_∞	Free-stream velocity
U_r	Reduced velocity
$\mathcal{V}$	Strain energy
v	Transversal displacement
$X,\ Y,\ Z$	Cartesian coordinates
y	Displacement variable defined as needed

Contents

Objectives and organization of the thesis

The main objective of the present thesis is to bring a discussion about the influence of the refinement of the projection functions over the quality reduced-order models developed with such functions. This main objective is complemented with the exposition of the advantages of different reduced-order models based on their conception, as well as the elaboration of analytical solutions for the models that allow it.

To achieve the proposed objectives, different problems from the offshore engineering are selected as motivational examples. Namely, the cases of parametric excitations of straight rods immersed in fluid, boundary imposed motion over curved elastic cables, and vortex-induced vibrations over straight rods are the chosen problems. To each of them, a mathematical model using partial differential equations is obtained, followed by a Galerkin discretization procedure in order to obtain the reduced-order models. In each case, different reduced-order models are obtained by varying the number and shape of the projection functions. Whenever possible, analytical solutions using the method of multiple time scales are also provided.

For a better organization of the text, the thesis is divided into seven chapters, with its contents as follows.

In the first Chapter, a brief introduction concerning typical offshore engineering problems is presented. Some important phenomena for design practice are presented, as well as on how the studies of the thesis are related to the field and can contribute to it.

The second Chapter brings a literature review concerning the different phenomena and structures involved in the discussions of the thesis. The review brings the historical contribution on the topics of parametric excitation, vortex-induced vibrations and responses associated with moving boundaries. It also reports the advances made in the field of curved cable dynamics, nonlinear modes of vibration and applications of all the previous topics in the offshore engineering field.

In the third Chapter, the basic mathematical models to describe the structural behaviour of flexible straight rods and of curved elastic cables are derived. This chapter is the starting point for the rest of the thesis, with all other chapters using the obtained models.

The first application is made in Chapter four. In this one, the problem of straight rods under parametric excitation is analysed by means of different reduced-order models and analytical techniques. It is also developed a simplified solution with polynomial expressions based on the obtained analytical solutions for application in electronic spreadsheets.

The fifth Chapter tackles the problem of curved elastic cables under the action of imposed boundary motion. The analysis is made with different reduced-order models, and it is shown what are the main aspects in the construction of such models that cannot be overlooked.

The case of vortex-induced vibrations is investigated in Chapter six. The structure is again a straight rod, and different reduced-order models are obtained and analysed. Giving sequence, a suitable reduced-order model is chosen to be further reduced by means of its nonlinear normal modes. Some particularities exist in the construction of such modes for this problem and are detailed.

Finally, the conclusions of the thesis are brought in Chapter 7. The chapter also brings suggestion for future works that can be started from the results of this thesis or by applying its suggestions in other problems.

Complementing the text, six appendices are also present in the thesis. In Appendix A, some algebraic steps for the deductions in Chapter 3 are detailed.

In Appendix B, the expressions for the modal shapes and frequencies considering linear and nonlinear modes of flexible rods under varying traction are deduced. This is made considering that such modes are largely used throughout the thesis.

The problem of obtaining nonlinear modes of free vibrations for statically curved cables is discussed in Appendix C. The cases of small or generic sag are treated, with a closed-form solution being presented for the former and a multiple scale method approach for the latter.

In Appendix D, a brief mathematical justification for the solvability condition of the method of multiple time scales is presented. It is shown how the condition is the consequence of the requirement for a solution to exist for the sequential problems that are part of the application of the method.

Appendix E presents the tables of polynomial coefficients obtained from the results of Chapter 4. Finally, a list of publication and works presented in international conferences is presented in Appendix F.

1 Introduction

With the increase of the oil consumption in the world along decades in different industries (fuel and chemical, for example), the search for new reserves of the resource intensified. One solution is the exploration of reserves located in regions of the ocean with crescent depth. This leads to the demand for structural solutions that can handle the deep water environment.

The depths occurring in practice nowadays can reach between 1000 and 3000 m, depending on the region. In order to extract oil from depths this large, a series of long structures are expected to be present in order to keep the operation running. In this context, risers are the structures responsible for conveying the mixture oil-gas-water from the seabed to the floating unit. Other kinds of risers can be found in the offshore industry, like drilling risers or injection risers. In structural terms, risers are very slender structures which can be put into two classifications.

Flexible risers are composed of an external polymer case with internal layers of polymers, steel armours and carcasses in order to support internal and external pressures, the actuating traction, asides giving the necessary structural strength. As the name suggest, they are more flexible than the other classification. On the other hand, rigid risers are composed of a solid and thick steel carcass, and are assembled by welding 12 meters long parts together, while the flexible risers are made whole.

In order to control the operation, umbilical cables are also employed in the offshore activity. Like the risers, this kind of structure is very slender and the difference lies on the functions and the internal composition of the structure. Umbilical cables do not have the hollow area that risers have for conveying fluid. In the cross-section of an umbilical cable, small fluid conductors for hydro-mechanical actuation, copper wire strands, and other types of elements, as optical fibers, for information transference and actuation can be found.

Finally, the floating unit must be kept in position during the operation, which sometimes is achieved by the use of tethers or also mooring lines. Those are essentially structural elements, working under high traction values. The number, configuration and importance of those elements is largely dependent on the type of floating unit.

The oil exploration is used as a practical motivation in this work. However, it is important to keep in mind that similar structures can be found in other applications of the offshore industry. Mooring lines of offshore wind turbines, vessels, wave converters among other structures to be used in the ocean can be mentioned. Some floating unities solutions are shown in Figure 1. Figure 2 shows some configurations for submarine cable

structures. The applications for wind and wave converters are presented in Figures 3 and 4 respectively.

Figure 1 – Some possible floating units solutions.

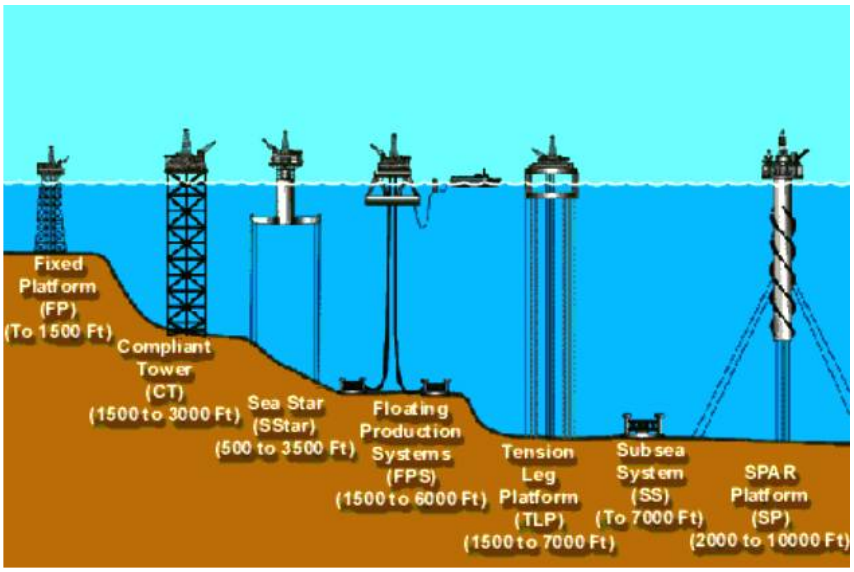

Source: http://www.bluebird-electric.net.

Figure 2 – Possible configurations for offshore cable structures.

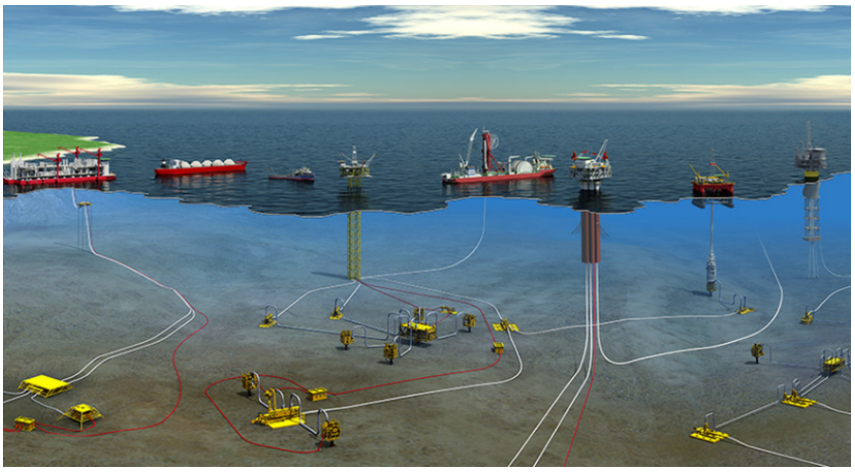

Source: http://www.genesisoilandgas.com.

All the cable structures mentioned share some common properties. They are all very slender flexible cylinders, subject to dynamical excitations from the surrounding environment, internal flow and/or pre-stressing, that demand a detailed structural analysis regarding operational safety. This leads then to the main motivation for this work that is the analytical and numerical studies on the nonlinear dynamical behaviour of this kind of structure.

Figure 3 – Some solutions for offshore wind turbines.

Source: https://www.firstmarinesolutions.com.

Figure 4 – Mooring system and umbilical cable for a wave turbine.

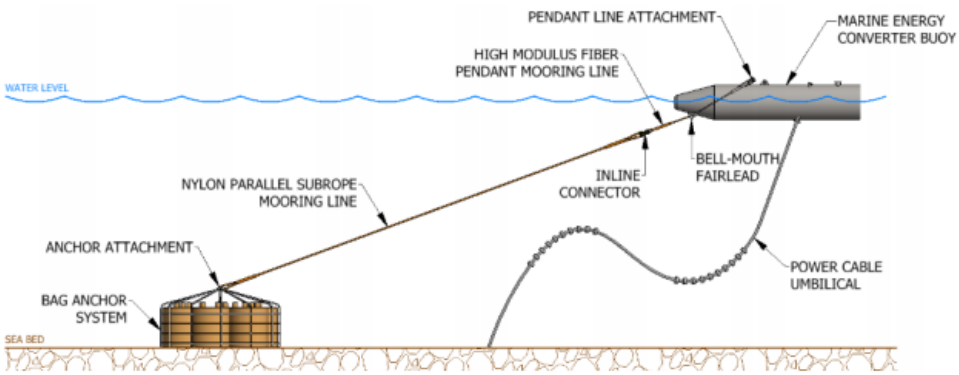

Source: Flory et al. (2016).

The first phenomenon to be expected is the parametric excitation. The floating units are subjected to the action of the ocean waves, changing their position with time. Since a great amount of the stiffness of very slender structures is given by the geometrical stiffness, the time-varying position of the floating unit will be perceived by them as a time-varying stiffness. Another phenomenon to occur are forcing terms along the structural length when the imposed motion generates displacements of the structure in a direction orthogonal to its axis by means of interaction with the surrounding fluid.

Secondly, due to the presence of sea currents, all those structures are subject to vortex-induced vibrations (VIV). This phenomenon may be of great impact in terms of the fatigue analysis. VIV leads to oscillations of the order of the structural diameter, and can cause multi-modal response of the structure, as well as the appearance of travelling waves.

This motivates the analysis made in the thesis about straight structures under VIV.

There are other phenomena that can occur in those structures, like dynamical effects of internal flow and vortex self-induced vibrations (VSIV). The internal flow is present in exploration risers and may lead to important effects over the dynamical response of the structure. On the other hand, VSIV is a phenomenon that occurs, for example, in catenary risers, when the motion of the structure in still fluid causes vortex-shedding, inducing additional vibrations to the structure. Even though important, internal flow excitations and the VSIV phenomenon are out of the scope of the thesis.

For the phenomena studied (parametric excitation and VIV), the investigations are carried out using reduced-order models (ROMs). The use of ROMs allows for a deep investigation of the main properties of a dynamical system by studying the behaviour of a system with a small number of degrees of freedom (DOFs). This small number of DOFs makes possible the use of techniques of applied nonlinear dynamics to investigate the phenomena, like the method of multiple scales, center manifold theorem, nonlinear normal modes, among others (see Nayfeh & Balachandran (1995)).

The use of ROMs is specially useful in the early stages of design, in which a large number of conditions must be simulated. Another use of the ROMs is the understanding of qualitative (and, sometimes, quantitative) aspects of response allowed by the mentioned techniques that cannot be applied to higher-order hierarchical models, for example, the ones based on the Finite Element Method (FEM), in a reasonable time for engineering practice. In this scenario, the present thesis is focused on qualitative aspects in the construction of reduced-order models (ROM). The thesis also brings advantages in using this type of model for analysis and engineering practice. This is done by performing ROM analyses for different scenarios of the offshore engineering, being them the cases of flexible rods, immersed in fluid and under parametric excitation, elastic and curved cables immersed in fluid and under the action of imposed boundary motion, and the last one is that of a flexible rod under VIV.

2 Literature review

In this chapter, the literature review with the basic concepts used along the thesis is presented. Some detailed aspects are left to be developed in subsequent chapters as they seem appropriate. The review is divided into six sections. Initially, the physical phenomena of interest to this thesis are presented with focus on the main concepts and modelling aspects. This is made in Section 2.1 where the phenomenon of parametric excitation is presented, while Section 2.2 brings a review of vortex-induced vibrations (VIV).

Following, the review of the dynamics of slender structures with special attention to the application under the occurrence of parametric excitation and/or VIV is made. Section 2.3 brings a review of the dynamics of vertical slender rods, with focus on applications to the phenomena of interest of the thesis. In the sequence, the same type of review is made for slender structures with curved static configuration in Section 2.4.

In the sequence, since nonlinear modes are used in the analysis of VIV, a review on the topic is presented in Section 2.5. Finally, Section 2.6 indicates how this thesis relates to the existing literature and with the identified open questions in the worked topics.

2.1 The parametric excitation phenomenon

Parametric excitation is the phenomenon that occurs when at least one of the internal properties that rules the dynamical behaviour of a system varies with time, in a time scale comparable to the expected response of such system. In order to clarify the importance of the time scale of such variation, two hypothetical examples are posed. The first one is of a steel beam that corrodes with time. In such case, some properties of the beam are expected to change with time. However, the time required for the changes to be noticeable is way larger than the periods of oscillation that the beam is expected to undergo as a structural element. Thus, this condition is not classified as parametric excitation. The second example is that of a pendulum under an imposed vertical motion to its support with a period of oscillation of the same order of magnitude of the natural period of oscillations of the pendulum. In this case the dynamical response of the pendulum will depend on the amplitude of the imposed motion and on the ratio between the imposed motion frequency and the natural frequency of the pendulum. This second case is qualified as a problem of parametric excitation.

In the particular case of mechanical systems written as second-order ordinary differential equations, one classical example of a parametrically excited system is given by Hill's equation, in which the stiffness of the system varies with time. Hill's equation for a

generic linear and undamped dynamical system of second order is written as

$$\ddot{g} + f(t)\, g = 0. \tag{2.1}$$

The function $f(t)$ can be any periodic function of time as long as it is not the constant function, and g is the degree of freedom (DOF) used to describe the dynamical system. In the particular case that f is composed of a constant term and one harmonic function, Hill's equation becomes the well-known Mathieu's equation, given as

$$\ddot{g} + (1 + \delta \cos(nt))\, g = 0, \tag{2.2}$$

or

$$\ddot{g} + (a + 2\varepsilon \cos(t))\, g = 0. \tag{2.3}$$

With δ and ε being small parameters representing the amplitude of the parametric excitation while n and a are real numbers representing the ratio between the excitation frequency and the natural frequency of the system or the square of the natural frequency of the system, respectively. Both equations are equivalent to each other and each one has its own advantages and drawbacks regarding results presentation, according to the desired objective.

Regarding linear systems, the main property to be investigated in parametrically excited systems regards the existence of limited solutions, which translates in this case in investigating the stability of the trivial solution. The Mathieu's equation has been extensively studied for this purpose, since it is a simple and linear equation that allows the realization of deep investigations in terms of the existence of stable solutions either by numerical or analytical means. Some rich investigations on the stability of Mathieu's equation solutions can be found in Meirovitch (1967), Bender & Orszag (1978) and Nayfeh & Mook (1979), among others.

The usual way of presenting the stability of Mathieu's equation solutions is by using the Strutt's diagram. This diagram is a map that for (ε, a) belonging to a region of interest in $\mathbb{R}^2$, which shows if the Mathieu's equation has bounded or unbounded solutions. For linear systems, the existence of bounded solutions implies this solution is the trivial one. Strutt's diagram can be obtained by different means, like the method of multiple scales or the Floquet theory (see for example Nayfeh & Mook (1979) and Nayfeh & Balachandran (1995)). An example of Strutt's diagram obtained with the method of multiple scales is presented in Fig. 5.

Figure 5 – Strutt's diagram for classical Mathieu's equation. Dashed regions lead to unbounded solutions while white regions lead to the trivial solution.

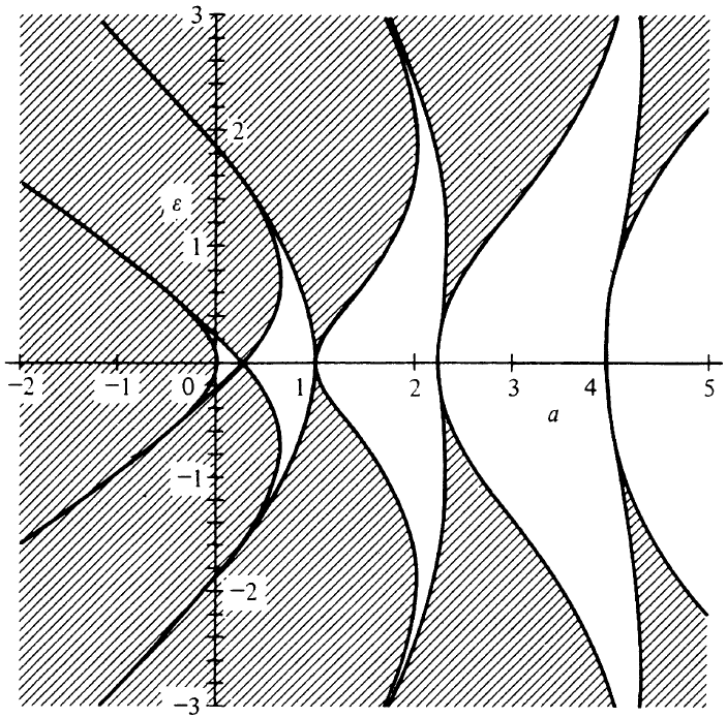

Source: Bender & Orszag (1978)

One of the most important features of Fig. 5 are the points where the solutions are unbounded even for the amplitude of excitation approaching zero ($\varepsilon \mapsto 0$). These cases correspond to the so-called parametric instability condition, which for the Mathieu's equation as in Eq. (2.3) are given as $a = i^2/4$, with $i \in \mathbb{N}_0$ (Bender & Orszag (1978)).

Two main points must be stated now about this type of stability chart. The first one is that the boundaries between bounded or unbounded solution regions are affected by adding linear damping to the system, with a reducing of the regions of unbounded response (see Fig. 6). Secondly, the inclusion of nonlinear terms in the equations of motion is necessary to turn the regions of unbounded response into regions where some bounded response is obtained. This latter point is of great importance for applications of dynamical systems where parametric excitation occurs and that will be discussed latter on the thesis (see, for example Chapter 4).

2.2 Vortex-induced vibrations (VIV)

The second phenomenon of interest in the applications of the present research is called vortex-induced vibrations (VIV). When solid elements are immersed in fluid flows, some form of interaction between the solid body and the fluid is expected. This type of

Figure 6 – Strutt's diagram for Mathieu's equation with damping effect. Dashed regions lead to unbounded solutions while white regions lead to the trivial solution.

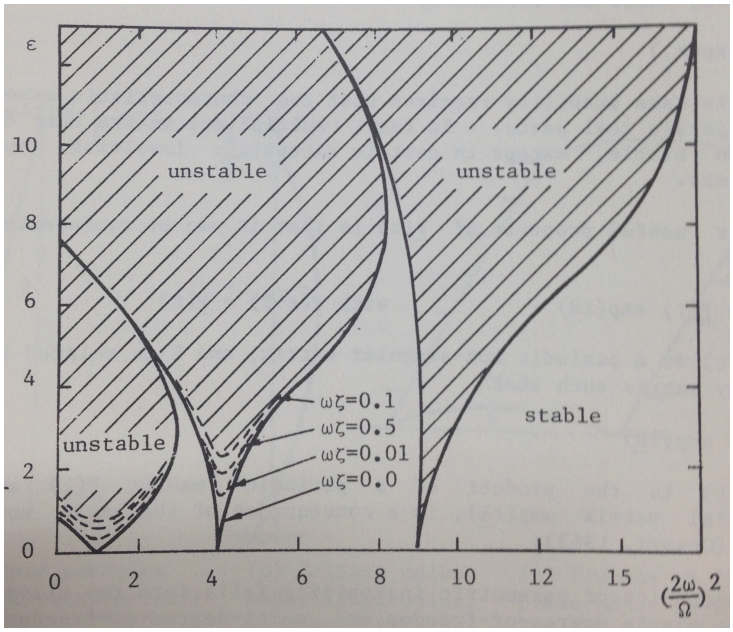

Source: Ibrahim (2008)

interaction consists the class of phenomena called fluid-structure interaction (FSI). One possible outcome of such interactions, depending on the structural and flow conditions, is the occurrence of a dynamical response of the structure, leading to the so called flow-induced vibration (FIV) phenomena. VIV is one specific type of FIV. This is a nearly resonant, self-excited and self-limited phenomenon that can occur when a bluff-body is immersed in a fluid stream.

A bluff-body is herein defined in similar manner to that made in Meneghini (2002), as the one in which the flow separation (or detachment) occurs in a significant portion of its surface.. With the detachment of the flow, the free shear layers start to interact, leading to the vortex-shedding phenomenon. A good way to understand how this occurs is by means of the two-dimensional model described in Gerrard (1966), sketched in Fig. 7.

The arrow on the left side of the cylinder in Fig. 7 indicates the free stream direction. The flow "**a**" is entrained into the growing vortex, with a vorticity opposite to the one already existing in such vortex, diminishing its total circulation. Flow "**b**" is the one that interrupts the further development of the growing vortex, avoiding it to receive more circulation from its original shear layer and causing the detachment of the vortex. Finally, flow "**c**" starts the generation of a new vortex that will restart the cycle, changing the shear layer and forming the next vortex to be detached. Further physical details about flow around bluff-bodies and some mathematical concepts of it can be found in Bearman (1984).

Figure 7 – Sketch for the vortex shedding mechanism. Two-dimensional case

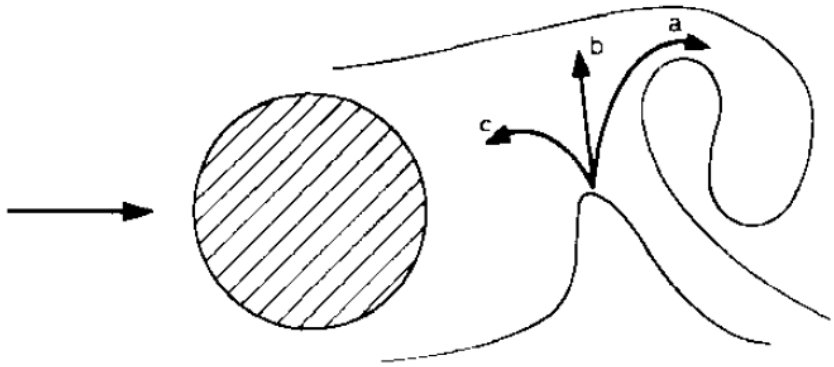

Source: Gerrard (1966)

One classical example of a bluff-body is a cylinder of diameter D, which is a very common element used for VIV investigations. The most basic set-up for investigating the problem in experiments and mathematical modelling is that in which a rigid cylinder is mounted on an elastic base that allows displacements only in the direction orthogonal to the free-stream, named then cross-wise direction. This condition is herein defined as a 1-DOF VIV. The vortex shedding is started by the flow passing around the cylinder. When the frequency of such vortex shedding is close to the natural frequency of the immersed system, the so called lock-in occurs. Let U_∞ be the free stream velocity of the flow and ω_n be the natural frequency of the system in still water[1]. The dimensionless parameter reduced velocity is defined as:

$$U_r = \frac{U_\infty 2\pi}{\omega_n D} \tag{2.4}$$

The lock-in phenomenon occurs for a range of reduced velocities typically within $3 < U_r < 12$. In this situation, since the vortices are being detached with a frequency close to the structural natural frequency, the lift force magnitude fluctuates with this same frequency. From the structural point of view, this is the situation of a system under the action of a nearly resonant loading. The onset of the phenomenon is independent of the initial condition of the cylinder and no external excitation is required, reason why the phenomenon is labelled as self-excited.

In response to the fluctuating lift force, the cylinder starts to move with increasing amplitudes of oscillation. It would be expected, for a linear and undamped system under

[1] For cylinders immersed in water, the natural frequency can be significantly different from the result obtained with the cylinder in air. The reason for such different is the added mass, which can be understood as the part of the hydrodynamic load in phase with the acceleration of the cylinder

resonant forcing, that such amplitude would grow indefinitely, but this is not the case for VIV. The explanation is that a phenomenological nonlinearity occurs when the cylinder starts to move since such motion interferes with the vortex shedding itself, disturbing it and consequently disturbing the fluctuation of the lift force. Such physically nonlinear interaction leads to a condition where the oscillations of the cylinder reaches a steady-state regime with limited amplitude, typically of the order of the structural diameter D. A typical response curve of an elastically mounted rigid cylinder oscillating only in the direction transversal to the flow is shown in Fig. 8. For more details regarding 1-DOF VIV, see Khalak & Williamson (1999).

Figure 8 – Amplitude response as a function of the reduced velocity for a rigid cylinder under 1-DOF VIV. Black markers for experiments in water and white filled markers for experiments in air, highlighting the key differences when the displaced fluid mass is of an order of magnitude close to the cylinder's mass.

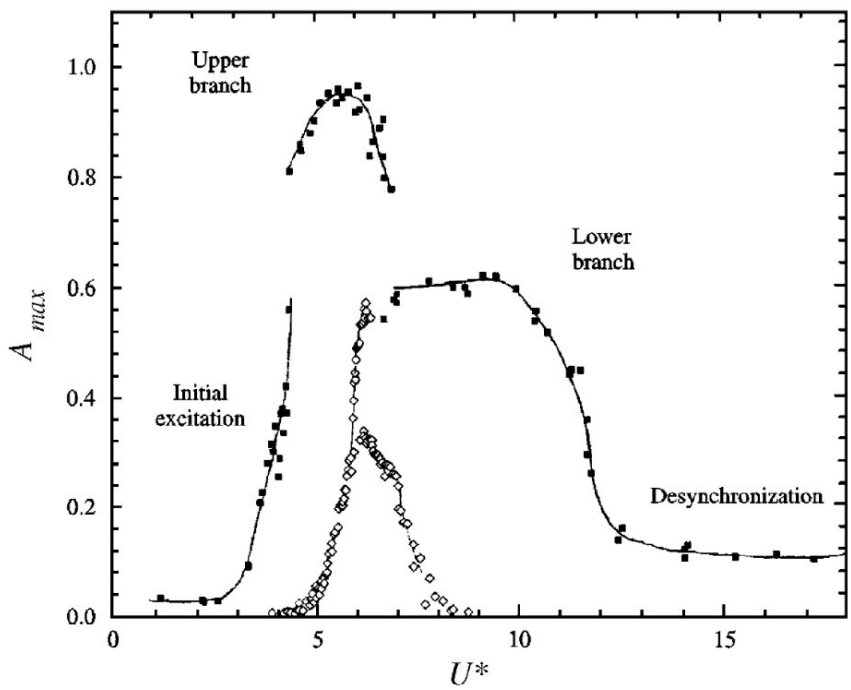

Source: Williamson & Govardhan (2008)

Adding up in the complexity of the phenomenon, the cylinder can also be left to oscillate in the direction parallel to the free stream, called in-line direction and leading to the condition herein named 2-DOF VIV. In that case, the fluctuations on the drag force due to the vortex shedding lead the cylinder to dynamically respond with an oscillatory motion in the corresponding direction. The frequency of the fluctuation of the drag force is twice that of the fluctuation of the lift force. This is naturally expected considering the alternate fashion of the vortex shedding. This correlation, combined with the relation between the structural stiffness in each direction, leads to various possible patterns for the plane

motions developed by the cylinder. Figure 10 depicts the trajectories on the horizontal plane for a cylinder under 2-DOF VIV obtained by Dahl et al. (2007) using experimental results. Another feature of importance in the 2-DOF VIV case is the cross-wise motion amplitude magnification due to the existence of the inline motion, with the intensity of such magnification depending on the mass ratio parameter m^*[2]. For the case where those values are very close to each other the magnification is stronger, which is illustrated in Fig. 9. More experimental results and investigations about 2-DOF VIV can be found in Jauvtis & Williamson (2004), Stappenbelt & Lalji (2008), Blevins & Coughran (2009), Franzini et al. (2012) and Franzini et al. (2013). For detailed reviews over VIV features, the interested reader should consult the papers Sarpkaya (2004) and Williamson & Govardhan (2004).

Figure 9 – Amplitude response as a function of the reduced velocity for a rigid cylinder under 2-DOF VIV.

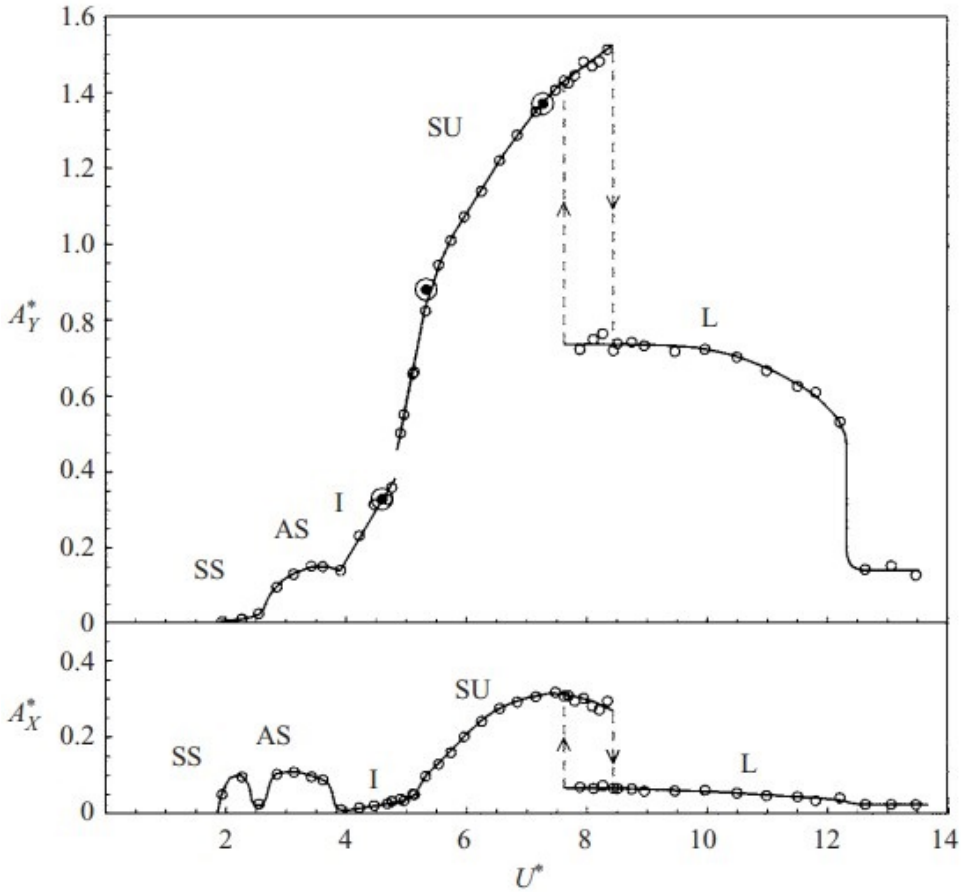

Source: Jauvtis & Williamson (2004)

In terms of mathematical modelling, a fundamental step is to obtain a suitable expression capable of representing the phenomenon in the fashion of a dynamical system.

[2] The mass ratio parameter m^* is defined as the ratio between the oscillating mass and the mass of fluid displaced by the body.

Figure 10 – Plane motion patterns for rigid cylinder under 2-DOF VIV. Reduced velocity in the horizontal axis and structural frequency ratio between in-line and cross-wise directions in the vertical axis.

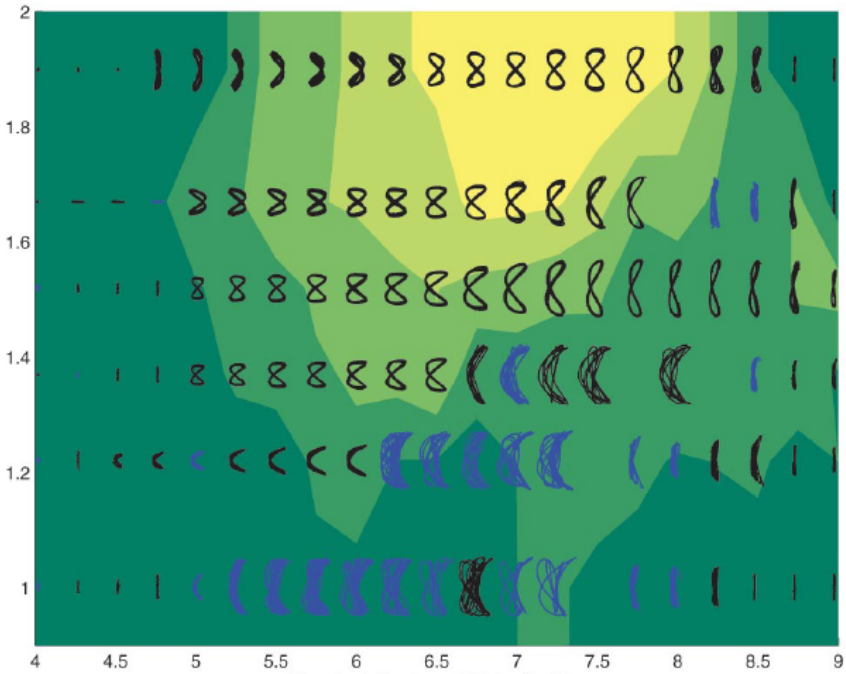

Source: Dahl et al. (2007)

The phenomenological approach is thus the one used within this research. This approach makes use of a nonlinear equation to represent the dynamics of a quantity that defines the fluid-structure interaction such as, for example, the lift coefficient.

Phenomenological models are based on and calibrated with experimental data, giving good results when working in the hypothesis and range of parameters of the experiments employed in calibration. Different works presented models for describing VIV with a dynamical equation for the wake (see Hartlen & Currie (1970), Iwan & Blevins (1974), Krenk & Nielsen (1999) and Facchinetti, de Langre & Biolley (2004)). The model presented in Facchinetti, de Langre & Biolley (2004) was obtained after different calibrations with different equation formats considering various possibilities of coupling between the phenomenological and the structural oscillators. The final model is a Van der Pol oscillator for the variable that represents the wake dynamics (particularly, the lift coefficient variation with time), coupled with the structural inertial term. In Ogink & Metrikine (2010) a slight variation is applied to the model of Facchinetti, de Langre & Biolley (2004), using the instantaneous lift and drag directions to decompose the force due to the vortex wake. In this model, a geometrically exact expression of the velocity of the cylinder was also included in the calculation of hydrodynamical forces. It is worth noticing that with a linearization of the hydrodynamic forcing terms and a proper choice

of the calibrated parameters, the model from Facchinetti, de Langre & Biolley (2004) can be obtained from the model by Ogink & Metrikine (2010).

In Franzini & Bunzel (2018), a phenomenological model for the VIV-2-DOF is presented. This model is proposed based on the one presented in Ogink & Metrikine (2010), with the inclusion of a second wake-variable, in order to represent the effects of the wake on the drag direction. Since there is a duality in VIV behaviour (see Fig. 10 and Dahl et al. (2007)) and the vortex shedding causes a variation on the drag force with twice the frequency of the variation on the lift force, a Van der Pol oscillator is also proposed for the second wake-variable. This second oscillator is assumed to pulsate with a frequency that is twice the one associated with the cross-flow direction. Notice, however, that this is an *ad-hoc* model, proposed by the authors from investigating energy harvesting using a piezoelectric circuit, which is a topic that will not be investigated in the thesis. Considering the success of such studies, the basic structure of a wake-oscillator adopted in this thesis is (see Facchinetti, de Langre & Biolley (2004), Ogink & Metrikine (2010) and Franzini & Bunzel (2018))

$$\ddot{q}_y + \varepsilon StU_r \left(q_y^2 - 1\right) \dot{q}_y + \left(StU_r\right)^2 q_y = A_y \ddot{y}. \tag{2.5}$$

The variable y is the generalized coordinate representing the cross-wise displacement of the structural model, A_y and ε are parameters obtained from experimental calibration, while q_y is the wake variable representing the effects in the same direction as y. A detailed and concise mathematical justification for representing the effects of the wake over the cylinder by a single variable is shown in Aranha (2004). For the case of a flexible cylinder, all the variables are supposed to vary with a position coordinate. So, letting t be time and s the arclength variable, then $q_y = q_y(s,t)$ and $y = y(s,t)$. For modelling methodologies based on projections, like the Galerkin scheme, it is usual to adopt the same projection function for the structural and the wake variables. This is an *ad-hoc* assumption used within this research considering no better alternative has being stated in the literature.

2.3 Dynamics of flexible and straight rods

Both the phenomena previously explained are of interest in offshore engineering applications, where slender structural members are under the action of such loads. For a better organization of the review, the case of parametric excitations is considered first. In the sequel, a review of existing research of such structures under VIV is carried out. The specifics about free vibrations of straight flexible rods are widely known and subject to basic courses of structural dynamics, thus not included in this review.

2.3.1 Straight flexible rods under parametric excitation

One example of a situation where parametric excitation occurs is the lateral vibrations of a flexible rod under the effect of a top-motion axial excitation. The examples herein adopted corresponding to that situation are vertical risers and tension leg platform's (TLP) tethers. These kind of structures are subject to top-motion excitation due to the motions of the floating unit caused by the first-order forces due to the waves. One of the first works to investigate immersed flexible rods under top-motion excitation is Hsu (1975). In this work, a heavy and inextensible string hanging in still fluid is subjected to top-motion excitation. First, the linear form of the equation of motion is investigated using the method of variables' separation. The author obtains the vibration modes of the string in terms of Bessel functions, and the equation that describes the modal amplitude with time turns to be the Mathieu's equation. Finally, a solution for the steady-state amplitude is presented when the quadratic hydrodynamical damping is taken into account, showing the main role that this kind of nonlinearity has on limiting the response amplitudes on the unstable regions of the Strutt's diagram.

In Patel & Park (1991), the response of TLP tethers under parametric excitation is addressed. In this work, the submerged weight of the tether is negligible compared to the mean traction along its length. This allows the authors to work as if the traction is constant along the tether, and that the modes of vibration of the structure would be trigonometric functions. The first mode of vibration is then used as shape function in a Galerkin scheme, leading to a 1-DOF ROM to describe the tether dynamics. The linearized problem is then used to create a Strutt diagram using trigonometric expansion for the solution of the equation. The obtained diagram is reproduced in Fig. 11. Following, the authors applied the averaging method (see Nayfeh & Mook (1979)) in order to obtain steady-state amplitudes when the Morison's quadratic damping is considered into the model.

Expanding these results, Simos & Pesce (1997) carried out an investigation of the TLP tethers under parametric excitation keeping the traction variation due to the immersed weight of the structure. Differently from Patel & Park (1991), in this work the bending stiffness was disregarded. A 1-DOF model was obtained using a Galerkin scheme, employing a mode of vibration of a heavy vertical cable as shape function. Some case studies were addressed and it was verified that when the immersed weight is not so small compared to the mean traction of the cable, the use of trigonometric functions as shape functions on Galerkin method can lead to significant discrepancies when compared to a model obtained with the vibration modes of the structure, given as Bessel functions.

The investigation of the effects of parametric excitation in a structure already under forced vibrations was considered in Patel & Park (1995). In this case, a vertical tether is subject to both vertical and horizontal top motions. As in Patel & Park (1991), the traction

Figure 11 – Strutt's diagram for the model of a vertical tether. Dashed for regions of unstable solutions and white for regions of stable solutions.

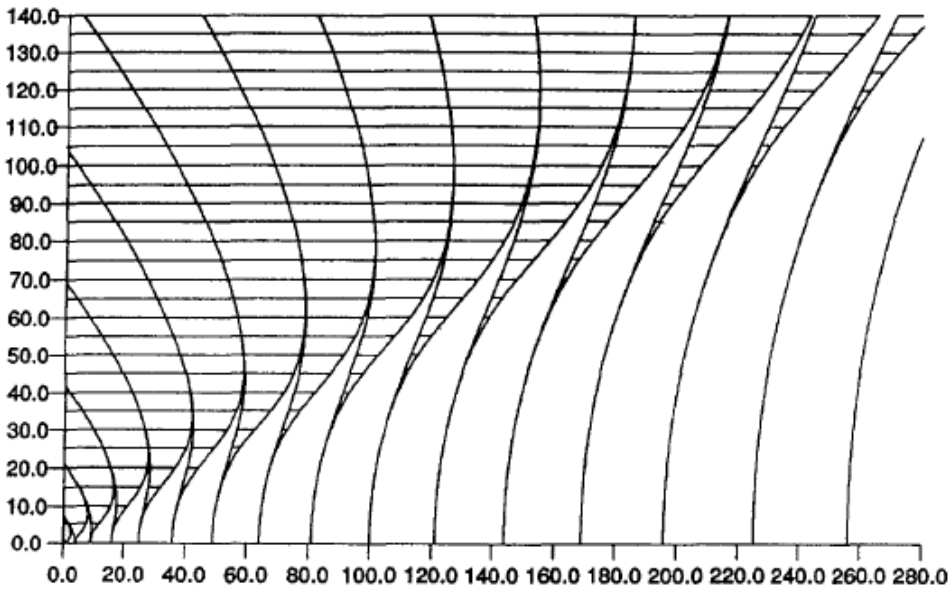

Source: Patel & Park (1991)

is considered constant along the tether and only the linear structural terms are considered in the equation of motion. A ROM is then obtained with a Galerkin scheme to investigate the problem, by considering that the response of the structure is the composition of four trigonometric modes. It is shown that the number of modes was adequate to represent the structure, since the amplitude response of the higher modes adopted was very small. Also, the authors conclude that the motion amplitude is significantly larger in comparison to the cases where only the parametric excitation or the forcing term are present.

In the aforementioned works, the axial dynamics was disregarded and only the linear behaviour of the structure was considered in the equations of motion. Chatjigeorgiou (2004) investigated the vertical tether under parametric excitation keeping the axial dynamics in the analysis and the nonlinear structural behaviour. The equations were then treated with a finite difference scheme and the Galerkin method, allowing for a comparison between the results of a projection method and a numerical solution applied directly to the continuous equations of motion. The methods presented good agreement and it was shown that internal resonances play an important role on the amplitude of motion of the structure under parametric excitation. It was also concluded that the nonlinear damping reduces the effects of the internal resonances.

In Zeng et al. (2008), a vertical TLP tether under simultaneous vertical and horizontal top motion is considered. The nonlinearities from the stretch of the structure are kept and a Galerkin scheme using trigonometric shape functions is applied. After

numerical simulations, a reduction of the resulting motion amplitude can be seen due to the structural nonlinearities. Furthermore, the presence of the nonlinearities allows for the possibility of parametric excitations occurring due to the horizontal top motion.

All of the mentioned works considered only the case of harmonic and monochromatic parametric excitations. Multi-frequency excitations are investigated in Yang, Xiao & Xu (2013). The axial dynamics is disregarded and, instead of keeping the nonlinearities of the structure, the authors wrote the traction as a trigonometric series with the same frequencies of the excitation. Stability charts are numerically obtained and it is shown that they present significant differences when compared to the monochromatic excitation. In Figs. 12 and 13 the stability charts for both cases, mono and multi-frequencies, are shown.

Figure 12 – Stability chart for a tether under a single frequency excitation. The horizontal axis stands for a while the vertical one stands for ε, both according to Eq. (2.3).

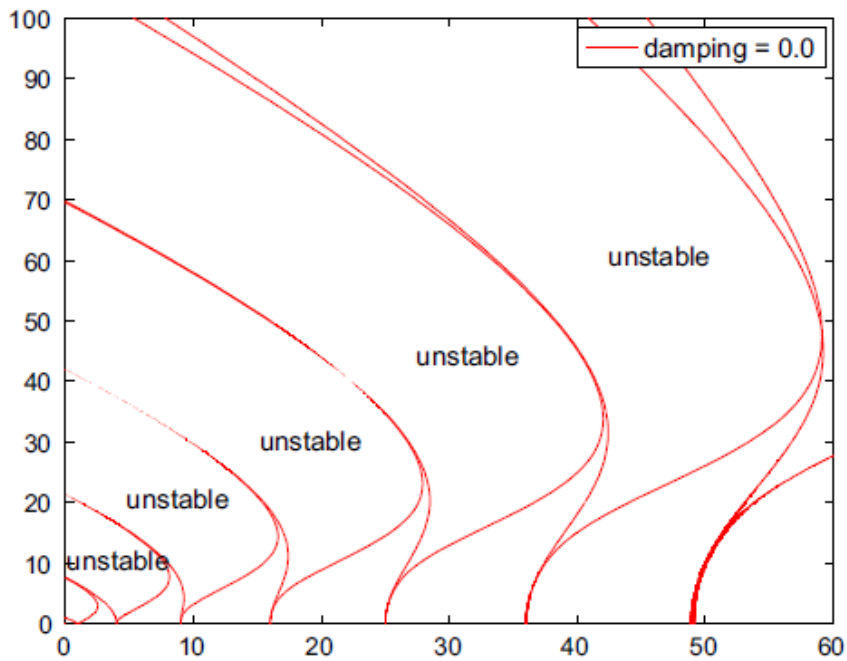

Source: Yang, Xiao & Xu (2013)

While the previous works focused on parametric excitations alone, in Yang & Xiao (2014) the combined effect of parametric excitation and VIV is investigated. For the structure, the strategy presented in Yang, Xiao & Xu (2013) of using a multi-frequency traction is used, with the inclusion of the immersed weight. For the effect of vortex shedding, a harmonic forcing term is inserted instead of a phenomenological approach. It is shown that the parametric excitation can significantly amplify the motion amplitudes due to VIV and that increasing the mean traction is an effective way of reducing this amplification. Regarding the use of the phenomenological approach to investigate the

Figure 13 – Stability chart for a tether under a multi-frequency excitation. The horizontal axis stands for a while the vertical one stands for ε, both according to Eq. (2.3).

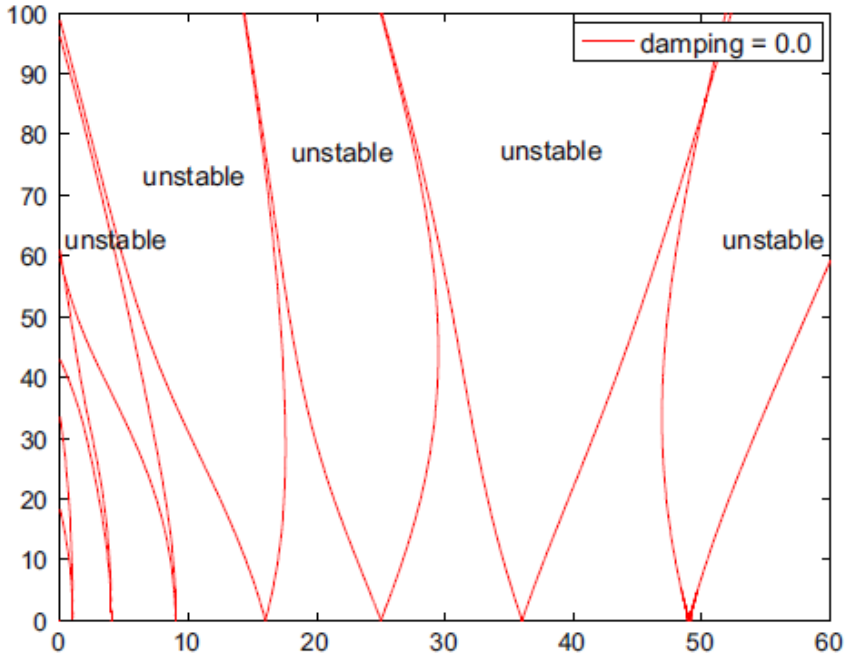

Source: Yang, Xiao & Xu (2013)

concomitant occurrence of parametric excitation and VIV, a FEM approach is developed in da Silveira et al. (2007), where the lift force is modelled with the aid of a phenomenological model for the wake dynamics in each node of the FEM model.

Some works developed in the last decade deal with the quality of the modelling adopted when investigating parametric excitations. Mazzilli & Dias (2015) compared different ROMs to a FEM solution and experimental data (LIFE-MO (2013)). One of the ROMs considered by the authors was obtained by using a Bessel-like mode (Mazzilli, Lenci & Demeio (2014)) as shape function on Galerkin projection. The other one, was obtained using a trigonometric function on the Galerkin scheme. The results obtained using the Bessel-like based ROM were in good agreement with the experimental ones. In Mazzilli, Rizza & Dias (2016) a ROM based on Bessel-like functions is also compared to experimental data, showing good agreement with it.

In the works Franzini et al. (2016a) and Franzini et al. (2016b) the effects of hydrodynamical coefficients are investigated using ROMs. In the former work, the ROM is constructed with trigonometric functions, while in the latter Bessel-like functions are used as shape functions in the Galerkin projection. These works show that the mean drag coefficient and added mass coefficient can strongly affect the amplitude of steady-state motion. Those works show one of the advantages of using ROMs, that is the deep

investigation of parameters that affect a certain mechanical problem. The investigations can be carried out with a refinement and range of parameters far greater than with experiments, that can then be planned at some points of the parameters maps under study for validating the obtained results.

In Franzini & Mazzilli (2016) a detailed analysis is made with a ROM obtained using three sinusoidal functions. Comparisons are also made with a ROM obtained with a single sinusoidal function. However, the analysis focused on the response of each degree of freedom alone, with no deep investigation on the composed motion. One important feature of this latter paper is that the authors present the instantaneous configuration for some time-steps and the shape that is recovered resembles the vibration modes obtained in Mazzilli, Lenci & Demeio (2014). This leads to two possible scenarios for decision when creating ROMs. By one side, models with fewer DOFs allow analytical investigations to be carried out with less effort and can produce numerical results with less computational effort. On the other hand, depending on the mechanical problem, obtaining suitable shape functions can be a hard or even impossible task. In that last situation, the use of a multi-function approach with simpler shape functions chosen in an *ad-hoc* manner can lead to valuable results.

Another useful result presented in some of the works (Mazzilli & Dias (2015), Mazzilli, Rizza & Dias (2016), Franzini et al. (2016a), Franzini et al. (2016b), Franzini & Mazzilli (2016)) is the map of post-critical amplitudes as a function of the excitation amplitude and frequency. In this kind of representation, various useful informations about the system's dynamics are condensed. It is possible to verify how the range of response of the structure varies with the excitation amplitude, how the response amplitude varies with the excitation amplitude for a given frequency, and which sub-harmonics are excited depending on the excitation amplitude. However, those maps were obtained using a high number of numerical simulations, which can demand a big amount of computational time.

Notice that the aforementioned works investigate the problem using numerical simulations. Experimental investigations can be found in Franzini et al. (2015) for the problem of a vertical and flexible rod immersed in still fluid and subjected to parametric excitation. The authors focus the analysis in the 1:1, 2:1 and 3:1[3] parametric resonances. The analysis are carried out using a Galerkin decomposition with trigonometric shape functions. It is shown that for the 1:1 resonance a travelling-wave is present on the response, while for the 3:1 resonance the steady-wave corresponding to the third mode of the rod is dominant. For the 2:1 resonance, two modes participate in the dominant response. Spectral analysis also show that the response of the structure can be dominated by more than one mode depending on the excitation frequency.

[3] The nomenclature n:1 indicates that the motion applied to the top has frequency equal to n times the natural frequency of the investigated mode.

2.3.2 Straight flexible rods under VIV

For the offshore application on risers, TLP tethers and similar structures, the behaviour of flexible bodies under the action of VIV is of great interest. Some aspects in this situation are very different compared to the analysis of rigid and elastically mounted cylinders under VIV. The excitation and response of the structure can occur in a multi-modal way. Also, travelling waves due to how the excitation occurs along the structure can have significant effects on the dynamical behaviour. In Wu, Ge & Hong (2012), a detailed review is presented, pointing out the phenomena of travelling-waves, and multi-modal response on slender flexible cylinders under VIV.

Some studies were carried out during the past decades for better understanding VIV in flexible cylinders. In Chaplin et al. (2005b), an experimental study is made considering the lower portion of the cylinder is immersed in fluid with flow, and the other portion is immersed in still fluid. The experiments show multi-modal responses of the cylinder, where some ranges of reduced velocity would lead to almost constant modal compositions. The authors also found that the response is dominated by travelling waves in the transition from a range of reduced velocity with the response dominated by one set of modes to a range dominated by a different set of modes. Following, in Chaplin et al. (2005a) more experiments with the same setup were conducted and compared to different numerical solutions. At that time, the results showed the capability of the empirical models to give results closer to the measured ones when compared to computational fluid dynamics (CFD) simulations. The range of difference between the numerical results and the experimental ones also shows that the phenomenon still needed investigation. It is also shown that the development of models capable of giving reliable results with low computational effort is still needed.

In Pesce & Fujarra (2000), experimental results indicated a jump phenomenon in the cross-flow response as function of the reduced velocity. Following, experiments with a cantilevered cylinder were conducted in Fujarra et al. (2001). The cylinder had different stiffness in both directions, which allowed the authors to notice a high-speed branch to appear in the cross-flow amplitude response. This was considered as a consequence of the excitation of the in-line response in high velocities, leading to oscillations in the cross-wise direction as well. Also, it was pointed out that while three branches of response are typically found for rigid cylinders, there were only two well defined branches of response for the flexible cylinder. The topic was revisited in an experimental campaign with the results and analysis presented in Defensor Filho, Franzini & Pesce (2022).

Flexible cylinders under low tension and VIV were experimentally studied in Huera-Huarte & Bearman (2009). It is shown that for lower values of geometric stiffness the cylinder's first mode amplitude response as a function of the reduced velocity is in good qualitative agreement with the experiments for a rigid cylinder. However, as the applied

traction grows, the resulting amplitudes are significantly smaller than those obtained in rigid cylinders. This is due to the fact that some of the response of the flexible cylinder occurs in higher modes of vibration.

In Franzini et al. (2016) experimental results of a vertical and flexible cylinder were obtained using a direct measure of the displacements of the structure with an optical device. The results were analysed in terms of the amplitudes of the modal responses of the cylinder. The modal amplitude analysis shows that for the lock-in of the first mode, there is a synchronization between the modal amplitudes in the in-line and cross-wise direction. For the second mode lock-in, a similar condition can happen, but it was also detected a regime of oscillation in which the cross-wise amplitudes are increased and the in-line ones are decreased.

Following, in Franzini et al. (2018) a vertical and flexible cylinder is subject to VIV and parametric excitation. The data is treated using the Galerkin projection. Modal analysis were conducted and it is shown that the presence of the parametric excitation changes the amplitude and the spectral content of the response of the cylinder. A major feature is that the parametric excitation causes an amplification of the modal amplitude for a wide range of reduced velocity. This feature can be seen in Fig. 14, where the response amplitude of the first mode of vibration is shown for the cases of pure VIV and concomitant VIV and parametric excitation in a relation of 2:1 or 3:1 of the top motion frequency with the structure's natural frequency.

Figure 14 – Response amplitude of the first mode of vibration for the cases of pure VIV and concomitant VIV and parametric excitation in a relation of 2:1 or 3:1 of the top motion frequency with the structure's natural frequency.

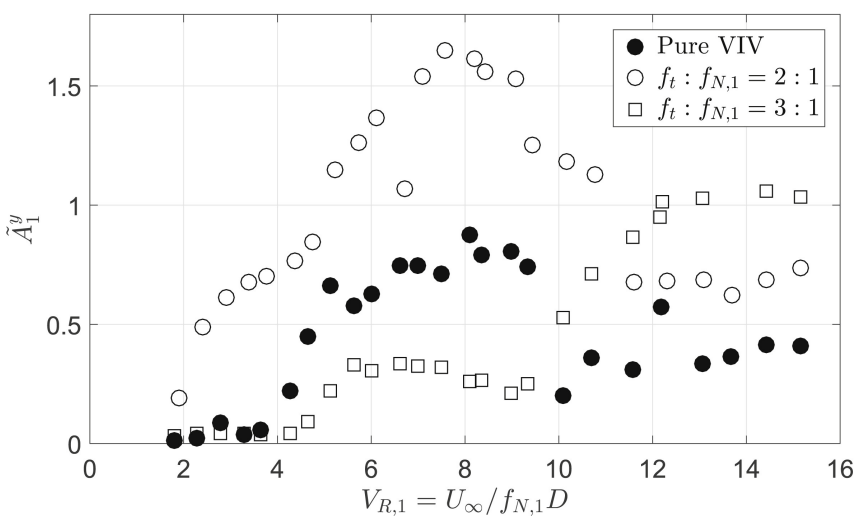

Source: Franzini et al. (2018)

2.4 Dynamics of flexible and statically curved structures

Differently from the case of straight flexible rods, the case of a curved reference configuration deserves special attention even in the "seemingly"[4] simple subject of free vibrations. Thus, the literature review regarding statically curved structures is herein divided into 3 subsections. First, a review regarding free vibrations and modal properties is carried out. The review then follows with the discussions of results found in the literature considering different forms of motion allowed to the supports of the structure. Finally, a brief review of fluid-structure interaction is made, closing this section.

2.4.1 Free vibrations and modal properties of statically curved structures

The studies about the dynamical behaviour of cables can be tracked to the investigations made by Daniel Bernoulli in 1732, where the vibrations of a cable suspended by only one tip were analysed. Those studies were carried out in an experimental perspective, whereas the analytical treatment of the problem has been done by Giuseppe Lagrangia (a.k.a Joseph Lagrange) from 1760 to 1788. Lagrangia considered a discrete model for a cable supported at both ends in the same vertical level, therefore starting the studies concerning a catenary. Later, in 1820, Poisson published the equations of motion for a cable element in Cartesian coordinates. Also at this time, the linear modes of free vibrations for a horizontal catenary[5] were obtained. Following that, the symmetric and antisymmetric modes of free vibrations for a shallow horizontal catenary were obtained by Routh in 1868, considering a maximum value of 1:10 for the ratio between the static sag and the distance between supports. For further details concerning the history of catenary applications and the development of mathematical models for this kind of structure the reader is referred to Irvine & Caughey (1974) and Irvine (1981).

Those earlier studies, before Irvine & Caughey (1974), were based upon the hypothesis that the cable is inextensible. When the concern is to obtain linear models for cables with a large ratio between static sag and cable length, this assumption leads to good results. This occurs due to the fact that in this situation the cable is able to vibrate without extension, achieving that with geometric compensation between tangent and transverse motions. Now, for the cases where the relation between static sag and cable length becomes smaller, approaching a horizontal taut string, the inextensibility condition is not a good approach. In fact, if one thinks about a horizontal taut string, the transversal vibrations are a geometric impossibility for an inextensible model. The investigation of this problem has been left aside until the discussion made by Irvine & Caughey (1974). The authors started the discussion due to the fact that, at their time, the

[4] As the reader can notice during the review, the subject is actually complex with a lot of possible phenomena not commonly found in the study of straight structural members.

[5] The nomenclature horizontal catenary is commonly found in the literature to name a catenary where the cable ends are at the same height.

existing expressions for the modal frequencies of a horizontal taut string and a parabolic cable[6] did not give the same results when the parabolic cable was close to a horizontal taut string. In mathematical language, the difference lays in the transcendental equations for the natural frequencies. The mentioned equations are (2.6) and (2.7) for the parabolic cable and the horizontal taut string respectively.

$$\tan\left(\frac{\lambda L}{2}\right) = \frac{\lambda L}{2} \tag{2.6}$$

$$\cos\left(\frac{\lambda L}{2}\right) = 0 \tag{2.7}$$

In Eqs. (2.6) and (2.7), L is the distance between supports and λ is a parameter obtained through the dispersion relation, given by $\lambda = \sqrt{\mu\omega^2/H}$. In this relation, μ is the mass per unit length, ω is a natural frequency (which are the values intended to be found) and H is the horizontal component of the traction. Aiming to solve the problem, Irvine & Caughey (1974) wrote the geometric compatibility considering the elasticity of the cable. In that way, Eq. (2.8) is obtained as the transcendental equation for the natural frequencies, which can be used for both horizontal parabolic cables and taut strings.

$$\tan\left(\frac{\lambda L}{2}\right) = \frac{\lambda L}{2} - \left(\frac{4}{\lambda_I^2}\right)\left(\frac{\lambda L}{2}\right)^3 \tag{2.8}$$

The parameter λ_I is called the Irvine parameter and is of fundamental importance in the type of solution for the vibration modes. This parameter accounts for the elastic and geometric effects of the cable vibrations and is given by Eq. (2.9) alongside the definition in Eq. (2.10).

$$\lambda_I^2 = \left(\frac{8d}{L}\right)^2 \frac{(EA)\,L}{HL_e} \tag{2.9}$$

$$L_e = \int_0^L \left(\frac{\mathrm{d}s}{\mathrm{d}x}\right)^3 \mathrm{d}x \tag{2.10}$$

In these equations, EA stands for the axial stiffness of the cable, d is the static sag, s is the arclength coordinate and x is the horizontal coordinate. The shift in frequency

[6] The name parabolic cable is used to refer a particular case of horizontal cables where the relation between static sag and horizontal span is small, allowing the use of a parabolic expression to approximate the catenary configuration.

between the small sag horizontal cable and the taut string is then explained due to the values assumed by λ_I in each case. For a small non-zero static sag, the inextensibility condition is given by $EA \to \infty$, which yields $\lambda_I \to \infty$, leading Eq. (2.8) to be the same as Eq. (2.6). On the other hand, letting the static sag to approach zero leads to $\lambda_I \to 0$, so that Eq. (2.8) is turned into Eq. (2.7).

Also, the investigation of Eq. (2.8) made possible for the authors to determine conditions for the occurrence of the cross-over phenomenon. For the definition of cross-over, one needs to consider a dynamical system where the natural frequencies are functions of a known parameter (Irvine parameter in the case in study), and let be defined a reference value of this parameter in order to enumerate the natural frequencies from the lowest to the highest. The cross-over phenomenon is then defined as the situation in which the change of the control parameter implies in a natural frequency of a certain vibration mode to become higher than the one of a higher mode in the reference value of the parameter. For the parabolic cable, regarding vertical oscillations and using $\lambda_I = 0$ as the reference condition, three example cases can be identified:

- $\lambda_I^2 < 4\pi^2$: The frequency of the first symmetric mode stays lower than that of the first antisymmetric mode;
- $\lambda_I^2 = 4\pi^2$: The frequency of the first symmetric mode becomes equal to that of the first antisymmetric mode, defining the first cross-over situation;
- $\lambda_I^2 > 4\pi^2$: The frequency of the first symmetric mode becomes higher than that of the first antisymmetric mode, and the modal shape of the first symmetric mode starts to have internal nodes.

This kind of analysis can be extended to values of λ_I that define additional cross-over situations for the first symmetrical mode or to the behaviour of cross-over phenomenon for other modes. The analytical predictions of Irvine & Caughey (1974) about the modal shapes and frequencies and also regarding the cross-over situations were obtained with good agreement in Gambhir & Batchelor (1978). In the latter, the natural modes and frequencies were studied throughout the finite element method.

Advancing in the studies of linear vibration modes of cables, Triantafyllou (1984) studied the problem of inclined taut cables. The solution is obtained considering that the analysis can be divided into the superposition of two kinds of behaviours for the cable vibrations. Firstly, the author considers the so called fast solution, where the cable is treated as a waveguide for travelling transversal waves. In this kind of solution, the rate of spatial change of the transversal displacement is large compared to that of the static solution, this difference being more pronounced for higher modes. The nomenclature “fast” is them borrowed for the spatial coordinate. Complementing the analysis, the slow solution

is derived considering that perturbations in the tangential direction travel at the speed of the elastic waves, resulting that, for the same frequency, the axial vibrations must have a greater wavelength than the one of transversal vibrations, resulting in perturbations that are slowly varying with space.

The linear modes of vibrations are then obtained as a composition of Bessel and Airy functions and are then named hybrid modes since they will assume a shape that is a combination of symmetric and antisymmetric functions along the cable length. How the hybrid shape will depend on each type of the so called classical modes is dependent on a parameter analogous to the Irvine parameter for accounting the geometric and elastic effects. It is worth to highlight that the inclined condition changes the model in a way that cross-overs are not possible. What happens in fact is an avoided crossings phenomenon, that is, when the frequency of an initially symmetric mode becomes closer of the subsequent initially antisymmetric mode, the frequency corresponding to the latter also starts to increase with the control parameter.

Assuming quasi-static stretching, Triantafyllou & Grinfogel (1986) derive asymptotic equations for the vibration modes and natural frequencies of taut inclined cables. The results are shown to be in good agreement with the predictions by Triantafyllou (1984). The results of both works, including the observance of the existence of hybrid modes and avoided crossings, were also experimentally obtained in Russell & Lardner (1998). Following the investigation on inclined cables, in Pesce et al. (1999) the modes of vibration of an inclined catenary are obtained. The axial dynamics is written as function of the transversal one and a WKB[7] (see Bender & Orszag (1978)) solution is obtained for the vibration modes as well as an analytical approximation using Bessel functions. One remarkable result is that the WKB solution can be applied to the problem of a catenary riser under sea current, considering the adequate statical solution.

Regarding the nonlinear free vibrations and the frequency-amplitude dependency of the vibration modes, initial investigations are presented in Hagedorn & Schäfer (1980), where a shallow horizontal cable is considered. Nonlinear terms originated from the inclusion of the cable elasticity are obtained, with the model being then discretized using the Galerkin method with a single DOF. The solution for the frequency-amplitude dependency is then obtained via the Lindstedt method and also through an analytical solution obtained by considering that the system is conservative and then performing quadratures over the mechanical energy expression. Following, in Luongo, Rega & Vestroni (1982) the same problem is considered with the inclusion of the out-of-plane motion of the cable, with the analysis limited to the first symmetric mode. For that, a 2-DOF model is required after the Galerkin discretization, allowing to investigate couplings between the in-plane and out-of-plane motions and how such couplings affect the frequency-amplitude relationship.

[7] The name of the method is an acronym of the names of its creators, Wentzel, Kramers and Brillouin

Figure 15 – First and second modes of an inclined cable. Shape variation with Irvine's parameter.

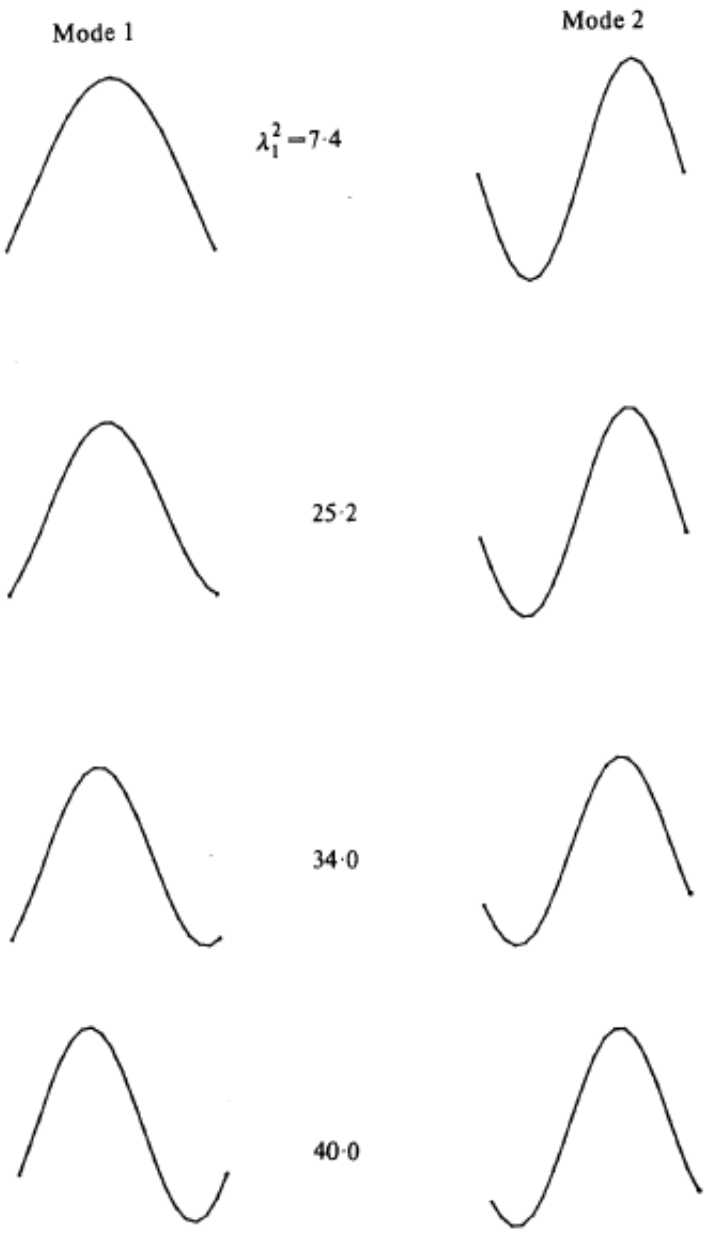

Source: Triantafyllou (1984)

The obtained ROM is then solved with the method of multiple time scales (MMTS), furnishing an analytical formulation for the desired computations. The investigation of other symmetric and antisymmetric modes for the in-plane vibrations is made in a similar manner in Rega, Vestroni & Benedettini (1984). Extending the results regarding the coupling and energy transfer between in-plane and out-of-plane modes, a study with a 2-DOF ROM is made in Benedettini, Rega & Vestroni (1986), with the solution obtained using MMTS. The obtained results show the importance of considering the internal

coupling between in-plane and out-of-plane modes under large vibrations.

Forced vibrations considering super and subharmonic resonances are investigated with similar approaches in Benedettini & Rega (1989) (1 : 1/2 and 1 : 1/3 cases) and Rega & Benedettini (1989) (1 : 2 and 1 : 3 cases), respectively. The resonance condition is obtained by applying an external harmonic load in a manner to obtain the desired conditions. The method of separation of variables is applied to the nonlinear equations, considering linear modal shapes as spatial functions. The method of multiple scales is applied to the resulting oscillators, allowing the authors to discuss the existence and stability of stationary solutions.

In Srinil, Rega & Chucheepsakul (2003), the condition of small sag-to-span ratio is dropped, considering then arbitrarily sagged and inclined cables. The nonlinear equations of motion are treated using the finite-*difference method, applied both in space and time. This work also treats the compatibility relation for the dynamic strain as nonlinear, while in Benedettini, Rega & Vestroni (1986), Benedettini & Rega (1989) and Rega & Benedettini (1989) this relation is linearized. The authors investigate the internal resonances and energy transfer between the linear vibration modes by applying an initial condition that matches the first mode and evaluating how the motion develops. The results show interaction between linear modes, both in the in-plane and swing motions, addressing the necessity of using more than one mode of vibration when considering linear modes for the construction of reduced-order models. Following the studies, in Srinil, Rega & Chucheepsakul (2004), the problem of a horizontal cable with arbitrary sag is considered, with particular focus being made in exploring the internal activations between symmetric and antisymmetric modes, as well as evaluating the enrichment of modal composition as the sag is enlarged. Advancing on the topic of arbitrarily sagged and inclined cables, 2:1 internal resonances are investigated in Srinil, Rega & Chucheepsakul (2006) and Srinil & Rega (2006). The former presents the modelling of the problem together with a MMTS solution and a validation of the model. The latter tackles the conditions for the internal resonances to occur as well as requirements for obtaining ROMs for the problem and the formulation of nonlinear normal modes of vibration.

In order to expand the analysis by dimensionless parameters as in Irvine & Caughey (1974), the horizontal cable is studied in Lacarbonara, Paolone & Vestroni (2007) considering only the geometric nonlinearities, that is, linearizing the terms dependent on dynamical perturbations in the equations of motion. Two parameters are used instead of only one as in Irvine & Caughey (1974). The eigenvalue problem is studied considering a Ritz-Galerkin procedure using trigonometric functions for the spatial interpolation. The authors then can extend the results presented in Irvine & Caughey (1974) about the cross-over phenomenon and modal shapes, showing the effects of the geometric nonlinearities measured by one of the control parameters over those behaviours. Also, a classification based on energy

contributions is presented for the vibration modes. Considering first the potential energy, the division in geometric and strain energy is made. The so called geometric energy refers to the variation in the potential energy of the system due to geometric changes in the cable without stretching, while the strain energy nomenclature follows the widely known internal energy of an elastic string due to strain variation. For the kinetic energy, the comparison is made between the total kinetic energy and the kinetic energy associated with only longitudinal motion. Finally, disregarding the cases of large portions of kinetic energy associated with longitudinal motions, analytical expressions are developed for the vibration modes in terms of the control parameters. Those expressions amplify the range of applications with respect to the the predictions made in Irvine & Caughey (1974).

In Zhou, Yan & Chu (2011), the idea of using two control parameters presented in Lacarbonara, Paolone & Vestroni (2007) is applied to inclined cables with small static sag. The authors also use equations of motion considering linearization in the dynamic perturbations, and the problem is treated considering a static condensation procedure. In that way, the equation of motion for transversal vibrations can be turned into a Bessel equation, allowing well known asymptotic results to be used. Since two parameters are employed, it is possible to show how the static configuration affects the predictions made with only one parameter in Triantafyllou & Grinfogel (1986).

Finally, in Mansour et al. (2018), the equations of motion for a cable supported at both ends with arbitrary inclination are presented. The equations are geometrically exact considering linear elasticity, and then are simplified with a linearization of the terms dependent on the dynamic perturbations. The compatibility relation is also linearized and analytical solutions for the linear modes considering the nonlinear effects induced by the geometry can be obtained. The great contribution of that work is that it can collect in one single formulation the effects studied previously.

2.4.2 Dynamics of statically curved structures with movable supports

The case in which some movement is allowed to the supporting ends of the structure is of particular interest for the present work. One pioneer approach to that is presented in Rega & Luongo (1980), where the linear free-vibrations of a horizontal shallow cable with flexible supports is considered. Only in-plane vibrations are considered, with the supports being modelled as springs in both the horizontal and the vertical directions. The study is carried out by means of a finite difference discretization, and an investigation similar to that in Irvine & Caughey (1974) is made.

For the specific case of prescribed motions of the supports, the initial studies were carried out during the 90's. In Perkins (1992) a cable with small sag is subjected to prescribed motion in one of the supports, with such motion aligned with the local axial direction of the equilibrium configuration. The problem is investigated by means

of a 2-DOF ROM which accounts for the three-dimensional motion of the cable. The model is investigated with MMTS and solutions for the frequency-amplitude relation as well as conditions for existence of stable periodic solutions are shown. The results are also compared to some experimental data, showing good adherence. The cable presents parametric excitation in the out-of-plane direction and a mix of parametric and forced excitations in the in-plane motion. This analysis is extended in Benedettini, Rega & Alaggio (1995), where a 4-DOF ROM is adopted and an external forcing is applied to the cable in combination to the support excitation, which now is not limited to the axial direction of the equilibrium configuration. The investigation is also made by means of MMTS and the existence and stability of steady-state solutions are evaluated. An experimental investigation regarding the simultaneous effects of external forcing and imposed support motion is made in Rega, Alaggio & Benedettini (1997). Finally, a similar analysis of that in Benedettini, Rega & Alaggio (1995) is made in El-Attar, Ghobarah & Aziz (2000), but considering general motions applied to both supports of the cable simultaneously. Expanding the investigations with simultaneous external excitation and imposed boundary motion, a bifurcation analysis is made in detail in Chen et al. (2010). By combining MMTS and continuation analysis, the authors investigate the various types of bifurcations that may arise and also reveal the possibility of chaotic motion.

A different approach in modelling the condition of imposed boundary motion is made in Guo et al. (2015a). In this work, the support motion is written as a small term and is considered to occur only in the out-of-plane direction, in a way that to the first order of the expansions in MMTS the problem is that of fixed boundaries, with the imposed motion effects appearing only at the level of the modulation equations. This methodology is used again in Guo et al. (2015b), where the in-plane vertical motion of the support is added to the problem. Following, in Guo et al. (2016a) the support is represented as a lumped oscillator consisting of a mass attached to a linear spring and a linear dashpot. The imposed motion is applied to this lumped element and it is shown how the tuning of the parameters of such element influence on the type of response the cable presents.

Another effect investigated in the literature is that of asynchronicity in the motions imposed to different supports. In Guo et al. (2016b), this is investigated for the out-of-plane imposed motion, where it is shown the effect of the phase between support motions over both the obtained responses and the conditions that lead to dynamical instabilities. In turn, for the case of in-plane support excitation, this analysis is made in Guo et al. (2017). The latter shows that the phase between support motions is responsible for enhancing the presence of antisymmetric modes in the response, while reducing the participation of the symmetric modes. All the cases so far presented of imposed support motion considered small sag-to-span ratios. This assumption is dropped in the analysis made in Warminski et al. (2016), while keeping the horizontal cable condition. Again, the problem is tackled by means of a ROM investigated with MMTS. The bifurcations that the response undergoes

are investigated, showing an evolution to chaotic regime as the excitation frequency is varied.

Regarding inclined cables, the problem is investigated for taut strings. A pioneer work is actually made for a horizontal scenario in Nayfeh, Nayfeh & Mook (1995). The analysis is made by directly applying MMTS to the PDEs of motion, and then numerically solving the modulation equations. Frequency-response curves are obtained for steady-state regimes as well as scenarios of modulated responses. The solution is also compared to experimental results, showing mostly good agreement for the stable branches of solution. In Gonzalez-Buelga et al. (2008) focus is made on the condition of 2:1 internal resonances. This is achieved by the input of a vertical motion imposed to one of the boundaries with twice the frequency of the first out-of-plane mode, leading to the occurrence of parametric excitations in the out-of-plane motion while causing forced excitations in the in-plane motion. This latter work also presents comparisons with experimental results. Complementing the studies considering in-plane imposed motion, in Wang & Zhao (2009) a detailed bifurcation analysis is carried out for the problem, considering both in-plane and out-of-plane responses.

The inclusion of out-of-plane boundary motion is made in Macdonald et al. (2010) together with the investigation of the modal stability of any chosen vibration mode under the combined forced and parametric excitation induced by the imposed motion. In Macdonald (2016), the multimodal nonlinear responses under general imposed boundary motion are investigated. In those two works, it is possible to find readily available analytical solutions for the response amplitude and the modal stability condition together with its boundaries. Closing the topic of taut strings, in Luongo & Zulli (2011) the effects of an external forcing combined with the support excitation are addressed. The external forcing in the case is due to galloping caused by a wind flow around the cable.

2.4.3 Fluid-structure interactions on statically curved structures

Note that most of the works mentioned investigated the problem of cables in air, with water being considered in Pesce et al. (1999), but only in what matters for the statical equilibrium configuration and linear modal effects. Some major differences can be expected when dealing with the case where the surrounding fluid is water. In this case, the effect of the difference of pressure of the inside and outside of the riser causes a change in the effective traction on the riser, leading to variations of the geometric stiffness. Also, due to sea currents and the motion of the riser, hydrodynamic forces, which are nonlinear and mathematically complicated to deal with in analytical treatments, are expected to act on the riser. Finally, the boundary conditions may present variation in time in addition to the imposed motion condition, since the point where a marine cable touches the ocean floor is not necessarily fixed. In Pesce (1997), a very detailed analysis on catenary risers is

made. Asymptotic solutions are presented for the static problem, considering effects due to sea current, soil stiffness and local bending stiffness on the riser ends. Also, the local dynamical problem in the touch-down zone is investigated, and asymptotic solutions are presented for the dynamical traction and curvature as functions of the movement of the touch-down point. Discussions about the effects of soil stiffness and the touch-down point movement at the dynamical response of a cable can be found in Pesce, Martins & Silveira (2006). The effects of local domain solutions close to the touch-down zone are included in the cable dynamics, and the results are compared to finite element simulations showing good agreement.

Regarding inclined cables with arbitrary sag surrounded by water, the mathematical modelling and solution presents strong challenges. In Alfosail & Younis (2018) an inclined riser[8] with arbitrary sag in the static configuration is subjected to VIV. To simplify the mathematical modelling and the analytical treatment, the authors represent the fluid-structure interactions by means of a harmonic forcing term in the equation of motion. The problem is then investigated with focus on the 2:1 internal resonance condition using MMTS. A similar analysis, with the same approach for modelling the fluid effects is made in Alfosail & Younis (2019), with focus now on the 3:1 internal resonance condition. Both those works show that the effects on the motion amplitude due to the additional mode activated by internal resonance is weak. However, this additional mode significantly contributes to a frequency shift in the response which is of great importance for fatigue analysis. Still with the same approach for the fluid-structure interaction modelling, multi-frequency forcing terms are considered in Alfosail & Younis (2020).

2.5 Nonlinear normal modes

One particularly interesting method of reducing the order of a dynamical system is by means of its nonlinear modes. These modes are the extensions of the well-known linear modes of vibration of a system, and their purpose is to reduce the motion dynamics to a specific set in the state-space. In what concern the present thesis, the nonlinear modes are used for analysis regarding VIV.

The beginning of the studies about nonlinear modes can be tracked back to the works of Rosenberg, that are well detailed in the review presented in Rosenberg (1966). The objective is the use of those nonlinear modes to analyse basic properties of a nonlinear system, such as frequency-amplitude dependence, bifurcations and phase space trajectory amongst others. Initial studies were focused on conservative systems with a small number of DOFs due to the original definitions and requirements for a nonlinear mode.

In Shaw & Pierre (1993), the use of invariant manifolds to describe a nonlinear

[8] The flexural stiffness is taken into account in this work.

mode gave more generality to the subject, also allowing a broader class of systems to be investigated with the technique. The latter work defines a nonlinear mode as a functional relation between a set of slave coordinates and a set of master coordinates. This definition implies the extension of a property of linear modes to the nonlinear ones, that is, if an initial condition belongs to a certain mode, the motion remains in that mode[9] in the absence of internal resonances. The mathematical procedure to determine those functional relations is borrowed from center manifold techniques, which involves eliminating the time derivatives from the equations of motion.

To clarify the mathematical process, consider a discrete dynamical system that can be put in the form of a system of first-order differential equations, with N DOFs, defined as

$$\dot{r}_i = s_i, \tag{2.11}$$

$$\dot{s}_i = f_i\left(\vec{r};\vec{s}\right). \tag{2.12}$$

Overdots are used to denote differentiation with time as usual, and the index i goes from 1 to N. Let $\vec{r} = [r_1, ..., r_N]^T$ be the vector of generalized coordinates, $\vec{s} = [s_1, ..., s_N]^T$ the vector of generalized velocities or quasi-velocities and $f_i\left(\vec{r};\vec{s}\right)$ the generalized forces normalized by the corresponding inertias. Note that nothing was said about the format of the generalized forces. For the basic proposal of the idea following Shaw & Pierre (1993), it is assumed that all coordinates can be written as functions of r_1 and s_1. Assuming then $(r_1, s_1) = (r, s)$, the sought relations are $r_i = R_i\left(r, s\right)$ and $s_i = S_i\left(r, s\right)$ for $i = 1, ..., N$. Notice that $R_1 = r$ and $S_1 = s$.

From these assumptions, all the functional relations will be represented by manifolds mapped by a two dimensional space. This methodology can be applied for higher-order manifolds by simply defining the functional relations in terms of more master coordinates, generating multi-modes instead. The use of higher-order manifolds are found in systems with internal resonances. Now, the system is put in autonomous form by using the same substitution idea of center manifold theory. This is achieved by using the rules

$$\frac{\mathrm{d}}{\mathrm{d}t} = \frac{\partial}{\partial r}\dot{r} + \frac{\partial}{\partial s}\dot{s} = \frac{\partial}{\partial r}s + \frac{\partial}{\partial s}f_1\left(\vec{r};\vec{s}\right). \tag{2.13}$$

Applying that rule to every pair of coordinate (r_i, s_i), an autonomous system is obtained as

[9] This property is know as invariance.

$$S_i = \frac{\partial R_i}{\partial r} s + \frac{\partial R_i}{\partial s} f_1 \left(r, R_2, ..., R_N; s, S_2, ..., S_N\right), \tag{2.14}$$

$$f_i \left(r, R_2, ..., R_N; s, S_2, ..., S_N\right) = \frac{\partial S_i}{\partial r} s + \frac{\partial S_i}{\partial s} f_1 \left(r, R_2, ..., R_N; s, S_2, ..., S_N\right). \tag{2.15}$$

The solution of these equations gives the geometry of the manifolds, however, in general they are as difficult to solve as the initial problem. The advantage of using this form is that it makes possible to use series expansions to find an approximated form for the manifolds near an equilibrium solution. In Shaw & Pierre (1993), a polynomial expansion is adopted, which, although correct, limits the analysis to small amplitudes around the equilibrium. Once the manifolds are determined, the modal Eqs. (2.16) and (2.17) are solved to obtain the modal dynamics for the problem.

$$\dot{r} = s, \tag{2.16}$$

$$\dot{s} = f_1 \left(r, R_2, ..., R_N; s, S_2, ..., S_N\right). \tag{2.17}$$

After the integration of the modal equations, analytically or numerically, the dynamics of all the coordinates can be assembled using the determined manifolds. Notice that other methods commonly used in nonlinear dynamics analysis, like MMTS, can still be applied to the system. This approach is even made easier thanks to the reduction in the number of DOFs of the system.

From the general definition, various works have been made in order to obtain and analyse the nonlinear modes, using different approaches. In Nayfeh, Chin & Nayfeh (1996), systems with cubic nonlinearities are investigated in the condition of 1:1 and 3:1 internal resonances. The nonlinear modes are obtained by writing the system in complex coordinates and applying MMTS. In King & Vakakis (1996), an energy approach is utilized to obtain the nonlinear modes. However, this approach is limited to conservative systems. Finally, a different approach to obtain the nonlinear modes is used in Pesheck, Pierre & Shaw (2002) and Jiang, Pierre & Shaw (2005). In these works, the mechanical variables are first written in the polar form, with the manifold equations being obtained in the new set of variables. Following, a Galerkin scheme is utilized to obtain the coefficients for a series to describe the manifold. This type of approach helps to solve the limitation of the polynomial expansion presented in Shaw & Pierre (1993), which can rapidly lose accuracy for large values of amplitude away from the equilibrium configuration.

Different approaches have also been developed to deal with continuous systems. In Soares & Mazzilli (2000), planar frames are discretized by FEM and the nonlinear

modes are obtained for the resulting system of equations. Following, in Mazzilli & Baracho Neto (2002), a general approach to obtain the nonlinear modes with MMTS for systems discretized by FEM. Finally, in Baracho Neto & Mazzilli (2005) the nonlinear modes for models discretized by FEM are obtained for systems with internal resonance. A different approach is to directly investigate the continuous equations of motion to obtain the nonlinear modes. In Nayfeh & Nayfeh (1994) the nonlinear modes for a class of structural systems are obtained, with a comparison being made between the analysis with the discretized system and attacking directly the continuous equations of motion. It is shown in the paper that the two approaches are in agreement when a complete modal basis for the linear problem is used in the discretization procedure with the Galerkin method. In Nayfeh, Lacarbonara & Chin (1999), a buckled beam which can undergo internal resonances is investigated. The nonlinear modes are obtained directly from the continuous equations of motion by means of MMTS. Following, in Lacarbonara, Rega & Nayfeh (2003) a general analytical approach for the analysis with nonlinear modes of one dimensional structural systems that may undergo internal resonance is presented in detail. The work keeps the possibility of not initially straight structures and internal resonances with the 1:1, 2:1 and 3:1 frequency relations. Finally, in Lacarbonara & Rega (2003) the conditions for activation and orthogonality of the nonlinear modes of shallow structural systems is presented.

Studies about bifurcation scenarios and the search for specific orbits in the phase space, such as homoclinic orbits, my be found in Lenci & Rega (2007) and Lenci & Rega (2010). In those works, buckled beams with different boundary conditions are analysed and the continuous system is discretized by a Galerkin scheme. Some qualitative conclusions about the homoclinic orbits and the system dynamics are then addressed with a combination of series expansions and analytical techniques by using the invariant manifold approach.

A detailed review about nonlinear modes, how to compute them and their use for practical analyses is present in Kerschen et al. (2009) and Peeters et al. (2009). In these works, it is possible to find some ways to compute the nonlinear modes, some with purely numerical schemes. It is also shown how to make bifurcation analysis with continuation techniques. More recently, a review on nonlinear modes and how to use them to obtain ROMs is presented in Mazzilli, Gonçalves & Franzini (2022).

Regarding the specific application of nonlinear modes to structures undergoing VIV, some few works can be found on the literature. In both Keber & Wiercigroch (2007) and Keber & Wiercigroch (2008) a slender riser under VIV is investigated, the difference lying in the inclusion of internal flow along the riser in the latter. In both works, the free dynamics of the structure containing both axial and transversal vibrations is reduced to a single DOF model by means of the nonlinear modes. The VIV is then considered as a forcing term in the reduced equation of motion and the fluid variable obeys a Van der

Pol type equation. The resulting dynamical system is then numerically integrated and analysed. Following, in Mazzilli & Sanches (2011) a slender riser is discretized by FEM. The structural model is reduced by means of nonlinear modes and the phenomenological model is incorporated afterwards. Again, no functional relation considering the dynamical system after the incorporation of the phenomenological model was investigated.

2.6 Relation of this thesis with ongoing research topics in the literature

Keeping in mind that the main focus of this thesis concerns obtaining ROMs and the advantages they may present for analysis, some wording regarding their formulation is necessary. The approach to obtain ROMs in this thesis is by means of the Galerkin projection over the PDEs of motion of the structure. The Galerkin projection ensures that the error will be minimum within the vectorial space spanned by the adopted projection functions basis. However, it does not guarantee the quality of the solution in the sense of replicating the original model, with such quality being strongly dependent on the adopted basis. The main problem is that, although some general idea of how to choose good projection functions is known, there is no methodology to ensure a given projection basis is actually a good one before performing comparisons with a solution obtained by other means, such as experiments, numerical simulations using higher-order hierarchical models or analytical solutions. Some examples of works where a comparison is made regarding the qualitative behaviour of different order reducing techniques are Rega et al. (1999) and Guo et al. (2020). It is noticeable, however, that focus in the qualitative aspects of conceiving the projection basis is not common in the literature.

This thesis then sheds some light in the matter of the effects of different projection functions, exploring even some cases where very similar functions are compared between each other but with the small differences leading to significant changes in the obtained results. Another explored situation is that where poor choices for the projection basis is not solved by simply enlarging the set of projection functions. The latter case is particularly important since it is a very present common belief that a poor representation is due to the lack of convergence of the ROM because its projection basis is not large enough. Sometimes, the problematic representation has its origin on qualitative aspects that must be present on the projection function[10]. This type of investigation herein made also shows a path to obtain minimalist ROMs, that is, the smallest possible ROM for a given problem while still keeping adequate accuracy.

[10] A simple mental exercise to illustrate that is the case of a damped mass-spring system. The solution is a trigonometric function with a specific frequency and an amplitude decaying exponentially with time. If one tries to solve it with a series of trigonometric function with constant amplitude, the desired solution will not be achieved no matter how many terms are included in the expansion.

Another element with room for discussions in the literature concerns the FSI, specially for the case of statically curved elements. There are some key features regarding the nonlinear hydrodynamic damping and the phenomenology of VIV that must be carefully taken into account in the mathematical model. Those features however tend to bring further complications in terms of analysis, specially when an analytical pathway is pursued. The usage of simplifications is then common, as it can be seen in linear approximations for the hydrodynamic nonlinear damping or assuming the VIV effects to be a given external forcing. Both approaches, however, have drawbacks in the results. The nonlinear damping is fundamental in the limitation of responses due to parametric excitation as shown in Chatjigeorgiou (2004), and interferes with the arising of internal resonances. Regarding VIV, the usage of a given forcing term eliminates from the model the fact that the structural response influences the vortex shedding itself.

This is another point where this thesis brings contributions. The classical Morison damping is considered in the investigations with still fluid, with techniques being presented to tackle its mathematical complications in pursuing analytical solutions. It is also used to show some of the advantages of refining the projection functions to obtain ROMs. In what concerns VIV, a phenomenological approach that considers an oscillator to represent the fluid is made, allowing for the interactions between fluid and structure to go both ways. Although the usage of such models is already present in the literature, this thesis brings a new way to perform an order reduction in this case by the usage of nonlinear normal modes.

Finally, the thesis also brings novel results obtained by applying MMTS directly over the PDEs of motion for the problem of straight structures under parametric excitation. It is important to highlight that the common practice is to apply the method over the ODEs of the discretized system, with few works focusing on a direct application over the PDEs. This leaves open room for such application in various different problems. In the particular case of the thesis, the case of parametric excitation of straight rods is investigated with this technique. The obtained solution is then combined with some series expansions and algebraic investigations in order to reduce it to the evaluation of a series of polynomials. This approach then leads to the creation of a simple methodology to create a design aiding tool using electronic spreadsheets, while it still keeps the essential characteristics of the solution obtained with advanced techniques.

3 Modelling flexible members in straight or curved configurations

The first step in studying the dynamics of a structural element is to obtain an adequate mathematical model for its behaviour, that is, the equations of motion for the problem. This can be achieved by different approaches, for instance, using a Newtonian or a Hamiltonian philosophy of modelling allied with either a Lagrangian or Eulerian reference system. The choice between different types of coordinate systems or modelling approaches can vary for each problem depending on the researcher's objectives and what is intended to be highlighted in the final form obtained for the equations of motion. In this thesis, all the equations are obtained with reference to a Lagrangian system while the choice between a Newtonian or Hamiltonian approach is case-dependent, being stated in the appropriate portions of the text.

In this chapter, only the equations of motion for the case of free dynamics are derived with boundary conditions closely related to the problems investigated along the thesis. The equations obtained in that fashion are easily adjusted to the specific problems of application with small and simple changes, thus presenting enough generality to be herein presented in highlight. Considering that key differences are posed in the modelling by the presence or absence of curvature in the adopted reference configuration of the structural member, this chapter is concisely divided in two sections. Section 3.1 brings the modelling of flexible elements that are perfectly straight in the reference configuration. Complementary to it, Section 3.2 brings modelling discussions regarding curved flexible elements with the dynamics contained in the same plane of the reference configuration.

3.1 Vertical flexible rods

The simplest structural model that appears in engineering problems is that of a flexible rod that can be considered to have a perfectly straight shape in its reference configuration. The fact that the structural element is initially straight allows for a deduction of the equations of motion with a simpler mathematical development. That is, although the algebraic manipulations are long and intricate, the required geometrical concepts are quite simple.

The deduction herein presented is made using Euler angles to describe the motion of a general cross-section, assuming that the structural element behaves within the classical Bernoulli-Euler kinematic assumption. This hypothesis states that plane cross-sections, initially orthogonal to the centroid axis of a rod, remains plane, undeformed and orthogonal

to the central axis for all displacements. This hypothesis define the kinematic behaviour of all the points of the rod as a function of the displacements of the centroid axis alone, as is shown in the following deduction. This hypothesis is particularly suitable for very slender structures as the ones investigated in this thesis. Non-slender structures such as very short beams require different hypothesis to be adopted such as the one made in the Timoshenko beam theory.

The mathematical development in this chapter for straight rods is based on the work by da Silva (1988), with the use of appropriate simplifications when suitable. The choice of this particular approach is due to the great generality presented in da Silva (1988), together with its capability of easily specify when further modelling hypothesis are made and their meaning and consequences. Some mathematical relations are obtained in a different sequence that is considered simpler by the author of this thesis and more straightforward from analytical geometry concepts.

3.1.1 3D Kinematics of the Bernoulli-Euler flexible rod

Consider an initially straight beam, with the centroid axis aligned with the Z coordinate axis and with principal axis of inertia aligned with the coordinate axes X and Y. At this point, no relationship is stated between those axes and meaningful physical directions such as the gravity direction. This allows for a general formulation to which small increments can be made at the final steps of modelling to relate it to specific cases without changing the fundamentals of the modelling process.

The reference frame $OXYZ$ is fixed, and has the origin O $(Z = 0)$ at the centroid of one of the ending cross sections of the rod. The unit vectors of the reference frame are named as $\widehat{i}$, $\widehat{j}$ and $\widehat{k}$, while the corresponding displacements on each direction are $U(Z,t)$, $V(Z,t)$ and $W(Z,t)$ respectively, with t representing time. Consider also the local cross-section frame $C_g\eta\zeta\xi$, with unit vectors $\widehat{\eta}$, $\widehat{\zeta}$ and $\widehat{\xi}$ with origin at the cross-section centroid C_g. The unit vectors are such that $\widehat{\xi}$ is parallel to the beam axis at the deformed configuration, while $\widehat{\eta}$ and $\widehat{\zeta}$ are always parallel according to the cross-section's principal axes that were initially aligned with the X and Y directions respectively.

One of the measures that can be defined only by means of the kinematics of the structure is the strain measure. To that end, consider two points over the rod axis, $M = (0,0,Z)_{XYZ}$ and $N = (0,0,Z+\mathrm{d}Z)_{XYZ}$. The positions of the points after the rod undergoes the defined displacements are given as $M^* = (U,V,Z+W)_{XYZ}$ and $N^* = (U+\mathrm{d}U, V+\mathrm{d}V, Z+\mathrm{d}Z+W+\mathrm{d}W)_{XYZ}$ respectively. The linear strain measure is, by definition, the ratio between the increment in length of an infinitesimal fiber of the structure and its original length. It is easier however to compute first the quadratic strain measure ε_q and use it to then obtain the linear strain measure. The quadratic strain is defined as half of the difference between the quadratic length of the fiber in the final and

original configurations divided by the quadratic of the original length. For the case at hand it reads

$$\varepsilon_q = \lim_{\mathrm{d}Z\to 0} \frac{1}{2}\left(\frac{\|M^*N^*\|^2 - \|MN\|^2}{\|MN\|^2}\right) = \frac{1}{2}\lim_{\mathrm{d}Z\to 0}\left(\frac{\mathrm{d}U^2 + \mathrm{d}V^2 + \mathrm{d}W^2 + 2\mathrm{d}Z\mathrm{d}W}{\mathrm{d}Z^2}\right)$$
$$= W' + \frac{1}{2}\left(U'^2 + V'^2 + W'^2\right). \tag{3.1}$$

Primes are used to denote partial differentiation with respect to the reference coordinate Z. The relationship between linear and quadratic strain is well-known and furnishes

$$\varepsilon_\ell = \sqrt{1 + 2\varepsilon_q} - 1 = \sqrt{1 + 2W' + U'^2 + V'^2 + W'^2} - 1. \tag{3.2}$$

Now, the final deformed configuration is described using Euler angles, through a step-by-step procedure. For a clear understanding of the angles at each step, they are graphically shown in Fig. 16. It is important to state that this choice is not unique, being possible to define a total of 24 different triads of Euler angles. The ones chosen in this work are based on da Silva (1988) and have a close relationship with commonly used quantities in studies of flexible one-dimensional structures.

Figure 16 – Definition of the Euler angles.

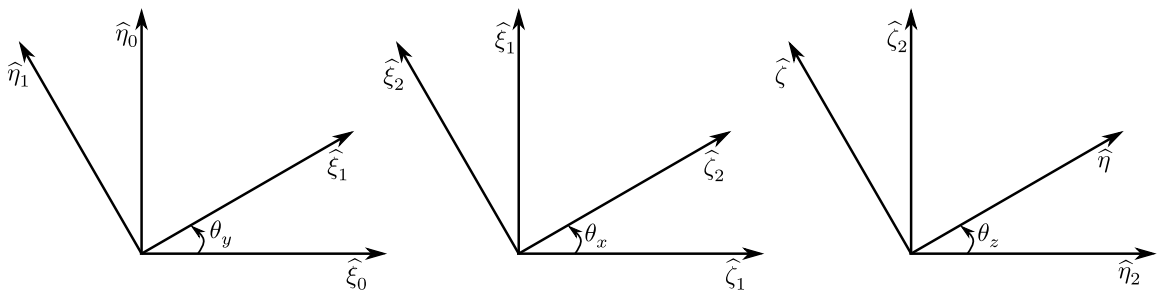

Source: The author.

At the reference configuration the cross-section frame is parallel to the reference frame, thus, $\widehat{\eta}_0//\widehat{i}$, $\widehat{\zeta}_0//\widehat{j}$, and $\widehat{\xi}_0//\widehat{k}$. Initially, a rotation θ_y around ζ_0 axis is made, leading the cross-section frame to the new directions $\widehat{\eta}_1$, $\widehat{\zeta}_1//\widehat{\zeta}_0$ and $\widehat{\xi}_1$. In the sequence, a rotation θ_x is applied around axis η_1, leading the cross-section frame to the directions $\widehat{\eta}_2//\widehat{\eta}_1$, $\widehat{\zeta}_2$ and $\widehat{\xi}_2$. Finally, a rotation θ_z is applied around axis ξ_2, leading the cross-section reference frame to $\widehat{\eta}$, $\widehat{\zeta}$ and $\widehat{\xi}//\widehat{\xi}_2$. Notice that this last angle θ_z is a purely twisting angle applied to the structure. Although the present research does not consider torsion in the analysis made

in further chapters, the formulation is herein made with the torsional response present for the sake of completeness.

Before moving into further calculations, it is useful to define the rotation matrices associated with each of those angles. Let those matrices to be identified as $[\theta_x]$, $[\theta_y]$ and $[\theta_z]$ in correspondence to the angles θ_x, θ_y and θ_z respectively. From common linear algebra relations, it is straightforward to write

$$[\theta_y] = \begin{bmatrix} \cos\theta_y & 0 & -\sin\theta_y \\ 0 & 1 & 0 \\ \sin\theta_y & 0 & \cos\theta_y \end{bmatrix}, \tag{3.3}$$

$$[\theta_x] = \begin{bmatrix} 1 & 0 & 0 \\ 0 & \cos\theta_x & \sin\theta_x \\ 0 & -\sin\theta_x & \cos\theta_x \end{bmatrix}, \tag{3.4}$$

$$[\theta_z] = \begin{bmatrix} \cos\theta_z & \sin\theta_z & 0 \\ -\sin\theta_z & \cos\theta_z & 0 \\ 0 & 0 & 1 \end{bmatrix}. \tag{3.5}$$

The inverse relationships are trivially given by $[\theta_i]^{-1} = [\theta_i]^{\mathrm{T}}$, with i denoting any of the subscripts and the superscript "T" denoting simple transposition when used as a matrix superscript. The next step is to obtain the relationship between the Euler angles θ_x and θ_y with the Cartesian displacements. Since θ_z is a purely twisting angle, it is not related to the Cartesian displacements of the points of the rod's centroid axis and instead is an independent DOF. A simple way to obtain the desired relations is by recalling the computation of the tangent vector of parametrized curves from basic calculus. For a curve $\vec{\Gamma}(s)$, where s is any parameter used to map it, the vector given as $\mathrm{d}\vec{\Gamma}/\mathrm{d}s$ is tangent to the curve. In the particular case that s is taken as the arclength coordinate, the tangent vector computed that way is unitary. With that, it is possible to assure that any tangent vector to the centroid axis of the rod is a multiple of

$$\vec{t} = U'\widehat{i} + V'\widehat{j} + (1 + W')\,\widehat{k}. \tag{3.6}$$

This vector can be taken to the local frame by means of Eqs. (3.3) to (3.5) by appropriate matrix multiplications. After some algebraic manipulation it is possible to write it as

$$
\begin{aligned}
\vec{t} = &\left(\left(U' \cos\theta_y - (1+W')\sin\theta_y\right)\cos\theta_z\right)\widehat{\eta} \\
&+ \left(\left(V'\cos\theta_x + \left(U'\sin\theta_y + (1+W')\cos\theta_y\right)\sin\theta_x\right)\sin\theta_z\right)\widehat{\eta} \\
&+ \left(\left(V'\cos\theta_x + \left(U'\sin\theta_y + (1+W')\cos\theta_y\right)\sin\theta_x\right)\cos\theta_z\right)\widehat{\zeta} \\
&- \left(\left(U'\cos\theta_y - (1+W')\sin\theta_y\right)\sin\theta_z\right)\widehat{\zeta} \\
&+ \left(-V'\sin\theta_x + \left(U'\sin\theta_y + (1+W')\cos\theta_y\right)\cos\theta_x\right)\widehat{\xi}.
\end{aligned} \tag{3.7}
$$

It is possible now to use a fundamental aspect of analytical geometry that is, in the local reference frame the tangent vector must be a multiple of $(0,0,1)_{\eta\zeta\xi}$, which means all terms in Eq. (3.7) that multiply $\widehat{\eta}$ and $\widehat{\zeta}$ must zero out. Also, since the angle θ_z is independent, the terms on $\cos\theta_z$ and $\sin\theta_z$ must cancel out independently, leading to

$$
U'\cos\theta_y - (1+W')\sin\theta_y = 0 \Rightarrow \tan\theta_y = \frac{U'}{1+W'}, \tag{3.8}
$$

$$
V'\cos\theta_x + \left(U'\sin\theta_y + (1+W')\cos\theta_y\right)\sin\theta_x = 0. \tag{3.9}
$$

Recalling that $\tan^2 x + 1 = \sec^2 x$, Eq. (3.8) furnishes

$$
\frac{U'^2}{(1+W')^2} + 1 = \frac{1}{\cos^2\theta_y} \Rightarrow \cos\theta_y = \frac{1+W'}{\sqrt{(1+W')^2 + U'^2}}, \tag{3.10}
$$

which leads to

$$
\sin^2\theta_y = 1 - \frac{(1+W')^2}{(1+W')^2 + U'^2} \Rightarrow \sin\theta_y = \frac{U'}{\sqrt{(1+W')^2 + U'^2}}. \tag{3.11}
$$

Notice that the positive sign is adopted in both cases where a square root extraction was applied. The reason behind this in Eq. (3.10) is to keep the angles between $\pm\pi/2$, domain where the cosine is positive. Notice that for common structural applications, not involving rigid body motions, $|W'| \ll 1$, ensuring that $(1+W') > 0$. In turn, the reason for the positive sign in Eq. (3.11) is that positive angles θ_y geometrically implies that the displacement U is crescent with the coordinate Z, meaning positive values of U' must be related to positive values of θ_y. Finally, to obtain relations for θ_x it is now possible to substitute Eqs. (3.10) and (3.11) in Eq. (3.9) leading to

$$V' \cos\theta_x + \left(\frac{U'^2 + (1+W')^2}{\sqrt{(1+W')^2 + U'^2}} \right) \sin\theta_x = 0 \Rightarrow \tan\theta_x = \frac{-V'}{\sqrt{(1+W')^2 + U'^2}}. \tag{3.12}$$

The process to obtain the corresponding sine and cosine of θ_x is exactly the same made for θ_y, reason why it is not repeated and only the final results are reported in Eqs. (3.13) and (3.14).

$$\cos\theta_x = \frac{\sqrt{(1+W')^2 + U'^2}}{\sqrt{(1+W')^2 + U'^2 + V'^2}}, \tag{3.13}$$

$$\sin\theta_x = \frac{-V'}{\sqrt{(1+W')^2 + U'^2 + V'^2}}. \tag{3.14}$$

With that, all the Euler angles are defined in terms of the DOF used in this thesis, that is U, V and W, together with the angle θ_z for completion. The next steps now involve the obtaining of the strain measure in any point P of the cross-section. So far, this measure has only being defined for points on the centroid axis as given by Eq. (3.2). For a better assimilation, the same letters used for the local reference frame unit vectors are employed to measure coordinates on this frame. Let then the generic point P have an associate position vector given by

$$\vec{r}_{\mathrm{P}} = \eta\widehat{i} + \zeta\widehat{j} + Z\widehat{k}, \tag{3.15}$$

while its position in the deformed configuration, given as point P* is

$$\vec{r}_{\mathrm{P}^*} = \eta\widehat{\eta} + U\widehat{i} + \zeta\widehat{\zeta} + V\widehat{j} + (Z+W)\,\widehat{k}. \tag{3.16}$$

Notice the use of the non-deformability condition of the cross-section in the measures over the local frame. Another assumption that is implicit in that expression for the final position after displacements is the absence of warping of the cross-section, which would imply adding up a term $f(\eta, \zeta, U, V, W, \theta_z)\widehat{\xi}$ to the expression, with f being a suitable warping function for the problem of desire. Applying simple differentiation rules it is possible to write in infinitesimal terms that

$$\mathrm{d}\vec{r}_{\mathrm{P}} = \mathrm{d}\eta\widehat{i} + \mathrm{d}\zeta\widehat{j} + \mathrm{d}Z\widehat{k}, \tag{3.17}$$

$$\mathrm{d}\vec{r}_{\mathrm{P}*} = \mathrm{d}\eta\widehat{\eta} + U'\mathrm{d}s\widehat{i} + \mathrm{d}\zeta\widehat{\zeta} + V'\mathrm{d}s\widehat{j} + (1+W')\,\mathrm{d}s\widehat{k} + \vec{C}\wedge\left(\eta\widehat{\eta}+\zeta\widehat{\zeta}\right)\mathrm{d}s, \tag{3.18}$$

with $\wedge$ denoting the classical cross product in $\mathbb{R}^3$. The vector $\vec{C}$ is the "spatial angular velocity" vector of the curve described by the displaced central axis mapped by the coordinate Z[1]. This name is used since, for differentiation rules, this vector assumes the same role as the angular velocity vector of a material point moving along a given curve parametrized by time. It expresses how the local frame changes in all its direction components with an advance in the mapping coordinate. For the case of the displaced curve considered, the expression is

$$\begin{aligned}\vec{C} &= \theta'_y\widehat{\zeta}_1 + \theta'_x\widehat{\eta}_2 + \theta'_z\widehat{\xi}\\ &= \left(\theta'_y\cos\theta_x\sin\theta_z + \theta'_x\cos\theta_z\right)\widehat{\eta} + \left(\theta'_y\cos\theta_x\cos\theta_z - \theta'_x\sin\theta_z\right)\widehat{\eta} + \left(\theta'_z - \theta'_y\sin\theta_x\right)\widehat{\xi}\\ &= C_\eta\widehat{\eta} + C_\zeta\widehat{\zeta} + C_\xi\widehat{\xi},\end{aligned} \tag{3.19}$$

with C_η, C_ζ and C_ξ being merely nomenclature definitions to reduce the algebraic work. As noted in da Silva (1988), the generalized curvature vector for the rod is simply given by $\vec{C}/(1+\varepsilon_\ell)$. Now, the Green strain tensor is used in order to obtain the complete set of local strains at the generic point P after displacements. By definition, this tensor is written as

$$\mathrm{d}\vec{r}_{\mathrm{P}*}\cdot\mathrm{d}\vec{r}_{\mathrm{P}*} - \mathrm{d}\vec{r}_{\mathrm{P}}\cdot\mathrm{d}\vec{r}_{\mathrm{P}} = 2\begin{pmatrix}\mathrm{d}Z & \mathrm{d}\eta & \mathrm{d}\zeta\end{pmatrix}\begin{bmatrix}\varepsilon_{zz} & \varepsilon_{z\eta} & \varepsilon_{z\zeta}\\ \varepsilon_{\eta z} & \varepsilon_{\eta\eta} & \varepsilon_{\eta\zeta}\\ \varepsilon_{\zeta z} & \varepsilon_{\zeta\eta} & \varepsilon_{\zeta\zeta}\end{bmatrix}\begin{pmatrix}\mathrm{d}Z\\ \mathrm{d}\eta\\ \mathrm{d}\zeta\end{pmatrix} \tag{3.20}$$

The calculation involving the scalar products are cumbersome, being made in Appendix A for the sake of readability. Expanding Eq. (3.20) and collecting the correspondent products, the components of the Green's strain tensor are given as

$$\varepsilon_{zz} = \frac{\left((1+\varepsilon_\ell)^2 - 1 + (\eta^2+\zeta^2)\,C_\xi^2 + \left(\zeta C_\eta - \eta C_\zeta\right)^2 + 2\,(1+\varepsilon_\ell)\left(\zeta C_\eta - \eta C_\zeta\right)\right)}{2}, \tag{3.21}$$

$$\varepsilon_{z\eta} = \frac{-\zeta C_\xi}{2}, \tag{3.22}$$

[1] This is obtained from Kirchhoff's kinetic analogy.

$$\varepsilon_{z\zeta} = \frac{\eta C_\xi}{2}, \tag{3.23}$$

$$\varepsilon_{\eta\eta} = \varepsilon_{\zeta\zeta} = \varepsilon_{\eta\zeta} = 0. \tag{3.24}$$

The consistency of the model developed so far can be verified by the constantly null values for all the strains that would involve deformations of the cross-section. Notice also that the distortion measures obtained this way are consistent with circular cross sections or closed sections made of thin members. For further nomenclature simplification, it is possible to define an auxiliary strain measure given as

$$\varepsilon^* = \varepsilon_\ell + \zeta C_\eta - \eta C_\zeta, \tag{3.25}$$

which allows to write

$$\varepsilon_{zz} = \frac{(1+\varepsilon^*)^2 - 1 + (\eta^2 + \zeta^2)\, C_\xi^2}{2}. \tag{3.26}$$

Finally, as in da Silva (1988), another simplification is made regarding strain. Along this thesis, all the structural elements are supposed to stay within the range of strain where the linear-elastic rheological model is valid. In this case the strain values are usually much smaller than unity, meaning that strain measures can be linearized with respect to other strain measures. In the case at hand, the expression for ε_{zz} is linearized with respect to ε^*, leading to

$$\varepsilon_{zz} = \varepsilon^* + \frac{(\eta^2 + \zeta^2)\, C_\xi^2}{2}. \tag{3.27}$$

It is important to emphasize that the final strain measure is linearized with respect to another strain measure and not with respect to the displacements. This is the proper way of mathematically dealing with strains since small strains do not imply in small displacements and linearizing the results with respect to the displacements would limit the range of validity of the modelling carried out so far. With that, all the needed kinematic quantities have been defined.

3.1.2 Equations of motion

For this problem, Hamilton's principle is chosen to proceed in obtaining the equations of motion. For the application of the principle, the development of the expressions for the kinetic and strain energy are needed. It is assumed that the cross-section center of mass coincides with its centroid, which is true for a wide range of shapes and combined designs. With that, the expression for the kinetic energy is

$$\mathcal{T} = \int_0^\ell \left(\frac{\mu}{2} \left(\dot{U}^2 + \dot{V}^2 + \dot{W}^2 \right) + \frac{J_\xi \omega_\xi^2}{2} \right) \mathrm{d}Z. \tag{3.28}$$

The quantity J_ξ is the mass moment of inertia for the cross section and μ is the mass per unit length of the structure and ω_ξ is the angular velocity around the $\widehat{\xi}$ axis. The angular velocities around other axes are not considered since their contribution to the total kinetic energy is negligible for slender structures for which the Bernoulli-Euler hypothesis is valid. The strain energy of the rod following linear elasticity is written as the volume integral

$$\mathcal{V} = \frac{1}{2} \iiint_V \left(\sigma_{zz} \varepsilon_{zz} + 2 \left(\sigma_{z\eta} \varepsilon_{z\eta} + \sigma_{z\zeta} \varepsilon_{z\zeta} \right) \right) \mathrm{d}V, \tag{3.29}$$

where σ denotes the stress corresponding to the directions of the strains. Considering the linear elastic model for the rod's material and the Young E and shear G moduli, the stresses are given as $\sigma_{zz} = E\varepsilon_{zz}$, $\sigma_{z\eta} = 2G\varepsilon_{z\eta}$ and $\sigma_{z\zeta} = 2G\varepsilon_{z\zeta}$, in a way that the energy expression becomes

$$\mathcal{V} = \iiint_V \left(\frac{E\varepsilon_{zz}^2}{2} + 2G \left(\varepsilon_{z\eta}^2 + \varepsilon_{z\zeta}^2 \right) \right) \mathrm{d}V, \tag{3.30}$$

which, when expanded, reads

$$\begin{aligned} \mathcal{V} = \iiint_V \Big(& \frac{E}{2} \Big(\varepsilon_\ell^2 + C_\eta^2 \zeta^2 + C_\zeta^2 \eta^2 + 2\varepsilon_\ell C_\eta \zeta - 2\varepsilon_\ell C_\zeta \eta - 2C_\eta C_\zeta \eta\zeta + \varepsilon_\ell C_\xi^2 \left(\eta^2 + \zeta^2 \right) \\ & + C_\eta C_\xi^2 \zeta \left(\eta^2 + \zeta^2 \right) - C_\zeta C_\xi^2 \eta \left(\eta^2 + \zeta^2 \right) + \frac{C_\xi^4}{4} \left(\eta^2 + \zeta^2 \right)^2 \Big) + \frac{G C_\xi^2}{2} \left(\eta^2 + \zeta^2 \right) \Big) \mathrm{d}V. \end{aligned} \tag{3.31}$$

Now, considering that the origin of the local frame is the centroid of the cross-section, it is possible to use geometrical area integrals to simplify the expression to

$$\mathcal{V} = \int_0^\ell \left(\frac{E}{2} \left(A\varepsilon_\ell^2 + C_\eta^2 I_\eta + C_\zeta^2 I_\zeta + \varepsilon_\ell C_\xi^2 \left(I_\zeta + I_\eta \right) + \frac{C_\xi^4}{4} I_4 \right) + \frac{G C_\xi^2}{2} \left(I_\zeta + I_\eta \right) \right) \mathrm{d}Z, \tag{3.32}$$

with I_η and I_ζ being the commonly known area moment of inertia, while I_4 is defined as

$$I_4 = \iint_A \left(\eta^2 + \zeta^2 \right)^2 \mathrm{d}A. \tag{3.33}$$

For means of putting the strain energy expression in a form with common coefficients used in strength of materials, Eq. (3.32) is rewritten as

$$\mathcal{V} = \int_0^\ell \left(\frac{E}{2} \left(A\varepsilon_\ell^2 + C_\eta^2 I_\eta + C_\zeta^2 I_\zeta + \varepsilon_\ell C_\xi^2 I_p + \frac{C_\xi^4}{4} I_4 \right) + \frac{G C_\xi^2}{2} I_t \right) \mathrm{d}Z, \tag{3.34}$$

where I_p is the polar moment of inertia which is always $I_p = I_\eta + I_\zeta$ and I_t is the torsional moment of inertia which is equal to I_p for circular or closed thin-walled sections but in general is different and is computed as a function of the distortion function over the cross-section. For the cases where $I_t \neq I_p$ the formulation in da Silva (1988) can be checked by the reader. Considering now that the Euler angles are small, which is valid while the displacements are small compared to the half-wave length of the expected motion developed by the rod, the expressions for the angles are taken as linear with regard to the displacements, as usual in the literature, leading to

$$\theta_x = -V', \tag{3.35}$$

$$\theta_y = U', \tag{3.36}$$

$$\omega_\xi = \dot{\theta}_z, \tag{3.37}$$

while $\vec{C}$ becomes

$$\vec{C} = -V''\widehat{\eta} + U''\widehat{\zeta} + \theta_z'\widehat{\xi}. \tag{3.38}$$

For small strains it is also possible to use

$$\varepsilon_\ell = \sqrt{1+2\varepsilon_q} - 1 \approx \varepsilon_q. \tag{3.39}$$

Finally, the term W'^2 is disregarded for being negligible compared to the others in usual applications of flexible rods undergoing transversal displacements in engineering, as exposed in Mazzilli et al. (2008). This assumption leads to

$$\varepsilon_\ell = W' + \frac{(U')^2}{2} + \frac{(V')^2}{2}. \tag{3.40}$$

Proceeding then to the variational calculations required in order to apply Hamilton's principle, the first variation of the kinetic energy is given as

$$\delta\mathcal{T} = \int_0^\ell \left(\mu\left(\dot{U}\delta\dot{U} + \dot{V}\delta\dot{V} + \dot{W}\delta\dot{W}\right) + J_\xi\dot{\theta}_z\delta\dot{\theta}_z\right)\,\mathrm{d}Z, \tag{3.41}$$

while the expression for the variation of the strain energy reads

$$\begin{aligned}\delta\mathcal{V} = \int_0^\ell \Big(&EA\varepsilon_\ell\delta\varepsilon_\ell + EI_\eta V''\delta V'' + EI_\zeta U''\delta U'' \\ &+EI_p\varepsilon_\ell\theta_z'\delta\theta_z' + \frac{EI_p}{2}\theta_z'^2\delta\varepsilon_\ell + EI_4\theta_z'^3\delta\theta_z' + GI_t\theta_z'\delta\theta_z'\Big)\,\mathrm{d}Z.\end{aligned} \tag{3.42}$$

Performing integration by parts in Eq. (3.42) to drop the primes from the variation terms leads to

$$\begin{aligned}\delta\mathcal{V} = &\left[EA\varepsilon_\ell\delta W + EAU'\varepsilon_\ell\delta U + EAV'\varepsilon_\ell\delta V + EI_\eta V''\delta V' - EI_\eta V'''\delta V\right]_0^\ell \\ &+\left[EI_\zeta U''\delta U' - EI_\zeta U'''\delta U + EI_p\varepsilon_\ell\theta_z'\delta\theta_z + EI_p\theta_z'^2\delta W + EI_pU'\theta_z'^2\delta U + EI_pV'\theta_z'^2\delta V\right]_0^\ell \\ &\left[EI_4\theta_z'^3\delta\theta_z + GI_t\theta_z'\delta\theta_z\right]_0^\ell - \int_0^\ell\left((EA\varepsilon_\ell)'\,\delta W + (EAU'\varepsilon_\ell)'\,\delta U + (EAV'\varepsilon_\ell)'\,\delta V\right)\,\mathrm{d}Z \\ &-\int_0^\ell\left(\left(EI_p\theta_z'^2\right)'\delta W + \left(EI_pU'\theta_z'^2\right)'\delta U + \left(EI_pV'\theta_z'^2\right)'\delta V + \left(EI_p\varepsilon_\ell\theta_z'\right)'\delta\theta_z\right)\,\mathrm{d}Z \\ &-\int_0^\ell\left(3EI_4\theta_z'^2\theta_z''\delta\theta_z + GI_t\theta_z''\delta\theta_z\right)\,\mathrm{d}Z + \int_0^\ell\left(EI_\eta V''''\delta V + EI_\zeta U''''\delta U\right)\,\mathrm{d}Z.\end{aligned} \tag{3.43}$$

Other contributions to the system's potential energy are not considered for now in order to ensure generality to the formulation. These other terms, such as the gravitational field, can be included by means of the variation of the work done by the external forces acting on the rod by using the extended Hamilton's principle. Using equations (3.41) and (3.43), Hamilton's principle can be applied leading to

$$\begin{aligned}
&\int_{t_1}^{t_2} \delta\mathcal{T} - \delta\mathcal{V}\,\mathrm{d}t = \int_{t_1}^{t_2} \left\{ \text{B.T.} + \int_0^{\ell} \left((EA\varepsilon_\ell)' + \left(EI_p\theta_z'^2\right)' - \mu\ddot{W} \right) \delta W\,\mathrm{d}Z \right\} \mathrm{d}t \\
&+ \int_{t_1}^{t_2} \left\{ \int_0^{\ell} \left((EAU'\varepsilon_\ell)' + \left(EI_pU'\theta_z'^2\right)' - EI_\zeta U'''' - \mu\ddot{U} \right) \delta U\,\mathrm{d}Z \right\} \mathrm{d}t \\
&+ \int_{t_1}^{t_2} \left\{ \int_0^{\ell} \left((EAV'\varepsilon_\ell)' + \left(EI_pV'\theta_z'^2\right)' - EI_\eta V'''' - \mu\ddot{V} \right) \delta V\,\mathrm{d}Z \right\} \mathrm{d}t \\
&\int_{t_1}^{t_2} \left\{ \int_0^{\ell} \left(\left(EI_p\varepsilon_\ell\theta_z'\right)' + 3EI_4\theta_z'^2\theta_z'' + GI_t\theta_z'' - J_\xi\ddot{\theta}_z \right) \delta\theta_z\,\mathrm{d}Z \right\} \mathrm{d}t,
\end{aligned} \tag{3.44}$$

where B.T. stands for "Boundary terms". In order to properly evaluate the results of such terms, the definition of the essential boundary conditions is necessary. For all the investigations in this thesis, the rods are pinned at both ends and the axial displacement is either null or imposed to the structure as a time series, with other boundary conditions being out of the scope. This means that the variations δU, δV and δW are all null in both $Z = 0$ and $Z = \ell$. Torsion is not considered in further investigations, but for the sake of the formulation presented here it is considered that the rotation angle is fixed at both ends, making $\delta\theta_z = 0$ at both of them. These conditions reduce the boundary terms to

$$\text{B.T.} = \left[EI_\eta V''\delta V' + EI_\zeta U''\delta U' \right]_0^{\ell}, \tag{3.45}$$

which leads to the four natural boundary conditions

$$EI_\eta V''(0) = EI_\eta V''(\ell) = EI_\zeta U''(0) = EI_\zeta U''(\ell) = 0, \tag{3.46}$$

as expected for pinned-pinned rods. The equations of motion for the free dynamics of the flexible rod are given by the integral terms in Eq. (3.44) as

$$\mu\ddot{W} - \left(EA\left(W' + \frac{U'^2}{2} + \frac{V'^2}{2} \right) + EI_p\theta_z'^2 \right)' = 0, \tag{3.47}$$

$$\mu\ddot{U} + EI_\zeta U'''' - \left[U'\left(EA\left(W' + \frac{U'^2}{2} + \frac{V'^2}{2}\right) + EI_p\theta_z'^2\right)\right]' = 0, \tag{3.48}$$

$$\mu\ddot{V} + EI_\eta V'''' - \left[V'\left(EA\left(W' + \frac{U'^2}{2} + \frac{V'^2}{2}\right) + EI_p\theta_z'^2\right)\right]' = 0, \tag{3.49}$$

$$J_\xi\ddot{\theta}_z - \left(EI_p\left(W' + \frac{U'^2}{2} + \frac{V'^2}{2}\right)\theta_z' + GI_t\theta_z' + EI_4\theta_z'^3\right)' = 0. \tag{3.50}$$

Of particular interest of this thesis is the case of planar dynamics, which implies in $U = \theta_z = 0$ and the equations of motion become

$$\mu\ddot{W} - EA\left(W'' + V'V''\right) = 0, \tag{3.51}$$

$$\mu\ddot{V} + EIV'''' - EA\left(W''V' + W'V'' + \frac{3\left(V'\right)^2}{2}V''\right) = 0. \tag{3.52}$$

The inclusion of different forcing terms is made in the specific cases of each investigation in the further chapters of the thesis. Discussions regarding static condensation, the effects of the static configuration and how to properly consider boundary imposed motions are also made for each particular case.

3.2 Statically curved and planar flexible cables

For the cases where the reference configuration is not straight, some key differences in modelling are introduced. Situations where this occurs are common in engineering practice, being it for offshore, bridges or transmission lines applications. It is worth pointing that, although the main focus of this thesis lies in structures on which the non-straight configuration is caused by static forces only, the methodology can be applied to known mean configurations when dynamic phenomena are considered, such as those caused by the mean drag force in marine cables under the load of surrounding fluid flows or the case of geometric imperfections. The generic reference configuration considered is presented in Fig. 17, in which some definitions are brought. As it can be seen, a fixed Cartesian frame is defined with Z being aligned with the direction of the local gravitational field but pointing in the opposite direction. The distance between the supports is considered to

be generic in both the horizontal and vertical directions, while the cable is considered to present an arbitrary sag[2]. It is also noticed that only the planar case is modelled, with three-dimensional scenarios not being investigated in this thesis for curved structures. A second reference frame is defined, being the local one over which the dynamical displacements are written, namely u for tangential displacements and v for transversal displacements. These local displacements are taken as Lagrangian measures in this work, that is, dynamical changes of directions of the local frame are not considered in the definitions of u and v, meaning the local frame adopted is fixed on the reference configuration. This type of approach is particularly useful for problems where the dynamics of the structure is characterized as a perturbation around the reference configuration, being inspired in the development made in Pesce (1997). It is also helpful to use the arclength coordinate s, measured as the length of cable from the reference support, the left one in the present study, in the static configuration. The use of the fixed Cartesian system is not prohibitive but implies in some complications in the modelling since for the same coordinate there can exist more than one point in the span of the cable.

Figure 17 – Basic model.

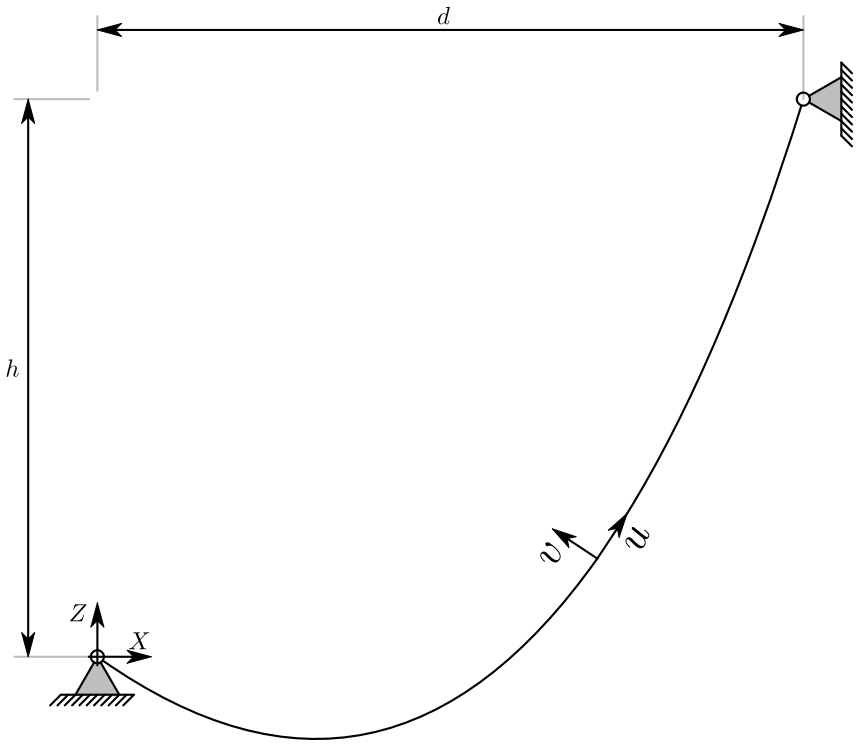

Source: The author.

Differently from the case of straight structures where the purely free dynamics has been considered in the general modelling, here the gravity force is already included. This is made since, in a great variety of applications, this force is the responsible for the statically

[2] The sag is defined as the largest distance between the curve defined by the cable and the straight line that passes through the supports.

curved configuration to occur. For the present modelling, it is also adopted that the bending stiffness and, consequently, the internal shear forces and bending moments, can be neglected. This approach is particularly valid while the wave-length of the typical dynamic response of the structure is significantly larger than the wave-length of flexural waves. This is analogous to say that the geometrical stiffness is dominant over the flexural stiffness for the dynamical behaviour of the structure. Differently from the straight configuration scenario, here a Newtonian approach is followed. For that, consider the infinitesimal element presented in Fig. 18, together with the forces acting over it on a general deformed configuration.

Figure 18 – Forces on a generic segment of the cable considering planar motion.

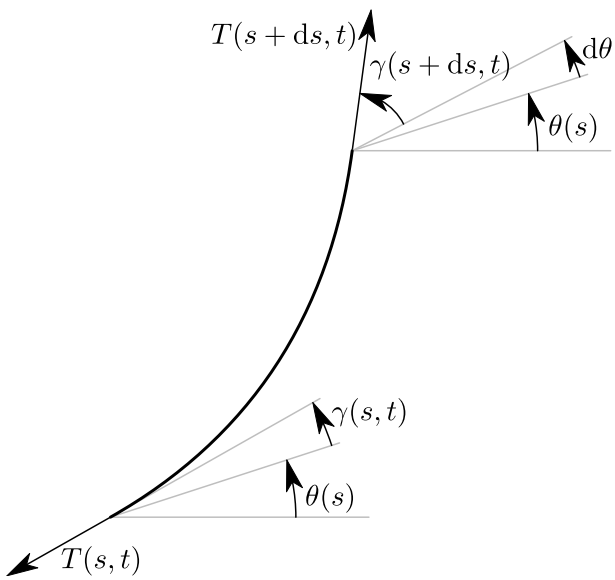

Source: The author.

In the condition depicted in Fig. 18, the infinitesimal cable element is subject to a total effective tension $T(s)$ (see Chucheepsakul, Monprapussorn & Huang (2003)) at one end and $T+\mathrm{d}T = T(s+\mathrm{d}s)$ at the other. Notice also that the angling of those forces with the horizontal direction is not the same, being $\theta(s)+\gamma(s)$ and $\theta+\mathrm{d}\theta+\gamma+\mathrm{d}\gamma = \theta(s+\mathrm{d}s)+\gamma(s+\mathrm{d}s)$ at the different ends, where θ stands for the angle of the cable axis with the horizontal direction in the reference configuration while the γ is used for the dynamic variation over such reference condition. Now, the resultant of the internal forces for the cable element $\mathrm{d}s$ are denoted as F_u and F_v for the u and v directions respectively. Decomposing the forces T and $T+\mathrm{d}T$ it is possible to write for those directions that

$$F_u = T\left(s+\mathrm{d}s\right)\cos\left(\mathrm{d}\theta+\gamma\left(s+\mathrm{d}s\right)\right) - T\left(s\right)\cos\left(\gamma\left(s\right)\right), \tag{3.53}$$

$$F_v = T\left(s+\mathrm{d}s\right)\sin\left(\mathrm{d}\theta+\gamma\left(s+\mathrm{d}s\right)\right) - T\left(s\right)\sin\left(\gamma\left(s\right)\right). \tag{3.54}$$

Asides those forces, the cable element is also under the action of external loads. Here only gravitational and buoyancy effects are considered, with other forces due to fluid-structure interaction being presented as opportune. That said, the "net weight" proposition is used, defined as the weight per unit length minus the respective buoyancy, and represented by γ_s. Using Newton's second law the equations of motion are then

$$F_u - \gamma_s \mathrm{d}s \sin\theta = m\ddot{u}\mathrm{d}s, \tag{3.55}$$

$$F_v - \gamma_s \mathrm{d}s \cos\theta = m_t\ddot{v}\mathrm{d}s. \tag{3.56}$$

Notice that two different inertial constants per unit length, m and m_t, are used for the acceleration terms. This is to let clearly stated that those are not necessarily equal when fluid-structure interactions[3] are considered. For the case of vibrations in air, it can be simply stated that $m_t = m$. Also, as usual in dynamical systems literature, overdots are used to designate differentiation with respect to time. Now, for an useful form of the equations of motion to be obtained, both Eqs. (3.55) and (3.56) are divided by $\mathrm{d}s$ and a limit operation is made, with $\mathrm{d}s \mapsto 0$. This operation is trivial for the inertial and external forcing terms, but rather involving in terms of algebra for the expressions of F_u and F_v. For clearness of exposition, those are made separately, leading to

$$\begin{aligned}
&\lim_{\mathrm{d}s\mapsto 0}\frac{F_u}{\mathrm{d}s} = \lim_{\mathrm{d}s\mapsto 0}\frac{T(s+\mathrm{d}s)\cos(\mathrm{d}\theta+\gamma(s+\mathrm{d}s)) - T(s)\cos(\gamma(s))}{\mathrm{d}s} = \\
&\lim_{\mathrm{d}s\mapsto 0}\left(\frac{T(s+\mathrm{d}s)\cos(\gamma(s+\mathrm{d}s)) - T(s)\cos(\gamma(s))}{\mathrm{d}s}\right. \\
&\left.-\frac{T(s+\mathrm{d}s)\sin(\gamma(s+\mathrm{d}s))\,\mathrm{d}\theta + O(\mathrm{d}\theta^2)}{\mathrm{d}s}\right) = \\
&T'\cos\gamma - T(\theta'+\gamma')\sin\gamma,
\end{aligned} \tag{3.57}$$

$$\begin{aligned}
&\lim_{\mathrm{d}s\mapsto 0}\frac{F_v}{\mathrm{d}s} = \lim_{\mathrm{d}s\mapsto 0}\frac{T(s+\mathrm{d}s)\sin(\mathrm{d}\theta+\gamma(s+\mathrm{d}s)) - T(s)\sin(\gamma(s))}{\mathrm{d}s} = \\
&\lim_{\mathrm{d}s\mapsto 0}\left(\frac{T(s+\mathrm{d}s)\sin(\gamma(s+\mathrm{d}s)) - T(s)\sin(\gamma(s))}{\mathrm{d}s}\right. \\
&\left.+\frac{T(s+\mathrm{d}s)\cos(\gamma(s+\mathrm{d}s))\,\mathrm{d}\theta + O(\mathrm{d}\theta^2)}{\mathrm{d}s}\right) = \\
&T'\sin\gamma + T(\theta'+\gamma')\cos\gamma.
\end{aligned} \tag{3.58}$$

For the present model, differentiation with respect to s is denoted by primes. The notation $O(\mathrm{d}\theta^2)$ used in the calculations means terms of order equal to or higher than

[3] For structures immersed in fluids, for example water, the added mass may be relevant. In addition, the added mass coefficient associated with the normal direction is not equal to the one associated with the tangential direction.

$\mathrm{d}\theta^2$. This is not an approximation. These are used to express terms that, when divided by $\mathrm{d}s$, will still remain with at least a first-order term $\mathrm{d}s$ and thus are zero when the limit $\mathrm{d}s \mapsto 0$ is taken. For further development, the tension is divided as $T = T_s + T_d$, where T_s designates the tension in the static configuration while T_d stands for the variation over such static component when the structure presents a dynamical response. With that division and using Eqs. (3.57) and (3.58) into Eqs. (3.55) and (3.56) it is possible to write

$$(T_s' + T_d')\cos\gamma - (T_s + T_d)(\theta' + \gamma')\sin\gamma - \gamma_s \sin\theta = m\ddot{u}, \tag{3.59}$$

$$(T_s' + T_d')\sin\gamma + (T_s + T_d)(\theta' + \gamma')\cos\gamma - \gamma_s \cos\theta = m_t\ddot{v}. \tag{3.60}$$

With a closer look in Eqs. (3.59) and (3.60), it is possible to identify the static equilibrium equations, by letting $T_d = \gamma = 0$, together with the elimination of the time derivatives. With that, the expressions that define the reference configuration are given as

$$T_s' - \gamma_s \sin\theta = 0, \tag{3.61}$$

$$T_s\theta' - \gamma_s \cos\theta = 0. \tag{3.62}$$

Notice that, in the present form, Eqs. (3.61) and (3.62) are exactly the same as the static configuration of an inextensible flexible cable (this correspondence can also be seen in Pesce (1997)). The key difference between the cases of extensible or inextensible cables is on the variables that must be solved in each case. For the inextensible cable, the static equilibrium can be obtained by solving for T_s and θ, and with θ it is possible to determine the reference planar shape. In turn, when an extensible cable is considered, the constitutive relations must be established in order to write T_s and θ as functions of the Cartesian coordinates X and Z of each point of the cable at rest. The main objective in separating the static part from the remaining of the equations of motion is to solve it beforehand by any means available, being then numerical or analytical. Substituting now Eqs. (3.61) and (3.62) back into Eqs. (3.59) and (3.60) leads to

$$T_s'(\cos\gamma - 1) - T_s(\theta' + \gamma')\sin\gamma + T_d'\cos\gamma - T_d(\theta' + \gamma')\sin\gamma = m\ddot{u}, \tag{3.63}$$

$$T_s'\sin\gamma - T_s\theta' + T_s(\theta' + \gamma')\cos\gamma + T_d'\sin\gamma + T_d(\theta' + \gamma')\cos\gamma = m_t\ddot{v}. \tag{3.64}$$

So far, no simplifying hypotheses have being made for the model, besides those just considering a planar dynamics, with the expressions obtained being exact. This framework can also be easily adapted to consider average hydrodynamic interactions such as the mean drag due to the existence of an external flow. Now, for the applications to be made, it is

assumed that the material stays in the linear-elastic range regarding deformations, which for marine structures engineering applications allows for the hypothesis of small strains. With such hypothesis adopted, it is admissible to adopt that the total strain at any given point of the structure can be decomposed as a sum of a static component with a dynamic variation over it, written as $\varepsilon \approx \varepsilon_s + \varepsilon_d$. Following the subscript convention adopted so far, ε_s is the strain at the static reference configuration while ε_d stands for the developed dynamical strain over it, function of both the displacements u and v. In order to define the relation between ε_d and the defined displacements, it is useful to recall the Green strain measure, also called quadratic strain ε_q, which is related to the linear strain by

$$1 + \varepsilon_d = \sqrt{1 + 2\varepsilon_q}. \tag{3.65}$$

The Green strain is easier to be obtained from purely geometrical relations, by simply observing the displacements of a generic infinitesimal element and evaluating the proper computation, which by differential geometry furnishes

$$\varepsilon_q = \left(u' - (v - uv' + u'v)\,\theta' + \frac{\left(u'^2 + v'^2 + (u\theta')^2 + (v\theta')^2\right)}{2} \right). \tag{3.66}$$

It is worth noticing that the expressions exactly reduce to common expression in the literature for straight structures if θ is set to zero. Also from differential geometry, it is possible to obtain for the angle γ some trigonometric relationships, leading to

$$\sin\gamma = \frac{(u\theta' + v')}{(1 + \varepsilon_d)}, \tag{3.67}$$

$$\cos\gamma = \frac{(1 + u' - v\theta')}{(1 + \varepsilon_d)}, \tag{3.68}$$

$$\gamma = \arcsin\left(\frac{(u\theta' + v')}{(1 + \varepsilon_d)} \right). \tag{3.69}$$

Finally, a link must be made between the traction and the strain, which ultimately establishes a link between the tension and the displacements of the structure. Since the focus is to investigate structures surrounded by fluid, the effective tension concept must be adopted, since the effective tension acting on a cross section in this case is not exactly the same as the resultant of wall stress on the pipe due to the effects of the pressure distribution of the outside and/or inside fluids. Details of the formulation regarding the effective tension are not exposed here, being well detailed in the literature, for example in Sparks (1984), which presents the same formulation as used in the present work. For a detailed explanation involving the cross-section deformation due to Poisson effect the

reader may refer to Chucheepsakul, Monprapussorn & Huang (2003). The effective tension acting on the cable cross-section, disregarding the existence of internal fluid, is then

$$T = EA\varepsilon + p_e A, \tag{3.70}$$

where p_e is the pressure of the surrounding fluid at the depth of the cross-section. From the geometry of the problem, the depth of a cross-section is given as $h_s - u\sin\theta - v\cos\theta$, with h_s being the depth of such cross-section in the static reference configuration. Using ρ to represent the external fluid's specific mass, the external pressure is then given as

$$p_e = \rho g\left(h_s - u\sin\theta - v\cos\theta\right). \tag{3.71}$$

Joining now Eqs. (3.70) and (3.71) together with the decomposition of tension and strain leads to

$$T_s + T_d = \left(EA\varepsilon_s + \rho g A h_s\right) + \left(EA\varepsilon_d - \rho g A\left(u\sin\theta + v\cos\theta\right)\right), \tag{3.72}$$

which, taking off the static components that can be solved independently of the dynamic part, leads to

$$T_d = EA\varepsilon_d - \rho g A\left(u\sin\theta + v\cos\theta\right). \tag{3.73}$$

In order to obtain a final form of the equations of motion, an expression is needed for γ', which can be obtained from the derivative of Eq. (3.69). After some algebraic manipulations, one obtains

$$\gamma' = \frac{1}{\cos\gamma}\left(\frac{(u\theta' + v')}{(1+\varepsilon_d)}\right)' = \frac{(1+\varepsilon_d)}{(1+u'-v\theta')}\left(\frac{(u\theta' + v')}{(1+\varepsilon_d)}\right)'. \tag{3.74}$$

Putting now together Eqs. (3.67), (3.74), (3.63) and (3.64), the equations of motion become

$$
\begin{aligned}
m\ddot{u} &= T_s'\left(\frac{u'-v\theta'-\varepsilon_d}{1+\varepsilon_d}\right) - T_s\left(\frac{(u\theta'+v')\,\theta'}{(1+\varepsilon_d)} + \frac{(u\theta'+v')}{(1+u'-v\theta')}\left(\frac{(u\theta'+v')}{(1+\varepsilon_d)}\right)'\right) \\
&- \rho g A\left((u'-v\theta')\sin\theta + (v'+u\theta')\cos\theta\right)\frac{(1+u'-v\theta')}{(1+\varepsilon_d)} + EA\varepsilon_d'\frac{(1+u'-v\theta')}{(1+\varepsilon_d)} \\
&+ \left[\left(\frac{(u\theta'+v')\,\theta'}{(1+\varepsilon_d)} + \frac{(u\theta'+v')}{(1+u'-v\theta')}\left(\frac{(u\theta'+v')}{(1+\varepsilon_d)}\right)'\right)\left(-EA\varepsilon_d + \rho g A u\sin\theta + \rho g A v\cos\theta\right)\right],
\end{aligned}
\tag{3.75}
$$

$$
\begin{aligned}
m_t\ddot{v} &= T_s'\frac{(u\theta'+v')}{(1+\varepsilon_d)} + T_s\left(\frac{(1+u'-v\theta')\,\theta'}{(1+\varepsilon_d)} + \left(\frac{(u\theta'+v')}{(1+\varepsilon_d)}\right)'\right) \\
&- \rho g A\left((u'-v\theta')\sin\theta + (v'+u\theta')\cos\theta\right)\frac{(u\theta'+v')}{(1+\varepsilon_d)} - T_s\theta' + EA\varepsilon_d'\frac{(u\theta'+v')}{(1+\varepsilon_d)} \\
&+ \left[\left(\frac{(1+u'-v\theta')\,\theta'}{(1+\varepsilon_d)} + \left(\frac{(u\theta'+v')}{(1+\varepsilon_d)}\right)'\right)\left(EA\varepsilon_d - \rho g A u\sin\theta - \rho g A v\cos\theta\right)\right].
\end{aligned}
\tag{3.76}
$$

It is important to emphasize that all terms depending on the static configuration can be considered as known functions in terms of the dynamical analysis. It is not actually important if the static solution is given as a closed-form expression or the interpolation function of a numerical solution as long as the analyst possess such configuration somehow. For further usage, specially regarding projection procedures, it is helpful to define the equations of motion as a vector of operators, with each component given by

$$\mathcal{L}_u(u,v) = 0, \tag{3.77}$$

$$\mathcal{L}_v(u,v) = 0, \tag{3.78}$$

for the axial and transversal directions respectively. Notice that, due the complexity of Eqs. (3.75) and (3.76), the usage of symbolic computation is advised and it is made in the present research. Thus, further simplifications of such equations are not explicitly written. Instead, the polynomial order of expansion adopted for the variables of interest is stated when necessary and the computations are made in a symbolic software such as Mathematica®.

4 Vertical and straight flexible rods under support excitation

This chapter brings investigations regarding the problem of vertical, straight and flexible rods immersed in still fluid under the action of an imposed boundary motion. Focusing on the offshore engineering application, such imposed motion is due to the response of a floating unit under the action of sea waves. This motion leads to a temporal variation of traction along the rod, which by consequence leads to a temporal variation of its geometrical stiffness, resulting in parametric excitation.

Along the chapter, different mathematical approaches and solutions are presented for the problem by means of analytical solutions of the PDEs, reduced-order modelling with its numerical integration or an analytical solution of such modelling. The obtained results are compared amongst each other and to a numerical reference obtained via the finite element method. This allows for an investigation of the advantages and drawbacks of each different approach and how they can be strategically combined to give support on tasks of engineering design.

The results of this chapter are published in Vernizzi, Franzini & Lenci (2019) and Vernizzi, Lenci & Franzini (2020), together with a presentation in the "Fourth International Conference on Recent Advances in Nonlinear Mechanics" (RANM2019).

4.1 Discussions regarding the mathematical model

A representation of the problem is illustrated in Fig. 19. The rod's mass per unit length is given by μ, the axial and bending stiffness products are given respectively by EA and EI, the length of the structure is denoted by ℓ and its immersed weight per unit length is given by γ. It is also useful to define the static pre-tension at the bottom section T_b, the external diameter D, a structural damping constant per unit length c for the transversal direction and a structural damping constant per unit length c_a on the axial direction. Finally, considering the static configuration, the tension along the structure's length is simply given by

$$T(z) = T_b + \gamma Z. \tag{4.1}$$

Recalling that very long elements are of common practice in the offshore engineering, Eq. (4.1) can impose key design limitations to the structure. It is desired that the element

Figure 19 – Basic sketch for the problem in study.

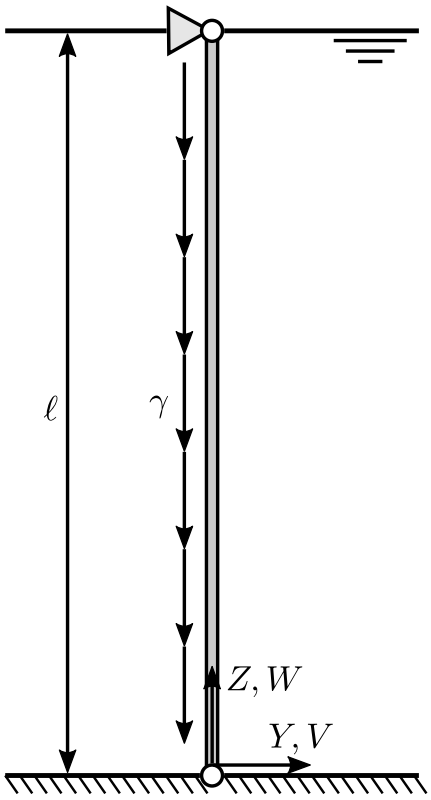

Source: The author.

does not undergo compression along its length, that is, to not go slack. For such objective, T_b must be positive[1] with a significant margin considering that the dynamical action will generate a temporal fluctuation of this value. However, due to the effect of self weight, the necessary static tension applied at the top, $T_t = T(\ell) = T_b + \gamma\ell$, may be impractical depending on the internal stresses that it may cause, limiting the range of usable lengths, materials and conception of the structural element.

Considering the planar vibrations scenario, the equations of motion for the problem can be obtained from Eqs. (3.51) and (3.52) by adding terms to model the fluid-structure interaction and the structural damping. Defining ρ as the specific mass of the surrounding fluid, $\overline{C}_D$ the mean drag coefficient for the rod's cross section and μ_a the potential added mass per unit length in the direction transversal to the structure's axis, the equations of motion, with the use of the Morison model for the fluid-structure interaction, become

[1] Negative values are uncommon in the offshore engineering but may be considered provided that the flexural stiffness is able to avoid local bucking.

$$\mu\ddot{W} + c_a\dot{W} + \gamma - EA\left(W'' + V'V''\right) = 0, \tag{4.2}$$

$$(\mu+\mu_a)\,\ddot{V}+c\dot{V}+\frac{1}{2}\rho D\overline{C}_D\left|\dot{V}\right|\dot{V}-EA\left(W''V'+W'V''+\frac{3}{2}\left(V'\right)^2V''\right)+EIV''''=0. \tag{4.3}$$

Notice that the equations of motion are not yet accounting for the solution of the static reference. This can be seen by the presence of the time-independent term γ in Eq. (4.2). Let then the axial displacement be divided into static (W_s) and dynamic (W_d) components as $W = W_s + W_d$. This division is not needed for the transversal displacement since it is trivial to notice its static component is null due to the absence of any time-independent terms in Eq. (4.3). Eliminating the terms dependent of V or W_d in Eq. (4.2) one retains

$$\gamma = EAW_s'', \tag{4.4}$$

which leads to

$$W_s = \frac{\gamma Z^2}{2EA} + \mathbb{C}_1 Z + \mathbb{C}_2, \tag{4.5}$$

with $\mathbb{C}_1$ and $\mathbb{C}_2$ being constants to be defined by means of the boundary conditions. From the condition of fixed boundary at $Z = 0$, it is directly obtained that $\mathbb{C}_2 = 0$. The second condition is that at the top of the structure, $Z = \ell$, the tension must achieve the imposed value T_t. Since for the static configuration this tension is simply given by

$$T(Z) = EAW_s', \tag{4.6}$$

then it is necessary that

$$T(\ell) = \gamma\ell + \mathbb{C}_1 = T_t = T_b + \gamma\ell \Rightarrow \mathbb{C}_1 = T_b. \tag{4.7}$$

Returning the obtained results into Eqs. (4.2) and (4.3) leads to

$$\mu\ddot{W}_d + c_a\dot{W}_d - EA\left(W_d'' + V'V''\right) = 0, \tag{4.8}$$

$$
\begin{aligned}
&(\mu+\mu_a)\,\ddot{V}+c\dot{V}+\frac{1}{2}\rho D\overline{C}_D\left|\dot{V}\right|\dot{V}+EIV''''-\gamma V'-(\gamma Z+T_b)\,V''\\
&-EA\left(W_d''V'+W_d'V''+\frac{3}{2}\left(V'\right)^2V''\right)=0.
\end{aligned}
\tag{4.9}
$$

Notice that new linear terms appeared on the transversal equation of motion (Eq. (4.9)). Those terms furnish the geometric stiffness provided by the tension along the rod, which is also obtained in the classical literature on the subject from the term $(TV')'$. This appearance deserves special attention, showing a modelling detail that may go overlooked if not properly addressed. The fact that the tension contributes to the appearance of linear terms in Eq. (4.9) ensures that it is important for some very basic properties for the structure's dynamics, like the natural frequencies and modes of vibration. However, the unsuspecting modeller may look at Eqs. (4.2) and (4.3) and perform an equivocated linearization at that step of modelling. Such linearization would eliminate the appearance of the contribution of the tension on the linear dynamics in the transversal direction since those terms originate from the apparently purely nonlinear terms $W''V'$ and $W'V''$ from Eq. (4.3).

Moving on, different approaches may now be taken to find a solution for Eqs. (4.8) and (4.9). Asides high hierarchy solutions such as those obtained by the finite element approach, it is possible to either perform an order reducing scheme to the equations of motion or directly tackle them as partial differential equations. Independently of the adopted strategy, it is possible to choose between dealing with both equations or to perform a reasonable static condensation procedure, eliminating one of them. In the present case, this can be made by disregarding the axial inertial term with the argument that this term is of small importance for the dynamical behaviour of the structure. Such hypothesis is reasonable, specially considering pinned-pinned rods where a mainly transversal response is expected, such as the present problem.

The static condensation herein presented is adapted from Mazzilli et al. (2008), consisting of writing the axial displacement as a function of the transversal one. Taking $\mu\ddot{W}_d=c_a\dot{W}_d=0$ and then integrating Eq. (4.8) leads to

$$
W_d'+\frac{1}{2}\left(V'\right)^2=\varepsilon_{d,0},
\tag{4.10}
$$

where $\varepsilon_{d,0}$ is a spacial integration constant, however function of time. The nomenclature for this constant is specifically chosen as presented since, by observing Eq. (4.10), it is the strain occurring on the structural axis due to the displacements W_d and V. In order to obtain the value of this constant, an averaging procedure is made by integrating Eq. (4.10) in the domain $Z\in[0,\ell]$, leading to

$$W_d|_0^\ell + \frac{1}{2}\int_0^\ell (V')^2 \, \mathrm{d}Z = \ell\varepsilon_{d,0} \Rightarrow \varepsilon_{d,0} = \frac{W_\ell}{\ell} + \frac{1}{2\ell}\int_0^\ell (V')^2 \, \mathrm{d}Z. \tag{4.11}$$

The term W_ℓ in the present case stands for the displacement imposed at the top boundary of the structure. Using now Eqs. (4.10) and (4.11), the dependence on W_d in Eq. (4.3) can be dropped, leading to the condensed form

$$\begin{aligned}&(\mu+\mu_a)\ddot{V} + c\dot{V} + EIV'''' - \gamma V' - \gamma Z V'' - T_b V'' - \frac{EA}{\ell}W_\ell V'' \\ &- \frac{EA}{2\ell}V''\int_0^L (V')^2 \, \mathrm{d}Z = -\frac{1}{2}\rho D\overline{C}_D\left|\dot{V}\right|\dot{V}.\end{aligned} \tag{4.12}$$

The static condensation procedure lets the dependence of the linear stiffness of the structure on the top motion explicitly written in the term $EAW_\ell V''/\ell$. This outcome is one advantage of the static condensation procedure over the option of tackling the original system of PDEs. In the original equations of motion, the top motion is merely a boundary condition, with its effects over the transversal dynamics not being explicitly shown by the equations. In turn, any effect that may be caused by the coupling of axial and transversal dynamics is lost from the moment where the condensation hypothesis was stated. This closes the modelling aspects regarding the problem at hand, with the subsequent sections tackling the obtaining of a solution for the rod dynamics.

4.2 Reduced-order modelling

The first option herein exposed for investigating the problem at hand is the use of reduced-order models (ROMs). This approach allows to simplify the mathematical work to that of a system of ordinary differential equations (ODEs), with a number of DOFs defined during the reduction process. In this thesis, the chosen method for obtaining ROMs is the Galerkin projection, which is of classical and recurrent use in structural mechanics and have the advantage of giving the minimum possible error within the chosen set of projection functions. For the purpose of the analysis using ROMs, the statically condensed model given by Eq. (4.12) is considered.

4.2.1 1-DOF reduced-order models

The first approach is to define ROMs with a single DOF. This is made because this is the simplest possible model for the transversal vibrations of a flexible rod. It is expected that the simplest model is also the one to be more suitable for analytical approaches to

be applied and also to have the best computational performance in simulations. Notice that, if the non-condensed model given by Eqs. (4.8) and (4.9) was used, the minimal model would have two DOFs, being one for the transversal direction and one for the axial direction. Now, it is assumed that the transversal displacement can be written as

$$V(Z,t) = v(t)\,\psi(Z)\,. \tag{4.13}$$

The main concern regarding this assumption is the choice of the projection function ψ. From a mathematically rigorous point of view, this function must fulfil the so-called essential boundary conditions, which in this case are $\psi(0) = \psi(\ell) = 0$. This, however, does not guarantee the quality of the obtained results, which is dependent on the shape of the adopted projection function. The question that now arises is how to define suitable projection functions to ensure the desired quality of the results. Two paths are thus explored in this research. The first one considers the use of the exact modes of vibration of the structure under investigation. The ROM conceived this way is herein called ROM(i). For a flexible rod under the action of its own weight the tensile force along its length varies, which such variation influencing on the mode shape. For this case, the mode of vibration is given in terms of "Bessel-Like" functions[2], obtained in Mazzilli, Lenci & Demeio (2014), whose expression simplified to the linear mode case is

$$\psi_b = \sqrt[4]{\frac{T_b + EI\,(m\pi/\ell)^2}{T_b + EI\,(m\pi/\ell)^2 + \gamma Z}}\,\sin\left(m\pi\frac{\sqrt{T_b + EI\,(m\pi/\ell)^2 + \gamma Z} - \sqrt{T_b + EI\,(m\pi/\ell)^2}}{\sqrt{T_b + EI\,(m\pi/\ell)^2 + \gamma \ell} - \sqrt{T_b + EI\,(m\pi/\ell)^2}}\right), \tag{4.14}$$

where m is the number of the vibration mode to be considered in the analysis. Notice that in the condition $\gamma \mapsto 0$ the modal function ψ_b reduces to a sine function, which is the mode of vibration of flexible rods under constant tension. Due to the mathematical expression of function ψ_b, it is not possible to furnish closed-form expressions for the results of the integrals that appear when the Galerkin scheme is applied to the model using such functions. Thus, the evaluation of the constants of the ROM need to be numerically performed. Applying Eq. (4.13) on (4.12) and using the Galerkin projection, the resulting model is written as

$$\alpha_1\ddot{v} + \alpha_2\dot{v} + \alpha_3 v + \alpha_4 W_\ell v + \alpha_5 v^3 + \alpha_6\dot{v}\,|\dot{v}| = 0, \tag{4.15}$$

with the definition of the parameters α_i given in Tab. 1

[2] The name "Bessel-Like" comes form the fact that the final expression is obtained via some approximation approaches used in particular conditions of the Bessel equation whereas the exact solution would be the Bessel functions themselves.

Table 1 – Parameters for the ROM of Eq. (4.15).

Parameter	Expression
α_1	$(\mu+\mu_a)\int_0^\ell \psi_b\psi_b\,\mathrm{d}Z$
α_2	$c\int_0^\ell \psi_b\psi_b\,\mathrm{d}Z$
α_3	$\int_0^\ell (EI\psi_b''''\psi_b - \gamma\psi_b'\psi_b - \gamma Z\psi_b''\psi_b - T_b\psi_b''\psi_b)\,\mathrm{d}Z$
α_4	$-\frac{EA}{\ell}\int_0^\ell \psi_b''\psi_b\,\mathrm{d}Z$
α_5	$-\frac{EA}{2\ell}\int_0^\ell \psi_b'\psi_b'\,\mathrm{d}Z\int_0^\ell \psi_b''\psi_b\,\mathrm{d}Z$
α_6	$\frac{1}{2}\rho D\overline{C}_D\int_0^\ell \psi_b^2\,\lvert\psi_b\rvert\,\mathrm{d}Z$

From Eq. (4.15), the natural frequency of this ROM is simply given by $\omega_b = \sqrt{\alpha_3/\alpha_1}$. Consider now a dimensionless displacement $r = v/D$ and a dimensionless time $\tau = \omega_b t$. In addition, the top motion is taken as a monochromatic oscillation $W_\ell = D\delta\cos(n\tau)$, with n being the ratio between the top-motion frequency and the natural frequency ω_b, while δ is the dimensionless amplitude of the top motion. With those definitions, the equation of motion for the ROM in dimensionless form reads

$$\frac{\mathrm{d}^2 r}{\mathrm{d}\tau^2} + \beta_1\frac{\mathrm{d}r}{\mathrm{d}\tau} + (1+\beta_2\delta\cos(n\tau))\,r + \beta_3 r^3 + \beta_4\left|\frac{\mathrm{d}r}{\mathrm{d}\tau}\right|\frac{\mathrm{d}r}{\mathrm{d}\tau} = 0, \tag{4.16}$$

with the parameters β_i being given in Tab. 2. Notice that the number of independent parameters is actually smaller than the number of parameters present in Eq. (4.15).

Table 2 – Parameters for the dimensionless ROM of Eq. (4.16).

Parameter	Expression
β_1	$\frac{\alpha_2}{\alpha_1\omega_b}$
β_2	$\frac{D\alpha_4}{\alpha_1\omega_b^2}$
β_3	$\frac{D^2\alpha_5}{\alpha_1\omega_b^2}$
β_4	$\frac{D\alpha_6}{\alpha_1}$

It is important to highlight that Eqs. (4.15) and (4.16) are independent of the shape function adopted, with the difference being only on the values that the coefficients

will assume. With that in mind, lets consider now trigonometric modes as shape functions, that is,

$$\psi_s = \sin\left(\frac{m\pi Z}{\ell}\right). \tag{4.17}$$

The suggestion of using trigonometric functions is due to the fact that this type of function is the actual mode of vibration of flexible rods under constant tension and also the fact that such functions are easier for algebraic work, allowing the advantage of obtaining a closed-form for the Galerkin scheme integrals. For the sake of clearness of reading, the notation is changed for the ROM based on one trigonometric shape function, from now on called ROM(ii) in this chapter, with its governing equation reading

$$a_1\ddot{v} + a_2\dot{v} + a_3 v + a_4 W_\ell v + a_5 v^3 + a_6\dot{v}\left|\dot{v}\right| = 0. \tag{4.18}$$

Using now the same dimensionless variables as for ROM(i), keeping in mind that for this case the natural frequency is given by $\omega_s = \sqrt{a_3/a_1}$, leads to

$$\frac{\mathrm{d}^2 r}{\mathrm{d}\tau^2} + b_1\frac{\mathrm{d}r}{\mathrm{d}\tau} + \left(1 + b_2\delta\cos\left(n\tau\right)\right)r + b_3 r^3 + b_4\left|\frac{\mathrm{d}r}{\mathrm{d}\tau}\right|\frac{\mathrm{d}r}{\mathrm{d}\tau} = 0. \tag{4.19}$$

For ROM(ii), the linearized natural frequency is $\omega_s = \sqrt{a_3/a_1}$ and its associated dimensionless time is given by $\tau = \omega_s t$. The parameters a_i and b_i are presented in Tab. 3.

4.2.2 3-DOF reduced-order model

Now, since the modes of vibration of a flexible rod with varying tension are not trigonometric in shape, it is expected that the representation of the structural response by a trigonometric function may not be good enough. However, the use of closed-form expressions for the parameters of the ROM is attractive, leading to the inspiration of conceiving a ROM with trigonometric functions as projection basis and that, at the same time, can represent the dynamic of the structure with a good quality. With that goal, and inspired in the analysis made in Franzini & Mazzilli (2016), the third ROM, now called ROM(iii), is obtained using a combination of three trigonometric functions as projection basis. The form of the solution is thus assumed as

$$V\left(Z,t\right) = v_1\left(t\right)\psi_1\left(Z\right) + v_2\left(t\right)\psi_2\left(Z\right) + v_3\left(t\right)\psi_3\left(Z\right), \tag{4.20}$$

with the projection basis given by

Table 3 – Parameters for ROM(ii).

Parameter	Expression
a_1	$(\mu+\mu_a)\dfrac{\ell}{2}$
a_2	$\dfrac{c\ell}{2}$
a_3	$EI\dfrac{\ell}{2}\left(\dfrac{m\pi}{\ell}\right)^4+\left(\dfrac{m\pi}{\ell}\right)^2\left(\dfrac{\gamma\ell^2}{4}+\dfrac{T_b\ell}{2}\right)$
a_4	$\dfrac{EA}{2}\left(\dfrac{m\pi}{\ell}\right)^2$
a_5	$\dfrac{EA\ell}{8}\left(\dfrac{m\pi}{\ell}\right)^4$
a_6	$\dfrac{2}{3\pi}\rho D\ell\overline{C}_D$
b_1	$\dfrac{a_2}{a_1\omega_s}$
b_2	$\dfrac{Da_4}{a_1\omega_s^2}$
b_3	$\dfrac{D^2a_5}{a_1\omega_s^2}$
b_4	$\dfrac{Da_6}{a_1}$

$$\psi_1=\sin\left(\frac{i\pi Z}{\ell}\right), \tag{4.21}$$

$$\psi_2=\sin\left(\frac{j\pi Z}{\ell}\right), \tag{4.22}$$

$$\psi_3=\sin\left(\frac{k\pi Z}{\ell}\right). \tag{4.23}$$

The constants i, j and k are merely indexes, taken as integer numbers accordingly to the desired modal representation. An example of strategy is to adopt j as the number of the mode under investigation, while i and k are assumed as $j-1$ and $j+1$ respectively. Applying the Galerkin projection, the equations of motion for ROM(iii) are

$$\begin{aligned}a_{1,1}\ddot{v}_1+a_{1,2}\dot{v}_1+a_{1,3}v_1+a_{1,4}W_\ell v_1+a_{1,5}v_2+a_{1,6}v_3\\ +a_{1,7}v_1^3+a_{1,8}v_1v_2^2+a_{1,9}v_1v_3^2+MR_1=0,\end{aligned} \tag{4.24}$$

$$\begin{aligned}a_{2,1}\ddot{v}_2+a_{2,2}\dot{v}_2+a_{2,3}v_2+a_{2,4}W_\ell v_2+a_{2,5}v_1+a_{2,6}v_3\\ +a_{2,7}v_2^3+a_{2,8}v_2v_1^2+a_{2,9}v_2v_3^2+MR_2=0,\end{aligned} \tag{4.25}$$

$$a_{3,1}\ddot{v}_3 + a_{3,2}\dot{v}_3 + a_{3,3}v_3 + a_{3,4}W_\ell v_3 + a_{3,5}v_1 + a_{3,6}v_2 \\ +a_{3,7}v_3^3 + a_{3,8}v_3v_1^2 + a_{3,9}v_3v_2^2 + MR_3 = 0, \tag{4.26}$$

The terms MR_i, $i = 1,\ 2,\ 3$, are the resulting components of the equations that arise from the Morison's drag force term after the Galerkin projection. Those terms cannot be evaluated beforehand since now a sum of different components appears inside the absolute value function. This leads to the necessity of evaluating this term in each step of simulation in a numeric scheme, and a performance loss can be expected from such needed operations. Again, the dimensionless displacements are defined as $r_i = v_i/D$, while the dimensionless time is defined accordingly to the natural frequency of the chosen mode to be investigated, ω_t. Note that, in order to obtain this frequency, it is necessary to linearize the system given by Eqs. (4.27) to (4.29) and solve the resulting eigenvalue problem. With the use of the dimensionless variables the equations of motion for ROM(iii) become

$$\ddot{r}_1 + b_{1,1}\dot{r}_1 + \Big(b_{1,2} + b_{1,3}\delta\cos(n\pi)\Big)r_1 + b_{1,4}r_2 + b_{1,5}r_3 \\ +b_{1,6}r_1^3 + b_{1,7}r_1r_2^2 + b_{1,8}r_1r_3^2 + \overline{MR}_1 = 0, \tag{4.27}$$

$$\ddot{r}_2 + b_{2,1}\dot{r}_2 + \Big(b_{2,2} + b_{2,3}\delta\cos(n\pi)\Big)r_2 + b_{2,4}r_1 + b_{2,5}r_3 \\ +b_{2,6}r_2^3 + b_{2,7}r_2r_1^2 + b_{2,8}r_2r_3^2 + \overline{MR}_2 = 0, \tag{4.28}$$

$$\ddot{r}_3 + b_{3,1}\dot{r}_3 + \Big(b_{3,2} + b_{3,3}\delta\cos(n\pi)\Big)r_3 + b_{3,4}r_1 + b_{3,5}r_2 \\ +b_{3,6}r_3^3 + b_{3,7}r_3r_1^2 + b_{3,8}r_3r_2^2 + \overline{MR}_3 = 0. \tag{4.29}$$

The parameters of Eqs. (4.27) to (4.29) are presented in table 4. The nonlinear damping terms $\overline{MR}_x$ can be put in the general form

$$\overline{MR}_x = \frac{\rho D^2\overline{C}_D}{2a_{x,1}}\int_0^\ell \psi_x\left|\dot{r}_i\psi_i + \dot{r}_j\psi_j + \dot{r}_k\psi_k\right|\left(\dot{r}_i\psi_i + \dot{r}_j\psi_j + \dot{r}_k\psi_k\right)\mathrm{d}Z. \tag{4.30}$$

Regarding this 3-DOF ROM, it is possible to find in the literature some approximated procedures to compute the natural frequency of the involved modes. In this work, it is adopted that the linearized natural frequencies estimated by the 3-DOF ROM are the

Table 4 – Parameters for 3-dof ROM.

Term	Expression	Term	Expression
$a_{1,1}$	$(\mu+\mu_a)\,\ell/2$	$a_{1,2}$	$c\ell/2$
$a_{2,1}$	$(\mu+\mu_a)\,\ell/2$	$a_{2,2}$	$c\ell/2$
$a_{3,1}$	$(\mu+\mu_a)\,\ell/2$	$a_{3,2}$	$c\ell/2$
$a_{1,3}$	$\frac{EI\ell}{2}\left(\frac{i\pi}{\ell}\right)^4+\left(\frac{i\pi}{\ell}\right)^2\left(\frac{\gamma\ell^2}{4}+\frac{T_b\ell}{2}\right)$	$a_{1,4}$	$\frac{EA}{2}\left(\frac{i\pi}{\ell}\right)^2$
$a_{2,3}$	$\frac{EI\ell}{2}\left(\frac{j\pi}{\ell}\right)^4+\left(\frac{j\pi}{\ell}\right)^2\left(\frac{\gamma\ell^2}{4}+\frac{T_b\ell}{2}\right)$	$a_{2,4}$	$\frac{EA}{2}\left(\frac{j\pi}{\ell}\right)^2$
$a_{3,3}$	$\frac{EI\ell}{2}\left(\frac{k\pi}{\ell}\right)^4+\left(\frac{k\pi}{\ell}\right)^2\left(\frac{\gamma\ell^2}{4}+\frac{T_b\ell}{2}\right)$	$a_{3,4}$	$\frac{EA}{2}\left(\frac{k\pi}{\ell}\right)^2$
$a_{1,5}$	$\gamma\,(i\pi)^2\left(\frac{2\cos(i\pi)\cos(j\pi)-2}{(i^2-j^2)^2\pi^2}\right)ij$	$a_{1,6}$	$\gamma\,(i\pi)^2\left(\frac{2\cos(i\pi)\cos(k\pi)-2}{(i^2-k^2)^2\pi^2}\right)ik$
$a_{2,5}$	$a_{1,5}\left(\frac{j}{i}\right)^2$	$a_{2,6}$	$\gamma\,(j\pi)^2\left(\frac{2\cos(j\pi)\cos(k\pi)-2}{(j^2-k^2)^2\pi^2}\right)jk$
$a_{3,5}$	$a_{1,6}\left(\frac{k}{i}\right)^2$	$a_{3,6}$	$a_{2,6}\left(\frac{k}{j}\right)$
$a_{1,7}$	$\frac{EA\ell}{8}\left(\frac{i\pi}{\ell}\right)^4$	$a_{1,8}$	$\frac{EA\ell}{8}\left(\frac{i\pi}{\ell}\right)^2\left(\frac{j\pi}{\ell}\right)^2$
$a_{2,7}$	$\frac{EA\ell}{8}\left(\frac{j\pi}{\ell}\right)^4$	$a_{2,8}$	$\frac{EA\ell}{8}\left(\frac{i\pi}{\ell}\right)^2\left(\frac{j\pi}{\ell}\right)^2$
$a_{3,7}$	$\frac{EA\ell}{8}\left(\frac{k\pi}{\ell}\right)^4$	$a_{3,8}$	$\frac{EA\ell}{8}\left(\frac{i\pi}{\ell}\right)^2\left(\frac{k\pi}{\ell}\right)^2$
$a_{1,9}$	$\frac{EA\ell}{8}\left(\frac{i\pi}{\ell}\right)^2\left(\frac{k\pi}{\ell}\right)^2$	$b_{1,1}$	$a_{1,2}/\left(a_{1,1}\omega_2\right)$
$a_{2,9}$	$\frac{EA\ell}{8}\left(\frac{j\pi}{\ell}\right)^2\left(\frac{k\pi}{\ell}\right)^2$	$b_{2,1}$	$a_{2,2}/\left(a_{2,1}\omega_2\right)$
$a_{3,9}$	$\frac{EA\ell}{8}\left(\frac{j\pi}{\ell}\right)^2\left(\frac{k\pi}{\ell}\right)^2$	$b_{3,1}$	$a_{3,2}/\left(a_{3,1}\omega_2\right)$
$b_{1,2}$	$a_{1,3}/\left(a_{1,1}\omega_t^2\right)$	$b_{1,3}$	$a_{1,4}D/\left(a_{1,1}\omega_t^2\right)$
$b_{2,2}$	$a_{2,3}/\left(a_{2,1}\omega_t^2\right)$	$b_{2,3}$	$a_{2,4}D/\left(a_{2,1}\omega_t^2\right)$
$b_{3,2}$	$a_{3,3}/\left(a_{3,1}\omega_t^2\right)$	$b_{3,3}$	$a_{3,4}D/\left(a_{3,1}\omega_t^2\right)$
$b_{1,4}$	$a_{1,5}/\left(a_{1,1}\omega_t^2\right)$	$b_{1,5}$	$a_{1,6}/\left(a_{1,1}\omega_t^2\right)$
$b_{2,4}$	$a_{2,5}/\left(a_{2,1}\omega_t^2\right)$	$b_{2,5}$	$a_{2,6}/\left(a_{2,1}\omega_t^2\right)$
$b_{3,4}$	$a_{3,5}/\left(a_{3,1}\omega_t^2\right)$	$b_{3,5}$	$a_{3,6}/\left(a_{3,1}\omega_t^2\right)$
$b_{1,6}$	$a_{1,7}D^2/\left(a_{1,1}\omega_t^2\right)$	$b_{1,7}$	$a_{1,8}D^2/\left(a_{1,1}\omega_t^2\right)$
$b_{2,6}$	$a_{2,7}D^2/\left(a_{2,1}\omega_t^2\right)$	$b_{2,7}$	$a_{2,8}D^2/\left(a_{2,1}\omega_t^2\right)$
$b_{3,6}$	$a_{3,7}D^2/\left(a_{3,1}\omega_t^2\right)$	$b_{3,7}$	$a_{3,8}D^2/\left(a_{3,1}\omega_t^2\right)$
$b_{1,8}$	$a_{1,9}D^2/\left(a_{1,1}\omega_t^2\right)$		
$b_{2,8}$	$a_{2,9}D^2/\left(a_{2,1}\omega_t^2\right)$		
$b_{3,8}$	$a_{3,9}D^2/\left(a_{3,1}\omega_t^2\right)$		

natural frequencies of the dynamical system given by Eqs. (4.24) to (4.26), which gives the exact frequencies of the obtained model. However, it is possible to approximate the natural frequencies with simpler computations. For that, the values of the natural frequencies are taken as the natural frequency of the oscillator obtained by doing a Galerkin projection with each of the shape functions independently as 1-DOF-ROMs. Such approximation furnishes the results presented in Franzini & Mazzilli (2016). Notice that the latter approach will give better results when the modes of vibration are closer to trigonometric functions.

4.2.3 Analytical solutions for the 1-DOF ROM

One first possible way to study the problem at hand is by means of analytical results. For the particular case of 1-DOF ROMs (ROM (i) and ROM (ii), given respectively by Eqs. (4.16) and (4.19)), where the spatial integral of the Galerkin projection of the Morison term can be analytically solved, solutions using the method of multiple scales can be found. The idea for the solution is to expand the Morison's drag force into a Fourier series, which is a strategy presented in Nayfeh & Mook (1979). To use the method, a bookkeeping parameter ϵ is created in a way that the relations $\beta_1 = \zeta_1\epsilon$, $\beta_2\delta = \zeta_2\epsilon$, $\beta_3 = \zeta_3\epsilon$ and $\beta_4 = \zeta_4\epsilon$ hold. The solution is sought using two time scales, being them $\tau_0 = \tau$ and $\tau_1 = \tau\epsilon$, leading to the form

$$r = r_0\left(\tau_0, \tau_1\right) + \epsilon r_1\left(\tau_0, \tau_1\right), \tag{4.31}$$

which turns the equation of motion into

$$\frac{\mathrm{d}^2 r}{\mathrm{d}\tau^2} + \zeta_1\epsilon\frac{\mathrm{d}r}{\mathrm{d}\tau} + \left(1 + \zeta_2\epsilon\cos\left(n\tau\right)\right) r + \zeta_3\epsilon r^3 + \zeta_4\epsilon\left|\frac{\mathrm{d}r}{\mathrm{d}\tau}\right|\frac{\mathrm{d}r}{\mathrm{d}\tau} = 0. \tag{4.32}$$

The following operators are needed in the expansion procedure, and correct up to order ϵ, they read

$$\frac{\mathrm{d}}{\mathrm{d}\tau} = \frac{\partial}{\partial\tau_0} + \epsilon\frac{\partial}{\partial\tau_1}, \tag{4.33}$$

$$\frac{\mathrm{d}^2}{\mathrm{d}\tau^2} = \frac{\partial^2}{\partial\tau_0^2} + 2\epsilon\frac{\partial^2}{\partial\tau_0\partial\tau_1}. \tag{4.34}$$

Applying the operators defined by Eqs. (4.33) and (4.34) in Eq. (4.32) and collecting terms with equal powers of ϵ, it is obtained that

$$\frac{\partial^2 r_0}{\partial \tau_0^2} + r_0 = 0, \tag{4.35}$$

$$\frac{\partial^2 r_1}{\partial \tau_0^2} + r_1 = -2\frac{\partial^2 r_0}{\partial \tau_0 \partial \tau_1} - \zeta_1 \frac{\partial r_0}{\partial \tau_0} - \zeta_2 \cos(n\tau) r_0 - \zeta_3 r_0^3 - \zeta_4 \left|\frac{\partial r_0}{\partial \tau_0}\right| \frac{\partial r_0}{\partial \tau_0}. \tag{4.36}$$

The solution for Eq. (4.35) is written as

$$r_0 = B_1(\tau_1) e^{i\tau_0} + c.c., \tag{4.37}$$

with i being the imaginary constant within this context and "*c.c.*" means the complex conjugate of the terms before its appearance. Together with the substituting of Eq. (4.37) into Eq. (4.36), some mathematical work is made with the quadratic term. Following Nayfeh & Mook (1979), a Fourier series is used to write the quadratic damping terms, allowing it to be represented as a sum of harmonic components, making it possible to evaluate which contribution of the quadratic term is relevant for eliminating the secular terms arising in Eq. (4.36). Regarding the effects of the parametric excitation near the principal instability region in the Strutt's diagram, the parameter n is defined as

$$n = 2 + \epsilon\sigma, \tag{4.38}$$

with σ being a detuning parameter. With those assumptions, Eq. (4.36) turns into

$$\frac{\partial^2 r_1}{\partial \tau_0^2} + r_1 = e^{i\tau_0}\left(-2i\frac{\mathrm{d}B_1}{\mathrm{d}\tau_1} - i\zeta_1 B_1 - 3\zeta_3 B_1^2 B_1^* - \frac{\zeta_2 B_1^*}{2} e^{i\sigma\tau_1} - f_1\left(r_0, \frac{\mathrm{d}r_0}{\mathrm{d}\tau_0}\right)\right) + c.c. + N.S.T. \,. \tag{4.39}$$

The function f_1 stands for the unitary dimensionless frequency term arising from the Fourier expansion of the Morison damping, while $N.S.T.$ stands for the non-secular terms of Eq. (4.39). Putting the complex function B_1 in polar form, $B_1 = R_1 e^{i\theta_1}$, with $R_1 > 0$[3] and θ_1 being real valued functions, the solvability condition is given by the complex valued equation

$$-2i\frac{\mathrm{d}R_1}{\mathrm{d}\tau_1} + 2R_1\frac{\mathrm{d}\theta_1}{\mathrm{d}\tau_1} - i\zeta_1 R_1 - 3\zeta_3 R_1^3 - \frac{\zeta_2 R_1}{2} e^{-2i\theta_1 + i\sigma\tau_1} - \frac{f_1\left(r_0, \frac{\mathrm{d}r_0}{\mathrm{d}\tau_0}\right)}{e^{i\theta_1}} = 0. \tag{4.40}$$

[3] Notice that assuming the amplitude of the polar form to be positive does not limit in any sense the possible solutions to be obtained since any opposite sign results can still be obtained by a simple rotation of π in θ_1.

Using the polar form in Eq. (4.37), it results that, at order ϵ^0, $r_0 = 2R_1 \cos(\tau_0 + \theta_1)$. The term of order ϵ^1 must not be included since the Fourier term under evaluation is already of order ϵ^1, so taking a term of order ϵ^1 in r_0 would result in Fourier terms of order ϵ^3 for the quadratic damping. With that, one arrives at

$$\frac{f_1}{e^{i\theta_1}} = \frac{\zeta_4}{2\pi}\int_0^{2\pi}(-2R_1\sin(\tau_0+\theta_1))\,|-2R_1\sin(\tau_0+\theta_1)|\,e^{-i(\tau_0+\theta_1)}\mathrm{d}\tau_0 = \frac{16iR_1^2\zeta_4}{3\pi}. \tag{4.41}$$

In order to obtain the solvability conditions in terms of R_1 and θ_1, Eq. (4.40) must be separated into its real and imaginary parts, leading to the system of equations

$$2R_1\frac{\mathrm{d}\theta_1}{\mathrm{d}\tau_1} - 3\zeta_3R_1^3 - \frac{\zeta_2R_1}{2}\cos(-2\theta_1+\sigma\tau_1) = 0, \tag{4.42}$$

$$-2\frac{\mathrm{d}R_1}{\mathrm{d}\tau_1} - \zeta_1R_1 - \frac{16R_1^2\zeta_4}{3\pi} - \frac{\zeta_2R_1}{2}\sin(-2\theta_1+\sigma\tau_1) = 0. \tag{4.43}$$

Let now the following variable change be defined as

$$\phi = \sigma\tau_1 - 2\theta_1 \Rightarrow 2\frac{\mathrm{d}\theta_1}{\mathrm{d}\tau_1} = \sigma - \frac{\mathrm{d}\phi}{\mathrm{d}\tau_1}. \tag{4.44}$$

Substituting now Eq. (4.44) in Eqs. (4.42) and (4.43) leads to

$$R_1\sigma - R_1\frac{\mathrm{d}\phi}{\mathrm{d}\tau_1} - 3\zeta_3R_1^3 - \frac{\zeta_2R_1}{2}\cos(\phi) = 0, \tag{4.45}$$

$$-2\frac{\mathrm{d}R_1}{\mathrm{d}\tau_1} - \zeta_1R_1 - \frac{16R_1^2\zeta_4}{3\pi} - \frac{\zeta_2R_1}{2}\sin(\phi) = 0. \tag{4.46}$$

The system of Eqs. (4.45) and (4.46) allows for the study of the stability of the steady-state solutions using the Lyapunov's indirect method. In order to obtain non-trivial steady-state solutions for the motion amplitude, the derivatives present in Eqs. (4.45) and (4.46) are taken as zero (steady-state condition). The trigonometric terms in those equations are isolated, with the resulting equations being then squared and added up, leading to

$$\left(2\sigma - 6\zeta_3R_1^2\right)^2 + \left(2\zeta_1 + \frac{32}{3\pi}R_1\zeta_4\right)^2 = \zeta_2^2. \tag{4.47}$$

Notice that Eq. (4.47) is a bi-quadratic polynomial if one of the damping parameters is considered null. If a solution with both damping contributions is desired, a numerical

search for the roots of the polynomial expression is needed. In turn, considering that the hydrodynamical damping is significantly larger than the structural damping for non-trivial solutions[4], it is possible to obtain a closed-form expression for the steady-state amplitude, written as

$$R_1^2 = \frac{\frac{-1024\zeta_4^2}{9\pi^2} + 24\zeta_3\sigma \pm \sqrt{\left(\frac{1024\zeta_4^2}{9\pi^2} - 24\zeta_3\sigma\right)^2 - 144\zeta_3^2\left(4\sigma^2 - \zeta_2^2\right)}}{72\zeta_3^2}. \tag{4.48}$$

Three scenarios can arise from such solution. The first is when no real solutions exist for R_1 from Eq. (4.48). In such case, the only possible solution is the trivial one $R_1 = 0$ which identically solves Eqs. (4.45) and (4.46). The second scenario is when only one real and non-zero solution exists for R_1. In this case, the trivial solution is unstable while the non-zero solution is stable. This can be concluded because, since only two solutions exist, then one of them must be stable and the other unstable. Recall now that the proposed solution define closed orbits in the phase space and that the problem does not possess unbounded solutions. If in this case the non-zero value of R_1 would be the unstable solution, then, using the Poincaré-Bendixon any flow inside the circle defined by R_1 would converge to the equilibrium point $(0, 0)$, while any flow outside of such circle would go to infinity. Since the solution is bounded, it is proofed by contradiction that the non-zero value of R_1 is the stable solution. Finally, the third scenario occurs when two non-zero positive solutions arise for R_1. In this last scenario, the trivial and the largest of the possible R_1 solutions are stable, while the intermediary value is unstable. The proof of the latter case is analogous as the one posed for the second case.

4.3 Analytical solution of the PDEs of motion

Another possibility to analyse the problem is by a direct approach over the PDEs (4.8) and (4.9). For this case, it is particularly useful to render the equations dimensionless before proceeding with the analysis. Let ω_0 be the linear natural frequency of free vibrations of a transversal mode of interest. Let now the dimensionless variables for displacements, time, and the position along the structure be defined respectively as $V = vD$, $W_d = wD$, $\tau = \omega_0 t$ and $Z = \ell\xi$. Then, the equations of motion can be rewritten as

$$\ddot{w} + a_1\dot{w} - a_2 w'' - a_3 v' v'' = 0, \tag{4.49}$$

$$\ddot{v} + b_1\dot{v} + b_2 v'''' - \left(b_3\xi + b_4\right) v'' - b_3 v' - b_5\left(w'v'\right)' - b_6\left(v'\right)^2 v'' = -b_7\left|\dot{v}\right|\dot{v}. \tag{4.50}$$

[4] This is particularly valid for the problem of parametric excitation, since the linear structural damping is unable to ensure bounded responses, while the nonlinear damping is able to generate an energy output that matches the energy input from the excitation.

For the sake of simplicity and to keep the equations in a lighter format, the notations for derivatives with respect to time and position are extended to the dimensionless variables. The dimensionless parameters present in Eqs. (4.49) and (4.50) are shown in Table 5. For the problem at hand, the essential boundary conditions are $v(0,\tau) = v(1,\tau) = w(0,\tau) = 0$ and $w(1,\tau) = \delta\cos(n\tau)$, where $\delta = W_\ell/D$ is the dimensionless amplitude of the top motion, and n is the ratio between the imposed top motion frequency and the chosen natural frequency ω_0. Completing the set of boundary conditions, the natural boundary conditions are $v''(0,\tau) = v''(1,\tau) = 0$.

Table 5 – Dimensionless parameters of Eqs. (4.49) and (4.50)

Parameter	Definition	Parameter	Definition
a_1	$\dfrac{c_a}{\mu\omega_0}$	b_3	$\dfrac{\gamma}{(\mu+\mu_a)\,\ell\omega_0^2}$
a_2	$\dfrac{EA}{\mu\ell^2\omega_0^2}$	b_4	$\dfrac{T_b}{(\mu+\mu_a)\,\ell^2\omega_0^2}$
a_3	$\dfrac{EAD}{\mu\ell^3\omega_0^2}$	b_5	$\dfrac{EAD}{(\mu+\mu_a)\,\ell^3\omega_0^2}$
b_1	$\dfrac{c}{(\mu+\mu_a)\,\omega_0}$	b_6	$\dfrac{3EAD^2}{2(\mu+\mu_a)\,\ell^4\omega_0^2}$
b_2	$\dfrac{EI}{(\mu+\mu_a)\,\ell^4\omega_0^2}$	b_7	$\dfrac{\rho D^2 C_D}{2(\mu+\mu_a)}$

A solution is then sought with MMTS for Eqs. (4.49) and (4.50). For that end, a scaling is adopted for the dimensionless parameters by means of a bookkeeping parameter ϵ, namely, $w \mapsto \epsilon w$, $v \mapsto \epsilon v$, $a_1 \mapsto \epsilon a_1$, $b_1 \mapsto \epsilon^2 b_1$, $b_7 \mapsto \epsilon b_7$ and $\delta \mapsto \epsilon^2\delta$. Within the time domain, three different scales are adopted, resulting in $\tau_0 = \tau$, $\tau_1 = \epsilon\tau$ and $\tau_2 = \epsilon^2\tau$. Some observations are important regarding the adopted scaling. Regarding the transversal motion alone, Eq. (4.50), all the terms are scaled in a way that the first appearance of each nonlinear term and the linear damping occurs at the same order in ϵ. This is made in order to not implicitly define any of the effects as being dominant upon the others, leaving that relationship to be established naturally by the solvability conditions. In addition, notice that the linear damping parameters a_1 and b_1 are not scaled in the same manner. In this case, the scaling of a_1 is merely a mathematical choice to facilitate the algebraic work during the solution. This happens because the term a_1, in the final results, is responsible for eliminating the presence of homogeneous solutions in the axial direction and the order in ϵ at which this occurs does not change the final results, with the chosen scaling ensuring this term appears as early as possible. This strategy, however, could not be used in the case in which there are any resonances, internal or external, with the axial modes of vibration. Proceeding with the analysis, the time differentiations over a general function f become

$$\dot{f} = D_0 f + \epsilon D_1 f + \epsilon^2 D_2 f, \tag{4.51}$$
$$\ddot{f} = D_0^2 f + 2\epsilon D_0 D_1 f + \epsilon^2 \left(D_1^2 f + 2 D_0 D_2 f \right). \tag{4.52}$$

The new operators D_0, D_1 and D_2 are simply short notations for the partial derivatives with respect to τ_0, τ_1 and τ_2 respectively. Seeking solutions of the form $w = w_0 + \epsilon w_1 + \epsilon^2 w_2$ and $v = v_0 + \epsilon v_1 + \epsilon^2 v_2$, applying the scaling definitions and using Eqs. (4.51) and (4.52) on (4.49) and (4.50), collecting terms of equal powers of ϵ, leads to three linear problems on different orders. For order ϵ^0 it arises that

$$D_0^2 w_0 - a_2 w_0'' = 0, \tag{4.53}$$
$$D_0^2 v_0 + b_2 v_0'''' - (b_3 \xi + b_4) v_0'' - b_3 v_0' = 0. \tag{4.54}$$

The boundary conditions must also be divided in orders accordingly to the adopted scaling. For order ϵ^0 it results in $v_0(0,\tau) = v_0(1,\tau) = v_0''(0,\tau) = v_0''(1,\tau) = w_0(0,\tau) = w_0(1,\tau) = 0$. Following, the problem of order ϵ^1 reads

$$\ddot{w}_1 - a_2 w_1'' = -2 D_0 D_1 w_0 - a_1 D_0 w_0 + a_3 v_0' v_0'', \tag{4.55}$$
$$\ddot{v}_1 + b_2 v_1'''' - (b_3 \xi + b_4) v_1'' - b_3 v_1' = -2 D_0 D_1 v_0 + b_5 \left(w_0' v_0' \right)', \tag{4.56}$$

with the boundary conditions given by $v_1(0,\tau) = v_1(1,\tau) = v_1''(0,\tau) = v_1''(1,\tau) = w_1(0,\tau) = 0$ and $w_1(1,\tau) = \delta \cos(n\tau)$. Lastly, the problem of order ϵ^2 is given by

$$\begin{aligned} &\ddot{w}_2 - a_2 w_2'' = -2 D_0 D_1 w_1 - D_1^2 w_0 - 2 D_0 D_2 w_0 - a_1 D_0 w_1 \\ &- a_1 D_1 w_0 + a_3 v_0' v_1'' + a_3 v_1' v_0'', \end{aligned} \tag{4.57}$$
$$\begin{aligned} &\ddot{v}_2 + b_2 v_2'''' - (b_3 \xi + b_4) v_2'' - b_3 v_2' = -2 D_0 D_1 v_1 - D_1^2 v_0 - 2 D_0 D_2 v_0 - b_1 D_0 v_0 \\ &+ b_5 \left(w_1' v_0' \right)' + b_5 \left(w_0' v_1' \right)' + b_6 \left(v_0' \right)^2 v_0'' - b_7 \left| D_0 v_0 \right| D_0 v_0, \end{aligned} \tag{4.58}$$

with the associated boundary conditions being $v_2(0,\tau) = v_2(1,\tau) = v_2''(0,\tau) = v_2''(1,\tau) = w_2(0,\tau) = w_2(1,\tau) = 0$.

Notice that Eqs. (4.53) to (4.58) present the same operator structure on the left-hand side of equality, which should be noticed it is a Sturm-Liouville operator in both axial and transversal directions. An important feature is that, for each order, the problem is that of a linear structure under a forcing term that is dependent on the previous order's solution, while the first problem is that of free vibrations of the structure, whose solution is

widely known. Starting the solution process, notice that there is no excitation on the axial direction of order ϵ^0, which allows to drop the solution of this order in the axial direction as made in Kloda, Lenci & Warminski (2018). Regarding the transversal problem, although there are no direct excitation mechanisms, it is expected that responses on this order will end up being generated due to the existence of the parametric excitation. At order ϵ^0 the problem is that of the linear free vibrations of a flexible rod under the action of a varying tension along the structural length. In this research it shall be considered the case where a single mode is mainly excited, so at this point multi-modal responses are being ruled out. Let ψ_0 be the modal shape associated with the problem in Eq. (4.54). Such shape can be be given in analytical terms (see Mazzilli, Lenci & Demeio (2014) and Appendix B) as "Bessel-like" functions, or it can be obtained by approximated or numerical means. The fundamental point is that the shape can be obtained somehow, with the path chosen to obtain it not being important for the present analysis. The natural frequency associated with ψ_0 is herein named ω_0, being equal to 1 in dimensionless variables. This leads to the solution of order ϵ^0 to be given as

$$w_0 = 0, \tag{4.59}$$

$$v_0 = \psi_0 \left(B_0 e^{i\tau_0} + \overline{B}_0 e^{-i\tau_0} \right) = \psi_0 B_0 e^{i\tau_0} + c.c. \ . \tag{4.60}$$

Now, Eqs. (4.59) and (4.60) are applied to the order ϵ^1 problem. In the axial direction, the problem becomes

$$D_0^2 w_1 - a_2 w_1'' = a_3 \psi_0' \psi_0'' \left(B_0^2 e^{2i\tau_0} + B_0 \overline{B}_0 \right) + c.c. \ , \tag{4.61}$$

which represents a linear structure under an external forcing consisting of a time-wise constant term and an oscillatory term with frequency $2\omega_0$. Asides that, the boundary condition $w_1(1, \tau) = \delta \cos(n\tau)$ generates a component of frequency $n\omega_0$ on the system response. Since the focus is to investigate the behaviour of the structure around the main parametric instability, it is assumed that $n = 2 + \epsilon^2 \sigma$, with σ being a detuning parameter. Since an undamped and linear oscillator's response consists of components with the same frequency as the forcing terms, the solution of Eq. (4.61) is given as

$$w_1 = \phi_{1a} A_{1a} + \phi_{1b} A_{1b} e^{2i\tau_0} + c.c. \ . \tag{4.62}$$

The detuning $\epsilon^2 \sigma$ is not present at the solution since it produces terms of higher orders in ϵ than the ones considered at the present stage. Another hypothesis is now made, namely, that $2\omega_0$ is not resonant with any axial natural frequency. This is particularly

valid for slender structures when lower modes are being considered. Looking at Eqs. (4.61) and (4.62), it is possible to see that the axial solution is of second order with respect to the transversal solution, which is a common assumption in problems involving hinged-hinged flexible rods. In order to obtain the functions $\phi_{1a}A_{1a}$ and $\phi_{1b}A_{1b}$, Eq. (4.62) is substituted into (4.61) with terms containing the same frequency being required to vanish independently. The obtained problems can then be solved using the method of variation of parameters, leading to

$$A_{1a} = \frac{-a_3}{a_2} B_0 \overline{B}_0, \tag{4.63}$$

$$A_{1b} = \frac{-a_3}{a_2} B_0^2, \tag{4.64}$$

$$\phi_{1a} = \int_0^{\xi} \frac{\left(\psi_0'(s)\right)^2}{2} \, \mathrm{d}s - \xi \int_0^1 \frac{\left(\psi_0'(\xi)\right)^2}{2} \, \mathrm{d}\xi, \tag{4.65}$$

$$\begin{aligned} \phi_{1b} = & \left(\frac{-a_2}{a_3 B_0^2} \frac{\delta e^{i\sigma\tau_2}}{2} + \alpha \right) \frac{\sin\left(\frac{2\xi}{\sqrt{a_2}}\right)}{\sin\left(\frac{2}{\sqrt{a_2}}\right)} - \frac{\sqrt{a_2}}{2} \cos\left(\frac{2\xi}{\sqrt{a_2}}\right) \int_0^{\xi} \sin\left(\frac{2s}{\sqrt{a_2}}\right) \psi_0'(s) \, \psi_0''(s) \, \mathrm{d}s \\ & + \frac{\sqrt{a_2}}{2} \sin\left(\frac{2\xi}{\sqrt{a_2}}\right) \int_0^{\xi} \cos\left(\frac{2s}{\sqrt{a_2}}\right) \psi_0'(s) \, \psi_0''(s) \, \mathrm{d}s = \left(\frac{-a_2}{a_3 B_0^2} \frac{\delta e^{i\sigma\tau_2}}{2} + \alpha \right) \phi_{1b,0} + \phi_{1b,p}. \end{aligned} \tag{4.66}$$

Since it is not always possible to furnish a closed-form expressions for integrals involving ψ_0 and its derivatives, the auxiliary variable s is used whenever needed for mathematical precision. The new constant α is obtained by imposing the boundary conditions of the problems, resulting in

$$\alpha = \frac{\sqrt{a_2}}{2} \cos\left(\frac{2}{\sqrt{a_2}}\right) \int_0^1 \sin\left(\frac{2\xi}{\sqrt{a_2}}\right) \psi_0' \psi_0'' \, \mathrm{d}\xi - \frac{\sqrt{a_2}}{2} \sin\left(\frac{2}{\sqrt{a_2}}\right) \int_0^1 \cos\left(\frac{2\xi}{\sqrt{a_2}}\right) \psi_0' \psi_0'' \, \mathrm{d}\xi. \tag{4.67}$$

For the transversal problem of order ϵ^1, only homogeneous boundary conditions are present, and the differential equation is

$$\ddot{v}_1 + b_2 v_1'''' - (b_3\xi + b_4) \, v_1'' - b_3 v_1' = -2i\psi_0 D_1 B_0 e^{i\tau_0} + c.c., \tag{4.68}$$

Notice now that there is a resonant term on the right-hand side, with frequency ω_0 (1 in the presented dimensionless form). From basic linear dynamical systems concepts it is expected that this can lead to unbounded responses of v_1. This case requires a solvability condition to be furnished in order to guarantee that the solution for v_1 is bounded, otherwise the scaled expansion made would not be valid. For the case of PDEs, this is made by using the adjoint operator together with Freedholm's alternative theorem (see Appendix D). Since in this case the boundary conditions are all homogeneous and using the fact that Sturm-Liouville operators are self-adjoint, the solvability condition is simply given by requesting the forcing term to be orthogonal to the solutions of the left-hand side, leading to

$$D_1 B_0 = 0, \tag{4.69}$$

which results in $B_0 = B_0(\tau_2)$. Equation (4.68) also possess a homogeneous solution. This solution is however disregarded since the operator is the same as in oder ϵ^0 in which case the homogeneous solution is considered, leading to $v_1 = 0$. With all the order ϵ^1 solutions obtained it is possible to move on to order ϵ^2. For the axial problem, it is obtained that

$$\ddot{w}_2 - a_2 w_2'' = -2ia_1\phi_{1b}A_{1b}e^{2i\tau_0} + c.c.\ . \tag{4.70}$$

In this case, the only forcing term has frequency $2\omega_0$ and no contributions are given by the boundary conditions. This leads to the solution for w_2 in the form

$$w_2 = \phi_2 A_2 e^{2i\tau_0} + c.c., \tag{4.71}$$

yet again the solution is obtained with the method of variation of parameters leading to

$$A_2 = \frac{2ia_1}{a_2}A_{1b}, \tag{4.72}$$

$$\begin{aligned}\phi_2 = {} & \frac{\beta}{\sin\left(\frac{2}{\sqrt{a_2}}\right)}\sin\left(\frac{2\xi}{\sqrt{a_2}}\right) - \frac{\sqrt{a_2}}{2}\cos\left(\frac{2\xi}{\sqrt{a_2}}\right)\int_0^{\xi}\sin\left(\frac{2s}{\sqrt{a_2}}\right)\phi_{1b}(s)\,\mathrm{d}s \\ & + \frac{\sqrt{a_2}}{2}\sin\left(\frac{2\xi}{\sqrt{a_2}}\right)\int_0^{\xi}\cos\left(\frac{2s}{\sqrt{a_2}}\right)\phi_{1b}(s)\,\mathrm{d}s.\end{aligned} \tag{4.73}$$

By means of the boundary conditions, the constant β is given as

$$\beta = \frac{\sqrt{a_2}}{2}\cos\left(\frac{2}{\sqrt{a_2}}\right)\int_0^1 \sin\left(\frac{2\xi}{\sqrt{a_2}}\right)\phi_{1b}\,\mathrm{d}\xi - \frac{\sqrt{a_2}}{2}\sin\left(\frac{2}{\sqrt{a_2}}\right)\int_0^1 \cos\left(\frac{2\xi}{\sqrt{a_2}}\right)\phi_{1b}\,\mathrm{d}\xi. \tag{4.74}$$

With that solution it is finally possible to tackle the order ϵ^2 transversal problem, which reads

$$\begin{aligned}
&\ddot{v}_2 + b_2 v_2'''' - (b_3\xi + b_4)\,v_2'' - b_3 v_2' = -b_7\,|D_0 v_0|\,D_0 v_0 - 2i\psi_0 D_2 B_0 e^{i\tau_0} - ib_1\psi_0 B_0 e^{i\tau_0}\\
&+ b_5\left(\phi_{1a}'\psi_0'\right)'\left(A_{1a}B_0 + \overline{A}_{1a}B_0\right)e^{i\tau_0} + b_5\left(\phi_{1b}'\psi_0'\right)'\left(A_{1b}B_0 e^{3i\tau_0} + A_{1b}\overline{B}_0 e^{i\tau_0}\right)\\
&+ b_6\left(\psi_0'\right)^2\psi_0''\left(B_0^3 e^{3i\tau_0} + 3B_0^2\overline{B}_0 e^{i\tau_0}\right) + c.c.,
\end{aligned} \tag{4.75}$$

Finally, the solvability condition for the order ϵ^2 transversal equation can be evaluated. Keeping in mind that terms of frequency ω_0 are originated from the function $|D_0 v_0|\,D_0 v_0$, the condition reads

$$\begin{aligned}
&-2iD_2B_0\int_0^1\psi_0^2\,\mathrm{d}\xi - ib_1B_0\int_0^1\psi_0^2\,\mathrm{d}\xi + b_5B_0\left(A_{1a}+\overline{A}_{1a}\right)\int_0^1\left(\phi_{1a}'\psi_0'\right)'\psi_0\,\mathrm{d}\xi\\
&+ b_5A_{1b}\overline{B}_0\int_0^1\left(\phi_{1b}'\psi_0'\right)'\psi_0\,\mathrm{d}\xi + 3b_6B_0^2\overline{B}_0\int_0^1\left(\psi_0'\right)^2\psi_0''\psi_0\,\mathrm{d}\xi = f_1b_7\int_0^1|\psi_0|\,\psi_0^2\,\mathrm{d}\xi.
\end{aligned} \tag{4.76}$$

The new term f_1 is the coefficient of the element with frequency ω_0 that arises from the Fourier series expansion of the Morison damping. The polar decomposition of complex numbers is used, making $B_0 = Re^{i\theta}$, with R and θ being real-valued functions. This allows to split Eq. (4.76) into its real and imaginary parts, as well as to write the term f_1 as

$$f_1e^{-i\theta} = \frac{16iR^2}{3\pi}. \tag{4.77}$$

After carrying out some algebraic manipulation, a system of equations for R and θ is obtained, given by

$$\beta_1D_2R + \beta_3R + \beta_6R\,|R| = \delta\beta_5R\sin\left(\sigma\tau_2 - 2\theta\right), \tag{4.78}$$

$$\beta_2RD_2\theta + \beta_4R^3 = -\delta\beta_5R\cos\left(\sigma\tau_2 - 2\theta\right) \tag{4.79}$$

The new parameters β are defined to simplify the notation, collecting all the relevant integrals over the structure. The parameters β_1 and β_2 are normalization parameters, that depend only on the shape function as

$$\beta_1 = \beta_2 = 2\int_0^1 \psi_0^2 \,\mathrm{d}\xi. \tag{4.80}$$

The parameter β_3 is a measure of the linear damping effect on the final solution, given by

$$\beta_3 = b_1 \int_0^1 \psi_0^2 \,\mathrm{d}\xi. \tag{4.81}$$

The nonlinear effects of structural origin are gathered in β_4 as

$$\beta_4 = -2b_5\frac{a_3}{a_2}\int_0^1 \left(\phi_{1a}'\psi_0'\right)'\psi_0 \,\mathrm{d}\xi - \alpha b_5\frac{a_3}{a_2}\int_0^1 \left(\phi_{1b,0}'\psi_0'\right)'\psi_0 \,\mathrm{d}\xi - b_5\frac{a_3}{a_2}\int_0^1 \left(\phi_{1b,p}'\psi_0'\right)'\psi_0 \,\mathrm{d}\xi$$
$$+ 3b_6\int_0^1 \psi_0''\left(\psi_0'\right)^2\psi_0 \,\mathrm{d}\xi. \tag{4.82}$$

The effect due to the existence of the top-motion is measured by β_5, written as

$$\beta_5 = \frac{b_5}{2}\int_0^1 \left(\phi_{1b,0}'\psi_0'\right)'\psi_0 \,\mathrm{d}\xi. \tag{4.83}$$

Finally, the effects due the Morison damping are collected in β_6, given by

$$\beta_6 = \frac{16b_7}{3\pi}\int_0^1 |\psi_0|\,\psi_0^2 \,\mathrm{d}\xi. \tag{4.84}$$

In order to proceed with the solution of Eqs. (4.78) and (4.79), a variable change is applied, defined by $2\theta = \sigma\tau_2 - \eta$, which leads to $2D_2\theta = \sigma - D_2\eta$. Since the objective is to analyse steady-state solutions, the relevant derivatives are considered zero, that is, $D_2\eta = D_2R = 0$. Dividing each of the remaining equations by R, squaring the results an adding them together leads to

$$\left(\beta_3 + \beta_6\,|R|\right)^2 + \left(\frac{\beta_2\sigma}{2} + \beta_4R^2\right)^2 = \beta_5^2\delta^2. \tag{4.85}$$

This equation rules the steady-state amplitude as a function of three parameters for any given pair (δ, σ), since β_2 and β_5 are merely a scaling of such pair. This solution can only be put in a closed-form expression for the particular cases of only one type of damping being considered. Another important feature is that, from Eq. (4.85) it is possible to obtain the backbone curve expression of the natural frequency of the rod. Taking out the damping and excitation sources, that is, letting $\delta = \beta_3 = \beta_6 = 0$, it results in

$$\sigma_0 = -\frac{2\beta_4 R^2}{\beta_2}, \tag{4.86}$$

where σ_0 is the value of σ in the particular case of free vibrations. Due to the polar solution adopted, it is easy to see that the frequency of oscillation is given as $\omega = 1 + \dot{\theta}$. Recalling that $2\theta = \sigma\tau_2 - \eta$, then $\dot{\theta} = \epsilon^2\sigma/2$ because $\dot{\eta} = 0$, which ultimately leads to

$$\omega = 1 + \dot{\theta} = 1 - \frac{\epsilon^2\beta_4 R^2}{\beta_2}. \tag{4.87}$$

Notice now that β_2 is the square of a norm, and thus is always positive. This means that the signal of β_4, given in Eq. (4.82) and related to the nonlinear structural terms, is what dictates if the behaviour of the structure will be that of hardening or softening in the particular case of nonlinear free vibrations.

4.3.1 Reduction of the analytical solution to a polynomial form

Although useful, it is noticeable that the analytical solution proposed with the MMTS directly over the PDEs of motion can be troublesome to compute. This is due to the integrals presented in Eqs. (4.80) to (4.84). These integrals do not possess a closed form for any shape function ψ_0, even when an expression for the shape function is known. In order to put this solution in a more "user-friendly" format to be used in design aid of real structures, a polynomial representation of the analytical solution is sought. The shape of the mode of interest can be written as (see Mazzilli, Lenci & Demeio (2014))

$$\psi_0 = \sqrt[4]{\frac{T_{bn}}{T_{bn} + \gamma\ell\xi}} \sin\left(n\pi \frac{\sqrt{T_{bn} + \gamma\ell\xi} - \sqrt{T_{bn}}}{\sqrt{T_{bn} + \gamma\ell} - \sqrt{T_{bn}}}\right), \tag{4.88}$$

recalling that the adjusted traction T_{bn} is given by

$$T_{bn} = T_b + EI\left(\frac{n\pi}{\ell}\right)^2. \tag{4.89}$$

This modal shape can be written as being a function of a certain parameter κ and the mode number n as

$$\psi_0 = \sqrt[4]{\frac{1}{1+\kappa\xi}} \sin\left(n\pi \frac{\sqrt{1+\kappa\xi}-1}{\sqrt{1+\kappa}-1}\right), \tag{4.90}$$

where κ is given by

$$\kappa = \frac{\gamma\ell}{T_{bn}}. \tag{4.91}$$

This means that almost all terms needed in the evaluation of the parameters β of the analytical solution can be written as a function of κ and n. The exceptions to this rule are the functions $\phi_{1b,0}$ and $\phi_{1b,p}$ together with the parameter α. For those, a further algebraic treatment will be applied when suitable. Special care must be taken with the nature of the two parameters ruling the calculations. While κ is a real-valued parameter, n can only assume positive integer values. Lets then consider cases where a specific mode number is chosen, no matter which. The mode ψ_0 then becomes a continuous function of κ, which can be continuously varied within the real numbers. This ensures that the integrals to be evaluated are also continuous functions of κ, and as such, they can be written as a series. For simplicity of implementation, a polynomial form is then adopted to represent all the resulting calculations. In this research, polynomials of tenth order are adopted, with its coefficients being obtained by a least squares fitting. The data source for the fitting is created by evaluating all the needed functions for $0 \leq \kappa \leq 10$ with a discretization step of 0.01 in κ. Let then a first polynomial be written as[5]

$$\int_0^1 \psi_0^2 \, \mathrm{d}\xi = p_1(\kappa). \tag{4.92}$$

The polynomial p_1 allows to write the coefficients β_1, β_2 and β_3 as

$$\beta_1 = \beta_2 = 2p_1(\kappa), \tag{4.93}$$

$$\beta_3 = b_1 p_1(\kappa). \tag{4.94}$$

[5] The equality sign is used for simplicity to denote the term that each polynomial approximately represents.

A second polynomial is defined to help the evaluation β_6 as

$$\int_0^1 |\psi_0| \, \psi_0^2 \, \mathrm{d}\xi = p_2(\kappa) \,, \tag{4.95}$$

which leads to

$$\beta_6 = \frac{16 b_7}{3\pi} p_2(\kappa) \,. \tag{4.96}$$

Regarding β_4 and β_5, the issue is the dependence of a_2 in the functions $\phi_{1b,0}$ and $\phi_{1b,p}$ together with the parameter α. However, the parameter a_2 is the square of the ratio between the first axial natural frequency and the frequency of the mode of interest being analysed. Such ratio is usually large for slender structures when lower transversal modes are the main concern, which means its inverse is a small value. This allows for an expansion in Taylor series up to the third order in ξ to be a reasonable approximation for the trigonometric functions that are dependent on this parameter. The expressions of interest to be expanded are

$$\cos\left(\frac{2\xi}{\sqrt{a_2}}\right) = 1 - \frac{2\xi^2}{a_2}, \tag{4.97}$$

$$\sin\left(\frac{2\xi}{\sqrt{a_2}}\right) = \frac{2\xi}{\sqrt{a_2}} - \frac{4\xi^3}{3a_2\sqrt{a_2}}. \tag{4.98}$$

With those approximations, the parameter α is given as

$$\begin{aligned}
\alpha &= \cos\left(\frac{2}{\sqrt{a_2}}\right) \int_0^1 \xi \psi_0'' \psi_0' \, \mathrm{d}\xi - \frac{2}{3a_2} \cos\left(\frac{2}{\sqrt{a_2}}\right) \int_0^1 \xi^3 \psi_0'' \psi_0' \, \mathrm{d}\xi \\
&- \frac{\sqrt{a_2}}{2} \sin\left(\frac{2}{\sqrt{a_2}}\right) \int_0^1 \psi_0'' \psi_0' \, \mathrm{d}\xi + \frac{1}{\sqrt{a_2}} \sin\left(\frac{2}{\sqrt{a_2}}\right) \int_0^1 \xi^2 \psi_0'' \psi_0' \, \mathrm{d}\xi \\
&= \cos\left(\frac{2}{\sqrt{a_2}}\right) \left(p_3(\kappa) + \frac{1}{a_2} p_4(\kappa)\right) + \sin\left(\frac{2}{\sqrt{a_2}}\right) \left(\sqrt{a_2} p_5(\kappa) + \frac{1}{\sqrt{a_2}} p_6(\kappa)\right).
\end{aligned} \tag{4.99}$$

In a similar manner, the parameter β_5 reads

$$\beta_5 = -\frac{b_5}{2}\frac{4}{a_2\sqrt{a_2}\sin\left(\frac{2}{\sqrt{a_2}}\right)}\int_0^1 2\xi\psi_0'\psi_0 + \xi^2\psi_0''\psi_0\,\mathrm{d}\xi$$
$$+\frac{b_5}{2}\left(\frac{2}{\sqrt{a_2}\sin\left(\frac{2}{\sqrt{a_2}}\right)}\int_0^1 \psi_0''\psi_0\,\mathrm{d}\xi + \frac{16}{3a_2^2\sqrt{a_2}\sin\left(\frac{2}{\sqrt{a_2}}\right)}\int_0^1 \xi^3\psi_0'\psi_0\,\mathrm{d}\xi\right)$$
$$= \frac{b_5}{2\sqrt{a_2}\sin\left(\frac{2}{\sqrt{a_2}}\right)}\left(p_7(\kappa) + \frac{p_8(\kappa)}{a_2} + \frac{p_9(\kappa)}{a_2^2}\right). \tag{4.100}$$

Lastly, for parameter β_4, a more cumbersome task appears. This case is dealt with a considerable amount of polynomials defined as

$$\int_0^1 \left(\phi_{1a}'\psi_0'\right)'\psi_0\,\mathrm{d}\xi = p_{10}(\kappa), \tag{4.101}$$

$$\int_0^1 \psi_0''\left(\psi_0'\right)^2\psi_0\,\mathrm{d}\xi = p_{11}(\kappa), \tag{4.102}$$

$$
\begin{aligned}
&\int_0^1 \left(\phi'_{1b,p}\psi'_0\right)' \psi_0 \,\mathrm{d}\xi = \int_0^1 \psi''_0\psi_0 \left(\int_0^\xi \psi''_0\psi'_0 \,\mathrm{d}s\right) \mathrm{d}\xi \\
&+ \frac{4}{a_2}\int_0^1 \left(\psi'_0\psi_0\left(\int_0^\xi s\psi''_0\psi'_0 \,\mathrm{d}s\right) - \xi\psi'_0\psi_0\left(\int_0^\xi \psi''_0\psi'_0 \,\mathrm{d}s\right) + \xi\psi''_0\psi_0\left(\int_0^\xi s\psi''_0\psi'_0 \,\mathrm{d}s\right)\right) \mathrm{d}\xi \\
&+ \frac{2}{a_2}\int_0^1 \left(-\psi''_0\psi_0\left(\int_0^\xi s^2\psi''_0\psi'_0 \,\mathrm{d}s\right) - \xi^2\psi''_0\psi_0\left(\int_0^\xi \psi''_0\psi'_0 \,\mathrm{d}s\right)\right) \mathrm{d}\xi \\
&+ \frac{8}{a_2^2}\int_0^1 \left(-\frac{1}{3}\psi'_0\psi_0\left(\int_0^\xi s^3\psi''_0\psi'_0 \,\mathrm{d}s\right) - \xi^2\psi'_0\psi_0\left(\int_0^\xi s\psi''_0\psi'_0 \,\mathrm{d}s\right)\right) \mathrm{d}\xi \\
&+ \frac{8}{a_2^2}\int_0^1 \left(\frac{1}{3}\xi^3\psi'_0\psi_0\left(\int_0^\xi \psi''_0\psi'_0 \,\mathrm{d}s\right) + \xi\psi'_0\psi_0\left(\int_0^\xi s^2\psi''_0\psi'_0 \,\mathrm{d}s\right)\right) \mathrm{d}\xi \\
&+ \frac{8}{a_2^2}\int_0^1 \left(-\frac{1}{3}\xi\psi''_0\psi_0\left(\int_0^\xi s^3\psi''_0\psi'_0 \,\mathrm{d}s\right) - \frac{1}{3}\xi^3\psi''_0\psi_0\left(\int_0^\xi s\psi''_0\psi'_0 \,\mathrm{d}s\right)\right) \mathrm{d}\xi \\
&+ \frac{4}{a_2^2}\int_0^1 \left(\xi^2\psi''_0\psi_0\left(\int_0^\xi s^2\psi''_0\psi'_0 \,\mathrm{d}s\right)\right) \mathrm{d}\xi \\
&+ \frac{16}{3a_2^3}\int_0^1 \left(\xi^2\psi'_0\psi_0\left(\int_0^\xi s^3\psi''_0\psi'_0 \,\mathrm{d}s\right) - \xi^3\psi'_0\psi_0\left(\int_0^\xi s^2\psi''_0\psi'_0 \,\mathrm{d}s\right)\right) \mathrm{d}\xi \\
&+ \frac{16}{9a_2^3}\int_0^1 \left(\xi^3\psi''_0\psi_0\left(\int_0^\xi s^3\psi''_0\psi'_0 \,\mathrm{d}s\right)\right) \mathrm{d}\xi = p_{12}(\kappa) + \frac{p_{13}(\kappa)}{a_2} + \frac{p_{14}(\kappa)}{a_2^2} + \frac{p_{15}(\kappa)}{a_2^3}.
\end{aligned}
\tag{4.103}
$$

Those polynomials allow to write β_4 as

$$
\begin{aligned}
\beta_4 = &-\frac{\alpha b_5 a_3}{a_2\sqrt{a_2}\sin\left(\frac{2}{\sqrt{a_2}}\right)}\left(p_7(\kappa) + \frac{p_8(\kappa)}{a_2} + \frac{p_9(\kappa)}{a_2^2}\right) - \frac{2b_5a_3}{a_2}p_{10}(\kappa) + 3b_6p_{11}(\kappa) \\
&- \frac{b_5a_3}{a_2}\left(p_{12}(\kappa) + \frac{p_{13}(\kappa)}{a_2} + \frac{p_{14}(\kappa)}{a_2^2} + \frac{p_{15}(\kappa)}{a_2^3}\right).
\end{aligned}
\tag{4.104}
$$

With that, all the parameters are calculated using polynomials, and the solution for the steady-state amplitudes can be computed from Eq. (4.85). One last polynomial is now defined because the modal function computed as in Eq. (4.90) is not normalized. Let $\widehat{\psi}_0$ be the maximum value of ψ_0 along the structural length. Then, the last polynomial is defined as $p_{16}(\kappa) = \widehat{\psi}_0$, which leads to the steady-state amplitude

$$\overline{A} = 2p_{16}(\kappa)R. \tag{4.105}$$

In order to organize all the 16 polynomials and its coefficients, they are written in the general form

$$^{n}p_i\left(\kappa\right) = \sum_{j=0}^{10} \left({}^{n}_{i}C_j \kappa^j \right). \tag{4.106}$$

The values of the constants ${}^{n}_{i}C_j$ are given in Appendix E.

4.4 Comparison between different approaches

Once different solutions are obtained, it is now time to evaluate the accuracy of each one of them and to address potential advantages of each. The assessment of the correctness of each model is made by comparison with a numerical reference obtained with simulations using the finite element method (FEM). To that end, the in-house software Giraffe[6] is used, which has being extensively used in the literature and has its quality assured. An important feature is that the fluid-structure interaction by means of the Morison model adopted in the formulation herein explored is exactly the same as implemented in Giraffe, allowing a comparison on the same modelling hypothesis. For details regarding Giraffe and the description of the elements used by the software the reader is refereed to Gay Neto, Martins & Pimenta (2013), Gay Neto (2016) and Gay Neto (2021). It is important to point out that neither Giraffe, nor the family of models herein derived consider FSI phenomena, such as VIV or VSIV. For the example adopted for comparison, consider the structural data presented in Table 6.

Regarding the ROMs, the numerical values of the parameters obtained with the proposed data are given in Table 7.

All the ROMs are numerically integrated by means of a Runge-Kutta scheme native to Matlab® as the "ode45" function. In order to evaluate the steady-state amplitude A_m, the average of the values of the response peaks of the last 1% of the time-series is taken. Together with the numerical integration, ROMs (i) and (ii) are also evaluated by means of the MMTS solution, presented since they are 1-DOF-ROMs. Before the comparisons can be actually made, a reconstruction of the continuous displacement field is necessary using the ROMs results. This is simply made by using the trial assumption adopted in the

[6] Giraffe is an acronym for "Generic Interface Readily Accessible for Finite Elements", a software developed by Prof. Alfredo Gay Neto, at the University of São Paulo, capable of performing analysis with geometrically-exact beam elements amongst other capabilities.

Table 6 – Data for the structural model.

Property	Value
μ	948.6 kg/m
$(\mu + \mu_a)$	1200.0 kg/m
EI	318.6×10^6 Nm^2
γ	3433.5 N/m
EA	8541.8×10^6 N
ℓ	2000 m
ρ	1025 kg/m^3
D	0.5588 m
T_b	13.133×10^6 N
c	0 Ns/m^2
c_a	0 Ns/m^2
$\overline{C}_D$	1.0

Table 7 – Numerical values of the parameters for the ROMs.

Par.	Value	Par.	Value	Par.	Value	Par.	Value
β_1	0	β_2	0.1475	β_3	0.0092×10^{-2}	β_4	0.1072
b_1	0	b_2	0.3251	b_3	0.0126×10^{-2}	b_4	0.1132
b_{11}	0	b_{12}	1.0075	b_{13}	0.1451	b_{14}	-0.3009
b_{15}	0	b_{16}	0.0100×10^{-2}	b_{17}	0.0400×10^{-2}	b_{18}	0.0901×10^{-2}
b_{21}	0	b_{22}	4.0307	b_{23}	0.5806	b_{24}	-0.0752
b_{25}	-0.7312	b_{26}	0.0016	b_{27}	0.0400×10^{-2}	b_{28}	0.0036
b_{31}	0	b_{32}	9.0713	b_{33}	1.3063	b_{34}	0
b_{35}	-0.3250	b_{36}	0.0081	b_{37}	0.0901×10^{-2}	b_{38}	0.0036

construction of each of the ROMs. In the sequence, the amplitude obtained for the point located at $Z = 968$ m, that is 48.4% of the rod length, is used in the comparison. This point is chosen for being the peak along the length of the rod in the shape of the first mode of vibration, considering the presented data. The chosen point thus presents the largest amplitude of oscillation along the rod, being of particular interest for engineering practice.

Now, considering the offshore engineering background motivating this research, the imposed top-motion is considered to present a natural period within 2 and 20 seconds, which is a typical range for sea-waves. This means that the modes that may undergo the principal parametric resonance are those with natural period within 4 and 40 seconds. The natural frequencies of the rod under study are presented in Table 8, accordingly to the different models under analysis.

Complementing the comparisons regarding natural mode properties, the shape of the first vibration mode obtained by each model is presented in Fig. 20.

By observing the obtained modal shapes and natural frequencies, it is clear that the “Bessel-like” function (ROM(i)) is the most suitable option to represent the modal

Table 8 – Natural frequencies of the rod modes calculated accordingly to each model.

Model	Mode	Frequency (rad/s)	Period (s)
FEM	1	0.1833	34.3
FEM	2	0.3667	17.1
FEM	3	0.5502	11.4
ROM(i)	1	0.1836	34.2
ROM(ii)	1	0.1643	38.2
ROM(iii)	1	0.1839	34.2
ROM(iii)	2	0.3674	17.1
ROM(iii)	3	0.5552	11.3

Figure 20 – Normalized modes of vibration obtained with each model. Modal shape comparison.

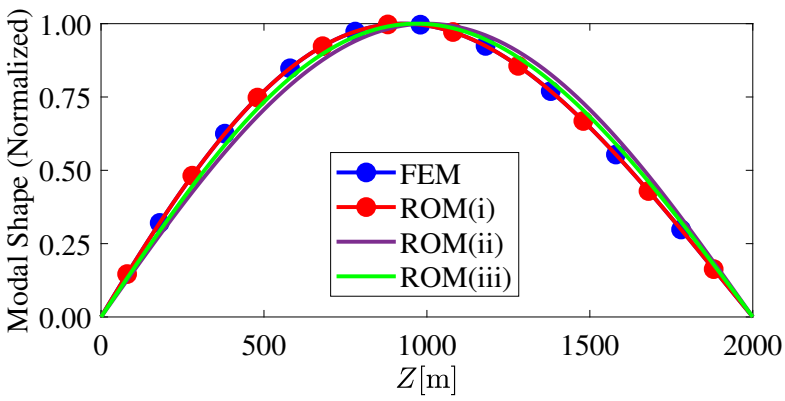

Source: Vernizzi, Franzini & Lenci (2019).

properties of the structure, with results presenting a superior quality even when compared to the case of multiple trigonometric functions combined (ROM(iii)). Notice also that the use of a single trigonometric function (ROM(ii)) does not furnish a good result for the natural frequency, even with the modal shape not being so different than the one given by a “Bessel-like" function.

This raises a discussion worth to be made regarding the choice of projection functions for ROMs. General intuition would suppose that if the shape is somewhat close to the actual vibration mode, then the results are expected to be good, which proved false in the presented example. A possible explanation requires a qualitative look at the linear part of the PDEs of motion, being the problem of topological order rather than simply of numerical convergence. This because the dependency of the structural response on a term proportional to V' vanishes only for the case of $\gamma = 0$, which is exactly the case whose mode of vibration is actually a sine function. This means that the mathematical model with the tension variation along the length has a structural difference in relation to the model without such variation, with this structural difference reflected on the modal shape functions, and, as the results shows, on the obtained values for the natural frequency. It is thus expected that the results furnished by ROM(ii) will not be adequate, since not even

the modal properties where recovered by this model with significant accuracy.

Following with the comparisons, the first one made regards the obtained analytical solution. To that end, post-critical amplitude maps as function of the dimensionless amplitude δ and the dimensionless excitation frequency n are presented. To build the maps, a 600×600 discretization was made in the range of values for δ and n. The maps obtained with numerical integration and with the analytical solution for ROM(i) are presented in Figs. 21 and 22, while Fig. 23 and 24 show the corresponding maps for ROM(ii).

Figure 21 – Post-critical amplitude map for ROM(i) in color-scale. Results obtained from the numerical integration of ROM(i); n indicating the dimensionless frequency of the imposed motion, A_m the dimensionless steady-state amplitude and δ indicating the dimensionless amplitude of the imposed motion.

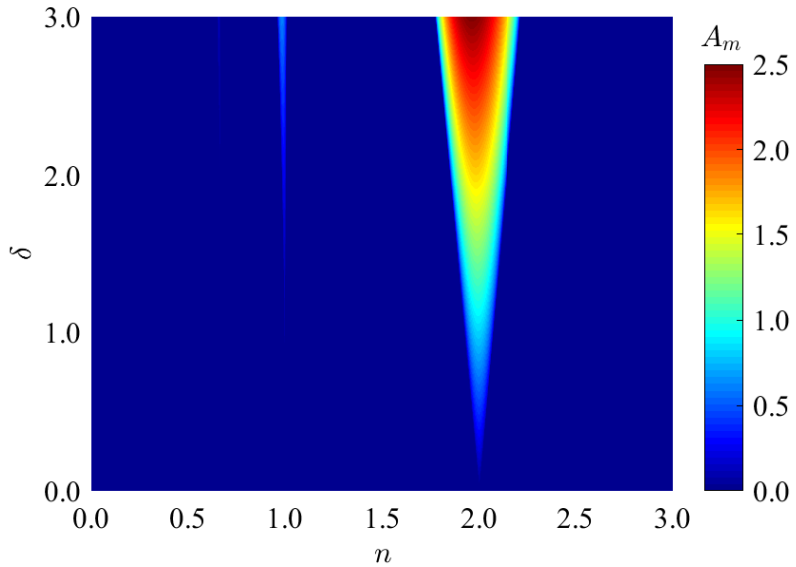

Source: Vernizzi, Franzini & Lenci (2019)

The first feature to be noticed with the observation of Figs. 21 to 24 is the good agreement of the analytical solution with the results obtained with numerical simulations, considering the range of validity of the analytical solution, that is, around $n = 2$. It is also noticeable the discrepancy in values between ROM(i) and ROM(ii). Although so far no comparisons have been made with the FEM reference in terms of dynamical response, by all the discussions already presented it is expected that the model giving a poor representation is ROM(ii). Looking now at ROM(iii), Fig. 25 brings its post-critical amplitude map considering a range of n to generate parametric resonance up to the third mode, while Fig. 26 shows a focused map around the parametric resonance of the first mode only.

The first aspect that gets the attention in Figs. 25 and 26 is that the regions of response due to the parametric excitation are very similar to each other, irrespective of the mode being excited. Another feature is that the parametric excitation focused on the

Figure 22 – Post-critical amplitude map for ROM(i) in color-scale based on the multiple scale analysis. n indicating the dimensionless frequency of the imposed motion, A_m the dimensionless steady-state amplitude and δ indicating the dimensionless amplitude of the imposed motion.

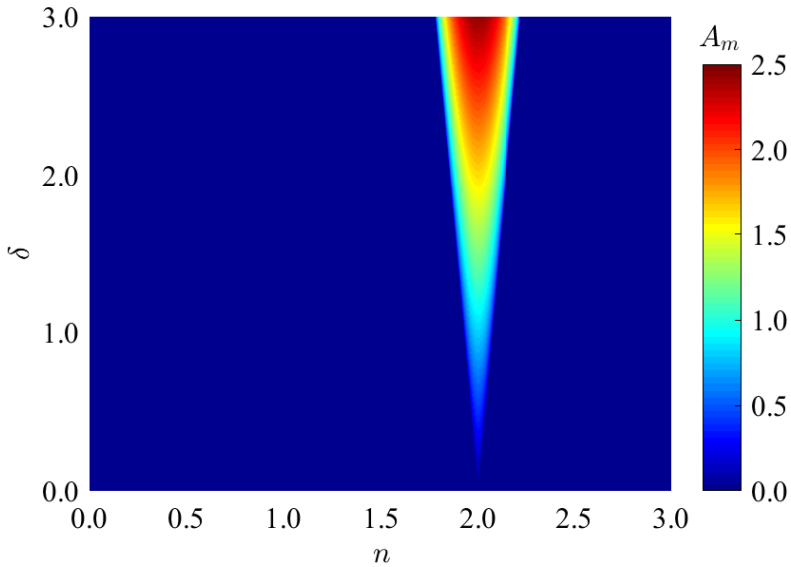

Source: Vernizzi, Franzini & Lenci (2019)

Figure 23 – Post-critical amplitude map for ROM(ii) in color-scale. Results obtained from the numerical integration of ROM(ii). n indicating the dimensionless frequency of the imposed motion, A_m the dimensionless steady-state amplitude and δ indicating the dimensionless amplitude of the imposed motion.

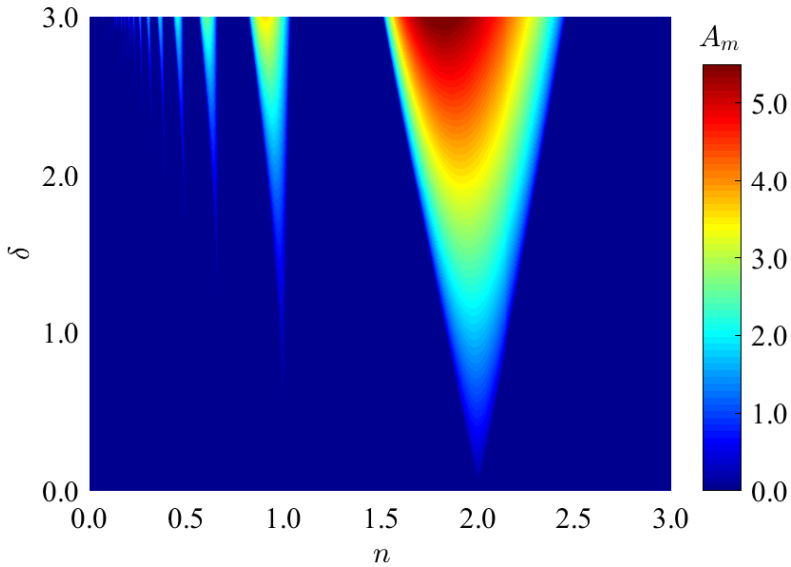

Source: Vernizzi, Franzini & Lenci (2019)

first mode is in good agreement with the results furnished by ROM(i).

With the ROMs addressed with the available analytical solution for the 1-DOF case,

Figure 24 – Post-critical amplitude map for ROM(ii) in color-scale based on the multiple scale analysis. n indicating the dimensionless frequency of the imposed motion, A_m the dimensionless steady-state amplitude and δ indicating the dimensionless amplitude of the imposed motion.

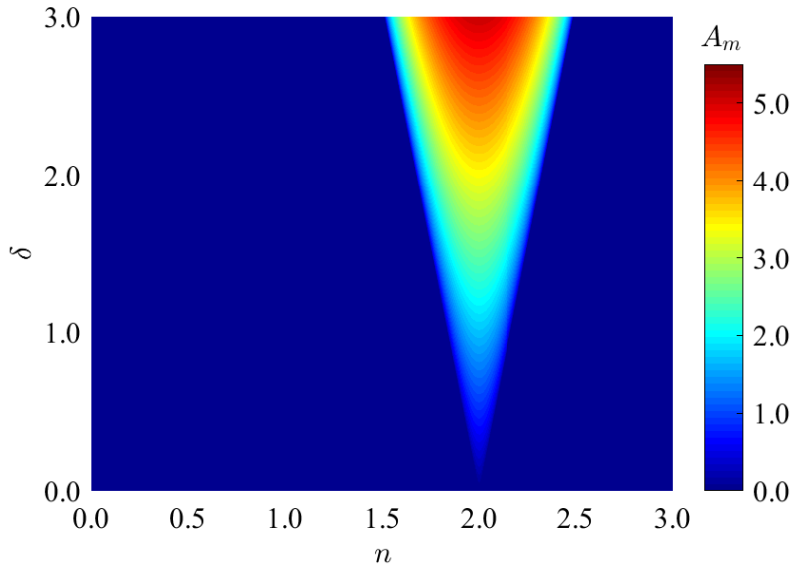

Source: Vernizzi, Franzini & Lenci (2019)

Figure 25 – Post-critical amplitude map for ROM(iii) in color-scale. Results obtained from the numerical integration of ROM(iii). n indicating the dimensionless frequency of the imposed motion, A_m the dimensionless steady-state amplitude and δ indicating the dimensionless amplitude of the imposed motion.

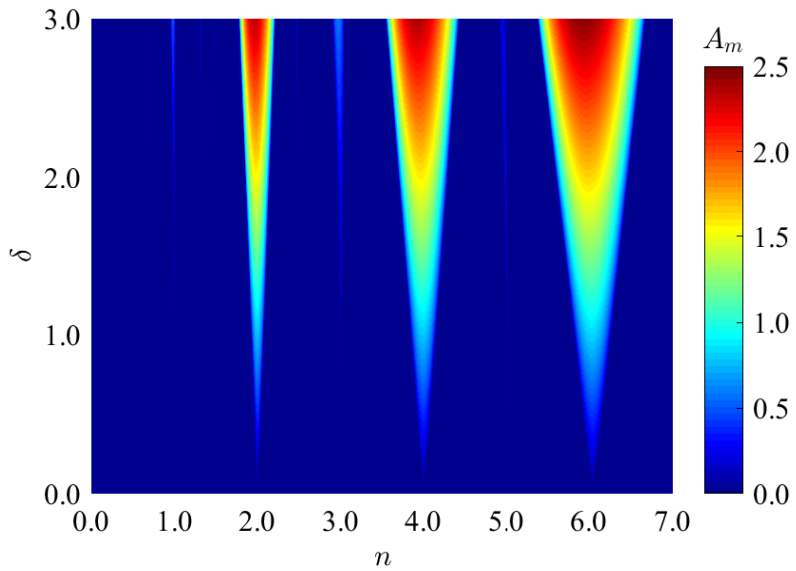

Source: Vernizzi, Franzini & Lenci (2019)

the necessity now is to compare the results with the chosen reference. Due to the amount of time required to perform each FEM simulation, the results are compared for a reduced

Figure 26 – Post-critical amplitude map for ROM(iii) in color-scale around the principal parametric excitation of the first mode. Results obtained from the numerical integration of ROM(iii). n indicating the dimensionless frequency of the imposed motion, A_m the dimensionless steady-state amplitude and δ indicating the dimensionless amplitude of the imposed motion.

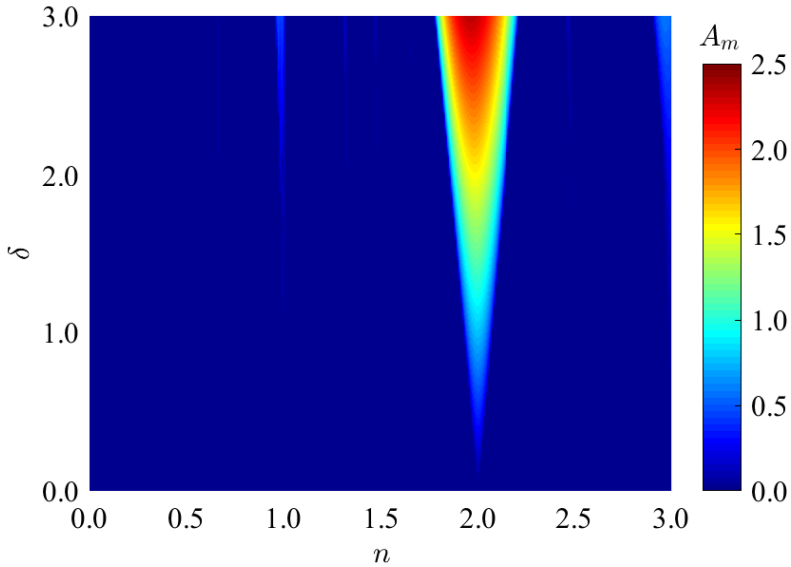

Source: Vernizzi, Franzini & Lenci (2019)

set of cases rather than the post-critical maps. That said, focus is put on the primary parametric resonance condition of the first mode, $n = 2$. Curves of the largest response amplitude, occurring at the selected point of comparison ($Z = 968$ m, are obtained as function of the dimensionless excitation amplitude δ, up to $\delta = 3$, with the results being shown in Fig. 27.

With the results in Fig. 27 it is clear that the initial insight that ROM(ii) would not give accurate results is confirmed. Another interesting feature is that, although both ROM(i) and (iii) are in good agreement with the reference, the adherence of ROM(i) is better, even being ROM(i) a simpler model, of only 1-DOF. This leads to an important conclusion regarding the modelling process, that is, investing more work on the projection functions used for the conception of ROMs can bring advantages in the final system to be simulated. In this case, a 1-DOF system is clearly simpler to integrate numerically than a 3-DOF one. Another advantage is the fact that the case with a single DOF allows for an analytical solution, while the case of multiple DOFs does not due to the Morison damping.

Another way to evaluate advantages between models is by means of the computational time required to obtain each solution. All the simulations of the ROMs, the FEM and the computations of the analytical solution were carried out in the same standard household computer. This allows for an honest, hardware independent comparison of the computational efficiency of each solution. For the case of the FEM simulation, the time of

Figure 27 – Post-critical dimensionless amplitude comparison for the different models on the principal parametric resonance ($n = 2$) as function of the dimensionless amplitude of excitation δ.

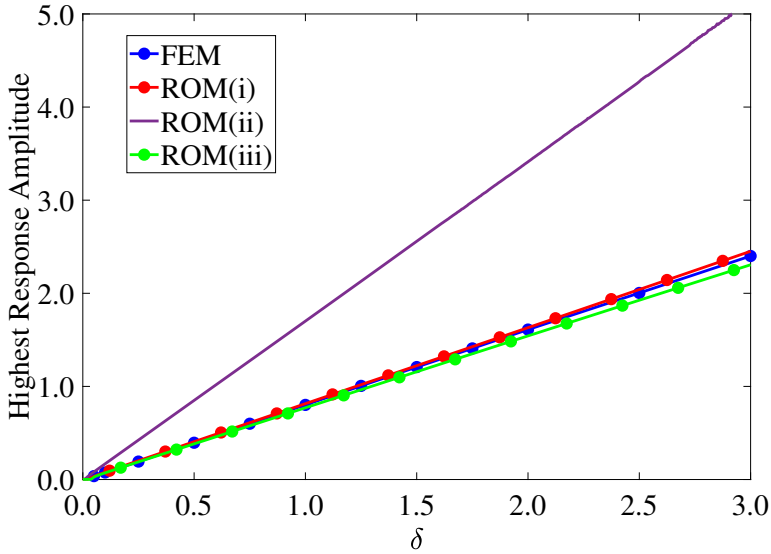

Source: Vernizzi, Franzini & Lenci (2019)

a single simulation is taken. For the ROMs, since each individual simulation is too short in time, the effort needed to evaluate a 600×600 post-critical amplitude map is measured, with the time of a single simulation being taken simply as the total necessary time divided by the number of simulations. The obtained measures are shown in Table 9

Table 9 – Comparison of computational time required by each type of solution.

Model	Method	Simulation of a 600×600 map (s)	Single simulation (s)
FEM	Numerical	–	1.342×10^3
ROM(i)	Numerical	29.3×10^3	0.082
ROM(i)	Analytical	11.5×10^{-3}	3.194×10^{-8}
ROM(iii)	Numerical	114.9×10^3	0.319

From the presented time consumption, other advantages of the different ROMs become clear. First of all, all the ROM-based solutions are significantly faster than the FEM one. This highlights the potential use of ROMs in design aid since they can be used to perform a great number of simulations in order to investigate how changes in the parameters affect the response of the structure or to define the most important design cases to be given a closer evaluation. This allows the designer to use the FEM only for the critical cases, selected with the help or ROMs, to be further investigated. Another important feature is that the analytical solution is much faster to be obtained than even the ROM simulations. This allows for an almost real-time evaluation procedure of the response of the structure under excitation. Highlight is made again to the fact that this was allowed due to the use of a well-thought projection function that lead to a minimal and accurate ROM which could be then investigated with analytical tools.

Moving on to a different type of solution, now the analytical results obtained with the MMTS directly over the PDEs of motion are addressed. The parameters for the structure are kept the same as for the ROMs approach and the "Bessel-like" function is used for the mode shape, leading to the parameters β presented in Table 10.

Table 10 – Parameters for the analytical solution.

Parameter	Value
β_1	0.998886
β_2	0.998886
β_3	0.000000
β_4	−0.000333
β_5	−0.036819
β_6	0.095966

As it was made for the ROMs, the first step is to compare the results with the FEM solution. Again, this is made for the case of the principal parametric excitation of the first mode, $n = 2$ (or $\sigma = 0$), with an amplitude of top-excitation up to $\delta = 3.0$. The obtained results are shown in Fig. 28.

Figure 28 – Amplitude of response for the principal parametric instability as function of the top motion amplitude δ. Comparison between analytical and FEM solutions.

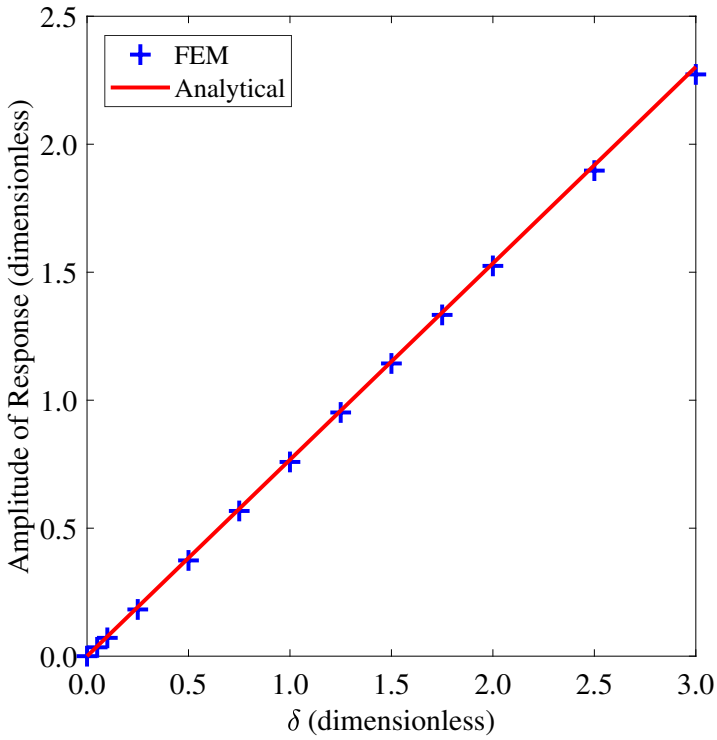

Source: Vernizzi, Lenci & Franzini (2020).

From the results shown in Fig. 28, a remarkable adherence between the analytical

and the numerical results is present, with the maximum relative difference between results being less than 1%. This analytical solution possess an accuracy even better than any of the ROMs explored, using an unnoticeable computational time of evaluation. In this case, another comparison is made, being the frequency-response curves obtained with the analytical solution against some chosen points for FEM simulation. The results are presented in Fig. 29.

Figure 29 – Amplitude of response as function of the top motion dimensionless frequency. Comparison between analytical and FEM solutions for three different top motion amplitudes.

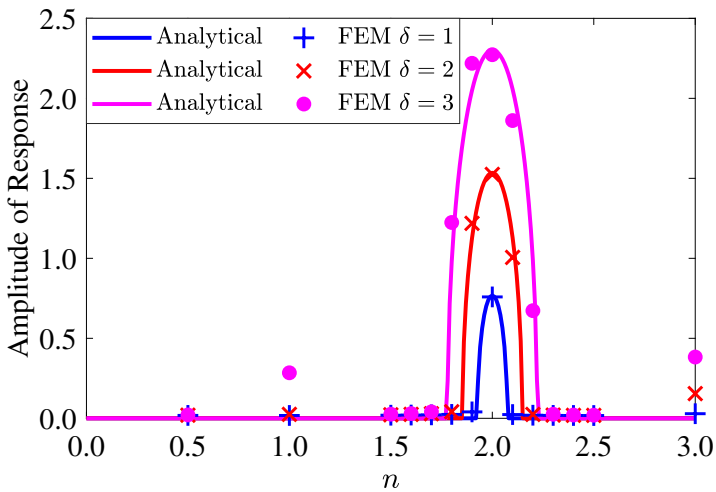

Source: Vernizzi, Lenci & Franzini (2020).

A very good agreement between the analytical solution and the numerical reference is shown in the results presented in Fig. 29. Notice that some responses in the dimensionless frequencies 1 and 3 are also obtained by the numerical reference but not by the analytical solution. This is expected since the latter is developed to give solutions around the main parametric instability condition, $n = 2$. Notice however that due to their magnitude, such responses on 1 and 3 are not of primary importance compared to the problem of $n = 2$.

4.4.1 Sensitivity studies with the PDE solution

After the excellent adherence presented by the analytical results with respect to the adopted reference, now is an adequate time to present one of the main advantages of possessing analytical solutions, which is the performing of parametric investigations. The main reason why the analytical solution is useful to that end is the necessary computational cost. With the analytical solution it is possible to evaluate the response of the structure for a wide range of the governing parameters, while such evaluation with high-hierarchy methods such as the FEM would not be feasible within an acceptable amount of time.

The analysis is made with respect to the parameters β_i since all the physical parameters may be reduced to the former and their use in the analytical solution is direct. The first investigation made involves β_4, which represents the effects of structural and geometrical nonlinearities. In Fig. 30, the backbone curves of the first vibration mode are shown for different values of β_4, while the other parameters are kept the same as in Table 10.

Figure 30 – Backbone curves for the first mode of vibration for different values of β_4 showing the relation between the actual vibration frequency ω and the linear natural frequency ω_0.

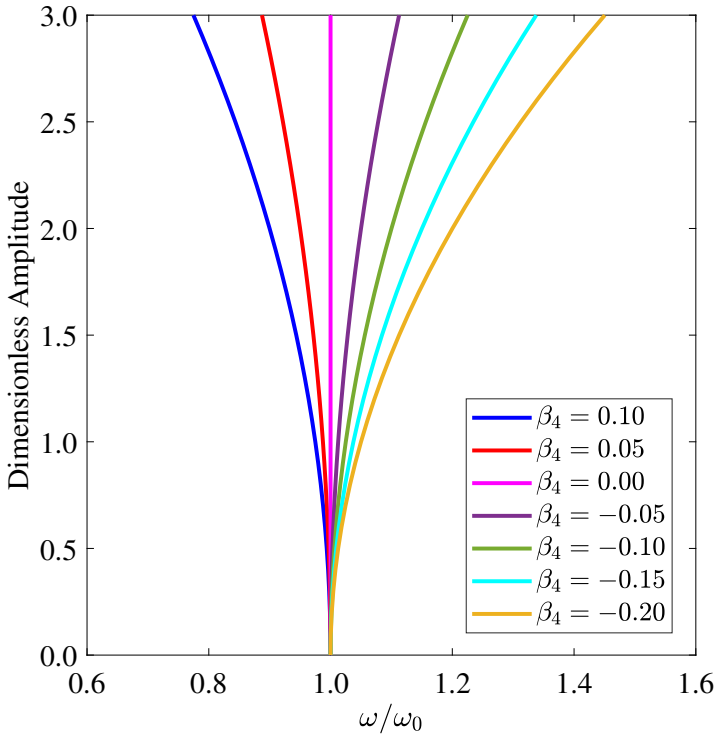

Source: Vernizzi, Lenci & Franzini (2020).

A strong dependence in β_4 is observed in the backbone curves for large oscillation amplitudes. Another interesting observation is that, by calibrating the structural properties in order to obtain $\beta_4 \approx 0$, it is possible to achieve a structure whose natural frequency is independent of the amplitude of vibration. This is of particular interest in terms of design, specially in the early stages, since the amplitudes of vibration are an unknown, while the typical frequencies of external sources are usually known. This may lead to scenarios of false conclusions when those are made based only on the linear natural frequency. For example, the linear frequency may be very different from any external excitation frequency, leading to the assumption that the latter will not be of importance for the problem. However, this may not be the case for when the effect of the response amplitude is taken into account for the natural frequency, depending on the values of such amplitude and of

β_4. To better illustrate such effect, consider the cases of $\beta_4 = -0.2$ shown in Fig. 31 and $\beta_4 = 0.2$ shown in Fig. 32.

Figure 31 – Amplitude of response as function of the top motion dimensionless frequency with $\beta_4 = -0.2$. The curve with the frequency of the principal parametric instability according to the backbone curve is also shown, named "Backbone" for the sake of the size of the legend.

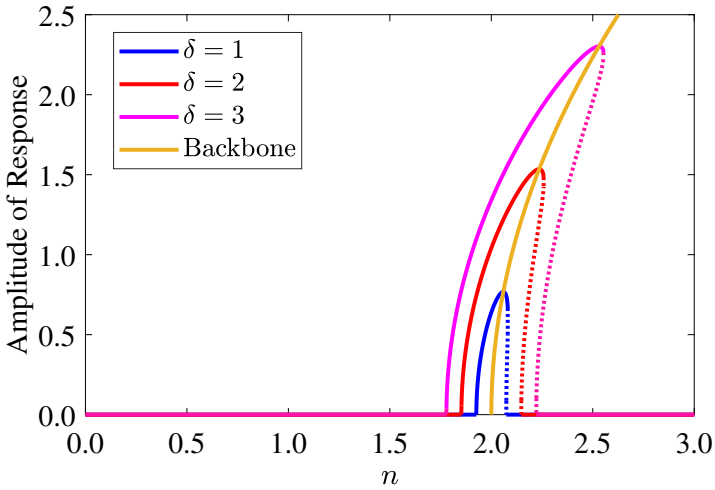

Source: Vernizzi, Lenci & Franzini (2020).

Figure 32 – Amplitude of response as function of the top motion dimensionless frequency with $\beta_4 = 0.2$. The curve with the frequency of the principal parametric instability according to the backbone curve is also shown, named "Backbone" for the sake of the size of the legend.

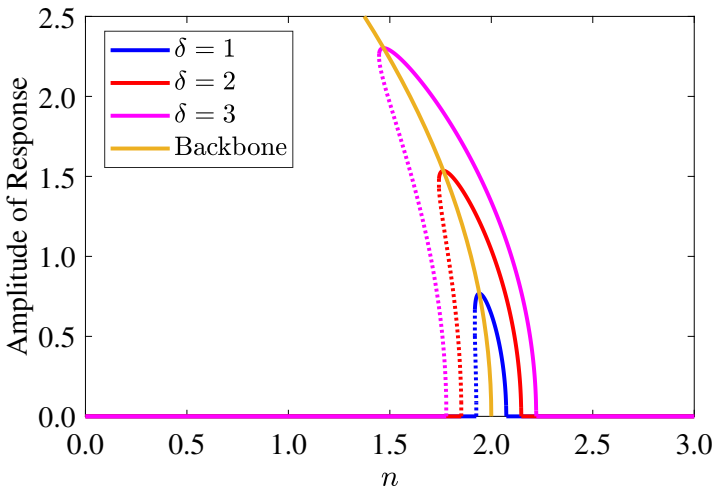

Source: Vernizzi, Lenci & Franzini (2020).

Notice that in both cases, the dependence of the natural frequency on the amplitude of response leads to conditions where the highest amplitudes of response are not achieved for $n = 2$. Instead, they occur when the parametric excitation frequency is twice the

nonlinear natural frequency, as represented by the golden line in both Figs. 31 and 32. Notice also that, due to the bending of the frequency-response curves, a branch of unstable response, represented by the dashed curves, appears. Those presented behaviours are of great importance to fatigue analysis, specially for the hardening case, where an external frequency that is higher than two times the linear natural frequency can actually cause high amplitude responses, matching the worst possible case for fatigue, high variations of stress with high frequency. On the other hand, softening may be worse from the point of view of dynamical integrity and imperfection sensitivity of critical control parameters

Another advantage of the analytical solution is that, instead of a discrete approach as presented in the frequency response curves, a smooth map can be obtained for wide range of parameters in a reasonable time. As an example, consider the post-critical maps presented in Figs. 33 to 35.

Figure 33 – Amplitude of response (A) map as function of the top motion dimensionless frequency (n) and amplitude (δ) using the reference parameters of Table 10.

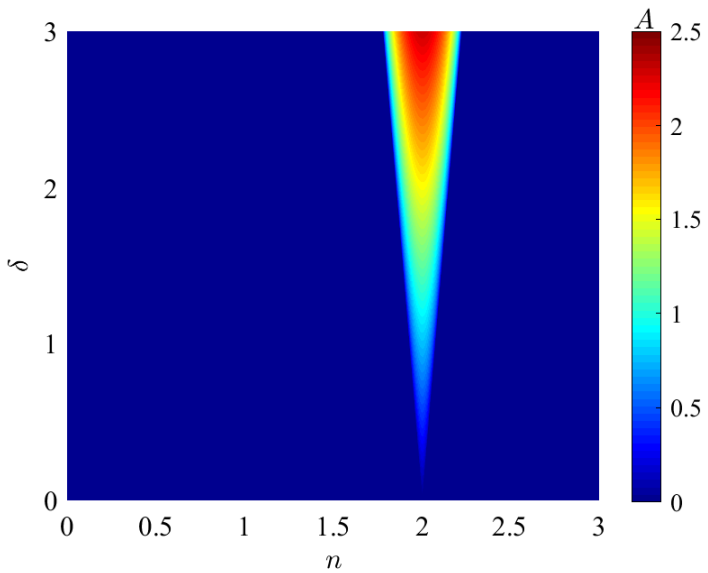

Source: Vernizzi, Lenci & Franzini (2020).

From the post-critical maps, it is clear that the influence of β_4 is mainly over the frequency dependency of the response and not on the achieved value of maximum amplitudes. That is, all the three cases achieved the same maximum amplitude, the only difference being the value of n for which it occurred. Notice that the information regarding the jump phenomenon is not as explicit as in Figs. 31 and 32, which are actually cross-sections of the maps for specific values of δ with more detailed information.

Following the investigations, consider now variations of β_6 which can be seen as variations of the $\overline{C}_D$ since there is a linear dependence between both. Investigations regarding the variation of $\overline{C}_D$ are made in Franzini et al. (2016b) and Franzini et al. (2016a) by means of the time integration of ROMs. In the present work, such investigations

Figure 34 – Amplitude of response (A) map as function of the top motion dimensionless frequency (n) and amplitude (δ) using $\beta_4 = -0.2$.

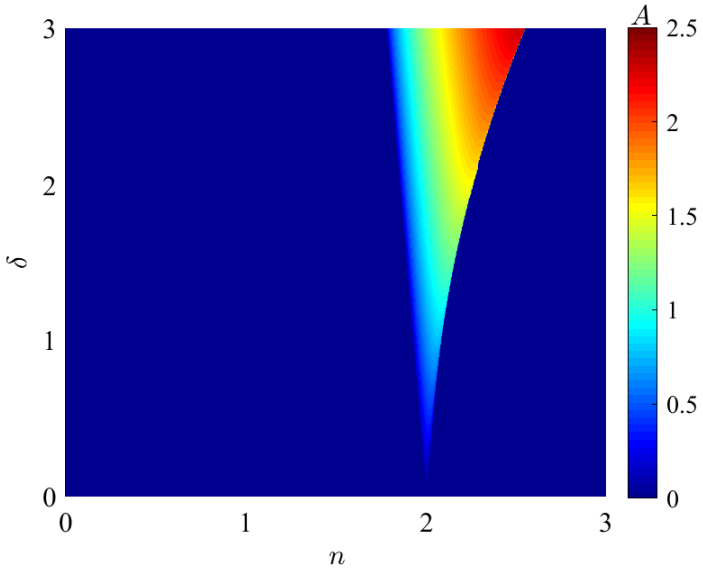

Source: Vernizzi, Lenci & Franzini (2020).

Figure 35 – Amplitude of response (A) map as function of the top motion dimensionless frequency (n) and amplitude (δ) using using $\beta_4 = 0.2$.

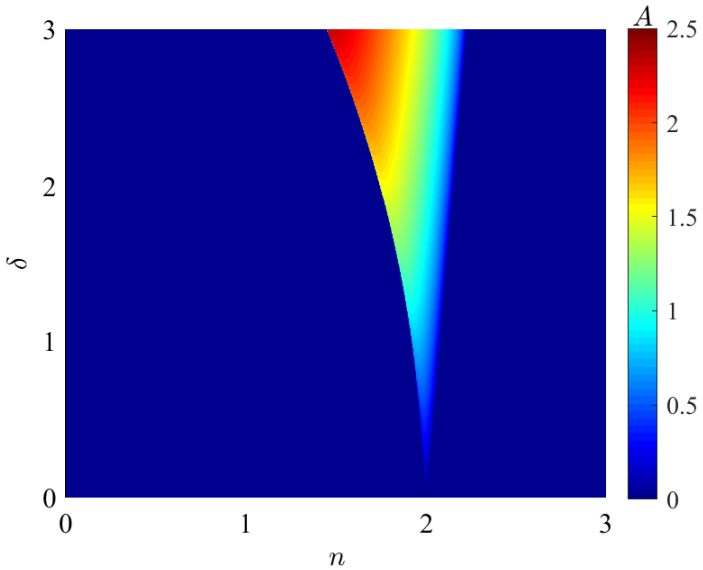

Source: Vernizzi, Lenci & Franzini (2020).

are made with the analytical solution, which demands significantly less computational time to be performed when compared to numerical integrations. In Fig. 36, the dependence of the amplitude of response on $\overline{C}_D$ is shown for different values of δ, fixing $n = 2$, while keeping the other parameters as in Table 10.

As expected, the hydrodynamic damping is of paramount importance for limiting the amplitudes of the response. It is also noticeable that, specially for smaller values of $\overline{C}_D$,

Figure 36 – Amplitude of response as function of the drag coefficient ($\overline{C}_D$) for different amplitudes of top motion with $n = 2$.

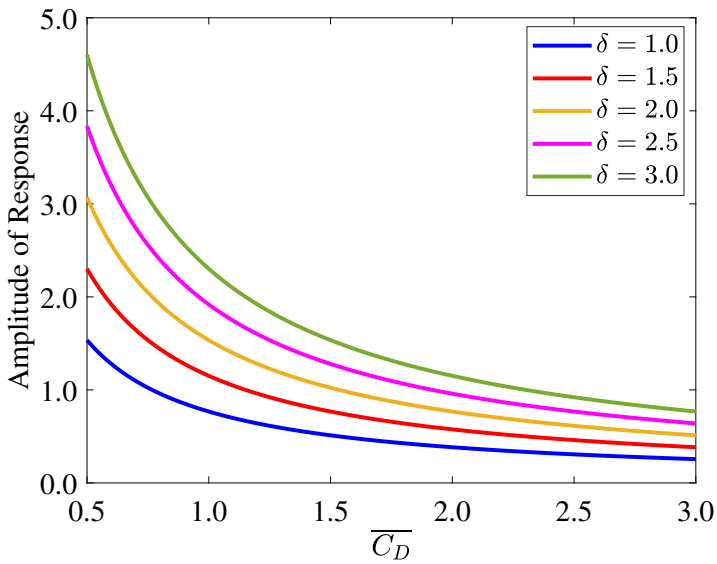

Source: Vernizzi, Lenci & Franzini (2020).

small variations of such coefficient may lead to large differences in the response amplitude.

In the sequel, the effects of the structural damping are addressed, which presents a linear relation with β_3. Due to the fact the the damping ratio is more commonly used in engineering rather the constant c, the former is considered for the analysis, being given as $\zeta = b_1/2$, with b_1 as presented in Tab. 10. It is known that the linear damping by itself is not able to limit the responses due to parametric excitation (see Nayfeh & Mook (1979) for example). That said, the results are shown in terms of the additional attenuation obtained for the response amplitudes when the structural damping is considered. In Fig. 37, it is reported the response amplitude as a function of $\overline{C}_D$, under the principal parametric instability for $\delta = 3$, for different values of damping ratio. Complementing those results, Fig. 38 presents the amount of reduction in the response amplitude furnished due to the presence of the structural damping with respect to the case where the structural damping is absent ($\zeta = 0.0\%$).

The limitation of values of $\overline{C}_D$ in Figs. 37 and 38 is due the fact that the percentage of attenuation furnished by the structural damping remains constant for larger values of $\overline{C}_D$. The main conclusion of the presented results, which are not obvious at a first look, is that, even though the structural damping is much weaker than the nonlinear hydrodynamic damping, it can have a significant effect over the final amplitudes of response.

Figure 37 – Response amplitude for different values of structural damping ratios as a function of $\overline{C}_D$, with $n = 2$.

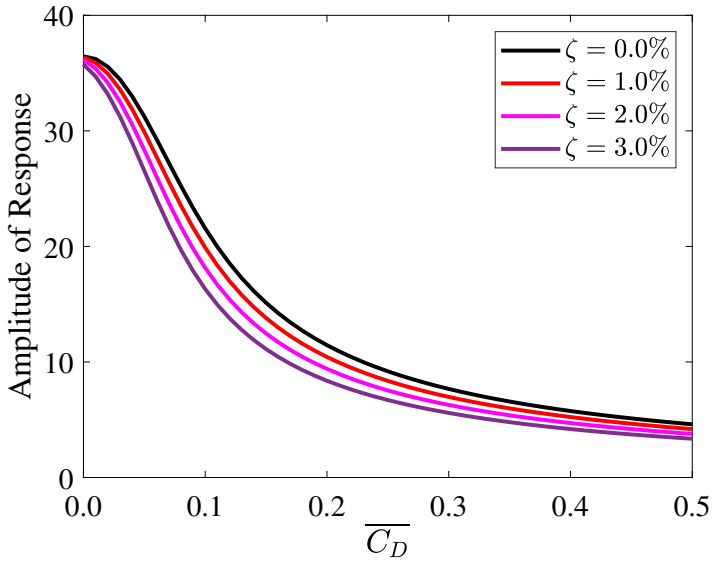

Source: Vernizzi, Lenci & Franzini (2020).

Figure 38 – Additional reduction of the response amplitude due to structural damping as a function of $\overline{C}_D$ for different structural damping ratios, with $n = 2$.

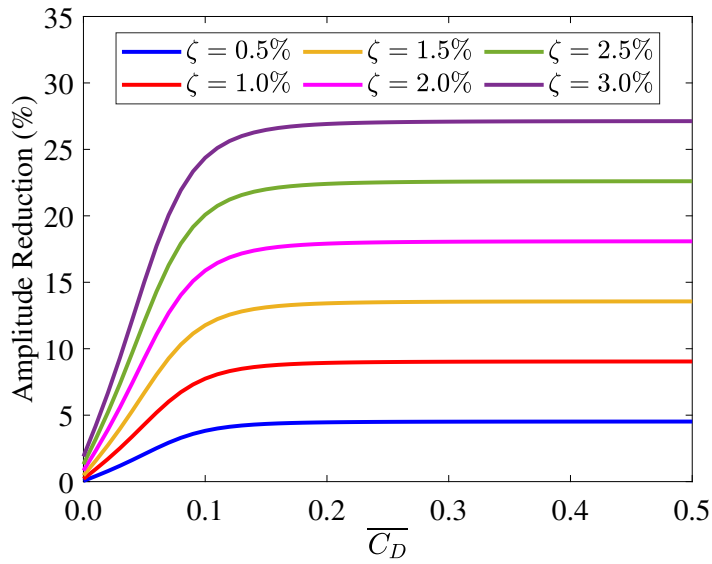

Source: Vernizzi, Lenci & Franzini (2020).

4.5 Design aiding tool based on polynomial solutions

Consider now the solution proposed by means of the polynomials described in Eq. (4.106). In order to illustrate the capability of the proposed solution, consider the structural data presented in Tab. 11, which have been adapted from Chandrasekaran, Chandak & Anupam (2006) and Lei et al. (2014). The cases are numbered and are referenced by such enumeration.

Table 11 – Structural data of different rods for evaluation with the simplified polynomial solution.

Case	EA	EI	μ	μ_a	γ	ℓ	T_b	$\overline{C}_D$	D
	MN	MNm^2	kg/m	kg/m	N/m	m	kN		m
1	8810.6	314.1	541.9	251.4	2849.8	500	427.5	0.8	0.56
2	8810.6	314.1	541.9	251.4	2849.8	1000	854.9	0.8	0.56
3	8810.6	314.1	541.9	251.4	2849.8	1500	1282.4	0.8	0.56
4	8810.6	314.1	541.9	251.4	2849.8	2000	1709.9	0.8	0.56
5	13455.6	663.1	794.3	350.7	4352.1	1166	21291.7	1.2	0.66
6	13455.6	663.1	794.3	350.7	4352.1	834	9030.0	1.2	0.66

From the structural parameters, the first step is to calculate the equivalent tension at the bottom support (T_{bn}, see Eq. (4.89)). This is made for modes 1 to 5 and the results are presented in Tab. 12.

Table 12 – Calculated values for the equivalent traction at the bottom for each case for modes 1 to 5. All values in kN.

Case	T_{b1}	T_{b2}	T_{b3}	T_{b4}	T_{b5}
1	439.9	477.1	539.1	625.8	737.4
2	858.0	867.3	882.8	904.5	932.4
3	1283.8	1287.9	1294.8	1304.4	1316.8
4	1710.6	1713.0	1716.9	1722.3	1729.2
5	21296.5	21310.9	21335.0	21368.7	21412.0
6	9039.4	9067.6	9114.7	9180.5	9265.2

In the sequence, the parameter κ is calculated for each case and for the modes of interest, following Eq. (4.91). The results are shown in Tab. 13.

Table 13 – Calculated values for the parameter κ of all cases for modes 1 to 5.

Model	κ_1	κ_2	κ_3	κ_4	κ_5
1	3.239	2.987	2.643	2.277	1.932
2	3.321	3.286	3.228	3.151	3.056
3	3.330	3.319	3.301	3.277	3.246
4	3.332	3.327	3.320	3.309	3.296
5	0.238	0.238	0.238	0.237	0.237
6	0.402	0.400	0.398	0.395	0.392

In order to proceed to the calculation of the steady-state amplitude, some steps are needed to be followed. Initially, the parameters defined in Tab. 5 must be calculated for each structure. Following, the parameters β_1 and β_2 can be directly calculated using Eq. (4.93), while parameter β_6 is calculated by Eq. (4.96). Then, the parameter α is calculated by means of Eq. (4.99), which then allows the evaluation of parameter β_4 with Eq. (4.104) and β_5 using Eq. (4.100). Finally, the value R is calculated by means of Eq. (4.85), which leads to the final step that is to evaluate the steady-state amplitude with Eq. (4.105).

The step-by-step evaluation has been made using a code in the programming language Julia. For the comparison, the top motion excitation frequencies correspond to periods between 3s and 30s, and the corresponding modes of vibration to undergo parametric resonance of each case are chosen as focuses of analysis. To create a comparison base, simulations are made with the in-house software Giraffe. The simulations are made around the principal parametric resonance of the modes of interest of each structure, with a discretization $\Delta n = 0.05$ of the dimensionless excitation frequency n, using the frequency of the first natural mode of each structure as reference. The results for case 1 are shown in Fig. 39.

Figure 39 – Comparison between the frequency response curves obtained with the polynomial (Simplified) solution or with FEM for different excitation amplitudes for case 1. The percentages in the labels refer to how much of the critical buckling load is induced by the amplitude of the prescribed top motion.

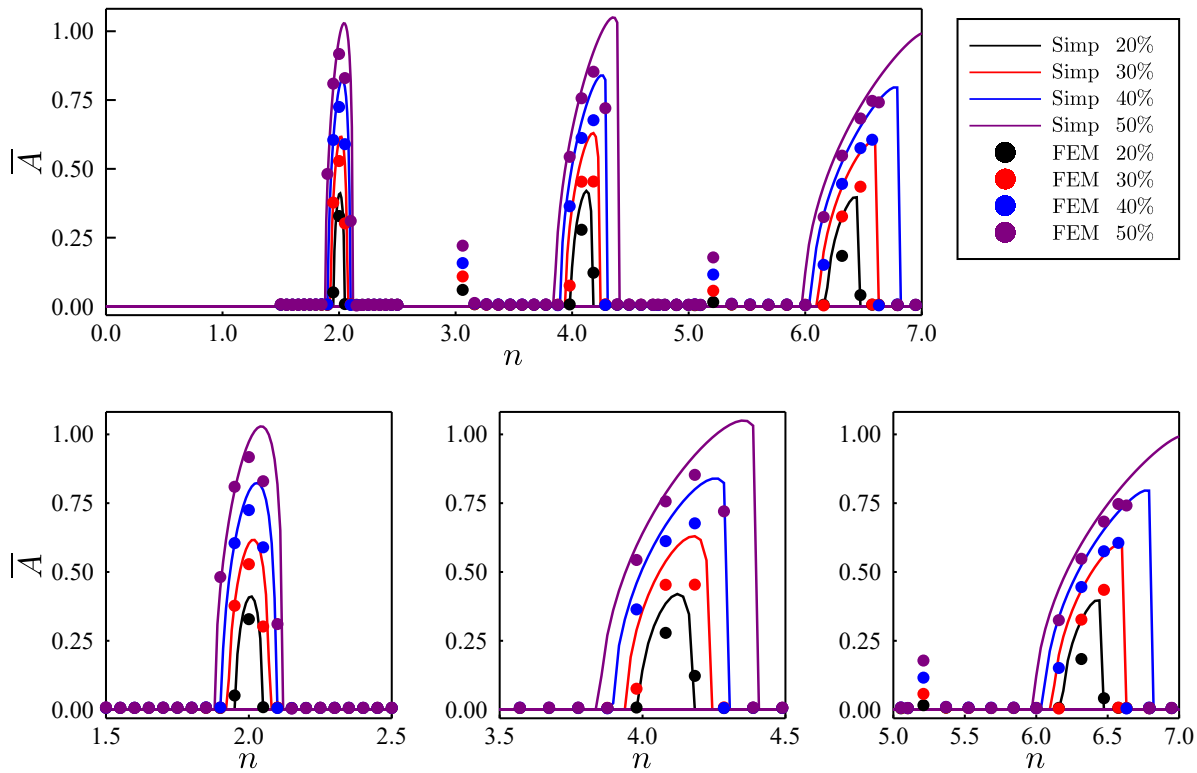

Source: The author.

As it can be seen, in the range of interest, the structure presents responses in the first three natural modes. It is possible to see that the agreement of the simplified solution is quite good, with a loss of representation quality near the jumps in the frequency response curves. There are some intermediary regions between the principal parametric response of different modes that are captured by the FEM solution. Such regions of small values of response are characterized by multimodal behaviour, coupling the two vibration modes that "surround" it in the response curve. In the sequel, the results for model 2 are shown in Fig. 40.

Figure 40 – Comparison between the frequency response curves obtained with the polynomial (Simplified) solution or with FEM for different excitation amplitudes for case 2. The percentages in the labels refer to how much of the critical buckling load is induced by the amplitude of the prescribed top motion.

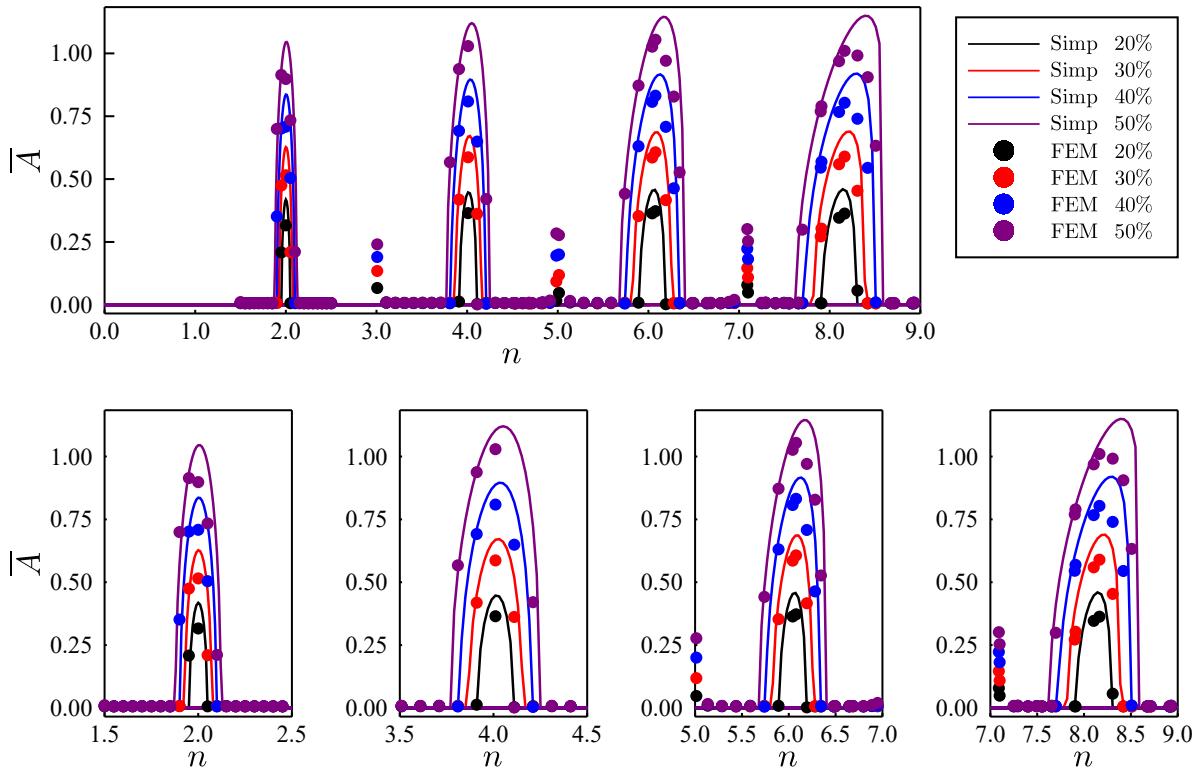

Source: The author.

In this case, the first four natural modes present responses to the parametric excitation. Notice also that the presence of a less sharp jump condition in the frequency response curve led to a condition of better agreement between the simplified model and the FEM solution. Again, the intermediary multimodal responses are present, and in a replication of the results of case 1, their amplitudes are small. Following, the results for case 3 are shown in Fig. 41.

Now, the first mode of vibration is not in the range of interest. Instead, modes 2 to 5 are the ones that presents responses to the excitation due to the prescribed top

Figure 41 – Comparison between the frequency response curves obtained with the polynomial (Simplified) solution or with FEM for different excitation amplitudes for case 3. The percentages in the labels refer to how much of the critical buckling load is induced by the amplitude of the prescribed top motion.

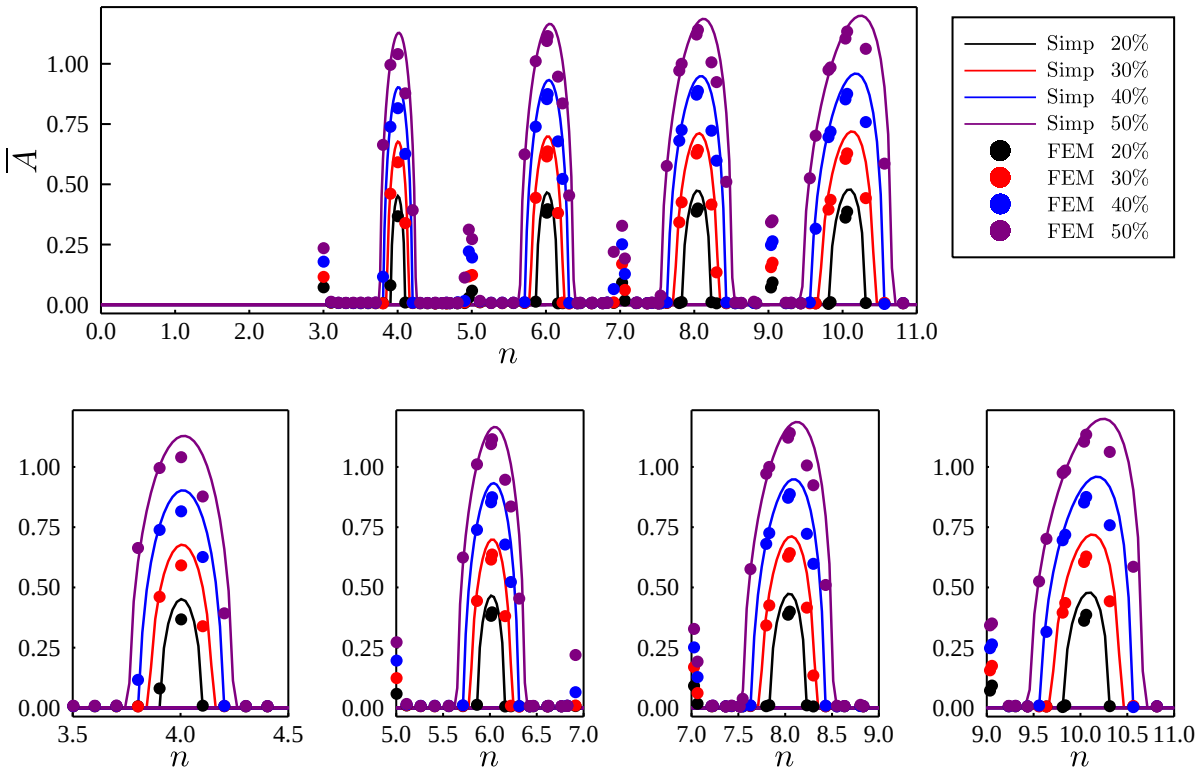

Source: The author.

motion. In this case the agreement is even better than in the previous examples. Other aspects follow what was already pointed out on the previous examples. Now, since no new phenomena is obtained, the next results are not evaluated individually. The comparisons for cases 4 to 6 are shown in Figs. 42 to 44.

With all the results exposed, some conclusions can be drawn about the polynomial solution. In terms of agreement, all the results obtained from the simplified model are definitively useful, being in good agreement with the FEM reference in the range of validity of hypothesis over which the models were obtained. The multimodal responses at intermediary values of n are thus not obtained, but considering the amplitudes obtained with the FEM solution, such responses do not configure critical cases for engineering design. Within the monochromatic responses, the cases in which the agreement of the simplified model is significantly reduced it does so by furnishing a larger value. Although this is not the best scenario from an economic point of view, it does ensure that it is furnishing a safe result for usage.

Another highlight to be made is that joining the results of single different modes into an unique response curve is actually feasible and furnishes a good representation

Figure 42 – Comparison between the frequency response curves obtained with the polynomial (Simplified) solution or with FEM for different excitation amplitudes for case 4. The percentages in the labels refer to how much of the critical buckling load is induced by the amplitude of the prescribed top motion.

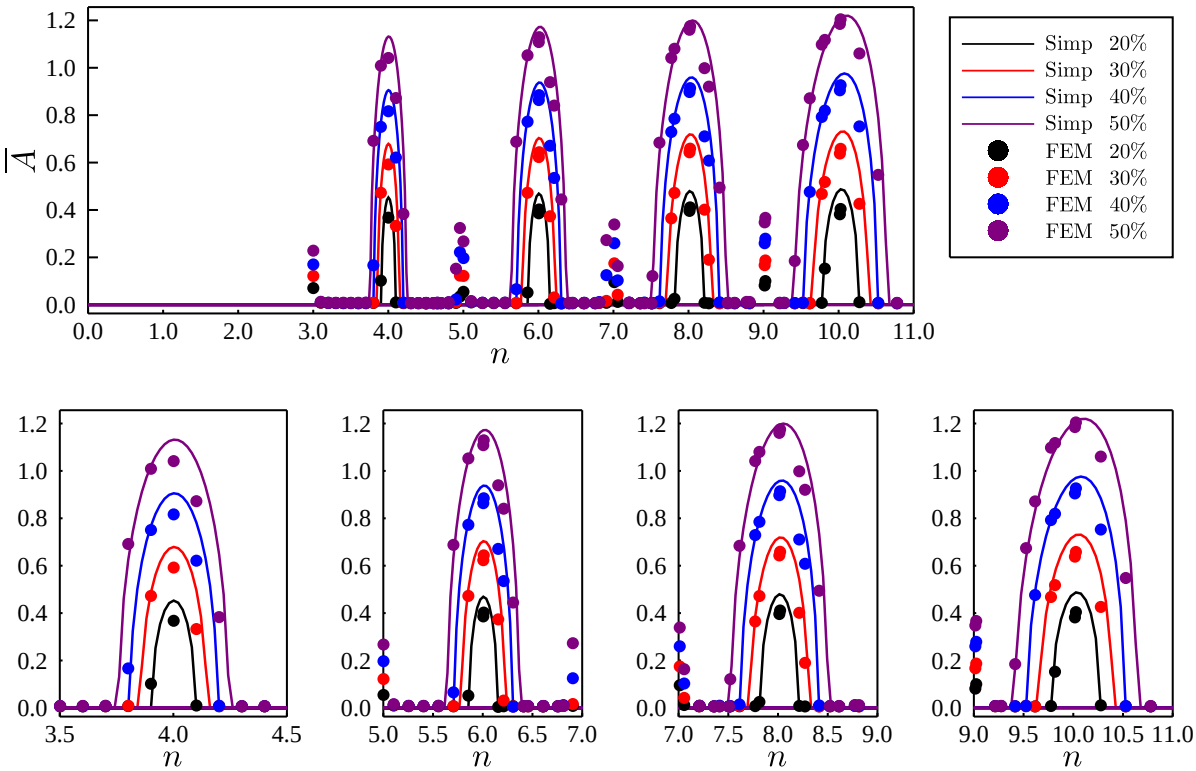

Source: The author.

of the actual behaviour of the models. Putting all those characteristics together, it is possible to conclude that the polynomial solution is actually safe and representative of the structural behaviour in order to be used as a basic design tool to help offshore engineering projects. A fundamental aspect of such solutions is that they can be easily implemented in an electronic spreadsheet considering that the polynomial coefficients are previously given. The use of a spreadsheet implementation allows for a real-time evaluation of the response at desired design scenarios.

Figure 43 – Comparison between the frequency response curves obtained with the polynomial (Simplified) solution or with FEM for different excitation amplitudes for case 5. The percentages in the labels refer to how much of the critical buckling load is induced by the amplitude of the prescribed top motion.

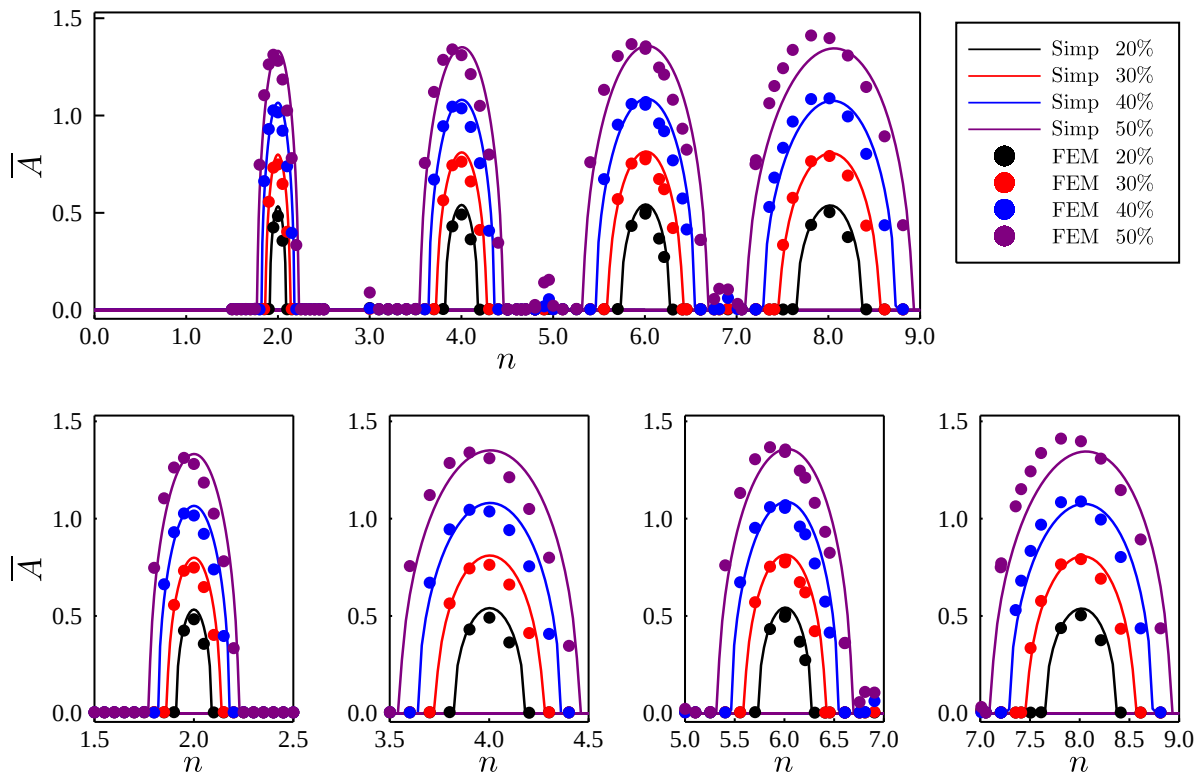

Source: The author.

Figure 44 – Comparison between the frequency response curves obtained with the polynomial (Simplified) solution or with FEM for different excitation amplitudes for case 6. The percentages in the labels refer to how much of the critical buckling load is induced by the amplitude of the prescribed top motion.

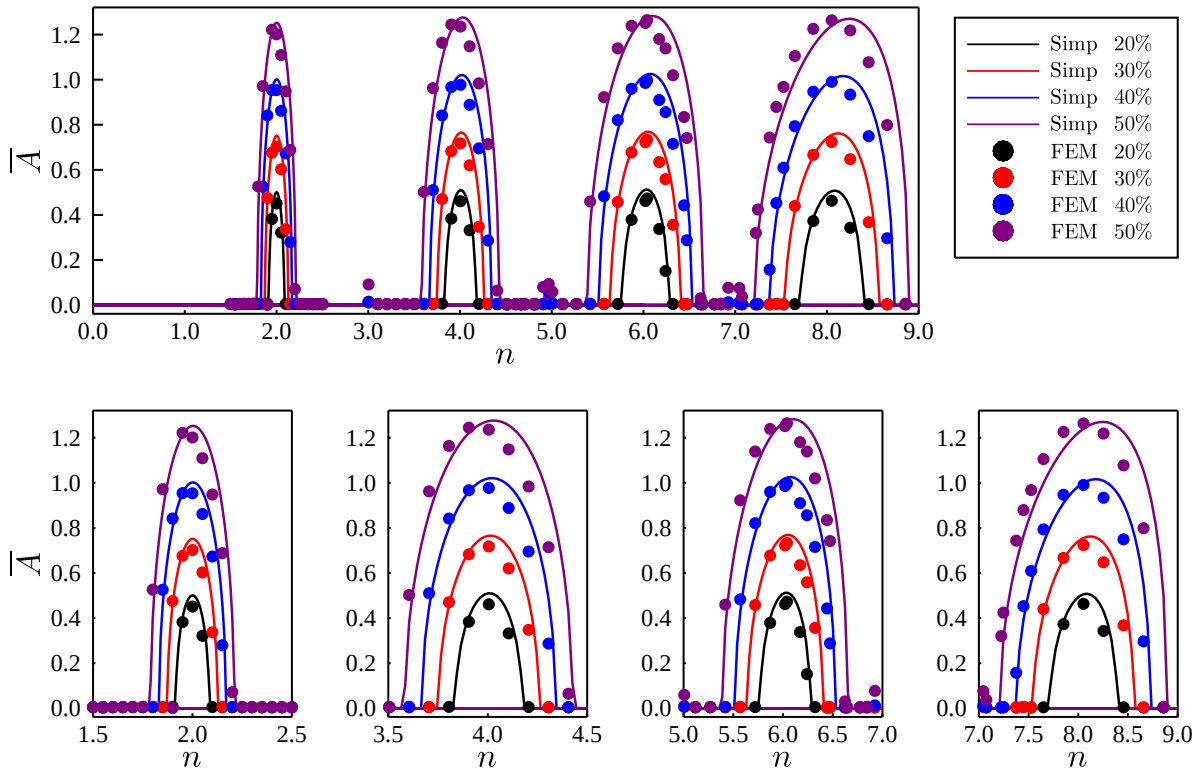

Source: The author.

5 Curved cables under support excitation

In this chapter, a flexible cable hanging between supports at different heights while immersed in still fluid is considered. The cable is subject to an imposed vertical boundary motion at the upper support and its responses are considered constrained to the plane of the static configuration. Again, as previously stated, the imposed motion is considered as a result of the response of a floating unit under the action of sea waves. However, differently from the case of a vertical structure, this imposed motion becomes a combination of influences in the axial and transversal directions along the structure.

For the investigation, different ROMs are formulated. A detailed discussion is made regarding different possibilities to conceive the ROMs in order to obtain guidelines for a proper conception of suitable models for analysis. As done for the case of vertical structures, the results are compared to a numerical reference obtained via the finite element method.

The results of this chapter resulted in the publication Vernizzi, Lenci & Franzini (2022) and were also presented in the "25th International Congress of Theoretical and Applied Mechanics" (ICTAM2020+1).

5.1 Problem sketch and equations of motion

The problem under investigation is illustrated in Fig. 45. From the representation, three particular hypothesis deserve special attention when applications in offshore engineering are intended. The first one is that an ideal monochromatic harmonic motion is applied to one of the supports of the structure. The second hypothesis is that the support at the bottom of the structure is considered fixed, which is made in order to avoid the complexity introduced by a moving support in the present work. Finally, the third strong hypothesis is that no point of the hanging portion of the structure experiences contact with the seabed.

The fixed Cartesian frame is given by the X and Z axis in the horizontal and vertical directions, respectively, while the frame origin coincides with the bottom support. The local frame is defined by the tangential direction u and the transversal direction v. Notice that the problem depicted is very similar to the one presented in Fig. 17, with the key differences being the imposed motion $W_L(t)$ and the presence of the surrounding fluid. This allows the use of Eqs. (3.75) and (3.76) with the addition of minor correction terms, being them the Morison damping in the transversal motion equation, and the imposed displacement as a boundary condition. This leads them to the PDEs of motion

Figure 45 – Sketch of an inclined hanging cable with time-varying imposed motion at one of its supports.

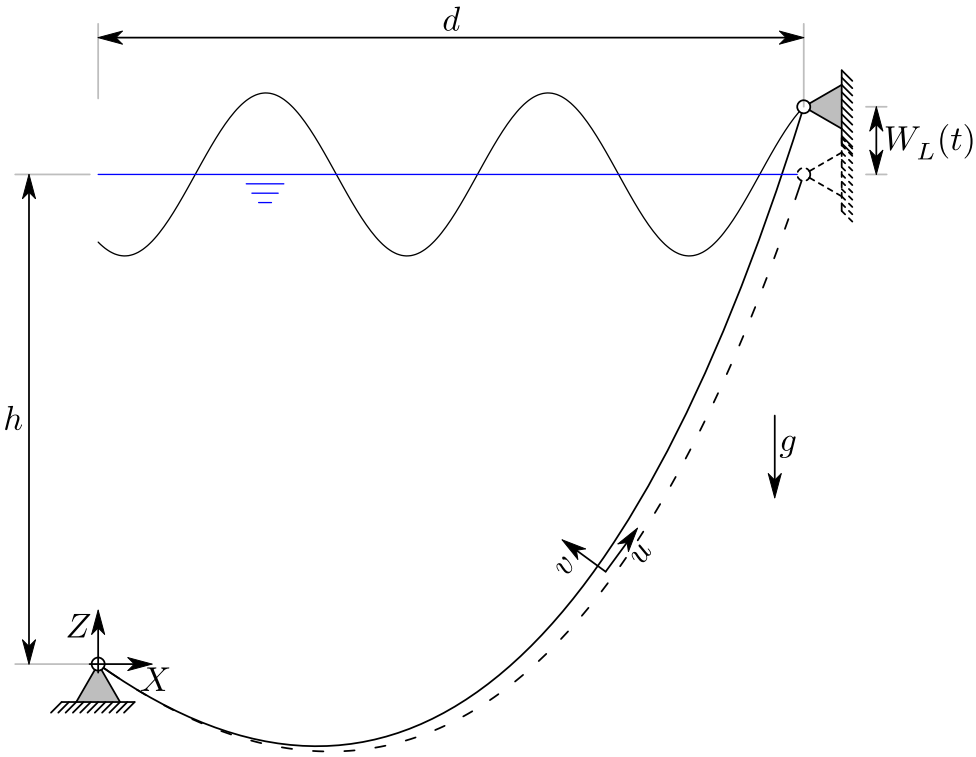

Source: Vernizzi, Lenci & Franzini (2022)

$$
\begin{aligned}
m\ddot{u} = {} & T_s' \left(\frac{u' - v\theta' - \varepsilon_d}{1+\varepsilon_d} \right) - T_s \left(\frac{(u\theta' + v')\,\theta'}{(1+\varepsilon_d)} + \frac{(u\theta' + v')}{(1+u'-v\theta')} \left(\frac{(u\theta' + v')}{(1+\varepsilon_d)} \right)' \right) \\
& - \rho g A \left((u' - v\theta') \sin\theta + (v' + u\theta') \cos\theta \right) \frac{(1+u'-v\theta')}{(1+\varepsilon_d)} + EA\varepsilon_d' \frac{(1+u'-v\theta')}{(1+\varepsilon_d)} \\
& + \left[\left(\frac{(u\theta' + v')\,\theta'}{(1+\varepsilon_d)} + \frac{(u\theta' + v')}{(1+u'-v\theta')} \left(\frac{(u\theta' + v')}{(1+\varepsilon_d)} \right)' \right) \left(-EA\varepsilon_d + \rho g A u \sin\theta + \rho g A v \cos\theta \right) \right],
\end{aligned}
\tag{5.1}
$$

$$
\begin{aligned}
m_t\ddot{v} + \frac{1}{2}\rho D \overline{C}_D \dot{v}\,|\dot{v}| = {} & T_s' \frac{(u\theta' + v')}{(1+\varepsilon_d)} + T_s \left(\frac{(1+u'-v\theta')\,\theta'}{(1+\varepsilon_d)} + \left(\frac{(u\theta' + v')}{(1+\varepsilon_d)} \right)' \right) \\
& - \rho g A \left((u' - v\theta') \sin\theta + (v' + u\theta') \cos\theta \right) \frac{(u\theta' + v')}{(1+\varepsilon_d)} - T_s\theta' + EA\varepsilon_d' \frac{(u\theta' + v')}{(1+\varepsilon_d)} \\
& + \left[\left(\frac{(1+u'-v\theta')\,\theta'}{(1+\varepsilon_d)} + \left(\frac{(u\theta' + v')}{(1+\varepsilon_d)} \right)' \right) \left(EA\varepsilon_d - \rho g A u \sin\theta - \rho g A v \cos\theta \right) \right],
\end{aligned}
\tag{5.2}
$$

subjected to the boundary conditions

$$u(0,t) = 0, \tag{5.3}$$
$$v(0,t) = 0, \tag{5.4}$$
$$u(L,t) = W_L(t)\sin(\theta_L), \tag{5.5}$$
$$v(L,t) = W_L(t)\cos(\theta_L). \tag{5.6}$$

For the sake of easiness of reading, the relevant terms for the mathematical model are repeated here in Tab. 14.

Table 14 – Relevant terms for the mathematical model.

Symbol	Meaning
m	Structural mass per unit length
m_t	Structural transversal inertia (mass and added mass) per unit length
T_s	Tension in the static configuration
ε_d	Additional strain developed in the dynamical response
ρ	Surrounding fluid specific mass
A	Area of the structural cross-section
θ	Angle with the horizontal in the static configuration
EA	Axial stiffness product
$\overline{C}_D$	Mean drag coefficient of the cross section

Finally, as made in Chapter 3, Eqs. (5.1) and (5.2) may be written using an operator notation, resulting in

$$\mathcal{L}_u(u,v) = 0, \tag{5.7}$$
$$\mathcal{L}_v(u,v) = 0. \tag{5.8}$$

For the sake of simplicity, the same notation is kept without loss of meaning.

5.2 Reduced-order models

By a simple inspection of Eqs. (5.1) and (5.2), it is natural to conclude that their solution by means of analytical techniques, even approximative ones, is rather cumbersome, if even feasible at all. This stimulates the analyst to take a different approach to solve the problem at hand. One possible way of tackling such system is by obtaining a ROM consisting of a system of ODEs obtained from the PDEs via a Galerkin procedure. To that end, a suitable basis of projection functions is necessary, which needs to obey the essential boundary conditions of the problem. In order to fulfil the latter requirement, the displacement field herein proposed is written as

$$u = W_L(t)\,\phi_s(s) + \sum_{k=1}^{n} A_k(t)\,\phi_k(s)\,, \tag{5.9}$$

$$v = W_L(t)\,\psi_s(s) + \sum_{k=1}^{n} B_k(t)\,\psi_k(s)\,. \tag{5.10}$$

This proposed displacement field assumes that the top motion results in an instantaneous effect along the cable span according to each direction, represented by the functions ϕ_s and ψ_s. It is thus important to highlight that such approach is quasi-static by default. Following, in order to actually satisfy the essential boundary conditions, it is clear that

$$\phi_s(L) = \sin\theta_L, \tag{5.11}$$

$$\psi_s(L) = \cos\theta_L, \tag{5.12}$$

$$\phi_k(0) = 0, \tag{5.13}$$

$$\phi_k(L) = 0, \tag{5.14}$$

$$\psi_k(0) = 0, \tag{5.15}$$

$$\psi_k(L) = 0. \tag{5.16}$$

The problem now is in the specific format of each spatial function to use. Although the Galerkin method ensures that the minimum possible error will be obtained within a chosen set, it does not give any tools to evaluate if the chosen set is adequate for representing the problem. Regarding the functions ϕ_s and ψ_s, there is no information about which shape to use asides the boundary conditions. Another issue is that, due to the presence of the surrounding fluid, the shape of these functions will dictate the shape of an imposed forcing term that will appear in Eq. (5.2). One possible way to obtain such functions would be to directly tackle the PDEs with analytical methods such as the MMTS. This, however, is not yet done in the literature for the case at hand, and due to the intricate expressions of the PDEs one can expect it to be a significantly cumbersome task. Circumventing then the lack of information, three different sets of functions ϕ_s and ψ_s are tried here, based on literature results obtained for somewhat similar problems. The simplest of such possibilities is to use a linear interpolation of the boundary conditions along the cable length, that is,

$$\phi_{s,1} = \left(\frac{s}{L}\right)\sin\theta_L, \tag{5.17}$$

$$\psi_{s,1} = \left(\frac{s}{L}\right)\cos\theta_L. \tag{5.18}$$

The expansion of the subscript is to indicate the set number for reference during the analysis. This type of interpolation appears in the problem of straight structures subjected to boundary motions, being implicit in commonly adopted static condensation procedures (see Vernizzi, Franzini & Lenci (2019) for example). A natural question that now arises is related to the influence of the curved static configuration over the top motion effects. In order to try to bring some of the effect of the curved configuration, a second set of trial functions related to the top motion is proposed. Consider now, that instead of a linear interpolation of the boundary conditions, the projection functions also obey the local rotation of the cross-section, resulting in

$$\phi_{s,2} = \left(\frac{s}{L}\right) \sin\theta, \tag{5.19}$$

$$\psi_{s,2} = \left(\frac{s}{L}\right) \cos\theta. \tag{5.20}$$

Notice that this proposed set still preserves mathematical simplicity, which is often desired in order for easiness of ROM creation. Finally, a third set is conceived, this time letting go the requirement of simplicity while trying to use further information about the model itself. Since the proposed displacement field in Eqs. (5.9) and (5.10) has a quasi-static portion, the test will be to use functions that are the difference between two static configurations of the cable, as made in Luongo & Zulli (2011). The process consists of calculating the displacement field that leads the structure from the original static configuration to a new static configuration where the support is moved by an unitary displacement in the direction of W_L. In particular cases of parabolic or almost inextensible cables, such as those given by the classical catenary equation, analytical expressions can be derived for such displacement field. However, in the general case, a numerical approach is necessary to obtain such functions. Mathematically speaking, consider then the original static configuration of the cable to be defined by the functions $X_0(s)$ and $Z_0(s)$ in the horizontal and vertical directions respectively. Let then the corresponding $X_1(s)$ and $Z_1(s)$ be the functions describing the cable static configuration after an unitary displacement in the same direction as W_L. The interpolation functions are given then as

$$\phi_{s,3} = (X_1 - X_0)\cos\theta + (Z_1 - Z_0)\sin\theta, \tag{5.21}$$

$$\psi_{s,3} = -(X_1 - X_0)\sin\theta + (Z_1 - Z_0)\cos\theta. \tag{5.22}$$

It is important to highlight that this approach does not take into consideration the effects of the fluid-structure interaction that occurs during the displacement, but is still the tool available in the literature for direct usage. This third set is the last one considered in the present work for the top motion interpolating functions.

Giving sequence, it is now necessary to define possible sets for the functions ϕ_k and ψ_k. Here two different objectives may be given to the sets, that is, to obtain a minimal set with accurate results, or to obtain a somewhat larger set but described by simpler known functions. The first set adopted, herein named 'set(i)', is defined by a single mode of vibration obtained from Eqs. (5.1) and (5.2), that is, an eigenvector of the system

$$\mathcal{L}_{u,1}(u,v) = 0, \tag{5.23}$$

$$\mathcal{L}_{v,1}(u,v) = 0, \tag{5.24}$$

where $\mathcal{L}_{u,1}$ and $\mathcal{L}_{v,1}$ are the linear parts of the operators $\mathcal{L}_u$ and $\mathcal{L}_v$ respectively. It is worth mentioning that, differently from the straight case, the vibration modes of curved structures present coupled shapes in the transversal and axial directions, leading to the condition $A_k = B_k$ in Eqs. (5.9) and (5.10). The choice of using vibration modes is very common in the literature, since it is expected that the response of the structure will be a composition of the response of different modes. In that sense, this first set is the one to ensure the minimal ROM, with a single DOF. A natural follower is then to use more modes of vibration in the ROM, which is then the approach for 'set(ii)'. For this case, three consecutive modes are adopted, leading to a 3-DOF ROM.

Lastly, one may deem suitable to use simpler projection functions, specially in the case of extensible cables since not always there will be analytical expressions available for the vibration modes, leading to the further complications in the ROM obtaining process. Consider then the use of trigonometric functions as basis for the set, which can be found in the literature for the case of vertical structures in Franzini & Mazzilli (2016) and Vernizzi, Franzini & Lenci (2019) for example. One factor that can be observed in the conclusions of Vernizzi, Franzini & Lenci (2019) is that the use of simpler functions that are not precisely the vibration modes leads to the need of a larger set. With that in mind, 'set(iii)' is composed of five sinusoidal functions for each direction. It must be remarked that, since those functions are not the eigenvectors of Eqs. (5.23) and (5.24), the relationships between the transversal and axial directions are not yet defined, leading to $A_k \neq B_k$ in the general case. This results in a ROM with 10 DOF.

In this work, the analysis is focused on the response of the first mode of vibration, so the first mode is considered for 'set(i)', the first three modes are considered for 'set(ii)', while for 'set(iii)' the projection functions are

$$\phi_k = \psi_k = \sin\left(\frac{k\pi s}{L}\right), \quad k = 1, ..., 5. \tag{5.25}$$

With all the necessary functions defined, it is now possible to apply the Galerkin projection to obtain the ROM. With the defined sets, a total of nine different ROMs

is possible. By utilizing the equations of motion written as in Eqs. (5.7) and (5.8), it is possible to write the system in a vectorial way as

$$[\mathcal{L}_u(u,v), \mathcal{L}_v(u,v)] = [0,0]. \tag{5.26}$$

The Galerkin method is then simply defined as an inner product operation over the vectorial Eq. (5.26), which for any case involving sets (i) and (ii) leads to

$$\langle [\mathcal{L}_u(u,v), \mathcal{L}_v(u,v)], [\phi_k, \psi_k] \rangle = 0, \tag{5.27}$$

with the product being made for each mode k. The procedure is just slightly different for the cases involving set (iii), which leads to five pairs of projections written as

$$\langle [\mathcal{L}_u(u,v), \mathcal{L}_v(u,v)], [\phi_i, 0] \rangle = 0, \tag{5.28}$$
$$\langle [\mathcal{L}_u(u,v), \mathcal{L}_v(u,v)], [0, \psi_i] \rangle = 0. \tag{5.29}$$

By letting the inner product to be defined as the integral of the involved functions along the cable span, the ODE for set(i) becomes simply

$$\begin{aligned} m_1\ddot{A}_1 &= m_q\ddot{W}_L + a_1A_1 + a_2W_L + a_3A_1^2 + a_4A_1W_L + a_5W_L^2 + a_6A_1^3 + a_7A_1^2W_L \\ &+ a_8A_1W_L^2 + a_9W_L^3 - \zeta\int_0^L \psi_1\left|\psi_1\dot{A}_1 + \psi_s\dot{W}_L\right|\left(\psi_1\dot{A}_1 + \psi_s\dot{W}_L\right)\,\mathrm{d}s, \end{aligned} \tag{5.30}$$

where m_1, m_q and each of the a_i are constant values resulting from the inner product, which will vary according to the functions ϕ_s and ψ_s of each case, while ζ is a constant defined merely to simplify the algebra, being $\zeta = \rho D\overline{C}_D/2$. One feature that deserves notice is the fact that, since the supposed displacement field involves the sum of at least two terms with a yet to be defined value, the integral of the Morison damping term cannot be evaluated at first. Instead, during numerical simulations this integral must be evaluated at each time step.

Now, for the ROMs obtained using set (ii), the resulting ODE relative to each mode k can be put in the general form

$$\left(\sum_{i=1}^{3} m_{k,i}\ddot{A}_i\right) = m_{k,q}\ddot{W}_L + \left(\sum_{i=1}^{3} a_{k,i}A_i\right) + a_{k,q}W_L + b_{k,q}W_L^2 + \left(\sum_{i=1}^{3} b_{k,i}W_L A_i\right)$$
$$+ \left(\sum_{i=1}^{3}\sum_{j=1}^{3} b_{k,i,j}A_iA_j\right) + c_{k,q}W_L^3 + \left(\sum_{i=1}^{3} c_{k,i}W_L^2 A_i\right) + \left(\sum_{i=1}^{3}\sum_{j=1}^{3} c_{k,i,j}W_L A_iA_j\right)$$
$$+ \left(\sum_{i=1}^{3}\sum_{j=1}^{3}\sum_{l=1}^{3} c_{k,i,j,l}A_iA_jA_l\right) - \zeta\int_0^L \psi_k \left|\left(\sum_{i=1}^{3}\psi_i\dot{A}_i\right) + \psi_s\dot{W}_L\right| \left(\left(\sum_{i=1}^{3}\psi_i\dot{A}_i\right) + \psi_s\dot{W}_L\right) \mathrm{d}s, \tag{5.31}$$

with the constants $m_{k,i}$, $m_{k,q}$, a, b and c being numerical values resulting from the inner product according to each set ϕ_s and ψ_s, as in the previous case. Notice that a small increase in the number of DOFs resulted in a large increment in the number of constants to be defined for the ROMs. It is expected that this effect may lead to a significant difference in computational effort to integrate the obtained model. Also, due to the large amount of constants to be evaluated combined with the intricate expressions of the PDEs, the use of symbolic computation is advised for the calculation of the ROM constants.

The ROMs obtained with the use of set (iii) are merely an extension of the case of set (ii), with pairs of equations, extending the summations to five terms and considering the couplings between the A_i with the B_i in the nonlinear terms.

5.3 Semi-analytical solution for particular models

As it has been made for the vertical case, analytical solutions may be pursued for some forms of the obtained ROMs. One should notice however that, for the problem of curved structures, the form of the nonlinear damping brings up a cumbersome problem to solve. This because now, even for the simplest of the ROMs, a sum of different terms appears inside the absolute value function, one of them being the unknown that is sought to be obtained. One way to circumvent this problem is to use an iterative approach that will be detailed later on. Taking now Eq. (5.30), a scaling may be proposed in which all the constants that multiply nonlinear terms or terms depending on W_L are mapped as

$$a \mapsto \epsilon a, \tag{5.32}$$

with ϵ being a small bookkeeping parameter and in this particular equation a being any generic constant. An expansion is then proposed for the solution, up to order ϵ, as

$$A_1 = A_{1,0}\left(t_0, t_1\right) + \epsilon A_{1,1}\left(t_0, t_1\right), \tag{5.33}$$

where t_0 and t_1 are two independent time scales, defined by means of the bookkeeping parameter as $t_i = \epsilon^i t$. Using such definitions, two differential operators for the time differentiations involved in the problem are useful for the subsequent analysis, been written as

$$\frac{\mathrm{d}}{\mathrm{d}t} = \frac{\partial}{\partial t_0} + \epsilon \frac{\partial}{\partial t_1} = D_0 + \epsilon D_1, \tag{5.34}$$

$$\frac{\mathrm{d}^2}{\mathrm{d}t^2} = \frac{\partial^2}{\partial t_0^2} + 2\epsilon \frac{\partial^2}{\partial t_0 \partial t_1} = D_0^2 + 2\epsilon D_0 D_1. \tag{5.35}$$

Both operators are correct up to terms of order ϵ. Applying those operators in Eq. (5.30) together with the proposed solution in Eq. (5.33) and then collecting terms of the same order in ϵ leads to two sequential equations. The first of such equations, for order ϵ^0, is given as

$$m_1 D_0^2 A_{1,0} - a_1 A_{1,0} = 0, \tag{5.36}$$

while the equation of order ϵ^1 reads

$$\begin{aligned} m_1 D_0^2 A_{1,1} - a_1 A_{1,1} &= -2m_1 D_0 D_1 A_{1,0} + m_q \ddot{W}_L + a_2 W_L \\ &+ a_3 A_{1,0}^2 + a_4 A_{1,0} W_L + a_5 W_L^2 + a_6 A_{1,0}^3 + a_7 A_{1,0}^2 W_L \\ &+ a_8 A_{1,0} W_L^2 + a_9 W_L^3 - \zeta \int_0^L \psi_1 \left| \psi_1 D_0 A_{1,0} + \psi_s D_0 W_L \right| \left(\psi_1 D_0 A_{1,0} + \psi_s D_0 W_L \right) \mathrm{d}s. \end{aligned} \tag{5.37}$$

Equation (5.36) is simply that of a linear free oscillator[1], resulting in the solution for $A_{1,0}$ been written as

$$A_{1,0} = B_0 e^{i\omega_0 t_0} + B_0^* e^{-i\omega_0 t_0} = B_0 e^{i\omega t_0} + c.c., \tag{5.38}$$

where i is the imaginary unity, ω_0 is the natural frequency of the linear oscillator, with $\omega_0 = \sqrt{-a_1/m_1}$. The symbol * denotes the complex conjugate of a term and *c.c.* stands for the complex conjugate of all the terms before its appearance. Focus is now placed on the case of 1:1 resonance between the structure and the imposed motion. To that end,

[1] It must be remarked here that it is expected that the constant a_1 will result negative, implying a positive sign for the linear stiffness. Any other case would generate an unstable system, with the need for searching which is the stable equilibrium configuration. This is not the focus of the thesis.

let $W_L = \eta \sin(\omega_0 t_0)$. A common practice in the literature that is not made here is the insertion of a detuning parameter in the forcing frequency. This is herein avoided since, for this particular problem, several mathematical difficulties are imposed by such detuning in the obtaining of steady-state solutions since they lead to a mixture of different frequencies being summed in the absolute value function involved in the Morison damping term. This leads to a problem where the necessary spatial integration actually depends on time as well, without a viable solution with the techniques herein proposed. Now, substituting the solution for $A_{1,0}$ in Eq. (5.37) together with the definition for W_L leads to

$$
\begin{aligned}
&m_1 D_0^2 A_{1,1} - a_1 A_{1,1} = -2im_1\omega_0 D_1 B_0 e^{i\omega_0 t_0} + \left(\frac{im_q\omega_0^2\eta}{2} - \frac{ia_2\eta}{2}\right) e^{i\omega_0 t_0} \\
&+ a_3\left(B_0^2 e^{2i\omega_0 t_0} + B_0 B_0^*\right) - \frac{ia_4\eta}{2}\left(B_0 e^{2i\omega_0 t_0} - B_0\right) - \frac{a_5\eta^2}{4}\left(e^{2i\omega_0 t_0} - 1\right) \\
&+ a_6\left(B_0^3 e^{3i\omega_0 t_0} + 3B_0^2 B_0^* e^{i\omega_0 t_0}\right) - \frac{ia_7\eta}{2}\left(B_0^2 e^{3i\omega_0 t_0} + \left(-B_0^2 + 2B_0 B_0^*\right) e^{i\omega_0 t_0}\right) \\
&- \frac{a_8\eta^2}{4}\left(B_0 e^{3i\omega_0 t_0} + \left(B_0^* - 2B_0\right) e^{i\omega_0 t_0}\right) + \frac{ia_9\eta^3}{8}\left(e^{3i\omega_0 t_0} - 3e^{i\omega_0 t_0}\right) + c.c. \\
&- \zeta \int_0^L \psi_1 \left|\psi_1 D_0 A_{1,0} + \psi_s D_0 W_L\right| \left(\psi_1 D_0 A_{1,0} + \psi_s D_0 W_L\right) \mathrm{d}s.
\end{aligned} \tag{5.39}
$$

For a bounded solution to exist for this problem, the terms on the right-hand side of the latter equation must not be in the kernel of the operator given by the left-hand side of the same equation. For the particular case of second order ODEs systems this is analogous to require that there are no terms on the right-hand side that oscillates with the same frequency as any of the natural frequencies of the system. In the particular case at hand, it must then be required that all terms with frequency ω_0 must vanish, leading to

$$
\begin{aligned}
&-2im_1\omega_0 D_1 B_0 + \frac{im_q\omega_0^2\eta}{2} - \frac{ia_2\eta}{2} + 3a_6 B_0^2 B_0^* + \frac{ia_7}{2}\eta B_0^2 \\
&- ia_7\eta B_0 B_0^* + \frac{a_8}{2}\eta^2 B_0 - \frac{a_8}{4}\eta^2 B_0^* - \frac{3ia_9}{8}\eta^3 + F_0 = 0,
\end{aligned} \tag{5.40}
$$

with the new term F_0 standing for any portion of the nonlinear damping that presents frequency ω_0. In order to obtain those terms, the relevant integral is separated as

$$
\begin{aligned}
&\int_0^L \psi_1 \left|\psi_1 D_0 A_{1,0} + \psi_s D_0 W_L\right| \left(\psi_1 D_0 A_{1,0} + \psi_s D_0 W_L\right) \mathrm{d}s = \\
&D_0 A_{1,0} \int_0^L \psi_1^2 \left|\psi_1 D_0 A_{1,0} + \psi_s D_0 W_L\right| \mathrm{d}s + D_0 W_L \int_0^L \psi_1\psi_s \left|\psi_1 D_0 A_{1,0} + \psi_s D_0 W_L\right| \mathrm{d}s.
\end{aligned} \tag{5.41}
$$

In this final format, a Fourier series expansion can be applied to each integral, following the suggestions in Nayfeh & Mook (1979), which allows to write them as

$$\int_0^L \psi_1^2 \left|\psi_1 D_0 A_{1,0} + \psi_s D_0 W_L\right| \, \mathrm{d}s = \sum_j \left(f_j e^{ij\omega_0 t_0} + c.c.\right), \tag{5.42}$$

and

$$\int_0^L \psi_1 \psi_s \left|\psi_1 D_0 A_{1,0} + \psi_s D_0 W_L\right| \, \mathrm{d}s = \sum_j \left(g_j e^{ij\omega_0 t_0} + c.c.\right). \tag{5.43}$$

The Fourier expansions can then be applied to Eq. (5.39), keeping in mind that terms with frequency ω_0 can be generated in the integrals via the combination of the Fourier terms with frequencies 0 and $2\omega_0$. This leads to

$$F_0 = -\zeta \left(i\omega_0 f_0 B_0 - i\omega_0 f_2 B_0^* + \frac{\omega_0 g_0 \eta + \omega_0 g_2 \eta}{2}\right). \tag{5.44}$$

It is important to mention that f_0 and g_0 are certainly real valued parameters, while both f_2 and g_2 are complex quantities in the general case. It is thus convenient to write the last two terms as $f_2 = f_{2r} + i f_{2c}$ and $g_2 = g_{2r} + i g_{2c}$. With all the expressions ready to advance with the solution, focus is now made on steady-state solutions, which are obtained by letting $D_1^0 B_0^0 = 0$. Considering also the Euler representation $B_0 = R_0 e^{i\varphi}$, the solvability condition given by Eq. (5.40) can be written in terms of its real and imaginary parts, which leads to the system of equations

$$\begin{aligned} &-\frac{\omega_0^2 \eta m_q}{2} \sin\varphi + \frac{a_2 \eta}{2} \sin\varphi + \zeta\omega_0 f_{2r} R_0 \sin 2\varphi - \zeta\omega_0 f_{2c} R_0 \cos 2\varphi - \frac{\zeta\omega_0 g_0 \eta}{2} \cos\varphi \\ &-\frac{\zeta\omega_0 g_{2r} \eta}{2} \cos\varphi - \frac{\zeta\omega_0 g_{2c} \eta}{2} \sin\varphi = 0 \end{aligned} \tag{5.45}$$

$$\begin{aligned} &-\frac{\omega_0^2 \eta m_q}{2} \cos\varphi + \frac{a_2 \eta}{2} \cos\varphi - \zeta\omega_0 f_0 R_0 + \zeta\omega_0 f_{2r} R_0 \cos 2\varphi + \zeta\omega_0 f_{2c} R_0 \sin 2\varphi \\ &+\frac{\zeta\omega_0 g_0 \eta}{2} \sin\varphi + \frac{\zeta\omega_0 g_{2r} \eta}{2} \sin\varphi - \frac{\zeta\omega_0 g_{2c} \eta}{2} \cos\varphi = 0 \end{aligned} \tag{5.46}$$

At this point the introduction of the aforementioned iterative approach is necessary. The problem with a direct solution lies in the fact that it is not possible to obtain the values for the constants f_0, f_2, g_0, and g_2 without knowing the solution for $A_{1,0}$. However, it is possible to find initial guesses for such values by setting $A_{1,0} = 0$. With this first evaluation, it is possible to solve Eqs. (5.45) and (5.46) for the variables R_0 and φ, leading

to an initial evaluation of $A_{1,0}$. This first solution can then be reinserted in the scheme to recalculate the constants f_0, f_2, g_0, and g_2, and with that, the iterative process is defined, to be repeated until it is considered that the results converged. It is worth-mentioning that, if there is interest in the investigation of a series of values for the imposed motion amplitude, one way to reduce the amount of necessary computation is to proceed with an incremental approach over the solution. This is made by setting the obtained result for $A_{1,0}$ under a given value of η as the starting point for the evaluation when η is changed.

5.4 Comparison between approaches

With the models at hand and a viable analytical solution, the path is laid to assess the quality of each of the possible ROMs herein defined. To that end, an inclined cable with a significant sag is chosen as example and the results are compared to a numerical reference obtained with the FEM. In the same manner as for the vertical case, the in-house software Giraffe is used for the FEM solution. The cable under investigation lays between supports presenting horizontal and vertical distances between each other of 1500 m and 1800 m respectively. The necessary structural and hydrodynamic parameters are presented in Tab. 15.

Table 15 – Structural and hydrodynamical properties for the curved structure. Adapted from Pesce, Martins & Silveira (2006).

Property	Description	Value
μ	Mass per length	108 kg/m
γ_s	Immersed weight per length	727 N/m
EA	Axial stiffness	2314.0×10^6 N
L	Length	2452.46 m
ρ	Fluid density	1025 kg/m^3
D	Structural diameter	0.2032 m
$\overline{C}_D$	Mean drag coefficient	1.2000
C_a	Added mass coefficient	1.0737

The resulting static configuration for this problem is shown in Fig. 46, where it is possible to verify that the case at hand is not limited to small inclination or sag.

A first step in the comparison is to analyse the frequencies and modes obtained with the FEM solution and with the PDEs. This is done specially because the equations of motion as presented in Eqs. (5.1) and (5.2) are in a format not commonly presented in the literature. This becomes then an indication of the correctness of the obtained equations. In order to obtain the modes and frequencies directly from the PDEs, a native solver from Mathematica® is applied. Such solver uses an internal finite element scheme over the

Figure 46 – Calculated static configuration for the structure using the data in Tab. 15.

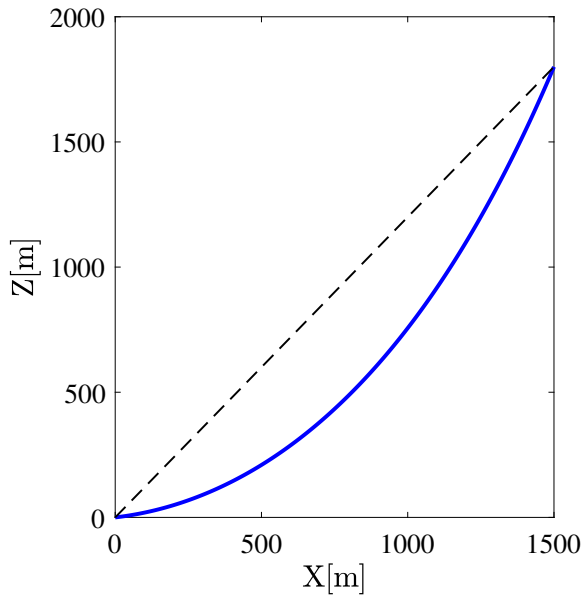

Source: Vernizzi, Lenci & Franzini (2022)

furnished PDEs. The convergence of both the Giraffe and Mathematica® solutions can be verified in Tabs. 16 and 17 respectively.

Table 16 – Natural frequencies (rad/s) obtained for the first five modes of vibration using the in-house software Giraffe as function of the number of elements along the cable length.

Mode	Number of elements				
	10	25	50	100	200
1	0.1984	0.1983	0.1983	0.1983	0.1983
2	0.3150	0.3147	0.3147	0.3147	0.3147
3	0.4419	0.4402	0.4402	0.4402	0.4402
4	0.5570	0.5524	0.5522	0.5522	0.5522
5	0.6838	0.6723	0.6719	0.6719	0.6719

With the convergence of both methods addressed it is now possible to compare them between each other. The natural frequencies for the first five modes of vibration are shown in Tab. 18, while the modal shapes for the first three modes are shown in Fig. 47.

From the results presented so far some conclusions can be drawn. The first one is that there are no meaningful differences in any of the mode shapes obtained, which indicates that the obtained PDEs in the alternative format herein presented are indeed correct. Regarding the natural frequency, the relative differences between the FEM solution and the PDEs do not exceed 1% (see Tab. 18), reinforcing the previous conclusion.

Regarding the obtained ROMs, the natural frequencies calculated from their

Table 17 – Natural frequencies (rad/s) obtained for the first five modes of vibration using the Mathematica® eigensystem solver over the PDEs of motion as a function of the maximum element size set for the software (in meters).

Mode	Maximum element size [m]				
	1000	500	100	10	1
1	0.2740	0.2184	0.2000	0.1998	0.1998
2	0.6042	0.3630	0.3172	0.3167	0.3167
3	0.9051	0.5541	0.4441	0.4431	0.4431
4	1.3733	0.8416	0.5575	0.5558	0.5558
5	2.1746	1.1399	0.6791	0.6762	0.6762

Table 18 – Comparison of the natural frequencies obtained for the structure considering the FEM or a direct obtaining from the PDEs.

Mode	Model	Freq. [rad/s]	Rel. diff. %
1	FEM	0.1983	-
1	PDE	0.1998	0.76
2	FEM	0.3147	-
2	PDE	0.3167	0.64
3	FEM	0.4402	-
3	PDE	0.4431	0.66
4	FEM	0.5522	-
4	PDE	0.5557	0.63
5	FEM	0.6719	-
5	PDE	0.6762	0.64

Figure 47 – Comparison between transversal modal shapes obtained by the FEM and a direct application over the PDEs of motion. Blue lines are used for the FEM while red lines are used for the direct solution. First mode indicated by circles, second mode by crosses and third mode by diamonds.

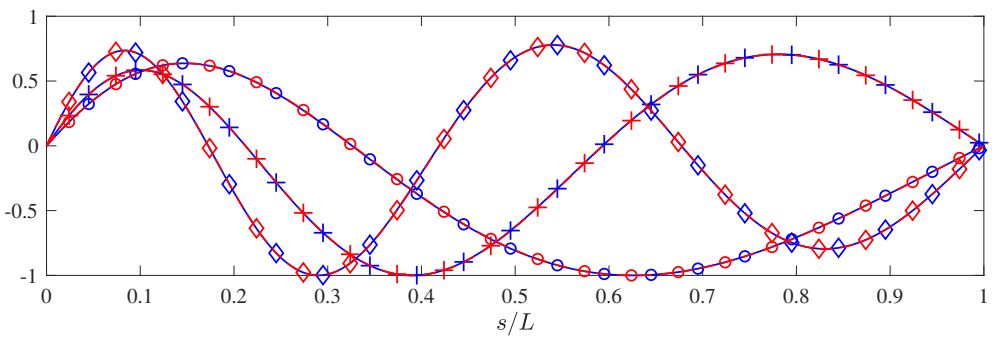

Source: Vernizzi, Lenci & Franzini (2022)

respective ODE systems are presented in Tab. 19. Also, since set (iii) does not make use of the natural modes of vibration of the structure, it becomes necessary to verify if such set is able to recover those modes. This can be verified by the modal shape comparisons present in Fig. 48.

Table 19 – Comparison of the natural frequencies obtained for the structure considering the FEM and the ROMs.

Mode	Model	Freq. [rad/s]	Rel. diff. %
1	FEM	0.1983	-
1	ROM(i)	0.1996	0.66
1	ROM(ii)	0.1995	0.61
1	ROM(iii)	0.1885	−4.94
2	FEM	0.3147	-
2	ROM(i)	-	-
2	ROM(ii)	0.3170	0.76
2	ROM(iii)	0.3351	6.48
3	FEM	0.4402	-
3	ROM(i)	-	-
3	ROM(ii)	0.4435	0.76
3	ROM(iii)	0.5610	27.44

Figure 48 – Comparison between transversal modal shapes obtained by a direct application over the PDEs of motion and the recovery achieved by the trigonometric shape functions of set (iii). Red lines are used for the direct solution while black lines are used for the recovery by trigonometric function. First mode indicated by circles, second mode by crosses and third mode by diamonds.

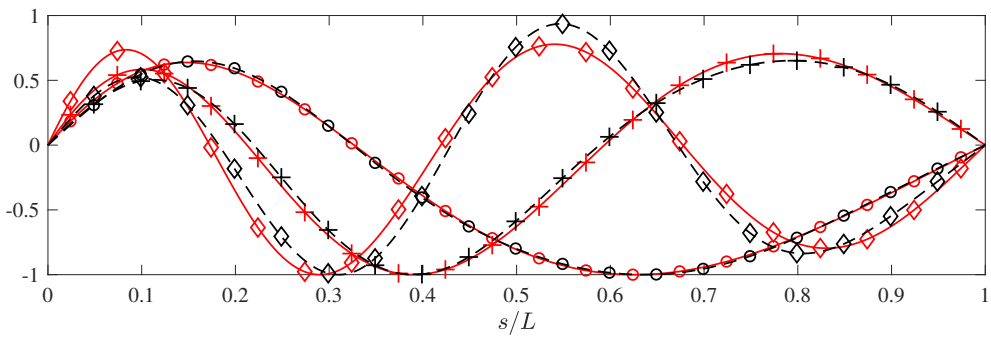

Source: Vernizzi, Lenci & Franzini (2022)

Concerning the modal shape recovery by set (iii), it is possible to see that the adherence is good, however with visible small differences. Recalling the case for vertical structures, the fact that the difference is small does not ensure by itself that the model will give a good representation. Focusing on the obtained natural frequencies it is possible to see that the relative error is insignificant for the ROMs based on the vibration modes,

while for set (iii) the errors are of noticeable magnitude, with the value obtained for the third mode natural frequency being very far off the correct one. This already anticipate, for the curved case, some expectations drawn from the straight structures, that is, a basis that can recover modal shapes is not necessarily good for the mathematical representation of the model.

Following now to further comparisons, steady-state results obtained from numerical simulations are compared. Each simulation was carried out through 1000 seconds, value that proved to be enough to achieve such regimes. The integrations of the ROMs are made with a Runge-Kutta scheme, native to the Matlab® ode45 function, while Giraffe uses its own Newmark method. For the sake of simplifying the nomenclature, since a total of 9 different ROMs are analysed, they are named $\mathrm{ROM}_{i,j}$, with i indicating the number of the set used as DOF projection functions, while j indicates the number of the type of interpolation of the top motion used in the ROM. Initially, a top motion amplitude of 1 meter is considered, with frequency matching the one of the first natural mode obtained with the PDEs using the Mathematica® solver. For ROMs of the type $\mathrm{ROM}_{1,j}$, the simulation results are presented as amplitude scalograms in Fig. 49.

Figure 49 – Amplitude scalograms of the transversal response of the structure in steady-state regime. (a) FEM solution. (b) Numerical integration of $\mathrm{ROM}_{1,1}$. (c) Numerical integration of $\mathrm{ROM}_{1,2}$. (d) Numerical integration of $\mathrm{ROM}_{1,3}$.

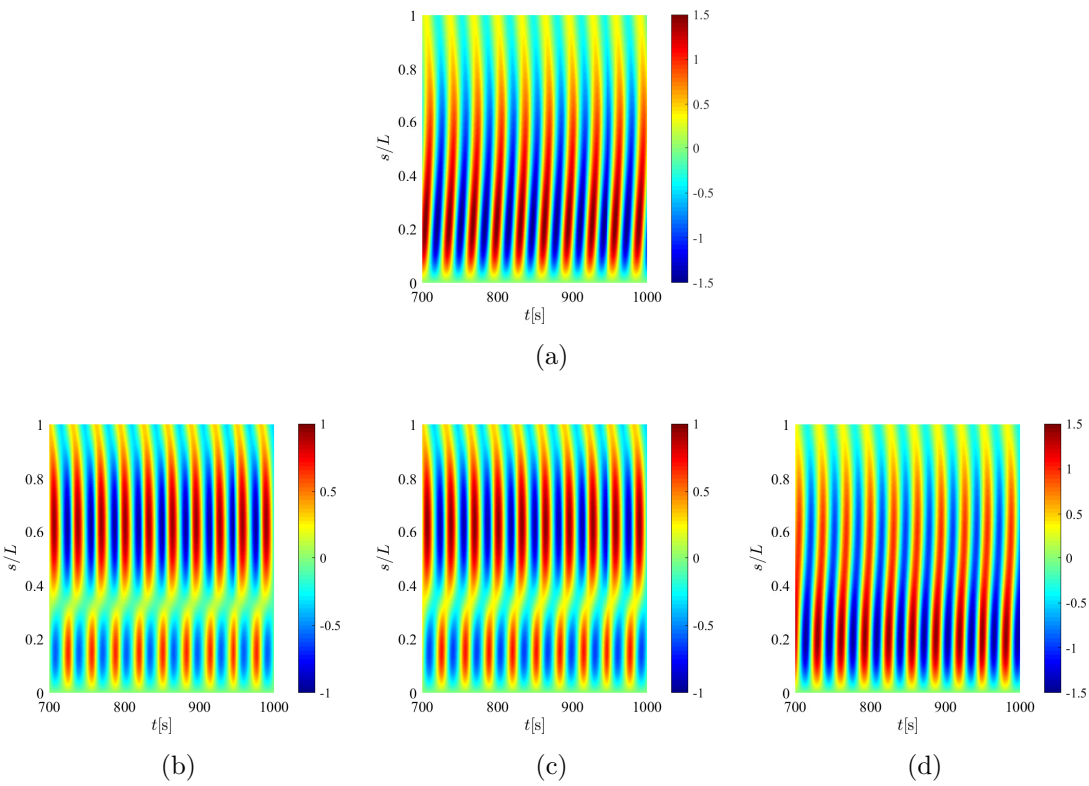

Source: Vernizzi, Lenci & Franzini (2022)

It is easy to notice that the results from the FEM simulation are not qualitatively

recovered by $ROM_{1,1}$ or $ROM_{1,2}$. The obtained amplitudes in both cases are significantly different from the FEM results, while the wave pattern formed is certainly not the same. In turn, $ROM_{1,3}$ gives an adherent result regarding the achieved amplitude in steady-state regime and in the resulting wave-pattern. Those results already give a glimpse that there are features of major importance regarding the adopted function to represent the effects of the imposed motion. In order to give more detail about the structural behaviour, considering $ROM_{1,3}$ that presented the best results in this first comparison, the time series and phase-space portraits of 4 different cross-sections are compared with the FEM results in Fig. 50. The chosen cross-sections are those of s/L values equal to 0.2, 0.4, 0.6 and 0.8.

The figure shows that the response along the length is in fact well recovered by $ROM_{1,3}$, with the resulting differences being small. It is also noticeable that the response frequency is visually the same, with an almost constant phase-shift that is due to the accumulation in the simulation time of the very small difference between such frequencies. In order to complement those results, Tab. 20 brings the maximum displacement amplitude achieved in each of the investigated cross-sections for $ROM_{1,3}$ and the FEM solution. Another result is shown in Fig. 51, which brings three snapshots for each of the compared solutions. A relative scheme is used to choose the instant of the snapshots to avoid discrepancies due to the phase shift between results. To that end, in any simulation a reference time is taken when the amplitude of motion achieves its minimum value for the cross-section at $s/L = 0.2$. This time is used for one of the snapshots, while the other two are taken after intervals of time equal to 1/8 and 1/4 of the natural period of the first mode.

Table 20 – Comparison between the FEM and $ROM_{1,3}$ results for the maximum amplitude of motion at different cross-sections. Results in meters.

s/L	FEM	$ROM_{1,3}$
0.2	1.5165	1.4452
0.4	1.2470	1.0795
0.6	0.9074	0.9652
0.8	0.5570	0.6801

Combining the time series displayed, the amplitude values in Tab. 20 and the snapshots taken, it is possible to conclude that $ROM_{1,3}$ presents good results in comparison to the FEM solution. For sure some improvements can be made but the quality obtained is certainly useful for analysis. Proceeding them to check how the results can be further enhanced by the use of a larger number of projection functions, the comparisons between the FEM solution and $ROMs_{2,j}$ start with the scalograms presented in Fig. 52.

The first result to draw attention is that, yet again, the top motion interpolations of type 1 and 2 are not able to ensure a satisfactory adherence with the reference result,

Figure 50 – Time series and phase-space portraits comparison between $\mathrm{ROM}_{1,3}$ (Red lines with crosses markers) and the FEM (blue line without markers) solution for a top motion amplitude of 1m. a) Time series for the cross-section at $s/L = 0.8$. b) Phase-space portrait for the cross-section at $s/L = 0.8$. c) Time series for the cross-section at $s/L = 0.6$. d) Phase-space portrait for the cross-section at $s/L = 0.6$. e) Time series for the cross-section at $s/L = 0.4$. f) Phase-space portrait for the cross-section at $s/L = 0.4$. g) Time series for the cross-section at $s/L = 0.2$. h) Phase-space portrait for the cross-section at $s/L = 0.2$.

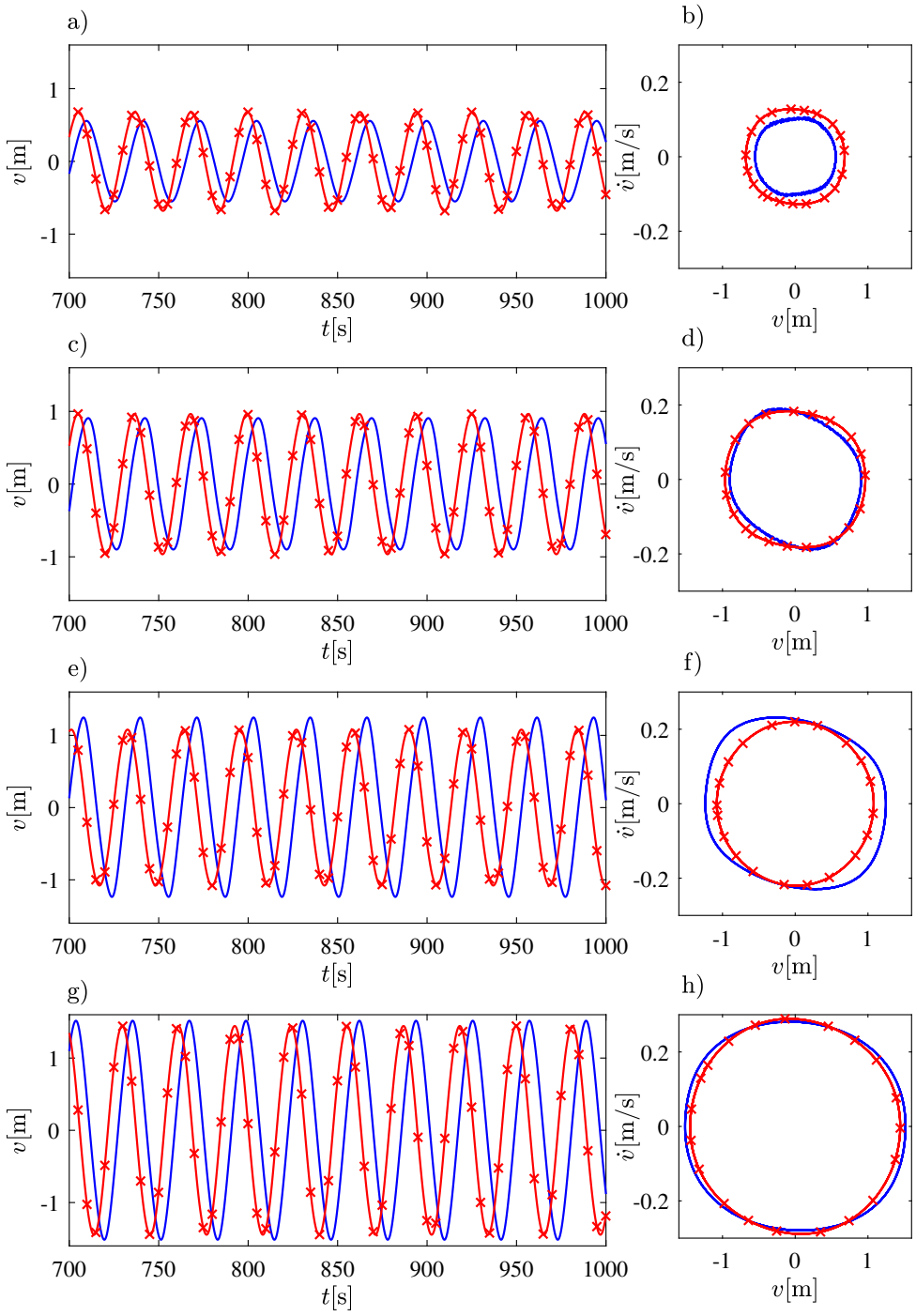

Source: Vernizzi, Lenci & Franzini (2022)

Figure 51 – Snapshots of the structural configuration for a reference instant correspondent to the occurrence of a peak in the response of the cross-section at $s/L = 0.2$ (lines without markers), an instant occurring 1/8 of the period of the structural response (lines with diamond markers) after the reference, and an instant occurring 1/4 of the period of the structural response (lines with diamond markers) after the reference. Comparison between FEM solution (blue continuous line) with $\text{ROM}_{1,3}$ (red dashed line).

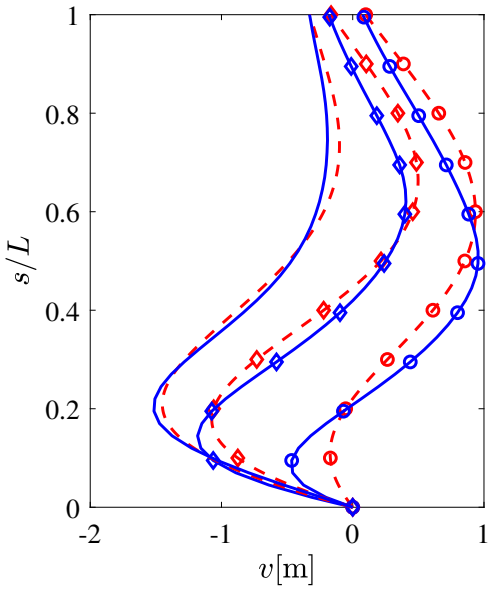

Source: Vernizzi, Lenci & Franzini (2022)

even though now there are more projection functions involved. Those two cases furnished amplitudes that are significantly different from the reference, together with a wave-pattern that, although closer than the ones obtained with $\text{ROM}_{1,1}$ and $\text{ROM}_{1,2}$, are still far from the expected result. On the other hand, the results obtained with the use of $\text{ROM}_{2,3}$ are very close to the reference, with barely any difference in the scalogram. For a more detailed analysis, the same complementary figures and results as made for $\text{ROM}_{1,3}$ are brought here. The time series and phase-space portraits of different cross-sections are shown in Fig. 53, while the maximum amplitude achieved by each of the same cross-sections are exposed in Tab. 21. Finally, three different snapshots as already defined before are shown in Fig. 54.

Table 21 – Comparison between the FEM and $\text{ROM}_{2,3}$ results for the maximum amplitude of motion at different cross-sections. Results in meters.

s/L	FEM	$\text{ROM}_{2,3}$
0.2	1.5165	1.4553
0.4	1.2470	1.2579
0.6	0.9074	0.8998
0.8	0.5570	0.5656

Figure 52 – Amplitude scalograms of the transversal response of the structure in steady-state regime. (a) FEM solution. (b) Numerical integration of $ROM_{2,1}$. (c) Numerical integration of $ROM_{2,2}$. (d) Numerical integration of $ROM_{2,3}$.

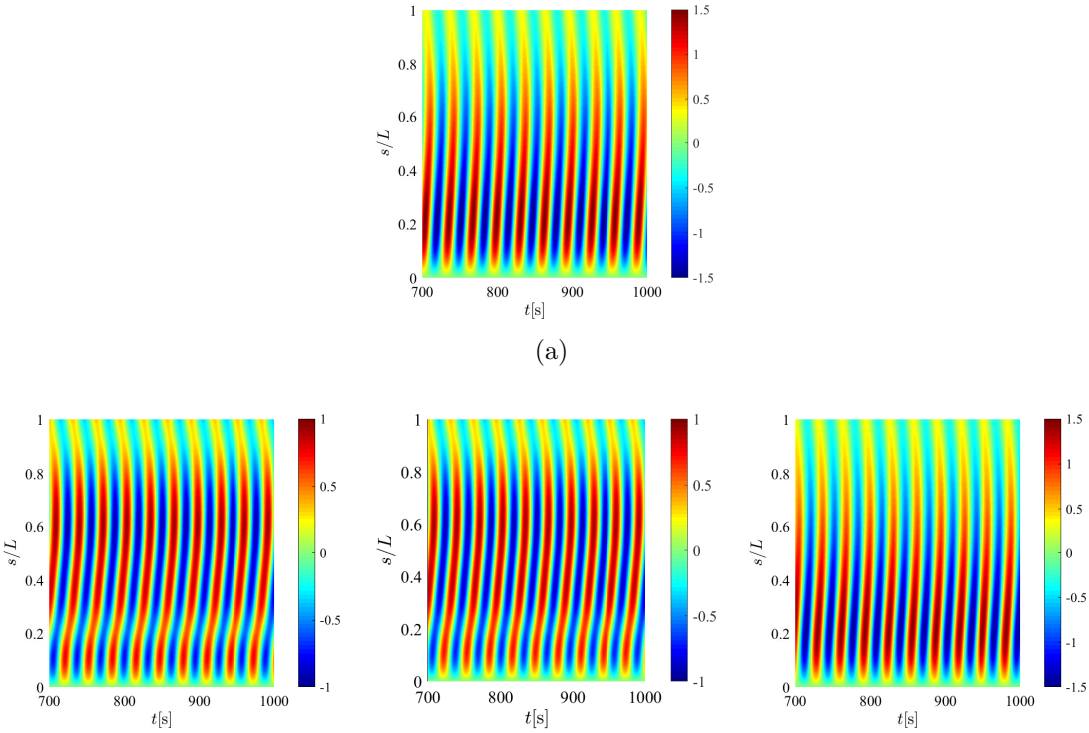

(a) (b) (c) (d)

Source: Vernizzi, Lenci & Franzini (2022)

Comparing the adherence of $ROM_{2,3}$ with $ROM_{1,3}$ it is clear that the enrichment of the projection basis by using more modes of vibration leads to more accurate results, being them on wave-patterns, maximum amplitudes or instantaneous configurations. It is important to notice however, that such improvements are not translated to the other two cases of top motion interpolation functions. This indicates that there is something more that is necessary for a good representation using ROMs based on the Galerkin scheme than just an enlargement of the projection basis until convergence is acquired. In order to settle the question regarding that aspect, the results of $ROMs_{3,j}$ are now investigated, starting with the scalograms in Fig. 55.

With the latter results, it is clear that the increase in the number of projection functions can enhance the obtained results, but it does not necessarily ensure convergence to a correct solution. Evaluating first what occurs when using types 1 and 2 of top motion interpolation functions, it is possible to see that the motion amplitude is somewhat close to the reference, but the wave pattern and the position at which the maximum displacement occurs are definitely not the same. Considering the third type of top motion interpolation, the result presents a better adherence, yet it is still worse than the one presented by $ROM_{2,3}$. Again, for a more detailed analysis of the results, the time series and phase-space

Figure 53 – Time series and phase-space portraits comparison between $\mathrm{ROM}_{2,3}$ (Black lines with circle markers) and the FEM (blue line without markers) solution for a top motion amplitude of 1m. a) Time series for the cross-section at $s/L = 0.8$. b) Phase-space portrait for the cross-section at $s/L = 0.8$. c) Time series for the cross-section at $s/L = 0.6$. d) Phase-space portrait for the cross-section at $s/L = 0.6$. e) Time series for the cross-section at $s/L = 0.4$. f) Phase-space portrait for the cross-section at $s/L = 0.4$. g) Time series for the cross-section at $s/L = 0.2$. h) Phase-space portrait for the cross-section at $s/L = 0.2$.

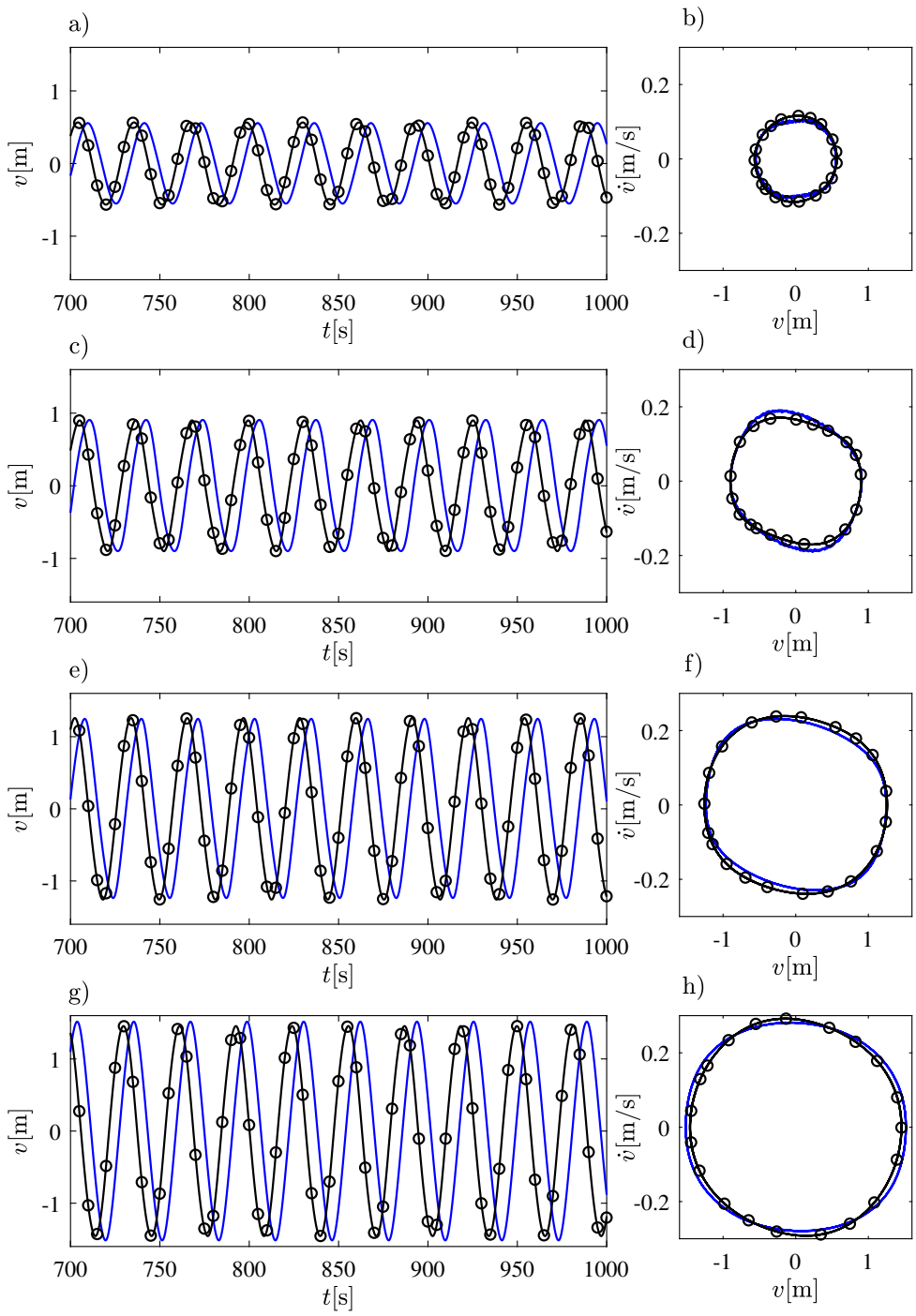

Source: Vernizzi, Lenci & Franzini (2022)

Figure 54 – Snapshots of the structural configuration for a reference instant correspondent to the occurrence of a peak in the response of the cross-section at $s/L = 0.2$ (lines without markers), an instant occurring 1/8 of the period of the structural response (lines with diamond markers) after the reference, and an instant occurring 1/4 of the period of the structural response (lines with diamond markers) after the reference. Comparison between FEM solution (blue continuous line) with $\mathrm{ROM}_{2,3}$ (black dotted line).

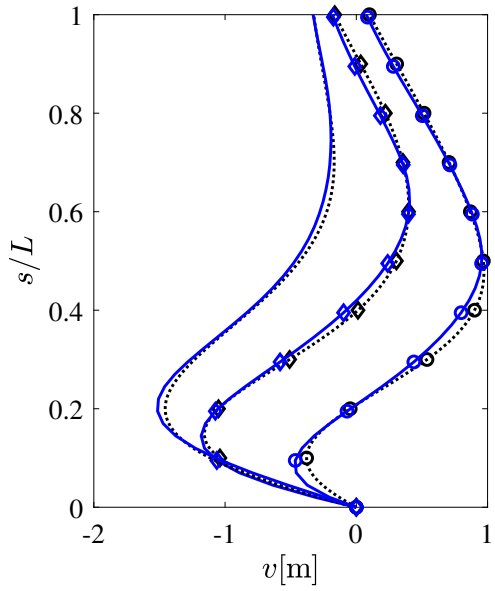

Source: Vernizzi, Lenci & Franzini (2022)

portraits of different cross-sections are shown in Fig. 56, the maximum observed amplitudes are shown in Tab. 22, and the snapshots in chosen instants are brought in Fig. 57

Table 22 – Comparison between the FEM and $\mathrm{ROM}_{3,3}$ results for the maximum amplitude of motion at different cross-sections. Results in meters.

s/L	FEM	$\mathrm{ROM}_{3,3}$
0.2	1.5165	1.4553
0.4	1.2470	1.2579
0.6	0.9074	0.8998
0.8	0.5570	0.5656

The results confirm that $\mathrm{ROM}_{3,3}$ is able to furnish good values for the maximum displacement amplitudes when the whole length of the cable is considered, but when particular points are taken, it becomes clear that such values are obtained in the wrong positions. The combination of the exposed results allows some conclusions to be drawn. The first one is that the interpolation functions concerning the imposed top motion play a major role on the success of the conceived ROMs, with a greater number of projection functions not being able to correct the flaws introduced by a poor choice of such interpolation functions. The second one is that by opting for a simpler format of the projection function,

Figure 55 – Amplitude scalograms of the transversal response of the structure in steady-state regime. (a) FEM solution. (b) Numerical integration of $ROM_{3,1}$. (c) Numerical integration of $ROM_{3,2}$. (d) Numerical integration of $ROM_{3,3}$.

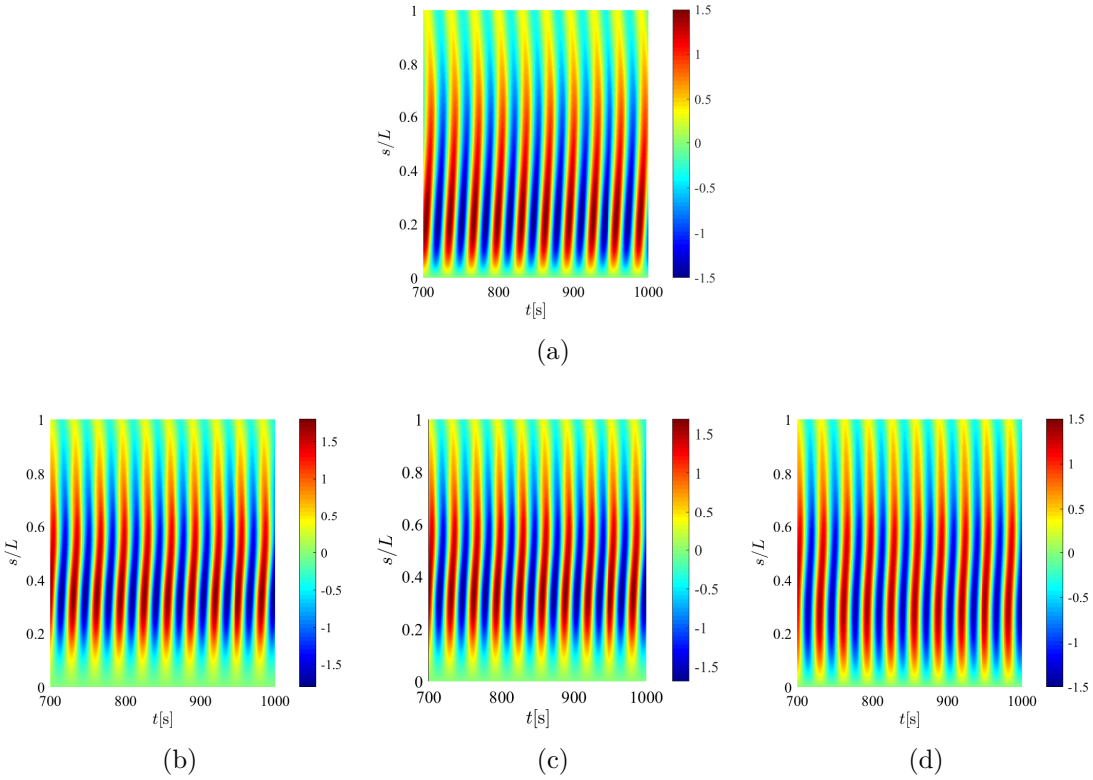

Source: Vernizzi, Lenci & Franzini (2022)

a significant amount of spatial representation quality is lost, not being recovered with the effort of using a larger number of projection functions. This highlights the importance of a qualitative analysis of the projection basis adopted when conceiving ROMs via projection methods and how the matter of accuracy of such models cannot be simply solved with larger models, even with the chosen basis being able to recover modal features. Recall that set (iii) is able to satisfactorily recover the frequency and shape of the first vibration mode, which is the main mode under excitation in this analysis.

With the conclusions about the importance of the interpolation functions for the top motion transmission settled, the analysis can move to further investigations, now taking into account only models of the form $ROM_{i,3}$. It has been mentioned so far that the frequency of the resulting motion is adequately recovered by the ROMs by means of a visual inspection over the obtained time series. In order to further clarify this reading, the spectral content of the solution for the different models are shown in Figs. 58 to 61.

It is possible to visualize that in all cases the spectra are concentrated around the region of the natural frequency of the first mode, indicating that the conclusion stated beforehand about the good recovering of the response frequency is actually correct. Notice

Figure 56 – Time series and phase-space portraits comparison between $\mathrm{ROM}_{3,3}$ (Magenta lines with square markers) and the FEM (blue line without markers) solution for a top motion amplitude of 1m. a) Time series for the cross-section at $s/L = 0.8$. b) Phase-space portrait for the cross-section at $s/L = 0.8$. c) Time series for the cross-section at $s/L = 0.6$. d) Phase-space portrait for the cross-section at $s/L = 0.6$. e) Time series for the cross-section at $s/L = 0.4$. f) Phase-space portrait for the cross-section at $s/L = 0.4$. g) Time series for the cross-section at $s/L = 0.2$. h) Phase-space portrait for the cross-section at $s/L = 0.2$.

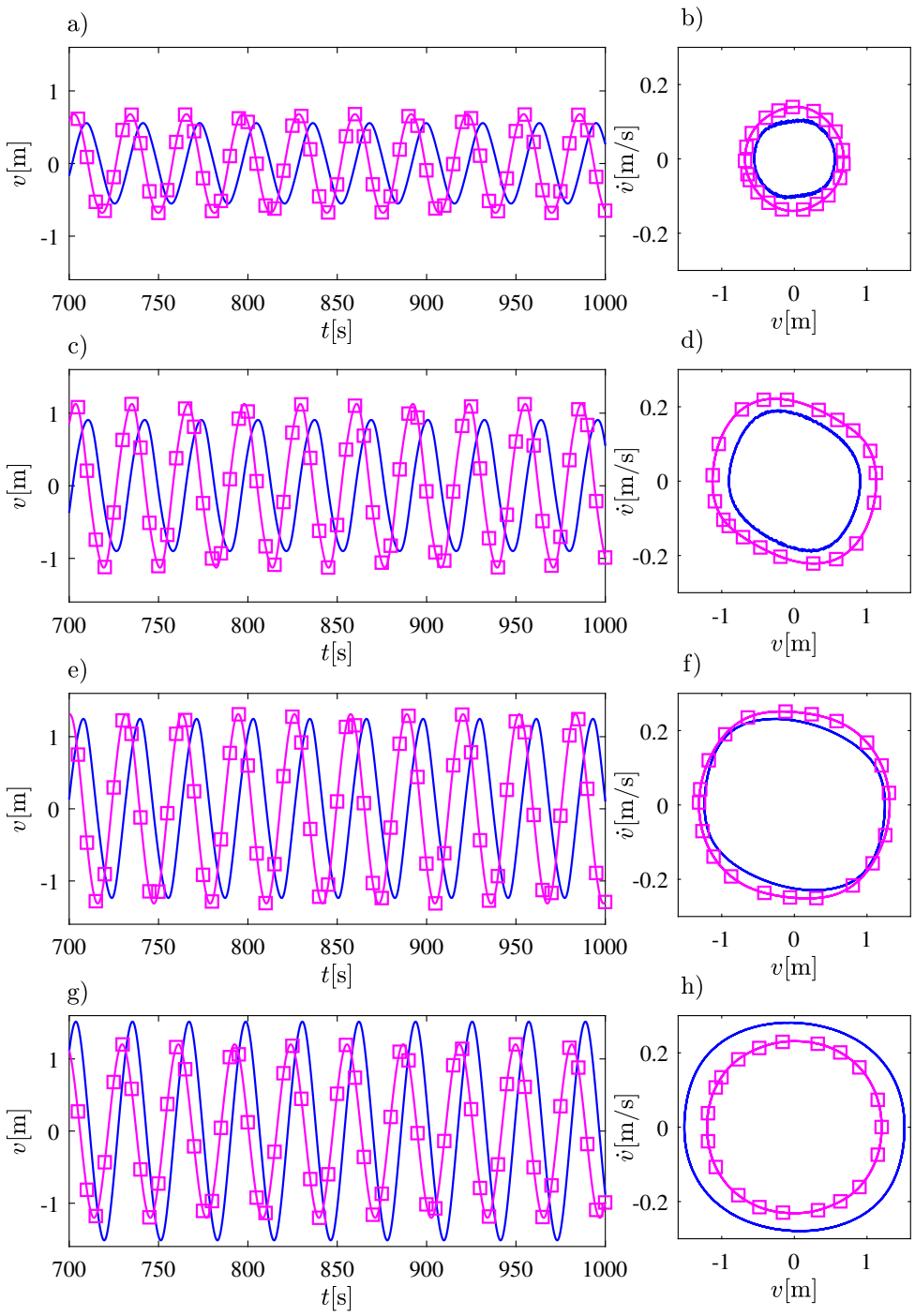

Source: Vernizzi, Lenci & Franzini (2022)

Figure 57 – Snapshots of the structural configuration for a reference instant correspondent to the occurrence of a peak in the response of the cross-section at $s/L = 0.2$ (lines without markers), an instant occurring 1/8 of the period of the structural response (lines with diamond markers) after the reference, and an instant occurring 1/4 of the period of the structural response (lines with diamond markers) after the reference. Comparison between FEM solution (blue continuous line) with $\mathrm{ROM}_{3,3}$ (magenta dash-dot line).

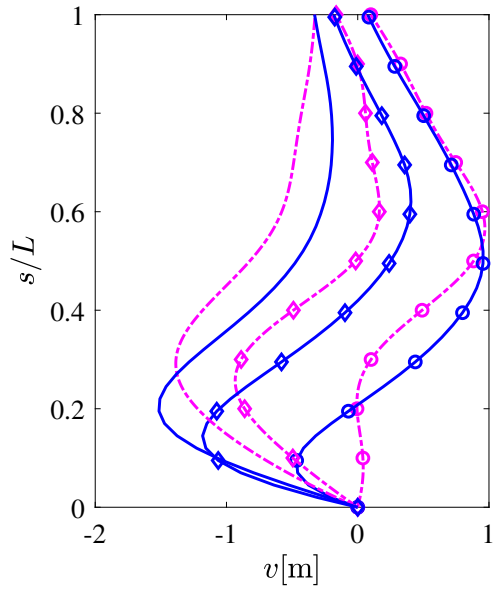

Source: Vernizzi, Lenci & Franzini (2022)

Figure 58 – Spanwise amplitude spectra along the cable length considering the FEM solution for a top motion amplitude of 1m, with the frequency normalized by the natural frequency of the first vibration mode f_0.

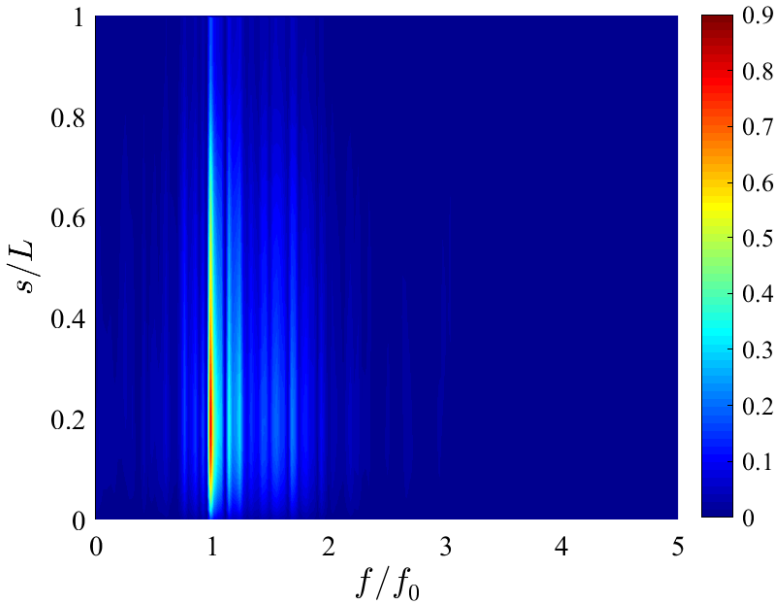

Source: Vernizzi, Lenci & Franzini (2022)

Figure 59 – Spanwise amplitude spectra along the cable length considering the $\mathrm{ROM}_{1,3}$ solution for a top motion amplitude of 1m, with the frequency normalized by the natural frequency of the first vibration mode f_0.

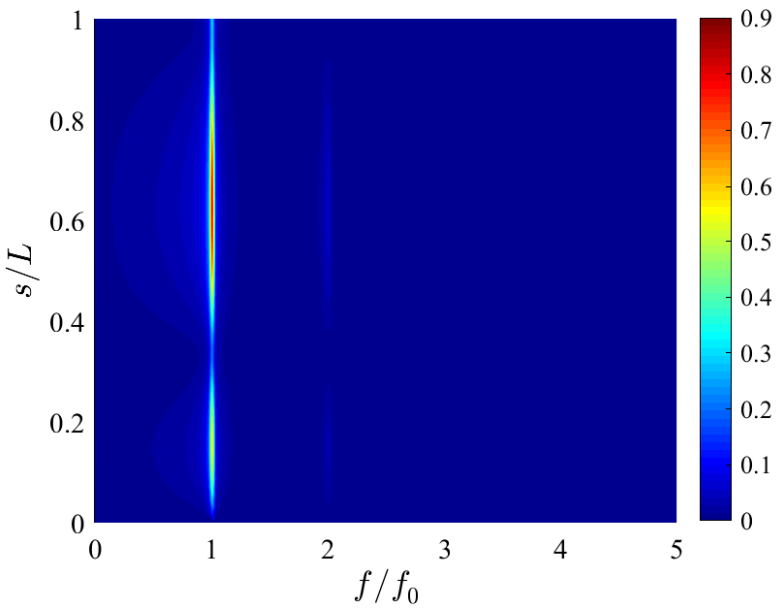

Source: Vernizzi, Lenci & Franzini (2022)

Figure 60 – Spanwise amplitude spectra along the cable length considering the $\mathrm{ROM}_{2,3}$ solution for a top motion amplitude of 1m, with the frequency normalized by the natural frequency of the first vibration mode f_0.

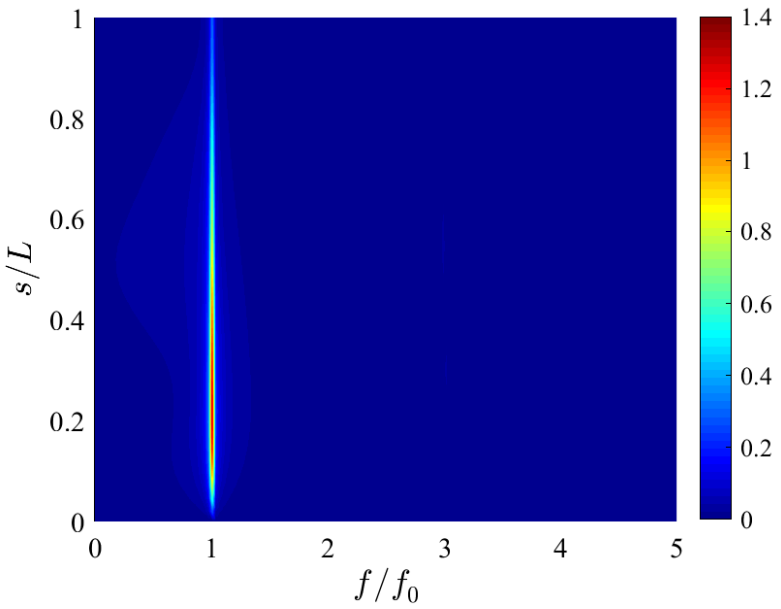

Source: Vernizzi, Lenci & Franzini (2022)

however that all the ROMs filter the spectral content in this region, while the FEM simulations present results with a broad band of frequency contribution. The origin of such

Figure 61 – Spanwise amplitude spectra along the cable length considering the $ROM_{3,3}$ solution for a top motion amplitude of 1m, with the frequency normalized by the natural frequency of the first vibration mode f_0.

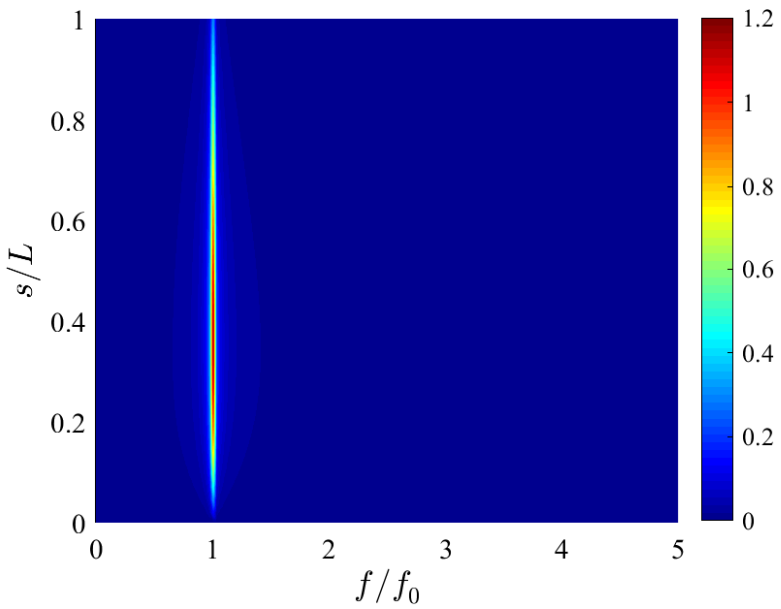

Source: Vernizzi, Lenci & Franzini (2022)

result is likely due to the fact that the transmission of the top motion does not occur in a quasi-static manner, but in reality by means of travelling waves advancing along the cable length. This also contributes to explain the small differences in the geometrical response of the ROMs compared to the FEM solution, even for the best scenario obtained with $ROM_{2,3}$.

So far, all the results were restrained to the case of 1m of top motion amplitude. It is now necessary to address the capability of the ROMs to reproduce results considering larger excitations. As made for the spectral analysis, only models of the type $ROMs_{i,3}$ are considered to that end. For the scenario of a top motion of 3m the resulting scalograms are shown in Figs. 62 to 65. In turn, Figs. 66 to 69 bring the analogous results for a top motion amplitude of 5m.

In order to obtain a clearer visualization for the best performing model, $ROM_{2,3}$, the time series and phase-space portraits for selected cross-sections are shown in Figs. 70 and 71 for the scenarios of 3m and 5m of top motion amplitude respectively.

From the scalograms it is clear that all the explored ROMs have a good degree of agreement with the reference, being the best result furnished by $ROM_{2,3}$ and the worst by $ROM_{3,3}$, with the major difference being in the spatial reconstruction of the displacement field. Notice also that, as the top motion amplitude is increased, more differences in wave pattern start to appear in all the ROMs. This can be due to the greater importance of the travelling waves that transfer the top motion effects, which are not reproduced in

Figure 62 – Amplitude scalogram of the transversal response of the structure in steady-state regime considering a top motion amplitude of 3m, FEM solution.

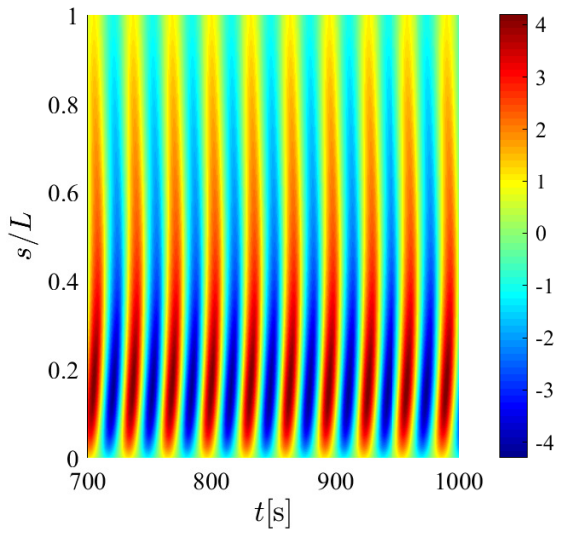

Source: Vernizzi, Lenci & Franzini (2022)

Figure 63 – Amplitude scalogram of the transversal response of the structure in steady-state regime considering a top motion amplitude of 3m, $\mathrm{ROM}_{1,3}$ solution.

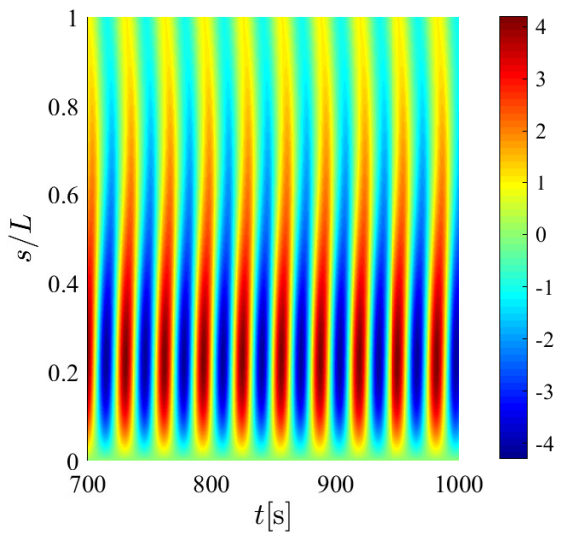

Source: Vernizzi, Lenci & Franzini (2022)

the approach taken for the ROM construction. Checking the selected cross-sections, it is possible to notice that, although the scalograms reveal a mismatch in the wave-pattern, in general $\mathrm{ROM}_{2,3}$ is able to furnish an adequate representation of the displacements along the structural length. The results also let clear that for larger top motion amplitudes, a further enrichment of the ROM would be necessary. Considering the conclusions made so far, such enrichment should be focused on the top motion interpolation functions.

Complementing the results shown, the maximum achieved amplitude considering

Figure 64 – Amplitude scalogram of the transversal response of the structure in steady-state regime considering a top motion amplitude of 3m, $ROM_{2,3}$ solution.

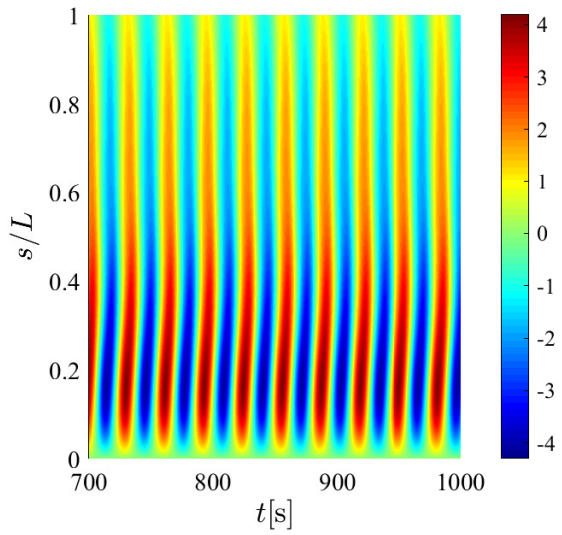

Source: Vernizzi, Lenci & Franzini (2022)

Figure 65 – Amplitude scalogram of the transversal response of the structure in steady-state regime considering a top motion amplitude of 3m, $ROM_{3,3}$ solution.

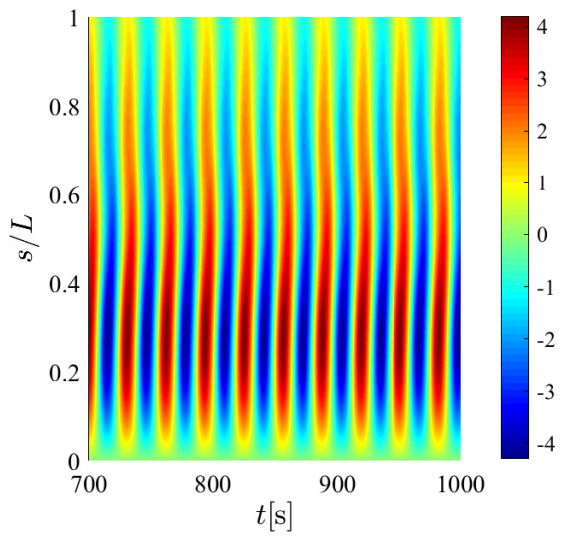

Source: Vernizzi, Lenci & Franzini (2022)

the different models, disregarding the position in which they occur, are shown in Fig. 72 as a function of the impose top motion amplitude. Aside the simulations results, the figure also presents the response curve obtained with the proposed iterative solution using the MMTS.

The maximum values are often valuable for design purposes. To that end, it is clear that all the ROMs presented suitable results. Care must be taken, however, when such results are converted to other properties such as strain, since for that the shape of the

Figure 66 – Amplitude scalogram of the transversal response of the structure in steady-state regime considering a top motion amplitude of 5m, FEM solution.

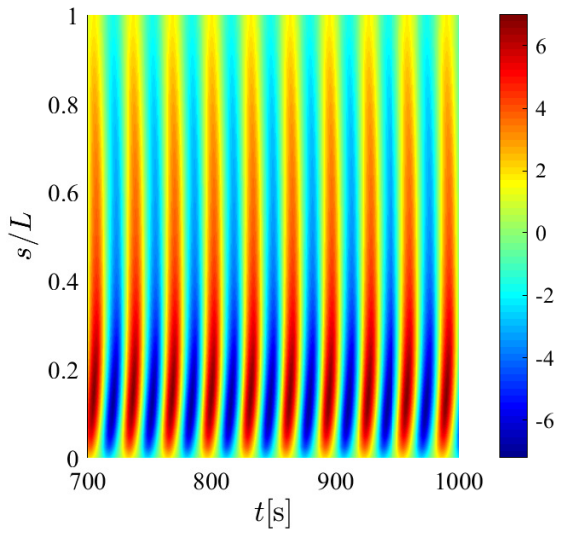

Source: Vernizzi, Lenci & Franzini (2022)

Figure 67 – Amplitude scalogram of the transversal response of the structure in steady-state regime considering a top motion amplitude of 5m, $\mathrm{ROM}_{1,3}$ solution.

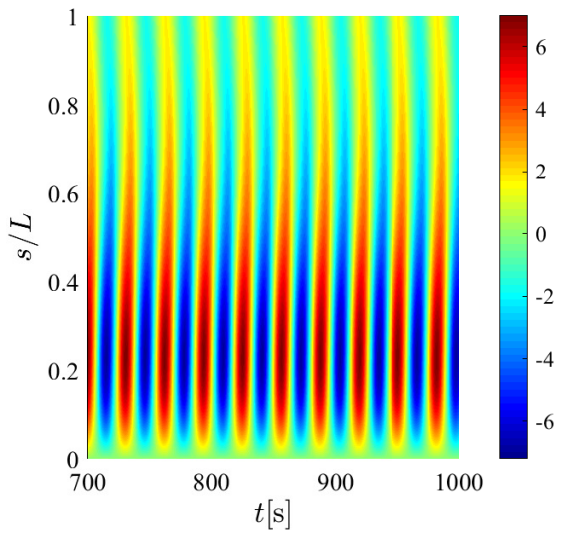

Source: Vernizzi, Lenci & Franzini (2022)

cable is of major importance. Notice as well that the proposed solution with the MMTS closely follows $\mathrm{ROM}_{1,3}$, which is the model over which it is based. Another remark is that all the conclusions about the behaviour of $\mathrm{ROM}_{1,3}$ can be extended to the MMTS solution, since the only difference in both of them is in how to obtain the steady-state amplitude of the involved DOF, while the displacement field in both cases is essentially the same. The advantage of the MMTS solution is that it can furnish the steady-state solution with less computational effort than the integration of the corresponding ROM. This ability

Figure 68 – Amplitude scalogram of the transversal response of the structure in steady-state regime considering a top motion amplitude of 5m, $ROM_{2,3}$ solution.

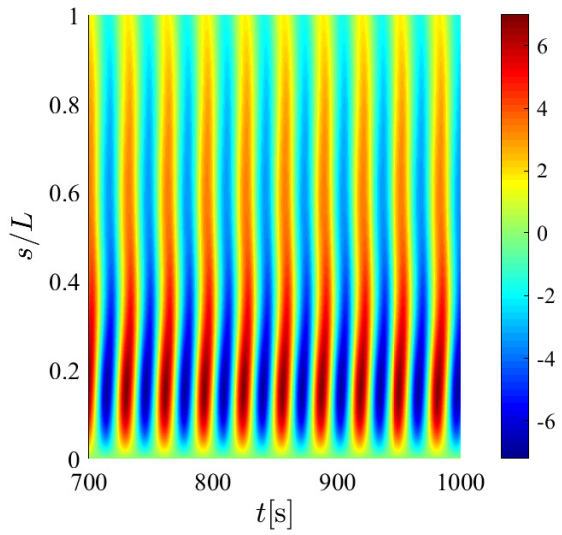

Source: Vernizzi, Lenci & Franzini (2022)

Figure 69 – Amplitude scalogram of the transversal response of the structure in steady-state regime considering a top motion amplitude of 5m, $ROM_{3,3}$ solution.

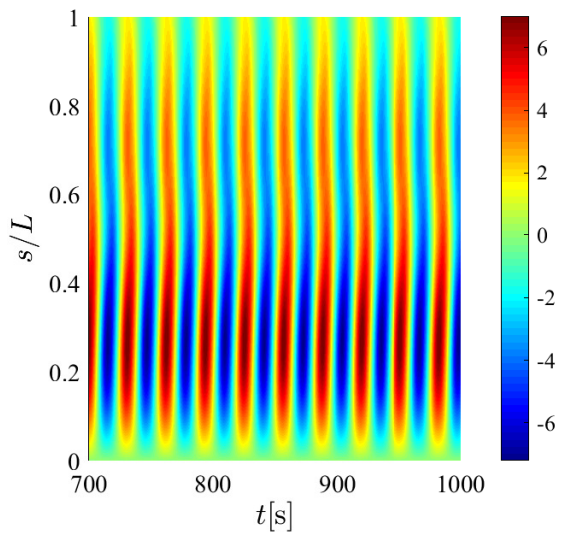

Source: Vernizzi, Lenci & Franzini (2022)

however, is limited to the number of DOFs of the associated ROM. The iterative method quickly becomes inefficient as the number of DOFs increase. Those results reinforce the importance of obtaining the minimal ROM with enough representation quality, which is achieved by a deep investigation on how to form the projection basis itself.

Another important aspect regarding the ROMs concerns their computational advantage over larger models such as the ones based on the FEM. To show how each of the conceived ROMs behave in that sense, Tab. 23 brings the simulation times necessary for

Figure 70 – Time series and phase-space portraits comparison between $\mathrm{ROM}_{2,3}$ (Black lines with circle markers) and the FEM (blue line without markers) solution for a top motion amplitude of 3m. a) Time series for the cross-section at $s/L = 0.8$. b) Phase-space portrait for the cross-section at $s/L = 0.8$. c) Time series for the cross-section at $s/L = 0.6$. d) Phase-space portrait for the cross-section at $s/L = 0.6$. e) Time series for the cross-section at $s/L = 0.4$. f) Phase-space portrait for the cross-section at $s/L = 0.4$. g) Time series for the cross-section at $s/L = 0.2$. h) Phase-space portrait for the cross-section at $s/L = 0.2$.

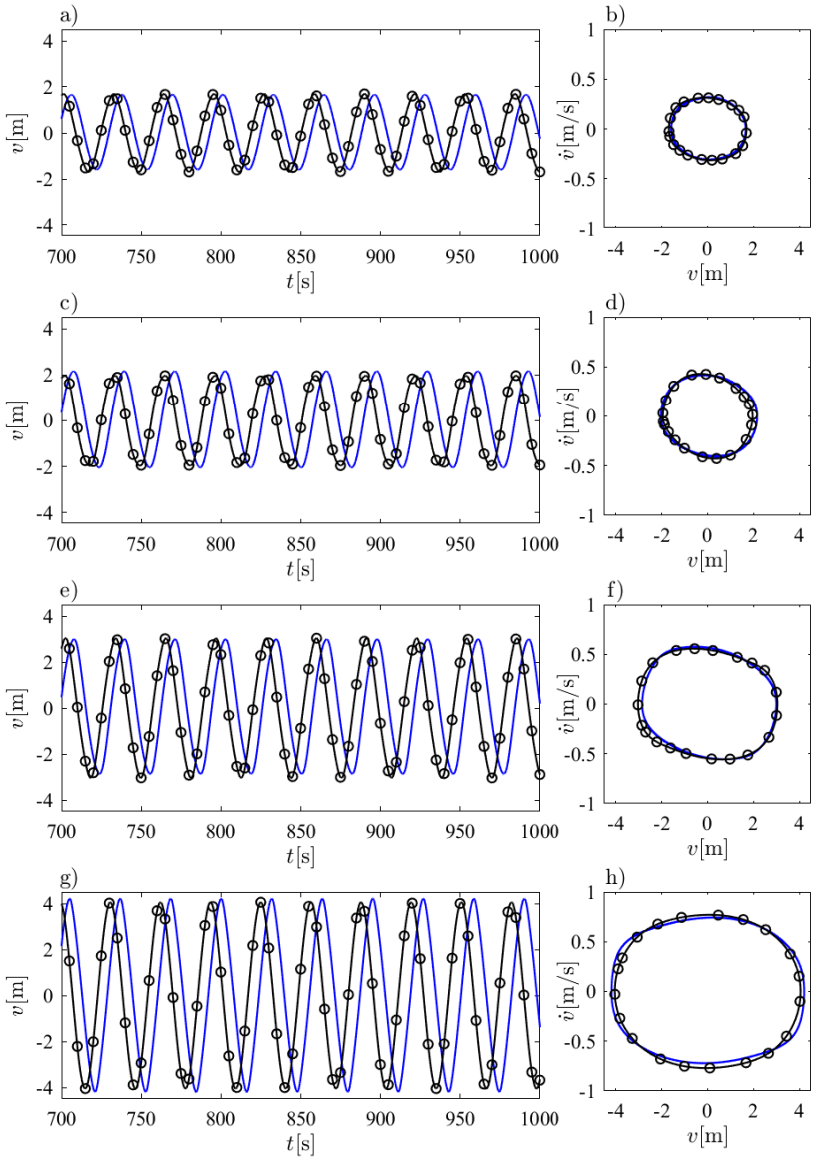

Source: Vernizzi, Lenci & Franzini (2022)

the integration of each model. All the simulations where carried out in the same standard microcomputer with a 7th generation i7 processor.

Figure 71 – Time series and phase-space portraits comparison between $ROM_{2,3}$ (Black lines with circle markers) and the FEM (blue line without markers) solution for a top motion amplitude of 5m. a) Time series for the cross-section at $s/L = 0.8$. b) Phase-space portrait for the cross-section at $s/L = 0.8$. c) Time series for the cross-section at $s/L = 0.6$. d) Phase-space portrait for the cross-section at $s/L = 0.6$. e) Time series for the cross-section at $s/L = 0.4$. f) Phase-space portrait for the cross-section at $s/L = 0.4$. g) Time series for the cross-section at $s/L = 0.2$. h) Phase-space portrait for the cross-section at $s/L = 0.2$.

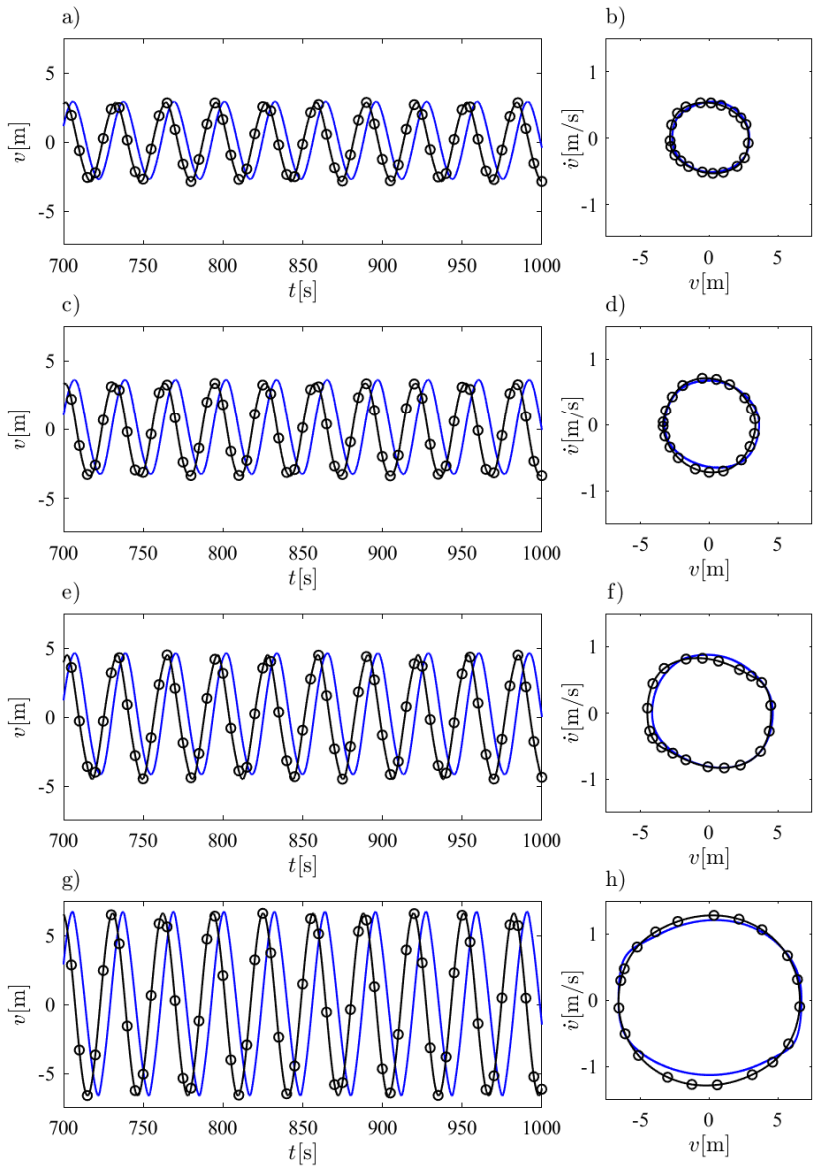

Source: Vernizzi, Lenci & Franzini (2022)

From the computational effort point of view, the advantage of the ROMs is clear. More than that, it is easy to see how the smallest ROM can present a significant economy

Figure 72 – Comparison of the maximum transversal displacement along the cable length for the case of 1:1 resonance as a function of the imposed motion amplitude. All curves consider the third type of top motion interpolation (quasi-static solution).

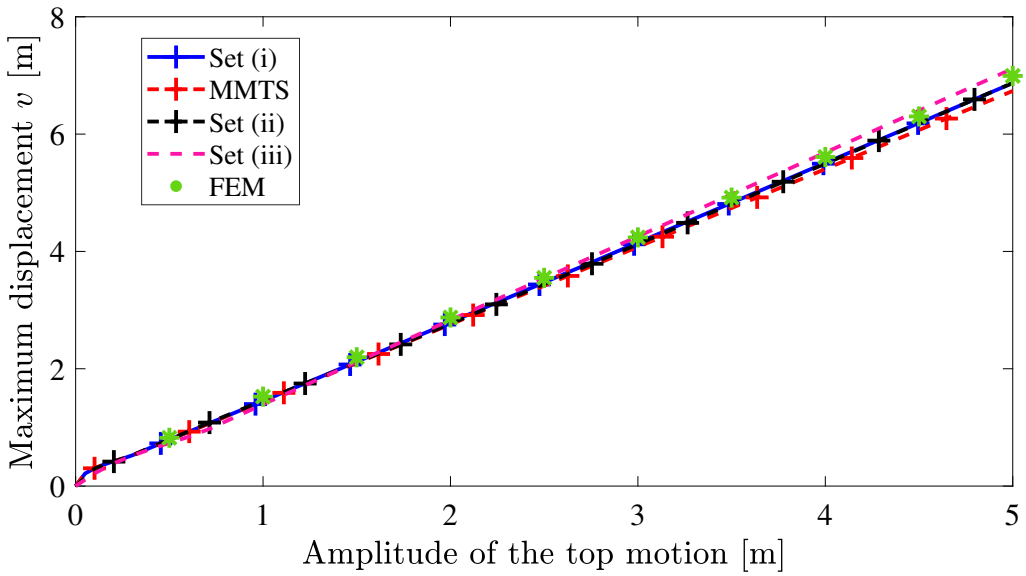

Source: Vernizzi, Lenci & Franzini (2022)

Table 23 – Time spent for the numerical simulation of one single scenario for each approach investigated.

Model	Time spent [s]
FEM	744.95
$ROM_{1,3}$	0.14
$ROM_{2,3}$	0.43
$ROM_{3,3}$	8.20

in the necessary time of simulation, specially if a large number of scenarios is scheduled to take place in a design process.

A final aspect that is now explored is the capability of a ROM to recover qualitatively good results considering top motion frequencies not exactly tuned in the 1:1 resonance. To that end, $ROM_{1,3}$ is simulated for some pairs of top motion amplitude and frequency, with the results being compared to FEM solutions in Fig. 73. It is possible to visualize that the ROM is able to maintain a consistent adherence to the numerical reference under the tested frequency variation.

Figure 73 – Comparison of the maximum transversal displacement along the cable length between the FEM and the $\mathrm{ROM}_{1,3}$ solutions as a function of the imposed motion frequency for three different top motion amplitudes.

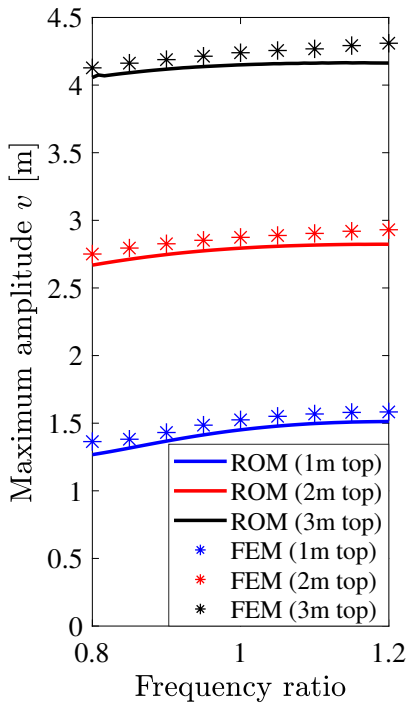

Source: Vernizzi, Lenci & Franzini (2022)

6 Vertical and straight flexible rods under vortex-induced vibrations

This chapter brings investigations regarding the problem of vertical, straight and flexible rods immersed in fluid under the action of VIV. This scenario is typical in offshore engineering, being usually associated with fatigue analysis due to the always existing sea-currents and the resonant characteristics of VIV. The development of minimal models that can accurately represent the problem is of great interest for design aid in this case, since simulations with high hierarchical models including the FSI can be very time consuming.

Along the chapter, different ROMs based on the Galerkin projection are investigated for the problem. As made for the case of parametric excitations, the models are evaluated in terms of the necessary number of projection functions against the complexity of such functions in order to well represent the problem. In the sequel, after defining a minimal ROM to represent the dynamical problem, a systematic way of obtaining nonlinear modes for this particular problem is presented, in order to further reduce the number of DOFs in the ROM, thus reducing even more the computational effort of evaluating it.

The results within this chapter where motivated by an initial study presented in the "XVIII International Symposium on Dynamic Problems of Mechanics" (DINAME2019), and were presented in the first edition of the "International Conference on Nonlinear Solid Mechanics" (ICoNSoM2019) and in the "International Conference on Engineering Vibration, 2020" (ICoEV2020).

6.1 Mathematical model

The problem now under investigation is that of a vertical and flexible cylinder, pinned at both ends, under the action of a sea current with velocity U_∞. This model is illustrated in Fig. 74. The structure has structural mass and the added mass per unit length given by μ and μ_a respectively. The products of axial and bending stiffness are given by EA and EI, respectively, the length is given by ℓ and the immersed weight by γ_s. The Cartesian reference frame is also shown in Fig. 74, with the Y axis being orthogonal to the plane of the figure, forming a positive system XYZ, with the corresponding displacements being given as U, V and W respectively.

The structure is also considered to be under the action of a previously applied tension, given by $T(0) = T_b$ at the bottom, resulting in a distribution along the length given by Eq. (6.1)

Figure 74 – Basic sketch for the studied problem.

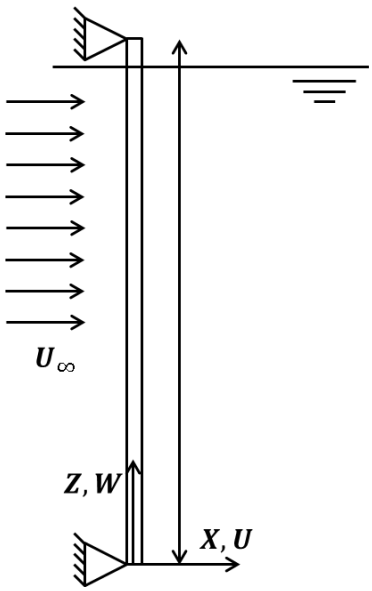

Source: The author.

$$T(Z) = T_b + \gamma_s Z. \tag{6.1}$$

Considering the spatial vibrations case, the equations of motion for the problem can be obtained from Eqs. (3.47) to (3.50) with the addition of terms to represent the VIV, which is herein made via a phenomenological approach, and the immersed weight. Let then the forces acting on the structure due to VIV to be represented by f_x and f_y in the X and Y directions respectively. No forcing is considered in the axial direction, implying in $f_z = -\gamma_s$. This is made since any term in such direction is caused by skin friction, which is much smaller than the effects at the directions orthogonal to the structure's axis. The equations of motion become

$$(\mu + \mu_a)\ddot{U} + EIU'''' - EA\left(U'\left(W' + \frac{(U')^2}{2} + \frac{(V')^2}{2}\right)\right)' = f_x, \tag{6.2}$$

$$(\mu + \mu_a)\ddot{V} + EIV'''' - EA\left(V'\left(W' + \frac{(U')^2}{2} + \frac{(V')^2}{2}\right)\right)' = f_y, \tag{6.3}$$

$$\mu\ddot{W} - EA\left(W' + \frac{(U')^2}{2} + \frac{(V')^2}{2}\right)' + \gamma_s = 0. \tag{6.4}$$

Notice that the torsional DOF is not present in the equations. This is simply obtained by considering that the term θ_z' is of the same order as V'^2 and U'^2. With such

hypothesis[1], the torsional problem decouples from the other ones when terms up to the cubic order are considered.

Now, prior to continuing with the development, it is important to recall that the static displacements at the axial direction caused by the applied tension will generate linear stiffness terms in the transversal equations. In order to obtain such terms, the axial displacement is decomposed in $W = W_s + W_d$, where W_s and W_d are, respectively, the static and dynamic portions of the total axial displacement. This static displacement is simply given as

$$W_s = \frac{T_b Z}{EA} + \frac{\gamma_s Z^2}{2EA}, \tag{6.5}$$

which leads to the equations of motion to be written as

$$(\mu + \mu_a)\,\ddot{U} + EIU'''' - ((T_b + \gamma_s Z)\,U')' - EA\left(U'\left(W_d' + \frac{(U')^2}{2} + \frac{(V')^2}{2}\right)\right)' = f_x, \tag{6.6}$$

$$(\mu + \mu_a)\,\ddot{V} + EIV'''' - ((T_b + \gamma_s Z)\,V')' - EA\left(V'\left(W_d' + \frac{(U')^2}{2} + \frac{(V')^2}{2}\right)\right)' = f_y, \tag{6.7}$$

$$\mu\ddot{W}_d - EA\left(W_d' + \frac{(U')^2}{2} + \frac{(V')^2}{2}\right)' = 0. \tag{6.8}$$

The next step is to incorporate the phenomenological model to the structural equations of motion. This process consists of defining new variables, each with its own equation of motion, and how such variables are used to describe the loads f_x and f_y. Three different possibilities are explored in this thesis, one for planar and two for three-dimensional vibrations, each of them being described in the following.

6.1.1 Planar vibrations model

The first model considered is that of planar vibrations of the structure, considering that it is somehow restricted to vibrate only in the Y direction. As a consequence, in this model the in-line displacement is considered as $U = 0$. For the phenomenological model, the one presented in Facchinetti, de Langre & Biolley (2004) is adapted. The model consists of a variable named "wake variable", denoted by q, which obeys a Van der Pol

[1] Such hypothesis must be carefully evaluated according to the structure under investigation. In this thesis the focus lies on very long structures and in the absence of direct torsional loads, which allows the use of the hypothesis. Another possibility of breaking that hypothesis include the cases where internal resonances between torsional and transversal modes occur.

equation with a forcing term proportional to the acceleration of the structure. Herein the wake variable q is considered as a continuous variable along the length of the structure. The only forcing term is then given by

$$f_y = \frac{1}{2}\rho U_\infty^2 D C_L^0 \frac{q}{\overline{q}} - \frac{\overline{C}_D}{4\pi S_t}\omega_s \rho D^2 \dot{V}, \tag{6.9}$$

leading to the equations of motion

$$\begin{aligned}
&(\mu + \mu_a)\ddot{V} + EIV'''' - ((T_b + \gamma_s Z)V')' - EA\left(V'\left(W_d' + \frac{(V')^2}{2}\right)\right)' \\
&+ \frac{\overline{C}_D}{4\pi S_t}\omega_s \rho D^2 \dot{V} = \frac{1}{2}\rho U_\infty^2 D C_L^0 \frac{q}{\overline{q}}, && (6.10)\\
&\mu \ddot{W}_d - EA\left(W_d' + \frac{(V')^2}{2}\right)' = 0, && (6.11)\\
&\ddot{q} + \varepsilon_y \omega_s \left(q^2 - 1\right)\dot{q} + \omega_s^2 q = \frac{A_y}{D}\ddot{V}. && (6.12)
\end{aligned}$$

In the equations, $\overline{C}_D$ is the mean drag coefficient of the cross section, S_t is the Strouhal number, ρ is the specific mass of the surrounding fluid, D is the external diameter of the structure, C_L^0 is the oscillation amplitude of the lift coefficient of a stationary cylinder, $\overline{q} = 2$ is the amplitude of steady-state regime of the Van der Pol oscillator, ω_s is the vortex shedding frequency, while A_y and ε_y are experimentally calibrated coefficients. Some details concerning the adopted model must be mentioned. The first one is that the phenomenological model and its parameters were calibrated for a rigid cylinder mounted on an elastic base. The use of this model for a continuous structure is a stretch of its capabilities and calibration. However, this model is still able to reproduce some qualitative aspects of the phenomenon, which is already considered enough for the objective of this thesis that is to investigate ROMs obtained from a mathematical model written as a system of PDEs. This discussion is retaken in detail in the conclusions.

Giving sequence to the mathematical modelling, Eqs. (6.10) to (6.12) are made dimensionless with some variable definitions. First, the space and time coordinates as well as the displacements are made dimensionless by defining $\xi = Z/\ell$, $\tau = \omega_n t$, $v = V/D$ and $w = W_d/D$. The natural frequency ω_n is the one expected to be excited in the lock-in condition, chosen accordingly to each problem. The definitions for the reduced velocity, $U_r = U_\infty 2\pi/\omega_n D$ and the relation between the natural and shedding frequencies $\omega_s = \omega_n U_r S_t$ are also necessary. With such definitions and some algebraic manipulations, the equations of motion become

$$\ddot{v} + \frac{\rho D^2 \overline{C}_D U_r}{4\pi\left(\mu+\mu_a\right)}\dot{v} + \frac{EIv''''}{\left(\mu+\mu_a\right)\omega_n^2\ell^4} - \frac{\left(T_b+\gamma_s\ell\xi\right)v''}{\left(\mu+\mu_a\right)\omega_n^2\ell^2} - \frac{\gamma_s v'}{\left(\mu+\mu_a\right)\omega_n^2\ell}$$
$$- \frac{EAD\left(w'v''+w''v'+\frac{3D}{2\ell}\left(v'\right)^2 v''\right)}{\left(\mu+\mu_a\right)\omega_n^2\ell^3} = \frac{\rho C_L^0 U_r^2 D^2}{16\pi^2\left(\mu+\mu_a\right)}q, \tag{6.13}$$

$$\ddot{w} - \frac{EA}{\mu\omega_n^2\ell^2}\left(w''+\frac{D}{\ell}v'v''\right) = 0, \tag{6.14}$$

$$\ddot{q} + \epsilon U_r S_t\left(q^2-1\right)\dot{q} + \left(U_r S_t\right)^2 q = A_y\ddot{v}. \tag{6.15}$$

Without loss of comprehensiveness, the dots and primes are kept as indicative of derivatives, but with respect to the dimensionless time and length when dimensionless equations are considered. This system of dimensionless equations can then be solved using different approaches, which will be discussed later in this chapter.

6.1.2 Spatial vibrations with a single wake variable VIV model

In this model, the structure is let free to oscillate in the X direction as well, liberating it to perform 3D motions. In what concerns the phenomenological model, different approaches may be used. In this thesis, a single wake variable is kept and the oscillations of the drag coefficient are not taken into account. This model is incomplete from the phenomenological point of view, since fluctuations of the drag coefficient do occur. Still, this is made without loss of generality of the investigations carried out in this thesis, with further refinements of the phenomenological model itself being left to future works. In order to proceed with this model, the relative velocity between the surrounding fluid and the structure must be properly written, accounting the three-dimensional characteristics of the motion. This is needed in order to write the lift and drag forces and later decompose them in the directions in which the equations of motion are written. Consider then the geometrical description of the involved velocities made in Fig. 75.

Figure 75 – Relative velocity composition

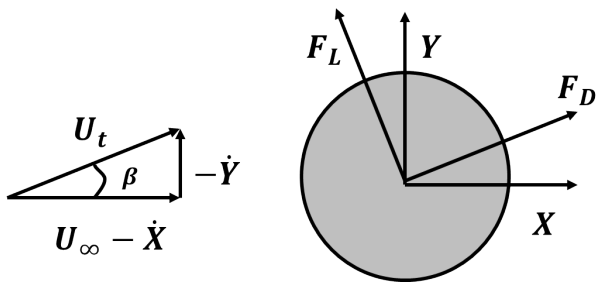

Source: The author.

By performing vectorial algebra over the elements present in Fig. 75, it is possible to obtain that

$$\cos\beta = \frac{U_\infty - \dot{U}}{U_t}, \tag{6.16}$$

$$\sin\beta = \frac{-\dot{V}}{U_t}, \tag{6.17}$$

$$U_t = \sqrt{\left(U_\infty - \dot{U}\right)^2 + \dot{V}^2}. \tag{6.18}$$

Using classical expressions for the drag and lift forces, it is then possible to write f_x and f_y as

$$f_x = \frac{1}{2}\rho U_t^2 D\left(-C_L \sin\beta + C_D \cos\beta\right), \tag{6.19}$$

$$f_y = \frac{1}{2}\rho U_t^2 D\left(C_L \cos\beta + C_D \sin\beta\right). \tag{6.20}$$

The lift and drag coefficients in Eqs. (6.19) and (6.20) are written in generic form. When the particular model herein adopted is considered, they are respectively given as $C_L = C_L^0 q/\overline{q}$ and $C_D = \overline{C}_D$. With the hydrodynamic forces defined, the equations of motion are given by

$$\begin{aligned}&(\mu+\mu_a)\ddot{U} + EIU'''' - \left((T_b+\gamma_s Z)U'\right)' - EA\left(U'\left(W_d' + \frac{(U')^2}{2} + \frac{(V')^2}{2}\right)\right)' \\ &= \frac{1}{2}\rho D\sqrt{\left(U_\infty - \dot{U}\right)^2 + \dot{V}^2}\left(C_L\dot{V} + C_D\left(U_\infty - \dot{U}\right)\right),\end{aligned} \tag{6.21}$$

$$\begin{aligned}&(\mu+\mu_a)\ddot{V} + EIV'''' - \left((T_b+\gamma_s Z)V'\right)' - EA\left(V'\left(W_d' + \frac{(U')^2}{2} + \frac{(V')^2}{2}\right)\right)' \\ &= \frac{1}{2}\rho D\sqrt{\left(U_\infty - \dot{U}\right)^2 + \dot{V}^2}\left(C_L\left(U_\infty - \dot{U}\right) - C_D\dot{V}\right),\end{aligned} \tag{6.22}$$

$$\mu\ddot{W}_d - EA\left(W_d' + \frac{(U')^2}{2} + \frac{(V')^2}{2}\right)' = 0, \tag{6.23}$$

$$\ddot{q} + \varepsilon_y\omega_s\left(q^2 - 1\right)\dot{q} + \omega_s^2 q = \frac{A_y}{D}\ddot{V}. \tag{6.24}$$

The presence of the square roots in the forcing terms is an issue for the subsequent definition of ROMs, since it would require them to be evaluated at each time-step of simulation. As a simplification, the square roots are expanded in series so the resulting expressions for the forcing terms are correct up to first order. This is done so the resulting model is analogous to the one used for the planar vibrations and can have the necessary

integrals of the Galerkin projection to be evaluated only once. It is important to mention now that the nonlinearity simplified by this procedure is the Morison term[2]. The reader may recall that this term is of fundamental importance in the definition of the steady-state regime in the case of parametric excitations, and it is known that its linear form cannot represent this qualitative behaviour. In the case now at hand, however, the steady-state regime is ensured by the coupling with the Van der Pol equation, with the impact of the Morison term on its full form being more of a quantitative than a qualitative importance. Using the proposed expansion, it then follows that

$$(\mu+\mu_a)\ddot{U}+EIU''''-((T_b+\gamma_s Z)U')'-EA\left(U'\left(W_d'+\frac{(U')^2}{2}+\frac{(V')^2}{2}\right)\right)'=$$
$$\frac{\rho D\overline{C}_D U_\infty^2}{2}-\rho D\overline{C}_D U_\infty\dot{U}, \tag{6.25}$$
$$(\mu+\mu_a)\ddot{V}+EIV''''-((T_b+\gamma Z)V')'-EA\left(V'\left(W_d'+\frac{(U')^2}{2}+\frac{(V')^2}{2}\right)\right)'=$$
$$\frac{\rho DC_L^0 U_\infty^2 q}{4}-\frac{\rho D\overline{C}_D U_\infty\dot{V}}{2}, \tag{6.26}$$
$$\mu\ddot{W}_d-EA\left(W_d'+\frac{(U')^2}{2}+\frac{(V')^2}{2}\right)'=0, \tag{6.27}$$
$$\ddot{q}+\varepsilon_y\omega_s\left(q^2-1\right)\dot{q}+\omega_s^2 q=\frac{A_y}{D}\ddot{V}. \tag{6.28}$$

Now, recalling the dimensionless variables $\xi=Z/\ell$, $\tau=\omega_n t$, $v=V/D$ and $w=W_d/D$, with the inclusion of $u=U/D$, the equations of motion can be written as

$$\ddot{u}+\frac{\rho D^2\overline{C}_D U_r}{2\pi(\mu+\mu_a)}\dot{u}+\frac{EIu''''}{(\mu+\mu_a)\omega_n^2\ell^4}-\frac{(T_b+\gamma_s\ell\xi)u''}{(\mu+\mu_a)\omega_n^2\ell^2}-\frac{\gamma_s u'}{(\mu+\mu_a)\omega_n^2\ell}$$
$$-\frac{EAD\left(w'u''+w''u'+\frac{D}{2\ell}\left(3(u')^2u''+2v'v''u'+(v')^2u''\right)\right)}{(\mu+\mu_a)\omega_n^2\ell^3}=\frac{\rho D^2\overline{C}_D U_r^2}{8\pi^2(\mu+\mu_a)}, \tag{6.29}$$
$$\ddot{v}+\frac{\rho D^2\overline{C}_D U_r}{4\pi(\mu+\mu_a)}\dot{v}+\frac{EIv''''}{(\mu+\mu_a)\omega_n^2\ell^4}-\frac{(T_b+\gamma_s\ell\xi)v''}{(\mu+\mu_a)\omega_n^2\ell^2}-\frac{\gamma_s v'}{(\mu+\mu_a)\omega_n^2\ell}$$
$$-\frac{EAD\left(w'v''+w''v'+\frac{D}{2\ell}\left(2u'u''v'+(u')^2v''+3(v')^2v''\right)\right)}{(\mu+\mu_a)\omega_n^2\ell^3}=\frac{\rho C_L^0 U_r^2 D^2}{16\pi^2(\mu+\mu_a)}q, \tag{6.30}$$
$$\ddot{w}-\frac{EA}{\mu\omega_n^2\ell^2}\left(w''+\frac{D}{\ell}(u'u''+v'v'')\right)=0, \tag{6.31}$$
$$\ddot{q}+\varepsilon_y U_r S_t\left(q^2-1\right)\dot{q}+(U_r S_t)^2 q=A_y\ddot{v}. \tag{6.32}$$

Notice that the terms from the phenomenological model in Eq. (6.30) are exactly the same as the ones in Eq. (6.13).

[2] This is recognized by noticing that for a generic function f it results that $f\sqrt{f^2}=f|f|$.

6.1.3 Spatial vibrations with two wake variables VIV model

Finally, a model with two DOF to represent the wake dynamics is presented. This model is an extension of the one present in Franzini & Bunzel (2018) to the continuum, in the same fashion as it was made for the one DOF case. Now, the drag coefficient can be modelled in accordance with its observed physical behaviour. Naming q_y the variable for the wake in the Y direction and q_x the analogous in the X direction. The lift and drag coefficients are then given as

$$C_L = C_L^0 \frac{q_y}{\overline{q}_y} = C_L^0 \frac{q_y}{2}, \tag{6.33}$$

$$C_D = \overline{C}_D + C_D^0 \frac{q_x}{\overline{q}_x} = \overline{C} + C_D^0 \frac{q_x}{2}. \tag{6.34}$$

For this case, Eqs. (6.21) to (6.24) are still valid to model the structure, however, a new oscillator must be added to the system, given by

$$\ddot{q}_x + 2\varepsilon_x \omega_s \left(q^2 - 1\right) \dot{q}_x + (2\omega_s)^2 q_x = \frac{A_x}{D} \ddot{U}. \tag{6.35}$$

Expanding the square roots in polynomial series and keeping in the equation only the resulting linear terms, the equations of motion can be written as

$$(\mu + \mu_a)\ddot{U} + EIU'''' - ((T_b + \gamma_s Z)U')' - EA\left(U'\left(W_d' + \frac{(U')^2}{2} + \frac{(V')^2}{2}\right)\right)' = \frac{\rho D \overline{C}_D U_\infty^2}{2} + \frac{\rho D C_D^0 U_\infty^2 q_x}{4} - \rho D \overline{C}_D U_\infty \dot{U}, \tag{6.36}$$

$$(\mu + \mu_a)\ddot{V} + EIV'''' - ((T_b + \gamma_s Z)V')' - EA\left(V'\left(W_d' + \frac{(U')^2}{2} + \frac{(V')^2}{2}\right)\right)' = \frac{\rho D C_L^0 U_\infty^2 q_y}{4} - \frac{\rho D \overline{C}_D U_\infty \dot{V}}{2}, \tag{6.37}$$

$$\mu \ddot{W}_d - EA\left(W_d' + \frac{(U')^2}{2} + \frac{(V')^2}{2}\right)' = 0, \tag{6.38}$$

$$\ddot{q}_y + \varepsilon_y \omega_s \left(q_y^2 - 1\right) \dot{q}_y + \omega_s^2 q_y = \frac{A_y}{D} \ddot{V}, \tag{6.39}$$

$$\ddot{q}_x + 2\varepsilon_x \omega_s \left(q_x^2 - 1\right) \dot{q}_x + (2\omega_s)^2 q_x = \frac{A_y}{D} \ddot{U}. \tag{6.40}$$

Using now the dimensionless variables already defined, the equations of motion can be rewritten as

$$\ddot{u} + \frac{\rho D^2 \overline{C}_D U_r}{2\pi\left(\mu+\mu_a\right)}\dot{u} + \frac{EIu''''}{\left(\mu+\mu_a\right)\omega_n^2\ell^4} - \frac{\left(T_b+\gamma_s\ell\xi\right)u''}{\left(\mu+\mu_a\right)\omega_n^2\ell^2} - \frac{\gamma_s u'}{\left(\mu+\mu_a\right)\omega_n^2\ell}$$
$$\frac{-EAD\left(w'u''+w''u'+\frac{D}{2\ell}\left(3\left(u'\right)^2u''+2v'v''u'+\left(v'\right)^2u''\right)\right)}{\left(\mu+\mu_a\right)\omega_n^2\ell^3} = F_0 + \frac{\rho D^2 U_r^2 C_D^0 q_x}{16\pi^2\left(\mu+\mu_a\right)}, \tag{6.41}$$

$$\ddot{v} + \frac{\rho D^2 \overline{C}_D U_r}{4\pi\left(\mu+\mu_a\right)}\dot{v} + \frac{EIv''''}{\left(\mu+\mu_a\right)\omega_n^2\ell^4} - \frac{\left(T_b+\gamma_s\ell\xi\right)v''}{\left(\mu+\mu_a\right)\omega_n^2\ell^2} - \frac{\gamma_s v'}{\left(\mu+\mu_a\right)\omega_n^2\ell}$$
$$-\frac{EAD\left(w'v''+w''v'+\frac{D}{2\ell}\left(2u'u''v'+\left(u'\right)^2v''+3\left(v'\right)^2v''\right)\right)}{\left(\mu+\mu_a\right)\omega_n^2\ell^3} = \frac{\rho C_L^0 U_r^2 D^2}{16\pi^2\left(\mu+\mu_a\right)}q_y, \tag{6.42}$$

$$\ddot{w} - \frac{EA}{\mu\omega_n^2\ell^2}\left(w'' + \frac{D}{\ell}\left(u'u''+v'v''\right)\right) = 0, \tag{6.43}$$

$$\ddot{q}_y + \varepsilon_y U_r S_t\left(q_y^2-1\right)\dot{q}_y + \left(U_r S_t\right)^2 q_y = A_y\ddot{v}, \tag{6.44}$$

$$\ddot{q}_x + 2\varepsilon_x U_r S_t\left(q_x^2-1\right)\dot{q}_x + \left(2U_r S_t\right)^2 q_x = A_x\ddot{u}. \tag{6.45}$$

The constant drag force per unit length F_0 is given by

$$F_0 = \frac{\rho D^2 U_r^2 \overline{C}_D}{8\pi^2\left(\mu+\mu_a\right)}. \tag{6.46}$$

With this, the definition of continuous models in the scope of this research is complete.

6.2 Definition of Reduced-order models for vertical beams under vortex-induced vibrations

The next step of the investigation is the definition of ROMs for the analysis of the problem at hand. In this research, they are obtained by using a Galerkin projection on the equations of motion. Observing Eqs. (6.29) and (6.30), it is possible to see that the equations in the directions X and Y have the same mathematical structure. With that in mind, the investigation concerning the quality of different ROMs is made for the case of planar motion for simplicity. To that end, let four different ROMs to be conceived, differing from each other by the set of functions as projection basis for the transversal motion. Again, the advantage of more complex functions over simpler ones is investigated. Recalling that the Bessel-like functions given in Mazzilli, Lenci & Demeio (2014) are a good approximation for the transversal vibration modes of vertical structures under a tension that varies linearly in the structural length, two of the ROMs are conceived with

such functions. Let then ROM(i) be written in terms of a single Bessel-like function, while ROM(ii) uses three of such functions. In addition, as made for the case of parametric excitations, let ROM(iii) and ROM(iv) to be written in terms of trigonometric functions, with the former using one function and the latter using three. In what concerns the axial direction, a single trigonometric function is used in all the ROMs. Notice that the axial vibration modes are actually given by sine functions.

The question that now arises is how to define a projection function for the wake-variable. Recalling that VIV is a resonant phenomenon and that an oscillator synchronism exist between the structural motion and the vortex shedding in the lock-in condition, a reasonable trial is to use for the wake-variable the same projection as for the transversal motion. With all the basis defined, the trial expansion for the Galerkin projection is given as

$$u(\xi,\tau) = \phi(\xi)\, w_1(\tau)\,, \tag{6.47}$$

$$v(\xi,\tau) = \sum_i \psi_i(\xi)\, v_i(\tau)\,, \tag{6.48}$$

$$q(\xi,\tau) = \sum_i \psi_i(\xi)\, q_i(\tau)\,. \tag{6.49}$$

Where ϕ_i and ψ_i are the projection functions for the axial and transversal directions respectively. With some algebraic work the ROMs with a single function in the transversal direction can be written as

$$\ddot{w}_1 + \alpha_1 w_1 + \alpha_2 v_1^2 = 0, \tag{6.50}$$

$$\ddot{v}_1 + U_r\beta_1\dot{v}_1 + \beta_2 v_1 + \beta_3 w v_1 + \beta_4 v_1^3 + U_r^2\beta_5 q_1 = 0, \tag{6.51}$$

$$\ddot{q}_1 + U_r\zeta_1\dot{q}_1 + U_r\zeta_2 q_1^2\dot{q}_1 + U_r^2\zeta_3 q_1 + \zeta_4\ddot{v}_1 = 0, \tag{6.52}$$

with α_j, β_j and ζ_j being constants resulting from the projection integrals, with different values accordingly to each ROM. In the sequel, the ROMs for the cases of three different functions in the transversal direction composing the displacement field can be written in the form

$$\ddot{w} + \alpha_{1,1}w + \alpha_{1,2}v_1^2 + \alpha_{1,3}v_2^2 + \alpha_{1,4}v_3^2 + \alpha_{1,5}v_1v_2 + \alpha_{1,6}v_1v_3 + \alpha_{1,7}v_2v_3 = 0, \tag{6.53}$$

$$\begin{aligned}
&\ddot{v}_i + U_r\beta_{i,1}\dot{v}_i + \beta_{i,2}v_1 + \beta_{i,3}v_2 + \beta_{i,4}v_3 + \beta_{i,5}v_1^3 + \beta_{i,6}v_1^2v_2 + \beta_{i,7}v_1^2v_3 + \beta_{i,8}v_1v_2^2 \\
&+ \beta_{i,9}v_1v_2v_3 + \beta_{i,10}v_1v_3^2 + \beta_{i,11}v_2^3 + \beta_{i,12}v_2^2v_3 + \beta_{i,13}v_2v_3^2 + \beta_{i,14}v_3^3 + \beta_{i,15}wv_1 \\
&+ \beta_{i,16}wv_2 + \beta_{i,17}wv_3 + U_r^2\beta_{i,18}q_i = 0,
\end{aligned} \tag{6.54}$$

$$\begin{aligned}
&\ddot{q}_i + U_r\zeta_{i,1}\dot{q}_i + U_rq_1^2\left(\zeta_{i,2}\dot{q}_1 + \zeta_{i,3}\dot{q}_2 + \zeta_{i,4}\dot{q}_3\right) + U_rq_2^2\left(\zeta_{i,5}\dot{q}_1 + \zeta_{i,6}\dot{q}_2 + \zeta_{i,7}\dot{q}_3\right) \\
&+ U_rq_3^2\left(\zeta_{i,8}\dot{q}_1 + \zeta_{i,9}\dot{q}_2 + \zeta_{i,10}\dot{q}_3\right) + U_rq_1q_2\left(\zeta_{i,11}\dot{q}_1 + \zeta_{i,12}\dot{q}_2 + \zeta_{i,13}\dot{q}_3\right) \\
&+ U_rq_1q_3\left(\zeta_{i,14}\dot{q}_1 + \zeta_{i,15}\dot{q}_2 + \zeta_{i,16}\dot{q}_3\right) + U_rq_2q_3\left(\zeta_{i,17}\dot{q}_1 + \zeta_{i,18}\dot{q}_2 + \zeta_{i,19}\dot{q}_3\right) \\
&+ U_r^2\zeta_{i,20}q_i + \zeta_{i,21}\ddot{v}_i = 0,
\end{aligned} \tag{6.55}$$

with the index i varying from 1 to 3 to form the complete set of ODEs.

In order to evaluate the quality of each of the ROMs, they are integrated using a fourth order Runge-Kutta scheme, using the native ode45 function in Matlab. A reference condition to serve as comparison base for the results is obtained with a finite difference scheme applied at the continuum equations of motion. Central differences are used in both space and time discretization and the first two time-steps are given to the simulation in order to obtain an explicit linear scheme. The structural properties of a real riser, extracted from Sparks (2002), are presented in table 24. The parameters and properties required for the wake-oscillator are presented in Tab. 25. These parameters are the ones used in all the examples from now on, with any minor change being explicitly mentioned.

Table 24 – Structural properties of a flexible riser.

Property	Value
$(\mu + \mu_a)$	1200 kg/m
EI	318.6×10^6 Nm^2
γ_s	3433.5 N/m
EA	8541.8×10^6 N
L	2000 m
D	0.5588 m
T_b	633000 N

Table 25 – Properties for the fluid-structure interaction model adapted from Franzini & Bunzel (2018).

Property	Value
ρ	1025 kg/m^3
$\overline{C}_D$	1.1856
C_L^0	0.3842
S_t	0.1932
ε_y	0.05
A_y	4

The first comparison made is for the natural frequency obtained with each ROM. To this end, a reference obtained with the finite element method (FEM) using Giraffe is also presented. The natural frequencies for the first three modes are shown in Tab. 26. It is possible to verify that there is a very good agreement between the ROMs using Bessel-like projection functions with the reference. It can also be seen that the ROMs based on trigonometric functions have some discrepancy with the reference case, achieving a relative difference of more than 10% for the frequency of the third mode.

Table 26 – Natural frequencies obtained for the modelled structure.

Mode	Model	Frequency (rad/s)
1	FEM	0.0788
1	ROM(i)	0.0786
1	ROM(ii)	0.0786
1	ROM(iii)	0.0914
1	ROM(iv)	0.0809
2	FEM	0.1598
2	ROM(ii)	0.1594
2	ROM(iv)	0.1692
3	FEM	0.2408
3	ROM(ii)	0.2402
3	ROM(iv)	0.2864

The next comparison made concerns the amplitude of response curve as function of the reduced velocity U_r. This comparison is of fundamental importance for the VIV analysis. In Fig. 76, the amplitude of response curves are shown for all the models, including the finite difference reference, labelled “reference” in the figures from now on. In Fig. 77, only the ROMs with one projection function in the transversal direction are shown together with the reference. Finally, in Fig. 78, the ROMs with three projection functions in the transversal direction are shown together with the results obtained with the finite differences method.

Figure 76 – Amplitude of steady-state response as function of the reduced velocity for different models. For the reference model, the motion of the point of maximum displacement according to the locked-in mode is considered.

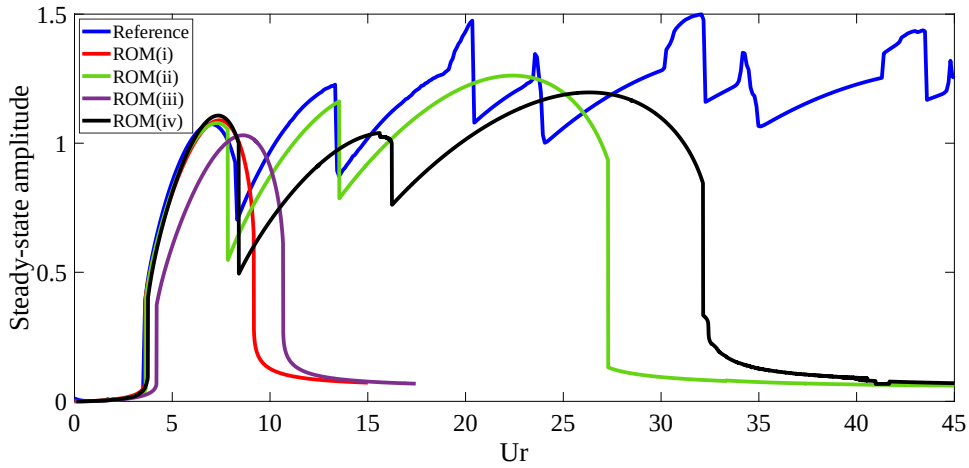

Source: The author.

Figure 77 – Amplitude of steady-state response as function of the reduced velocity for different models.

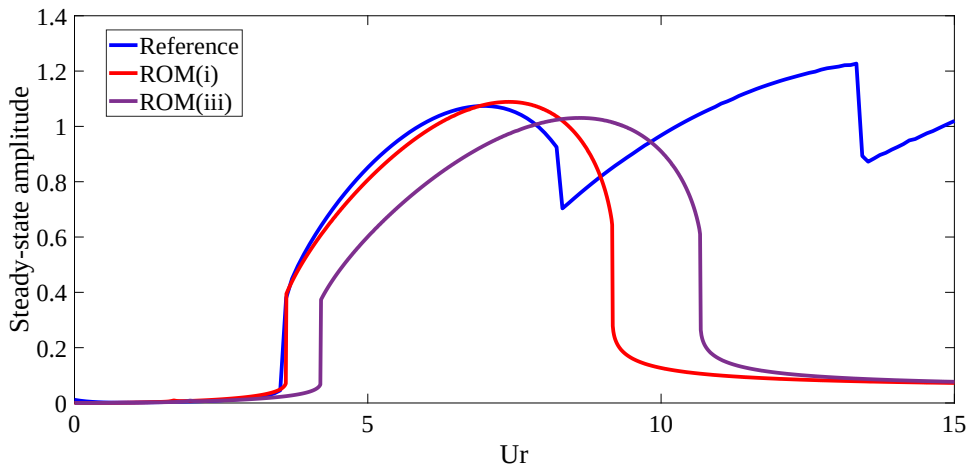

Source: The author.

It is possible to see that the models based on Bessel-like functions are the ones with better agreement. ROM(iv) has a good agreement in the lock-in of the first mode only, but a similar quality can be achieved with ROM(i) with a single projection function in the transversal direction. It is also possible to notice that the use of the same projection function for the transversal motion and the wake variable seems adequate. Another characteristic that is easily visible is that the ROMs have a maximum reduced velocity up to which they produce suitable results. This is expected since greater values of U_r result in lock-in within higher modes, not contained within the projection basis adopted. This highlights the

Figure 78 – Amplitude of steady-state response as function of the relative velocity for different models.

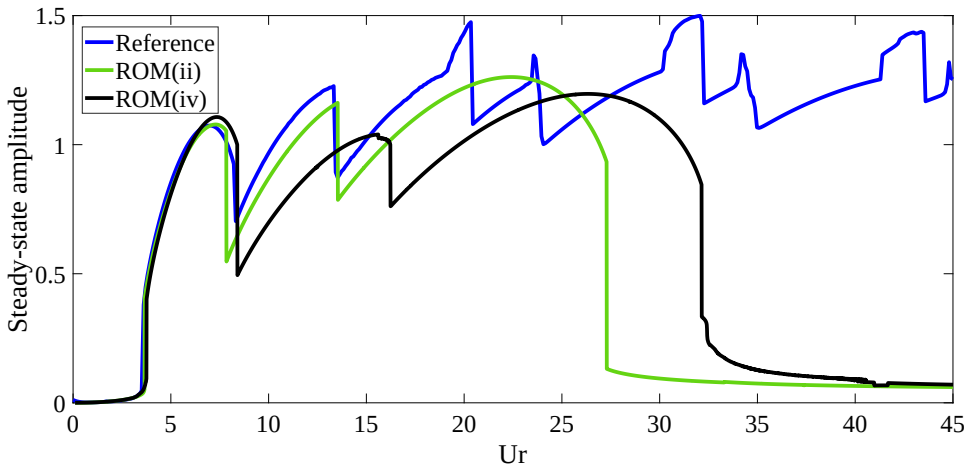

Source: The author.

importance of defining beforehand the expected range of solicitation in order to conceive smaller ROMs. Another feature present in the reference solution are "spikes" of amplitude in certain narrow bands of U_r. To clarify why this happens further analysis are carried-out.

Considering the clear disadvantage of using the trigonometric functions in the projection for this case, the next analysis are carried out only with ROMs (i) and (ii). Focus is made in the transition zones of response, near amplitude jumps. To that end, consider the range of reduced velocities shown in Fig. 79. In the figure, four values of U_r are also indicated by black vertical lines, being them $U_r = 8.6$, $U_r = 20.6$, $U_r = 22.0$ and $U_r = 25.0$. A more detailed investigation is now carried for such values.

Beginning with the case of $U_r = 8.6$, the analysis is made by means of the spectral content of the response obtained by the different models. The spectral content of the response obtained with ROMs (i) and (ii), as well as for the reference solution, can be seen in Fig. 80.

By checking the values in Tab. 26, it is possible to see that the natural frequencies of the structure follow an almost linear relation with the mode number. That said, the spectral content in Fig. 80 clearly shows that, for $U_r = 8.6$, both ROM (ii) and the reference solution obtain a response concentrated on the second mode of vibration. This mode is not included in ROM (i), which is then unable to predict the dominance of the lock-in of the second mode over that of the first mode. This however does not diminish the value of ROM (i), since, as it can be seen in detail in Fig. 77, this model is able to give a good prediction of the structural response on the entire region where the first mode response dominates the dynamics. In a design scenario where such a region is of interest, this ROM is clearly suitable for analysis.

Figure 79 – Amplitude of steady-state response as function of the relative velocity for different models. For the reference model, the motion of the point of maximum displacement according to the locked-in mode is considered.

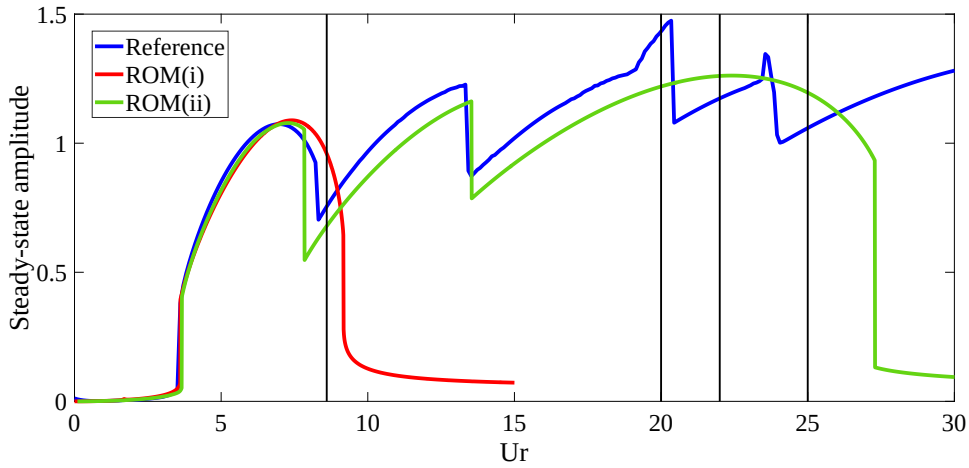

Source: The author.

Figure 80 – Spectrum components comparison between different models for $U_r = 8.6$.

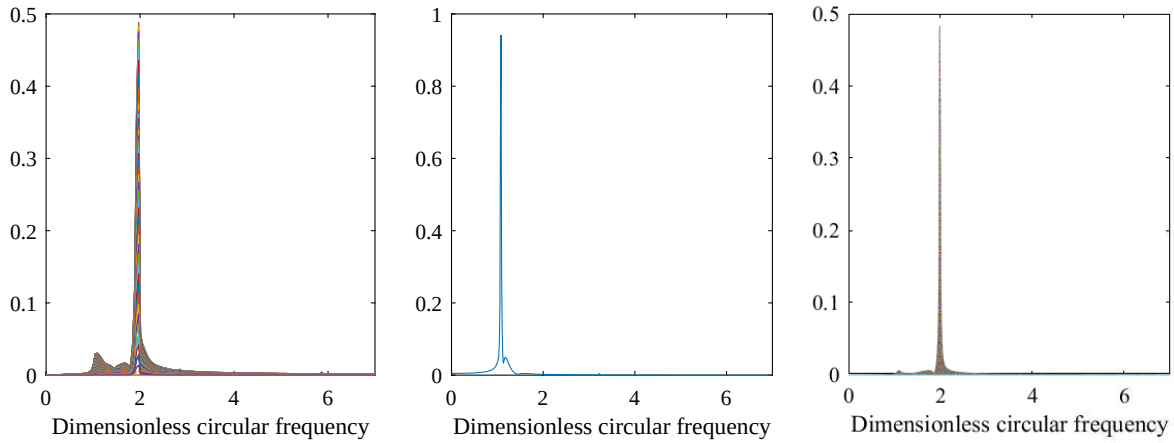

(a) Finite differences. (b) ROM (i). (c) ROM (ii).

Source: The author.

Another feature present in the spectral content is the apparent filtering of frequencies in the ROMs results. This is likely due to the adoption of the same projection functions for the transversal displacements and the wake variable, whereas in the reference solution the wake variable can give responses as governed by its ruling equation without spatial shape restrictions. This filtering in the response frequency is also able to justify the difference that exists between the reference and ROM (ii) in terms of the steady-state amplitude.

Following, the case of $U_r = 20$ is investigated, where the first spike in the amplitude response can be noticed in the reference solution, while the ROM is unable to recover such

behaviour. The spectral content of the responses given by the reference and ROM (ii) are shown in Fig. 81.

Figure 81 – Spectrum components comparison between different models for $U_r = 20$.

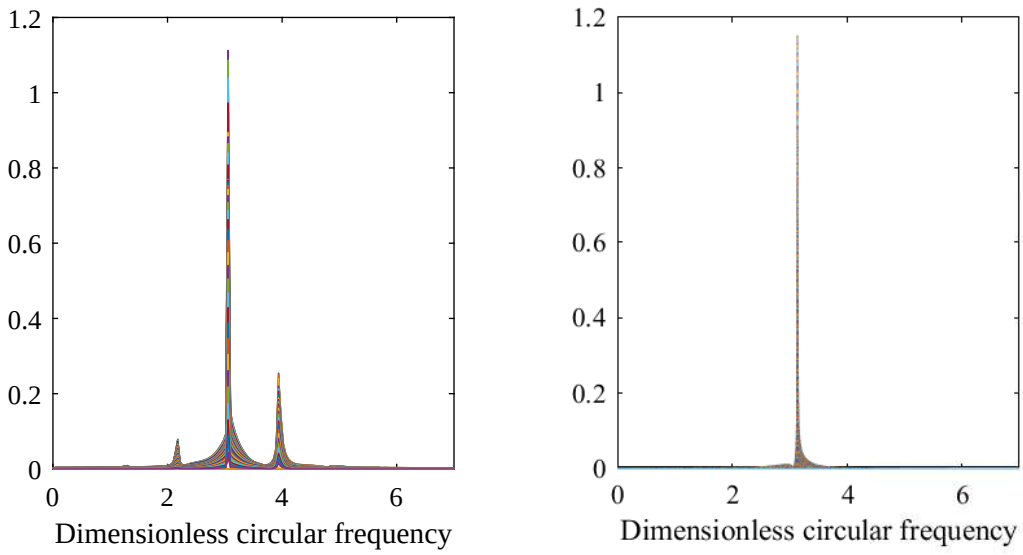

(a) Finite differences. (b) ROM (ii).

Source: The author.

In this case, two aspects deserve attention. The first one is that, in the reference solution, a significant contribution from the fourth mode of vibration is present. This is one of the factors that contributes to the discrepancy of the ROM, since the latter does not possess the fourth mode in its conception. The second aspect is that there is some contribution of the second mode in the reference solution that is not present in the ROM solution, even though the ROM possess the second mode on its basis. This exhibits again the filtering behaviour of the conceived ROMs, which in turn shows that such spikes in the amplitude response cannot be recovered by them, at least using the projection basis herein defined. Complementing this analysis, consider the phase space diagram in Fig. 82. It is interesting to notice that, although ROM (ii) is unable to capture the multi-frequency response, it obtained a trajectory that is close to the average between both limits of the torus developed by the reference solution.

Finally, Figs. 83 and 84 illustrate the limitation of ROM (ii) in obtaining frequencies of modes that are higher than the ones used in the projections functions of its basis, as expected. It is noteworthy however, that in both cases the ROM is able to furnish a good estimate of the steady-state amplitude.

Another interesting phenomenon to point out is what happens to the reconstitution of the displacement field along the entire structure using the results furnished by the ROMs when evaluations are made moving outside their ideal range of application. To that

Figure 82 – Phase-space comparison between different models for $U_r = 20$. For the reference model, the motion of the point of maximum displacement according to the locked-in mode is considered.

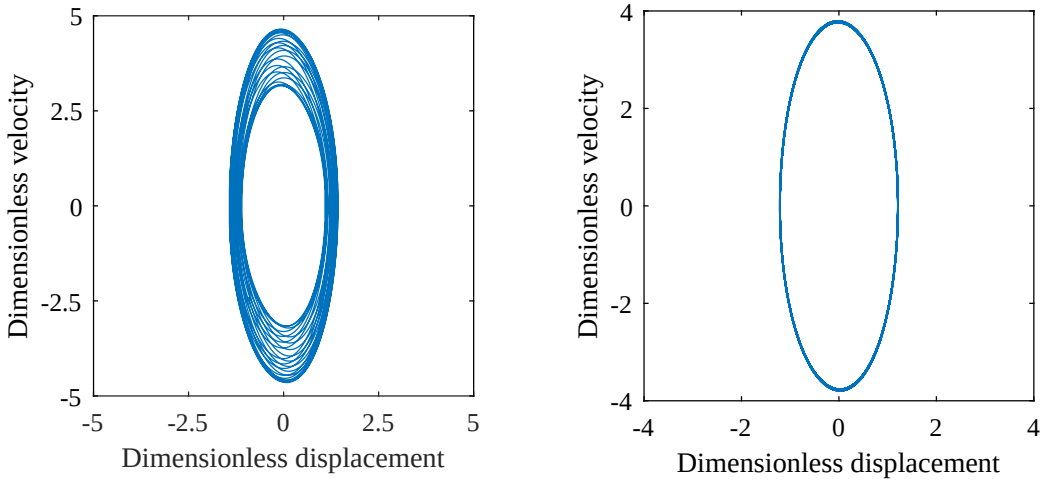

(a) Finite differences. (b) ROM (ii).

Source: The author.

Figure 83 – Spectrum components comparison between different models for $U_r = 22$.

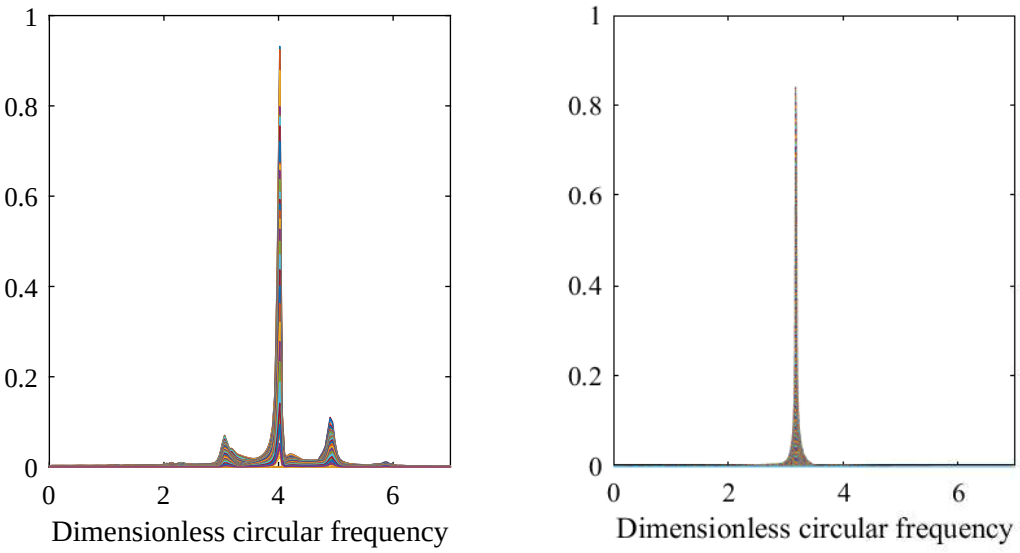

(a) Finite differences. (b) ROM (ii).

Source: The author.

end, the displacement field at $U_r = 25$ is shown in Fig. 85 for the reference solution and for ROMs (ii) and (iv).

As it can be seen, although none of the ROMs (ii) or (iv) can recover the correct displacement field for that mode in lock-in, ROM (iv) also presents a more serious qualitative problem. While ROM (ii) presents the largest displacement near the bottom of the structure, in agreement with the reference and with what is expected from the problem

Figure 84 – Spectrum components comparison between different models for $U_r = 25$.

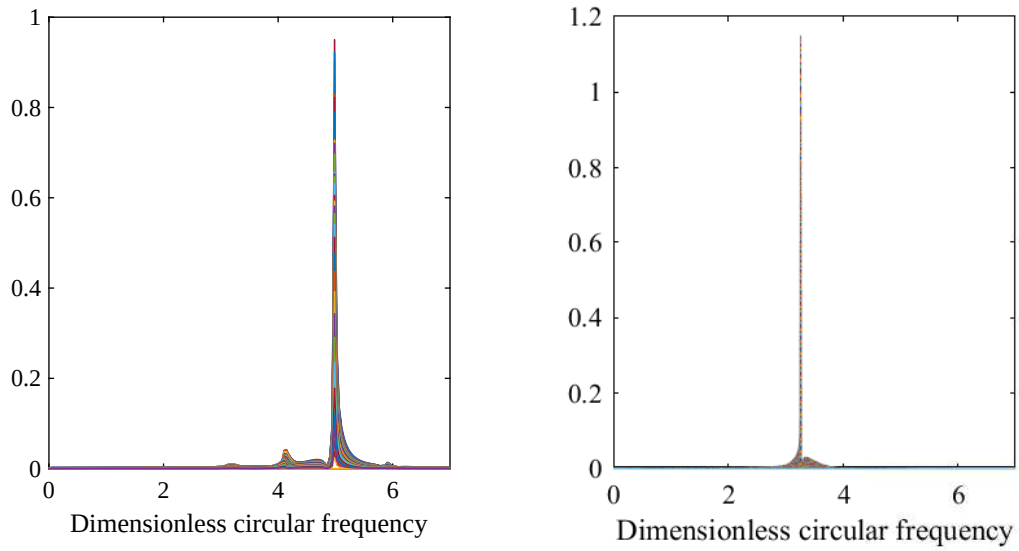

(a) Finite differences. (b) ROM (ii).

Source: The author.

Figure 85 – Comparison of displacement field obtained with different models for $U_r = 25$. Snapshots taken with 1/24 of the response period as sampling.

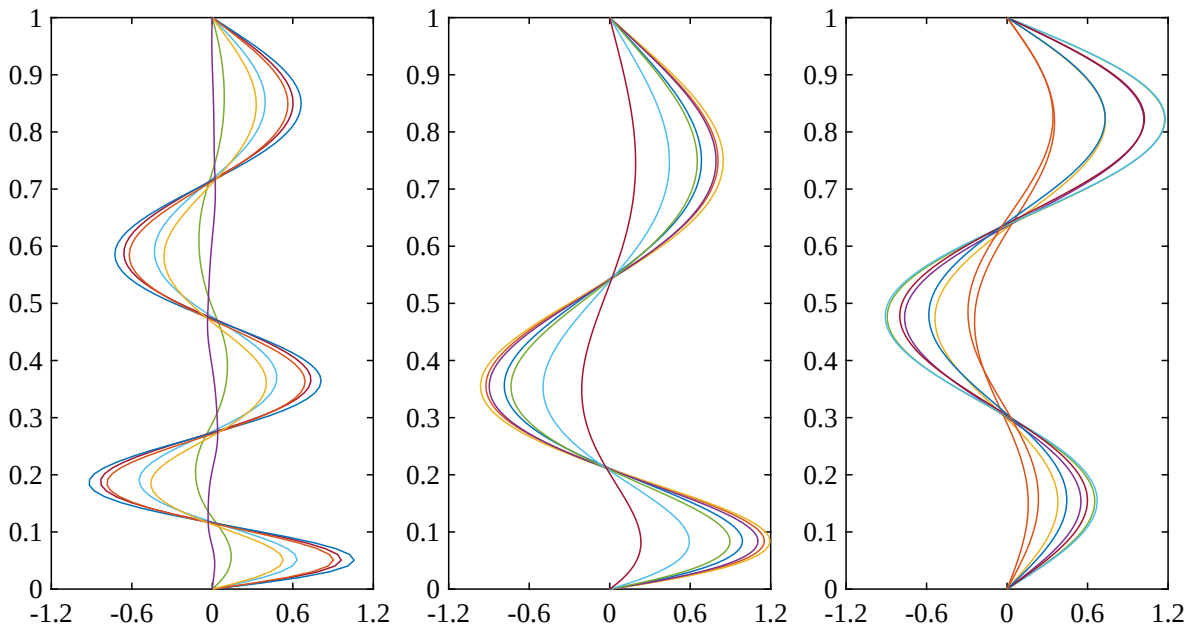

(a) Finite differences. (b) ROM (ii). (c) ROM (iv).

Source: The author.

since the tension is smaller at the bottom, ROM (iv) brings an inverse result, with larger displacements near the top. This indicates another advantage in the use of more detailed projection functions, that is, the range in which its results may be somewhat stretched. This can be done since some qualitative aspects of the displacement field are still kept by

ROM (ii), with a steady-state amplitude that is not far from the actual response. Care, however, must be taken with the frequency, specially for fatigue analysis, highlighting the importance for the analyst to know beforehand the limitations of the ROMs in use.

With all the results presented so far, some considerations can be made about the use of ROMs for flexible structures undergoing VIV. First of all, the idea of a ROM is to use the smallest possible number of DOFs without significant quality loss in the obtained solution when compared to a reference. As the results show, this is possible by adopting even only one or a small number of projection functions close to the modes that are in lock-in, as long as care is taken to adequately choose the modes to be in the projection according to the expected reduced velocities to be relevant for the evaluated scenario. Following, the actual modes of vibration are better than approximations with trigonometric functions, not just from a quantitative point of view but also the qualitative behaviour of the structure, even in the cases where their geometrical difference is small. This conclusion was already made for the case of parametric excitations, reinforcing that it is a behaviour of trying to input a shape function that does not obey the mathematical structure of the represented problem.

Another important detail concerns the case in which the free stream velocity varies with the depth. In such condition, multiple modes can be excited together, and for a good representation of the ROM all of the modes of interest must be incorporated.

6.3 Analysis of planar VIV with invariant manifolds

In possession of a minimal ROM that can furnish good results in qualitative and quantitative terms for the represented mode, further mathematical treatment is now made in order to reduce even further the number of DOFs in the problem. To this end, the NNMs as defined in Shaw & Pierre (1993) are sought for the system of ODEs describing the ROM, with the intention of reducing the number of DOFs from 3 to 1 for the planar case. The task at hand is not simple, with some key mathematical difficulties in the process. The discussion in this section starts with trials to obtain the manifolds that represent the NNMs using polynomial expansions, as proposed in Shaw & Pierre (1993).

6.3.1 The limitation of polynomial expressions for the manifolds

The use of polynomial series to obtain invariant manifolds that can represent the NNMs of the problem at hand is a very attractive idea due to the apparent simplicity of proceeding in that manner. This strategy is the one followed in Shaw & Pierre (1993) and it allows to obtain the solution using a step-by-step procedure. The idea is to solve the coefficients for the linear part of the manifold equations, then use these results to compute the coefficients of the quadratic terms, and so on for cubic and higher-order

terms. Another advantage is that, from an algebraic point of view, polynomials are easier to handle than other types of mathematical terms such as exponentials or trigonometric functions. In order to investigate this approach, first the equations of motion of the ROM for the planar model with one DOF for the VIV in dimensionless form are recalled (Eqs. (6.50) to (6.52)), being given as

$$\ddot{w}_1 + \alpha_1 w_1 + \alpha_2 v_1^2 = 0, \tag{6.56}$$

$$\ddot{v}_1 + U_r\beta_1\dot{v}_1 + \beta_2 v_1 + \beta_3 w_1 v_1 + \beta_4 v_1^3 + U_r^2\beta_5 q_1 = 0, \tag{6.57}$$

$$\ddot{q}_1 + U_r\zeta_1\dot{q}_1 + U_r\zeta_2 q_1^2\dot{q}_1 + U_r^2\zeta_3 q_1 + \zeta_4\ddot{v}_1 = 0. \tag{6.58}$$

To simplify this first investigation, the axial dynamics is disregarded, leading to

$$\ddot{v}_1 + U_r\beta_1\dot{v}_1 + \beta_2 v_1 + \beta_4 v_1^3 + U_r^2\beta_5 q_1 = 0, \tag{6.59}$$

$$\ddot{q}_1 + U_r\zeta_1\dot{q}_1 + U_r\zeta_2 q_1^2\dot{q}_1 + U_r^2\zeta_3 q_1 + \zeta_4\ddot{v}_1 = 0. \tag{6.60}$$

Now, the auxiliary variables r and s are defined as $v_1 = r$, $\dot{v}_1 = s$, together with the functional representation $q_1 = R(r,s)$ and $\dot{q}_1 = S(r,s)$. Using the chain rule for derivatives and the equation of motion for q_1, it is possible to obtain the differential equations that define the geometry of the manifolds represented by R and S as

$$\begin{aligned} S = {} & \frac{\partial R}{\partial r}s + \frac{\partial R}{\partial s}\left(-U_r\beta_1 s - \beta_2 r - \beta_4 r^3 - U_r^2\beta_5 R\right), \\ & - U_r\zeta_1 S - U_r\zeta_2 R^2 S - U_r^2\zeta_3 R - \zeta_4\left(-U_r\beta_1 s - \beta_2 r - \beta_4 r^3 - U_r^2\beta_5 R\right) \end{aligned} \tag{6.61}$$

$$= \frac{\partial S}{\partial r}s + \frac{\partial S}{\partial s}\left(-U_r\beta_1 s - \beta_2 r - \beta_4 r^3 - U_r^2\beta_5 R\right). \tag{6.62}$$

In order to proceed with the investigation, it is considered the value $U_r = 6$ as example, which is around the first peak of lock-in for VIV. For the solution of the manifold equations, trials with two different polynomial expansions are made, one up to cubic order terms and the other up to fifth-order terms. The expressions for the manifolds of the two modes (indicated by indexes 1 and 2 near the manifold variable from now on) obtained with a cubic series are presented in Eqs. (6.63) to (6.66), while the ones obtained with a fifth-order series are presented in Eqs. (6.67) to (6.70). The numerical procedure to obtain all the necessary constants was implemented in Mathematica®. Note that the terms up to cubic order in the fifth-order expansions are exactly the same as the ones obtained in the cubic expansions, as expected from the step-by-step procedure used to obtain such constants. The geometry of these manifolds are shown in figures 86 to 89.

$$R_1 = -10.6468r + 12.6109r^3 + 16.4605s - 27.8736r^2s + 20.0202rs^2 - 33.8843s^3, \tag{6.63}$$

$$S_1 = -19.9991r + 38.6426r^3 - 6.82112s - 27.9595r^2s + 84.7255rs^2 - 16.5716s^3, \tag{6.64}$$

$$R_2 = -4.41074r - 1.08734r^3 - 7.50425s - 1.65443r^2s - 1.89416rs^2 - 2.47202s^3, \tag{6.65}$$

$$S_2 = 8.02958r + 1.98221r^3 - 1.97409s + 1.61731r^2s + 6.18687rs^2 + 0.945111s^3, \tag{6.66}$$

$$\begin{aligned} R_1 = &-10.6468r + 12.6109r^3 - 6.12521r^5 + 16.4605s - 27.8736r^2s + 58.3758r^4s \\ &+ 20.0202rs^2 - 48.5358r^3s^2 - 33.8843s^3 + 141.628r^2s^3 - 47.9115rs^4 + 85.0898s^5, \end{aligned} \tag{6.67}$$

$$\begin{aligned} S_1 = &-19.9991r + 38.6426r^3 - 81.358r^5 - 6.82112s - 27.9595r^2s + 152.901r^4s \\ &+ 84.7255rs^2 - 392.273r^3s^2 - 16.5716s^3 + 346.644r^2s^3 - 375.38rs^4 + 163.603s^5, \end{aligned} \tag{6.68}$$

$$\begin{aligned} R_2 = &-4.41074r - 1.08734r^3 - 0.31006r^5 - 7.50425s - 1.65443r^2s - 0.87950r^4s \\ &- 1.89416rs^2 - 1.24399r^3s^2 - 2.47202s^3 - 2.23775r^2s^3 - 1.1207rs^4 - 1.49509s^5, \end{aligned} \tag{6.69}$$

$$\begin{aligned} S_2 = &8.02958r + 1.98221r^3 + 1.04189r^5 - 1.97409s + 1.61731r^2s + 1.72151r^4s \\ &+ 6.18687rs^2 + 5.11809r^3s^2 + 0.94511s^3 + 4.18195r^2s^3 + 5.71863rs^4 + 1.99361s^5. \end{aligned} \tag{6.70}$$

Now, the dynamics of the system is simply given by Eq. (6.59), by substituting the expressions of q_1 and $\dot{q}_1$ using the correspondent manifolds. In order to verify the quality of the obtained models, the resulting time-series using the nonlinear modes and the one obtained by integrating the original ROM are presented in Figs. 90 to 94.

What can be observed is that one of the obtained nonlinear modes in each case dies out and the remaining one gives the actual response. In the case of the cubic polynomial, the time series has the same qualitative behaviour as the reference scenario, however, the magnitude of the response is far from correct. In turn, the fifth-order polynomial gave an unbounded solution, which shows that increasing the order of the polynomial for the manifold does not solve this specific problem. Two possibilities are then raised to explain

Figure 86 – Manifolds describing the first nonlinear mode obtained with a cubic polynomial series.

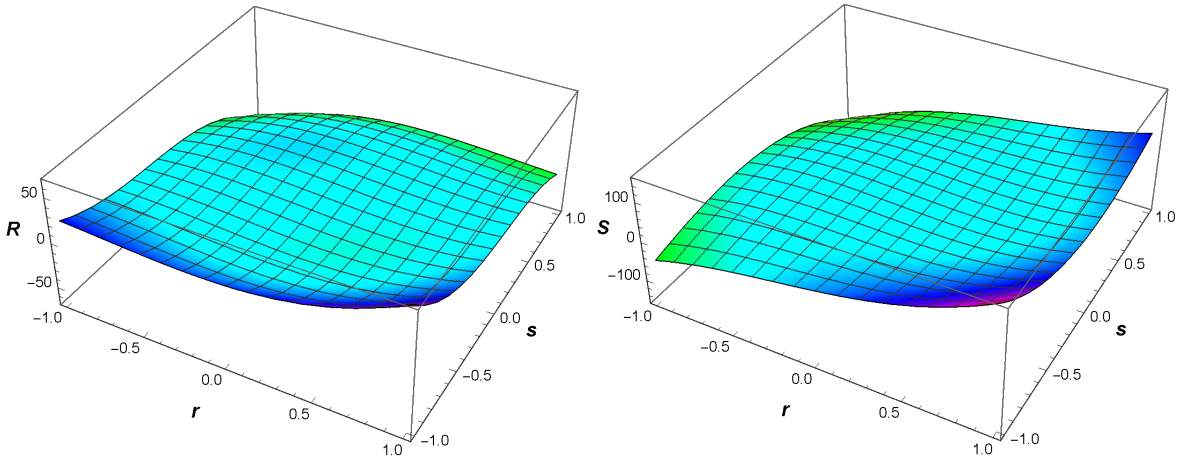

(a) Manifold R. (b) Manifold S.

Source: The author.

Figure 87 – Manifolds describing the second nonlinear mode obtained with a cubic polynomial series.

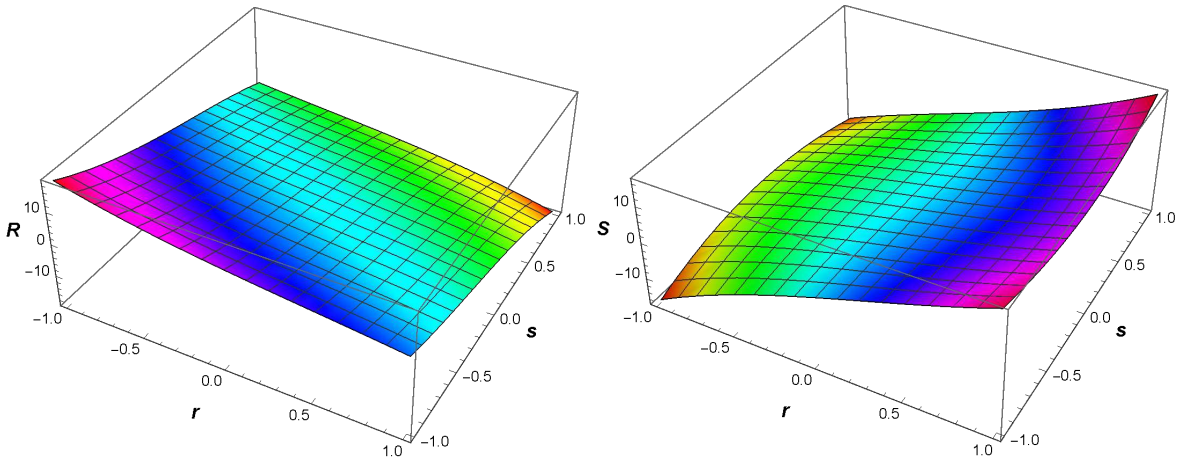

(a) Manifold R. (b) Manifold S.

Source: The author.

the origin of such problem. The first one is that for the VIV case, the manifolds may need to be governed by more than one single pair of master coordinates (multi-mode approach). The second possibility is that the problem is intrinsic to the use of a polynomial expression for the manifolds. The first possibility is the first one to be tried in this research, using as motivation the use of modes with more master variables in systems with internal resonance, commonly found in the literature. This approach requires a system with more than two DOFs, so, as initial step, recall the model for spatial vibrations with a 2 DOF wake oscillator, given as

Figure 88 – Manifolds describing the first nonlinear mode obtained with a fifth order polynomial series.

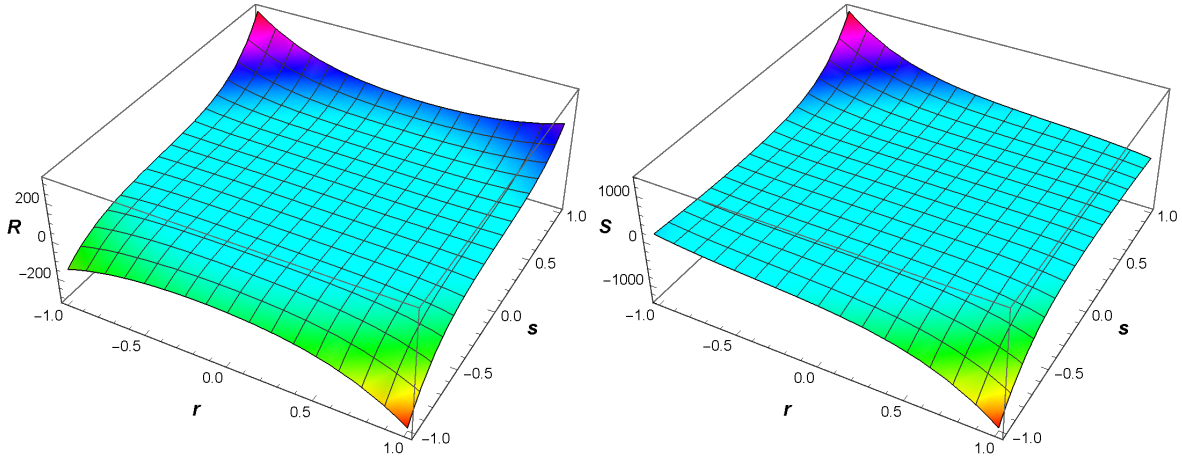

(a) Manifold R. (b) Manifold S.

Source: The author.

Figure 89 – Manifolds describing the second nonlinear mode obtained with a fifth order polynomial series.

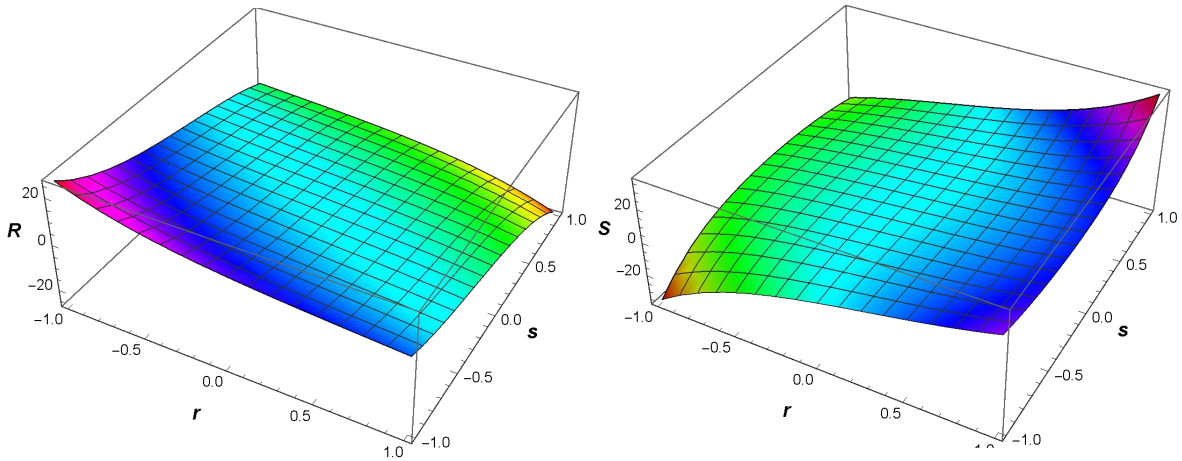

(a) Manifold R. (b) Manifold S.

Source: The author.

$$\ddot{u} + \frac{\rho D^2 \overline{C}_D U_r}{2\pi\left(\mu+\mu_a\right)}\dot{u} + \frac{EIu''''}{\left(\mu+\mu_a\right)\omega_n^2\ell^4} - \frac{\left(T_b+\gamma_s\ell\xi\right)u''}{\left(\mu+\mu_a\right)\omega_n^2\ell^2} - \frac{\gamma_s u'}{\left(\mu+\mu_a\right)\omega_n^2\ell}$$
$$\frac{-EAD\left(w'u''+w''u'+\frac{D}{2\ell}\left(3\left(u'\right)^2u''+2v'v''u'+\left(v'\right)^2u''\right)\right)}{\left(\mu+\mu_a\right)\omega_n^2\ell^3} = F_0 + \frac{\rho D^2 U_r^2 C_D^0 q_x}{16\pi^2\left(\mu+\mu_a\right)}, \tag{6.71}$$

Figure 90 – Time series obtained by the first nonlinear mode using the cubic polynomial series.

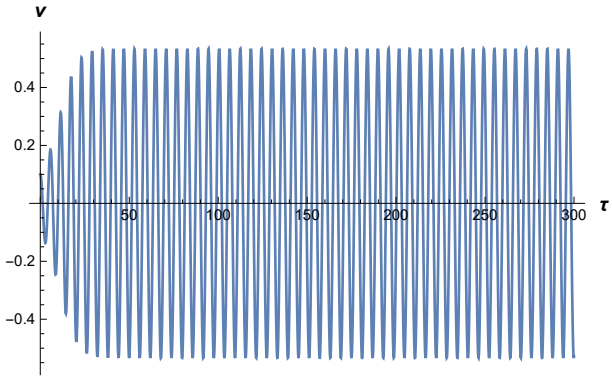

Source: The author.

Figure 91 – Time series obtained by the second nonlinear mode using the cubic polynomial series.

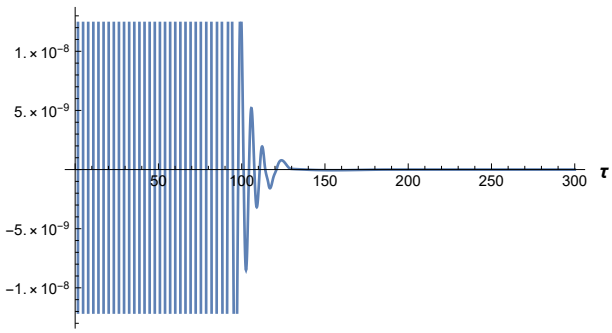

Source: The author.

Figure 92 – Time series obtained by the first nonlinear mode using the fifth order polynomial series.

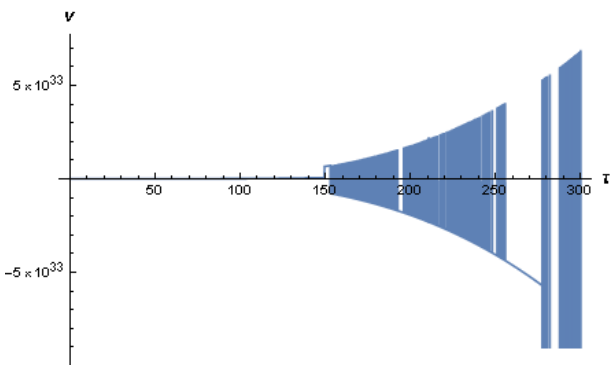

Source: The author.

$$\ddot{v} + \frac{\rho D^2 \overline{C}_D U_r}{4\pi\left(\mu+\mu_a\right)}\dot{v} + \frac{EIv''''}{\left(\mu+\mu_a\right)\omega_n^2\ell^4} - \frac{\left(T_b+\gamma_s\ell\xi\right)v''}{\left(\mu+\mu_a\right)\omega_n^2\ell^2} - \frac{\gamma_s v'}{\left(\mu+\mu_a\right)\omega_n^2\ell}$$
$$- \frac{EAD\left(w'v''+w''v'+\frac{D}{2\ell}\left(2u'u''v'+\left(u'\right)^2v''+3\left(v'\right)^2v''\right)\right)}{\left(\mu+\mu_a\right)\omega_n^2\ell^3} = \frac{\rho C_L^0 U_r^2 D^2}{16\pi^2\left(\mu+\mu_a\right)}q_y, \tag{6.72}$$

Figure 93 – Time series obtained by the second nonlinear mode using the fifth order polynomial series.

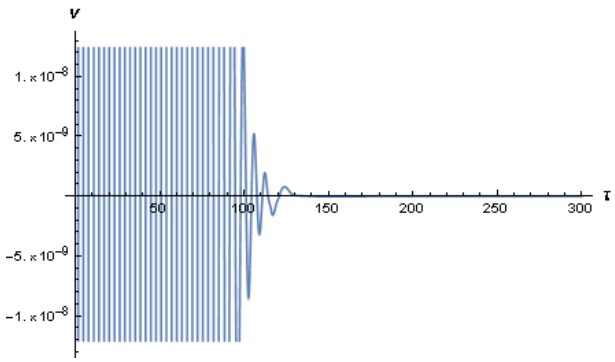

Source: The author.

Figure 94 – Time series reference obtained by simulating the original ROM.

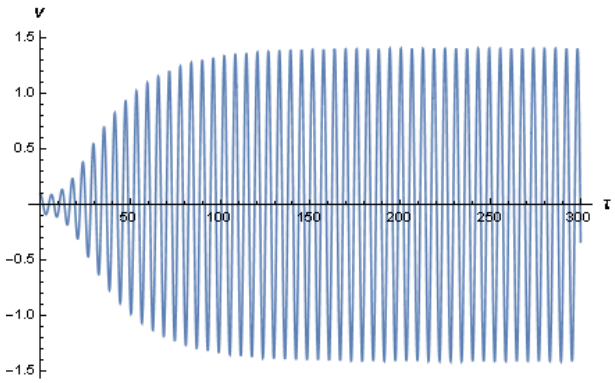

Source: The author.

$$\ddot{w} - \frac{EA}{\mu\omega_n^2\ell^2}\left(w'' + \frac{D}{\ell}\left(u'u'' + v'v''\right)\right) = 0, \tag{6.73}$$

$$\ddot{q}_y + \varepsilon_y U_r S_t \left(q_y^2 - 1\right)\dot{q}_y + \left(U_r S_t\right)^2 q_y = A_y \ddot{v}, \tag{6.74}$$

$$\ddot{q}_x + 2\varepsilon_x U_r S_t \left(q_x^2 - 1\right)\dot{q}_x + \left(2U_r S_t\right)^2 q_x = A_x \ddot{u}. \tag{6.75}$$

For this particular case, the values $A_y = 2$, $A_x = 12$, $\varepsilon_y = 0.0107$, $\varepsilon_x = 0.6$, $S_t = 0.17$ and $C_D^0 = 0.2$ are considered. Using a single projection function for each variable in the Galerkin projection, it is possible to obtain a ROM in the format

$$\ddot{u}_1 + U_r\eta_1\dot{u}_1 + \eta_2 u_1 + \eta_4 u_1^3 + U_r^2\eta_5 q_{x1} + \eta_6 v_1^2 u_1 = U_r^2 f_0, \tag{6.76}$$

$$\ddot{v}_1 + U_r\beta_1\dot{v}_1 + \beta_2 v_1 + \beta_4 v_1^3 + U_r^2\beta_5 q_{y1} + \beta_6 u_1^2 v_1 = 0, \tag{6.77}$$

$$\ddot{q}_{y1} + U_r\zeta_{11}\dot{q}_{y1} + U_r\zeta_{12}q_{y1}^2\dot{q}_{y1} + U_r^2\zeta_{13}q_{y1} + \zeta_{14}\ddot{v}_1 = 0, \tag{6.78}$$

$$\ddot{q}_{x1} + U_r\zeta_{21}\dot{q}_{x1} + U_r\zeta_{22}q_{x1}^2\dot{q}_{x1} + U_r^2\zeta_{23}q_{x1} + \zeta_{24}\ddot{u}_1 = 0. \tag{6.79}$$

Again, for simplicity, the axial dynamics is disregarded in the ROM. Now the master variables are chosen as $v_1 = r$, $\dot{v}_1 = s$, $q_{y1} = g$ and $\dot{q}_{y1} = h$. In the case of a single

pair of master variables, a cubic expansion requires nine coefficients for each manifold to be determined. Now, with two pairs of master coordinates, 34 coefficients are needed for each of the manifolds to achieve cubic order, and an extra term is needed to deal with the constant f_0 in the axial direction. Due to their size, these expansions are not described here, being a merely extension of the ones already presented. The difference in the total number of terms makes clear a key difficulty in finding nonlinear modes, that is, the exponentially increasing mathematical work for more complex models with larger number of DOFs. The slave variables are now given by $u_1 = R(r, s, g, h)$, $\dot{u}_1 = S(r, s, g, h)$, $q_{x1} = G(r, s, g, h)$ and $\dot{q}_{x1} = H(r, s, g, h)$. The expressions obtained for these manifolds, with the aid of symbolic computation, are given as

$$
\begin{aligned}
R &= 0.279248 - 0.000493696r^2 - 0.000122043rs - 0.000938322s^2 \\
&+ 7.71181 \times 10^{-6}rg + 3.90256 \times 10^{-6}sg + 2.73002 \times 10^{-7}g^2 - 1.71964 \times 10^{-6}rh \\
&- 0.0000287658sh + 1.15147 \times 10^{-7}gh - 1.10979 \times 10^{-7}h^2 \qquad (6.80)\\
S &= 0.000121448r^2 + 0.000903459rs + 0.000168565s^2 \\
&- 5.128 \times 10^{-6}rg - 7.94554 \times 10^{-6}sg - 2.37213 \times 10^{-8}g^2 + 0.0000359637rh \\
&+ 6.25783 \times 10^{-6}sh + 9.91404 \times 10^{-8}gh + 1.12726 \times 10^{-7}h^2 \qquad (6.81)\\
G &= -0.000335625r^2 - 0.00732494rs - 0.000513751s^2 \\
&- 0.000109359rg - 0.0000791923sg - 2.16965 \times 10^{-6}g^2 - 0.000172324rh \\
&+ 0.0000932933sh + 1.34127 \times 10^{-6}gh + 2.3224 \times 10^{-6}h^2 \qquad (6.82)\\
H &= 0.00742303r^2 + 0.00129498rs - 0.00719859s^2 \\
&+ 0.0000750388rg - 0.000214475sg - 3.1741 \times 10^{-6}g^2 - 0.000210524rh \\
&- 0.000265911sh - 6.77234 \times 10^{-6}gh + 1.39194 \times 10^{-6}h^2 \qquad (6.83)
\end{aligned}
$$

As it can be seen by the coefficients of terms involving g and h in the equations, the influence of the wake-oscillator variable in the manifolds is small. Since the manifolds are now four dimensional, two of the coordinates must be fixed in order to properly represent them in a three dimensional figure. Considering that, as pointed out, the dominant variables over the manifolds are r and s, for geometrical visualization the other two are fixed as $g = 0$ and $h = 0$. The manifolds for that condition are presented in Figs. 95 and 96.

Finally, the time series obtained for the variables of interest, u, v, q_y and q_x, are presented in Figs. 97 to 100. The results of integration of the full ROM used as reference are shown together with the former for comparison.

As it can be seen, in this case the integrated modal equations, relative to v and q_y, gave good results. However, the slave variables had a poor representation. The wake variable q_x has a negligible activation using the nonlinear modes. On the other hand,

Figure 95 – Manifolds describing the nonlinear mode using four master variables. $g = 0$ and $h = 0$.

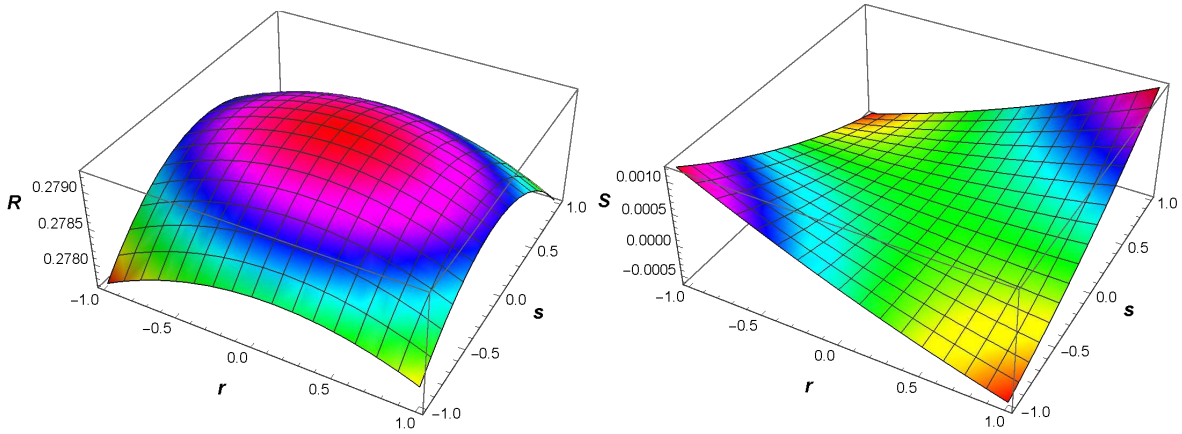

(a) Manifold R. (b) Manifold S.

Source: The author.

Figure 96 – Manifolds describing the nonlinear mode using four master variables. $g = 0$ and $h = 0$.

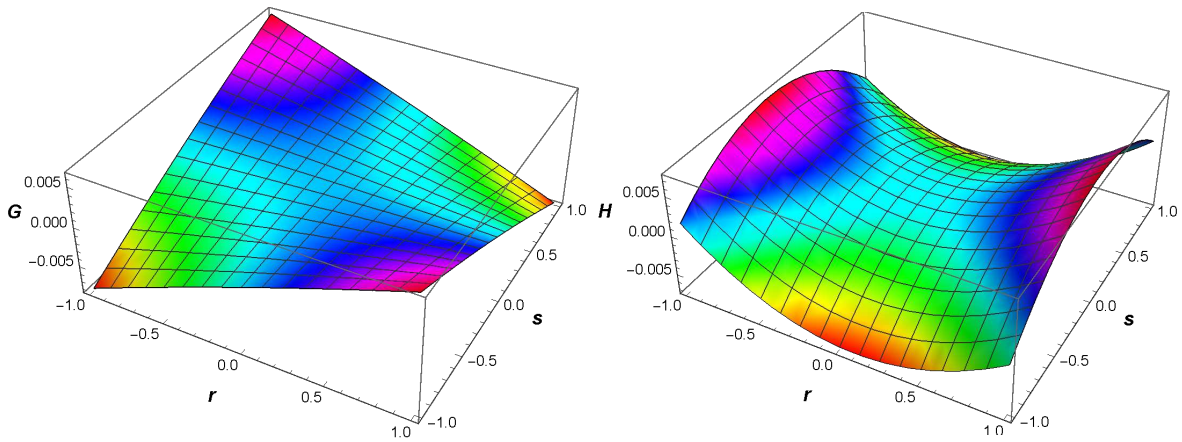

(a) Manifold G. (b) Manifold H.

Source: The author.

the displacement u had its qualitative behaviour recovered, but with a bad evaluation of the amplitude of oscillation. Different trials with two pairs of master variables were also investigated but not herein reported. Namely they are, using v and u to define the pairs of master variables or using q_y and q_x. All of these trials lead to poor results, which indicates that the problem lies in the polynomial representation of the manifolds and not in the variables that rule them.

Figure 97 – Time series of the coordinate v. Reference (Ref) and nonlinear mode solution (NM).

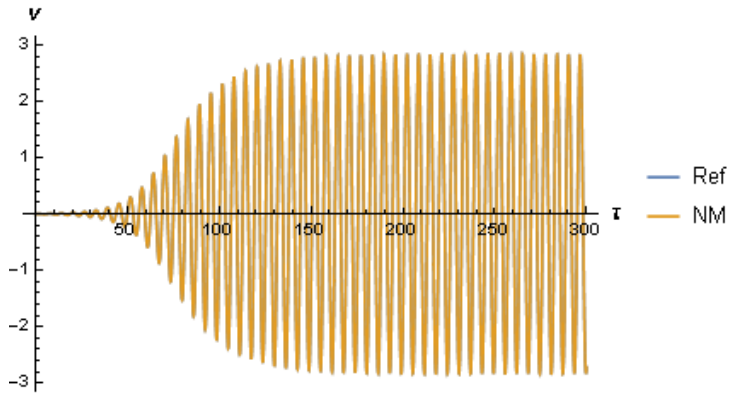

Source: The author.

Figure 98 – Time series of the coordinate q_y. Reference (Ref) and nonlinear mode solution (NM).

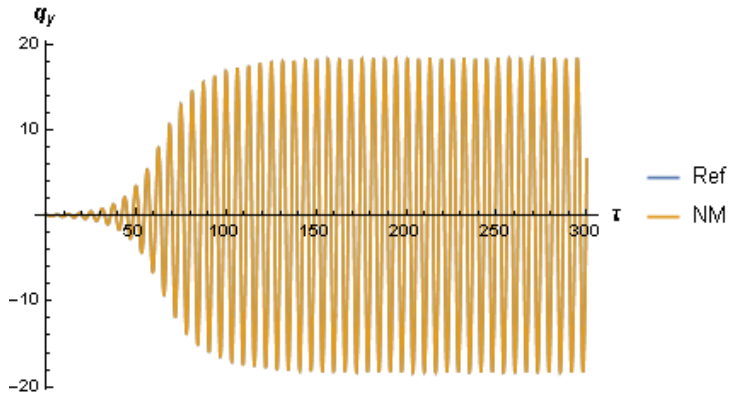

Source: The author.

Figure 99 – Time series of the coordinate u. Reference (Ref) and nonlinear mode solution (NM).

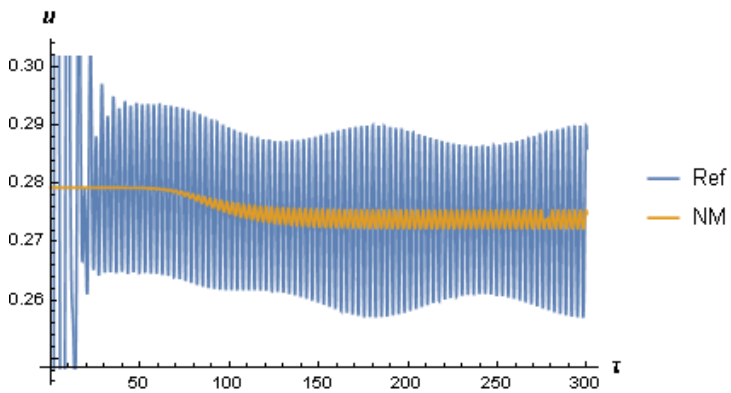

Source: The author.

Figure 100 – Time series of the coordinate q_x. Reference (Ref) and nonlinear mode solution (NM).

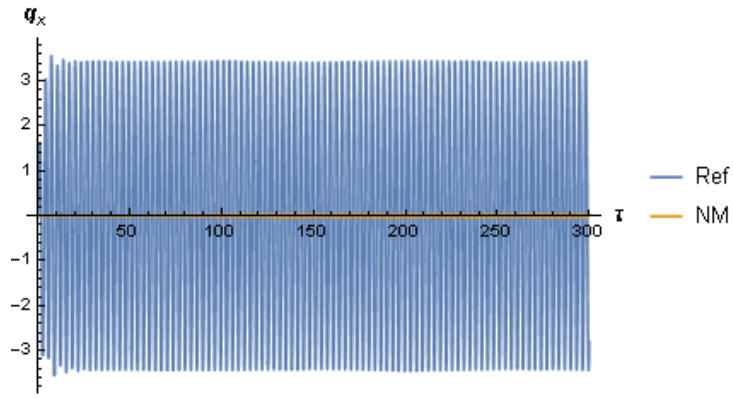

Source: The author.

6.3.2 Polar coordinate approach

Since the polynomial expansion does not furnish suitable representations for the nonlinear modes, a different approach is proposed. The idea is adapted from Pesheck, Pierre & Shaw (2002), and it consists of applying a coordinate transformation in the ROM and using the new coordinates as a master pair for the nonlinear mode. First, the planar ROM is recalled, given as

$$\ddot{w}_1 + \alpha_1 w + \alpha_2 v_1^2 = 0, \tag{6.84}$$

$$\ddot{v}_1 + U_r\beta_1\dot{v}_1 + \beta_2 v_1 + \beta_3 w_1 v_1 + \beta_4 v_1^3 + U_r^2\beta_5 q_1 = 0, \tag{6.85}$$

$$\ddot{q}_1 + U_r\zeta_1\dot{q}_1 + U_r\zeta_2 q_1^2\dot{q}_1 + U_r^2\zeta_3 q_1 + \zeta_4\ddot{v}_1 = 0. \tag{6.86}$$

Now, a coordinate transformation is proposed as

$$v_1 = \rho_v \cos\phi, \tag{6.87}$$

$$\dot{v}_1 = -\rho_v \sin\phi. \tag{6.88}$$

With some algebraic work, the second order equation for the transversal motion can then be written as a system of first order differential equations given as

$$\begin{aligned}\dot{\rho}_v &= \left(\beta_2\rho_v\cos\phi + \beta_3 w\rho_v\cos\phi + \beta_4\left(\rho_v\cos\phi\right)^3\right)\sin\phi \\ &+ \left(U_r^2\beta_5 q_1 - \rho_v\cos\phi - U_r\beta_1\rho_v\sin\phi\right)\sin\phi,\end{aligned} \tag{6.89}$$

$$\begin{aligned}\dot{\phi} &= -U_r\beta_1\sin\phi\cos\phi + \sin^2\phi \\ &+ \left(\beta_2\rho_v\cos\phi + \beta_3 w\rho_v\cos\phi + \beta_4\left(\rho_v\cos\phi\right)^3 + U_r^2\beta_5 q_1\right)\frac{\cos\phi}{\rho_v}.\end{aligned} \tag{6.90}$$

The problem is then divided into two sub-problems in order to result in an easier computation of the nonlinear modes. The first problem is to obtain the nonlinear mode to describe the axial displacement in terms of the transversal one for the free vibrations of the structure. This is made because the wake-oscillator does not excite directly the axial motion, thus, a representation of the axial dynamics as dependent only on the transversal one is likely suitable. This nonlinear mode is particularly easy to obtain with the polynomial approach and it gives good results. With some abuse of notation to represent the nonlinear modes, the functional relationships for the axial direction are given as

$$w_1 = -0.000182418r^2, \tag{6.91}$$

$$\dot{w}_1 = -0.000365037rs. \tag{6.92}$$

The presence of only second order terms is not a surprise, since the term dependent on the transversal displacement in Eq. (6.84) is a quadratic term. The geometry of these manifolds are given in Fig. 101. For representation, the notation $v_1 = r$ and $\dot{v}_1 = s$ is used.

Figure 101 – Manifolds describing the nonlinear mode for the axial displacement.

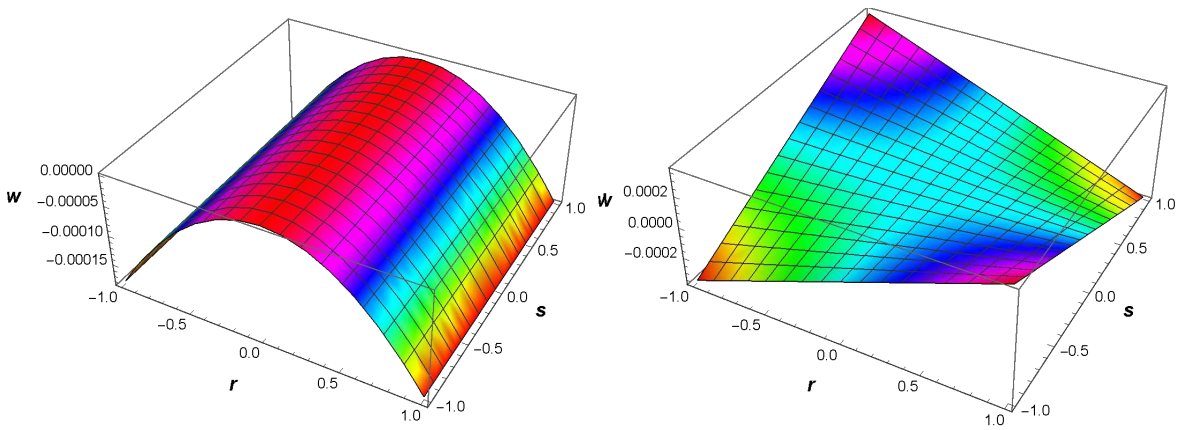

(a) Manifold for w. (b) Manifold for $\dot{w}$.

Source: The author.

Following, the wake variable is represented by the manifolds $q_1 = R$ and $\dot{q}_1 = S$. Differently from the polynomial expansions, the manifolds are now sought in the form

$$R = \left(a_1\rho_v + a_2\rho_v^3\right)\cos\phi + \left(a_3\rho_v + a_4\rho_v^3\right)\sin\phi, \tag{6.93}$$

$$S = \left(b_1\rho_v + b_2\rho_v^3\right)\cos\phi + \left(b_3\rho_v + b_4\rho_v^3\right)\sin\phi. \tag{6.94}$$

One aspect that should be noticed is that the use of polar coordinates allows to obtain more detailed geometries than those furnished by polynomials. Another aspect that

deserves attention is that the proposed shape of the manifolds does not include quadratic terms in the amplitude variable ρ_v. This is made since the presence of v_1 in the equation for q_1 can only occur by means of linear and cubic terms. In fact, trials were made considering the possibility of terms depending on ρ_v^2. However, as expected, those terms resulted null asides very small numerical residues. Following, a Galerkin procedure is used to determine the coefficients of the trial manifold in a similar manner to the one made in Pesheck, Pierre & Shaw (2002). After numerical computations, the expressions for the manifolds result in

$$R = 3.39515\rho_v^3 \sin\phi + 0.497565\rho_v^3 \cos\phi - 11.8168\rho_v \sin\phi - 5.89219\rho_v \cos\phi, \tag{6.95}$$

$$S = -1.55053\rho_v^3 \sin\phi + 3.72556\rho_v^3 \cos\phi + 7.06644\rho_v \sin\phi - 12.8473\rho_v \cos\phi. \tag{6.96}$$

The geometry of these manifolds are represented in Figs. 102 to 104. In these figures, it is possible to see that the obtained manifolds have a richer geometry when compared to the ones obtained with a polynomial expansion.

Figure 102 – Manifolds describing the nonlinear mode for the wake variable.

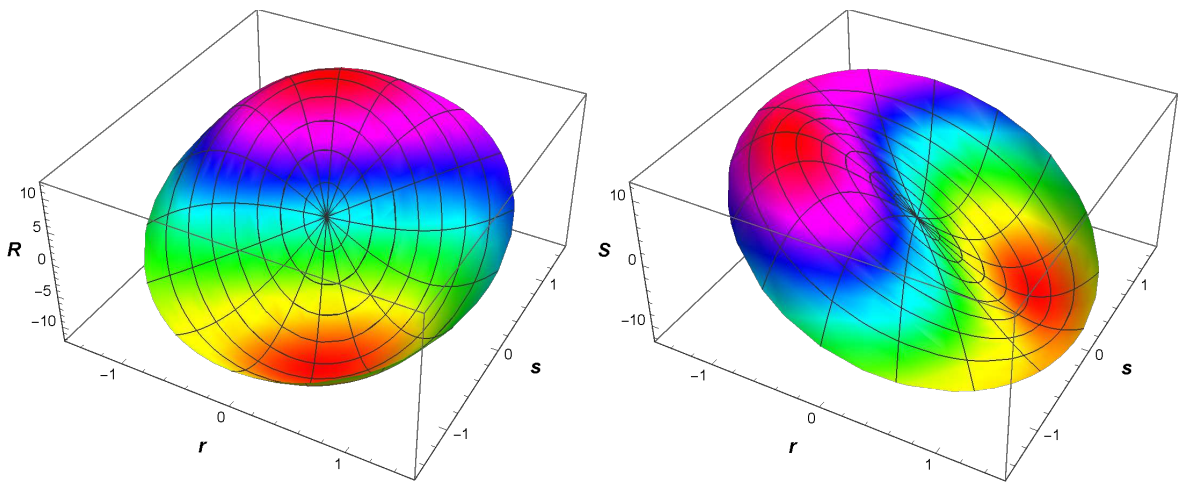

(a) Manifold R. (b) Manifold S.

Source: The author.

As made for the polynomial case, to evaluate the quality of the results furnished by the obtained nonlinear modes, the time series for each of the relevant variables are shown in Figs. 105 to 107. In Figs. 108 and 109, the phase space portrait for v and q are shown. Finally, in Figs. 110 and 111, the results of the reference simulation are plotted over the manifolds, to verify the geometric accuracy of the former.

From the time series, it is possible to conclude that the use of nonlinear modes with this approach furnishes good results, with a slight difference in the duration of the transient regime only. The difference between the nonlinear mode solution and the reference is more visible in the wake variable. Checking the phase space portraits, it is possible to see that

Figure 103 – Manifolds describing the nonlinear mode for the wake variable. View of the r axis.

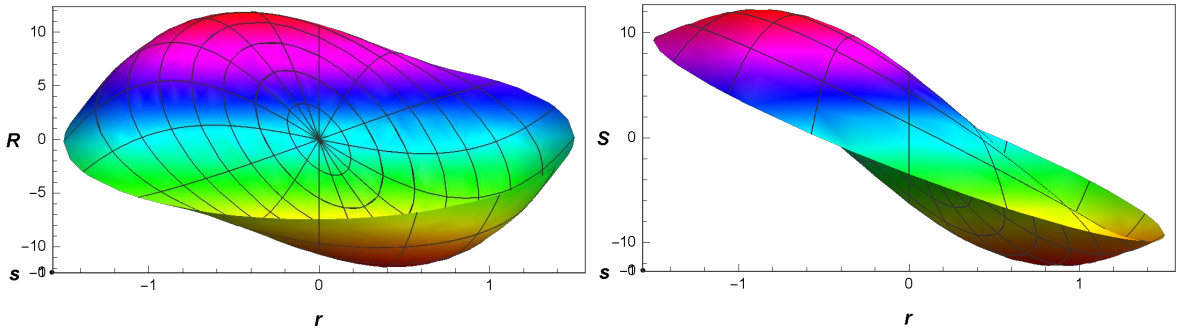

(a) Manifold R. (b) Manifold S.

Source: The author.

Figure 104 – Manifolds describing the nonlinear mode for the wake variable. View of the s axis.

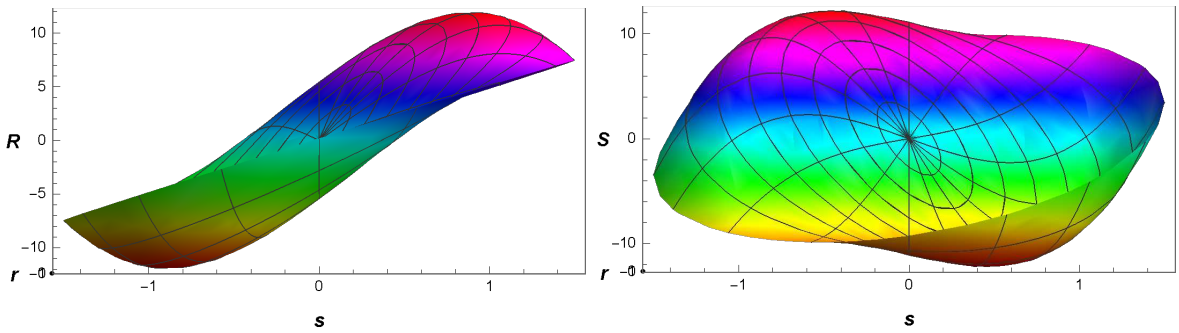

(a) Manifold R. (b) Manifold S.

Source: The author.

Figure 105 – Time series of the coordinate v. Reference (Ref) and nonlinear mode solution (NM).

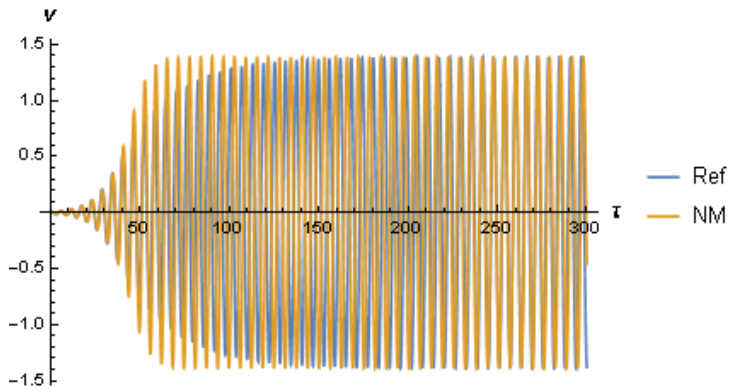

Source: The author.

the qualitative behaviour of the response is also recovered. It is also possible to conclude that the nonlinear mode can be further refined for a better representation of the wake

Figure 106 – Time series of the coordinate q. Reference (Ref) and nonlinear mode solution (NM).

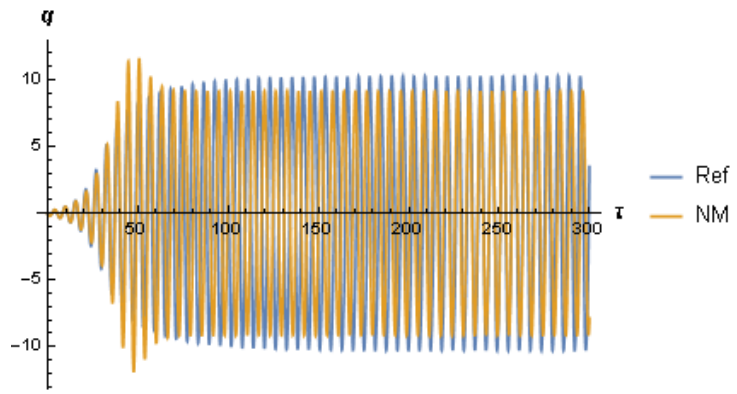

Source: The author.

Figure 107 – Time series of the coordinate w. Reference (Ref) and nonlinear mode solution (NM).

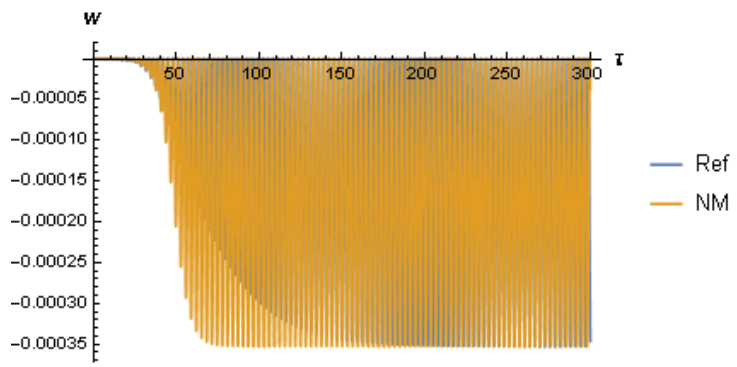

Source: The author.

Figure 108 – Phase portrait of the coordinate v. Reference in blue and nonlinear mode solution in red.

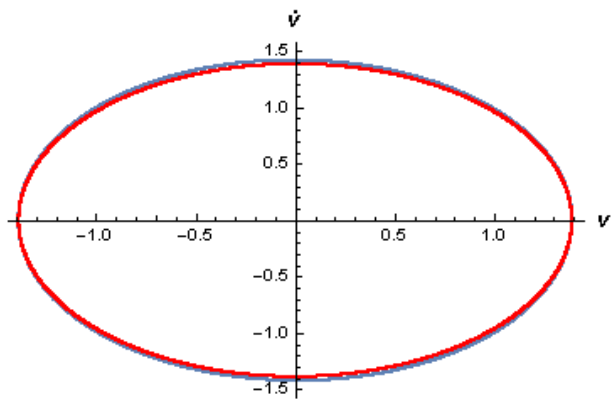

Source: The author.

variable. This last conclusion can be also visualized in the points of the reference solution plotted over the obtained manifold. The problem of performing more refinements is that

Figure 109 – Phase portrait of the coordinate q. Reference in blue and nonlinear mode solution in red.

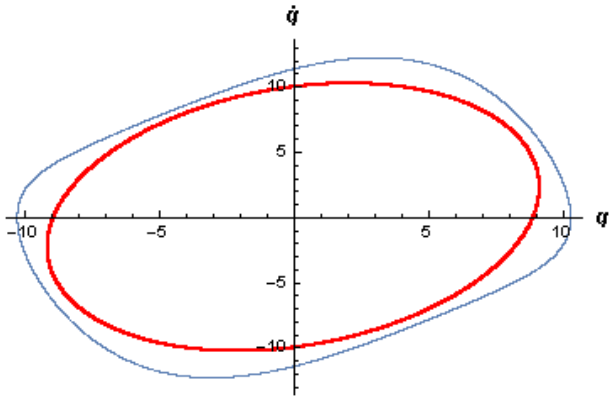

Source: The author.

Figure 110 – Reference solution (red dots) over the defined manifold for the variable q.

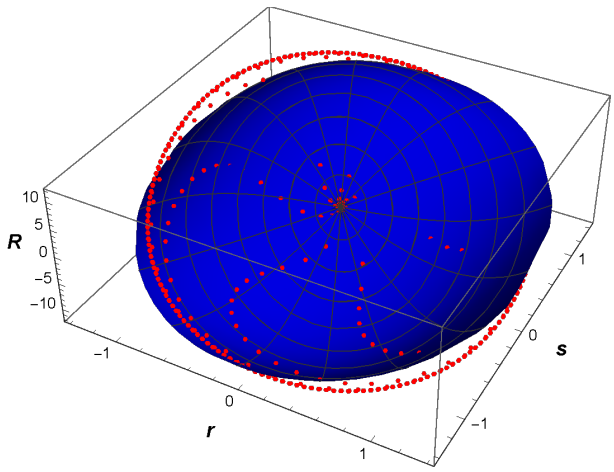

Source: The author.

Figure 111 – Reference solution (red dots) over the defined manifold for the variable u.

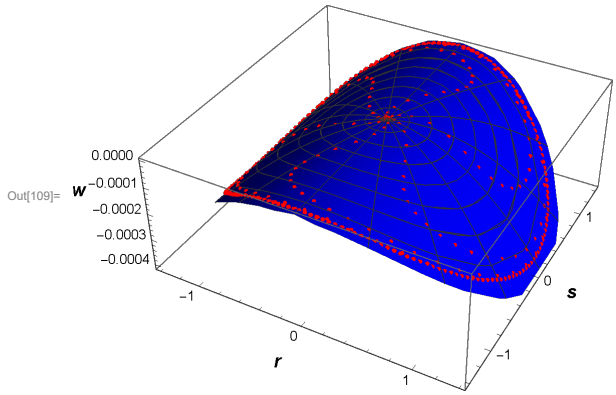

Source: The author.

the mathematical computations quickly become impractical due to the time demanded for their evaluation, when possible.

6.4 Analysis of spatial VIV with one wake variable using invariant manifolds

With a working methodology to obtain the nonlinear modes that recovers good results for the planar case by means of the polar coordinate approach, it is now possible to analyse the spatial vibrations of the structure, still using a single variable for the phenomenological model. Recalling the defined models, the ROM in this case is written as

$$\ddot{w}_1 + \alpha_1 w_1 + \alpha_2 v_1^2 + \alpha_3 u_1^2 = 0, \tag{6.97}$$

$$\ddot{u}_1 + U_r \eta_1 \dot{u}_1 + \eta_2 u_1 + \eta_4 u_1^3 + \eta_6 v_1^2 u_1 = U_r^2 f_0, \tag{6.98}$$

$$\ddot{v}_1 + U_r \beta_1 \dot{v}_1 + \beta_2 v_1 + \beta_4 v_1^3 + U_r^2 \beta_5 q_{y1} + \beta_6 u_1^2 v_1 = 0, \tag{6.99}$$

$$\ddot{q}_1 + U_r \zeta_1 \dot{q}_1 + U_r \zeta_2 q_1^2 \dot{q}_1 + U_r^2 \zeta_3 q_1 + \zeta_4 \ddot{v}_1 = 0. \tag{6.100}$$

The definitions $v_1 = r$, $\dot{v}_1 = s$, $q_1 = R$ and $\dot{q}_1 = S$ are kept. The model is the same as the one used for the polynomial approach. Here, both the axial and in-line displacements are not directly excited by the wake variable (noted by the absence of q_1 in the equations for w and u), so, to simplify the mathematical work, the nonlinear modes to represent w and u are obtained for the free vibrations case, including the constant mean drag force f_0. In both cases the manifolds are obtained with a cubic polynomial expansion, leading to the expressions

$$\begin{aligned} w = &-0.0000265027r - 0.000165451r^2 - 3.59373 \times 10^{-6} r^3 - 0.0000264854s \\ &+ 0.00002034rs - 4.62794 \times 10^{-6} r^2 s + 0.0000171023s^2 \\ &- 4.62175 \times 10^{-6} rs^2 - 3.60025 \times 10^{-6} s^3, \end{aligned} \tag{6.101}$$

$$\begin{aligned} \dot{w} = &\, 0.0000255973r - 0.0000196548r^2 + 4.47505 \times 10^{-6} r^3 - 0.0000224967s \\ &- 0.000367105rs - 1.13945 \times 10^{-6} r^2 s + 0.0000151951s^2 \\ &+ 2.61448 \times 10^{-6} rs^2 - 3.00423 \times 10^{-6} s_1^3, \end{aligned} \tag{6.102}$$

$$\begin{aligned} u = &\, 0.28078 + 0.0000757086r - 0.000264001r^2 - 0.0000100968r^3 - 0.000108288s \\ &- 0.0000789569rs + 0.0000530442r^2 s - 0.000526985s^2 + 0.0000551515s^3, \end{aligned} \tag{6.103}$$

$$\begin{aligned} \dot{u} = &\, 0.000106362r + 0.0000723737r^2 - 0.0000494571r^3 + 0.0000911053s \\ &+ 0.00049728rs - 0.0000337798r^2 s + 0.0000810668s^2 \\ &- 0.0000548185rs^2 - 0.0000246287s^3 \end{aligned} \tag{6.104}$$

The geometries of these manifolds are given in Figs. 112 and 113. Note that the presence of the cross-wise motion does not give qualitative changes in the axial manifolds, even though it introduces terms that are not quadratic in v_1 in the expressions for the axial manifolds.

Figure 112 – Manifolds describing the nonlinear mode for the axial motion.

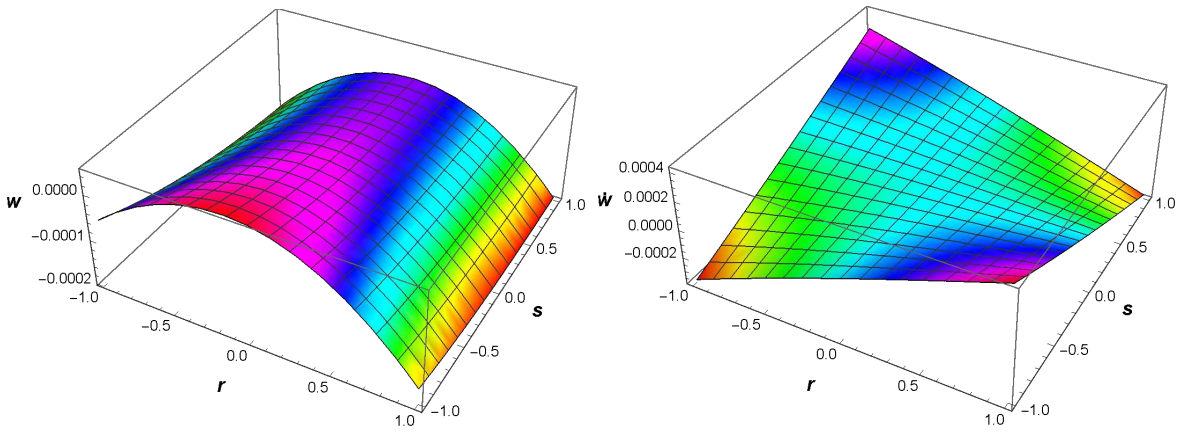

(a) Manifold for w. (b) Manifold for $\dot{w}$.

Source: The author.

Figure 113 – Manifolds describing the nonlinear mode for the cross-wise motion.

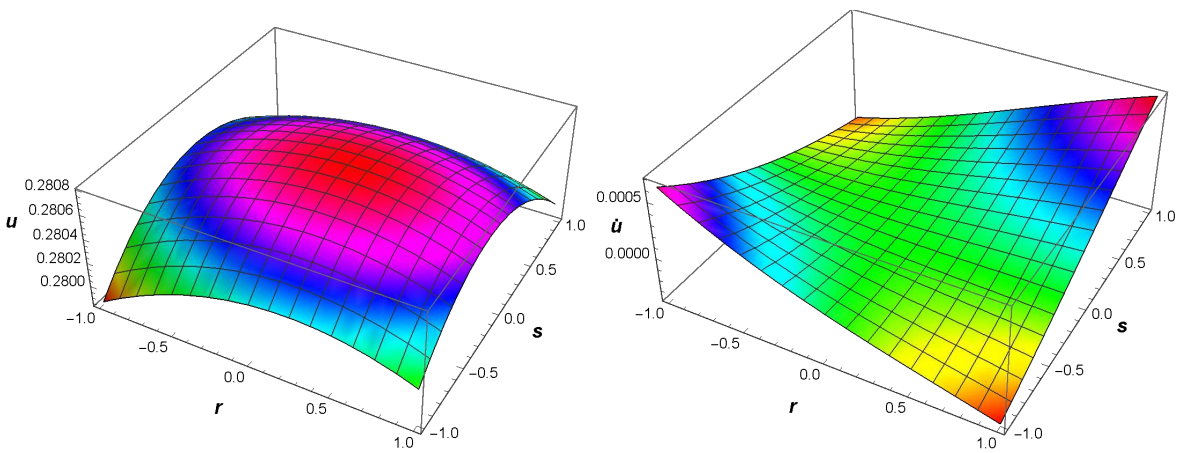

(a) Manifold for u. (b) Manifold for $\dot{u}$.

Source: The author.

For the manifolds representing the wake variable, no significant difference from the ones presented in Figs. 103 and 104 is present, thus they are not repeated. The results for this model are also in good agreement with the simulation of the full ROM, with some discrepancies in the axial and cross-wise displacements. These features can be verified in the time series presented in Figs. 114 to 117. The phase space portraits are very similar to the planar case and thus are not shown.

Figure 114 – Time series of the coordinate v. Reference (Ref) and nonlinear mode solution (NM).

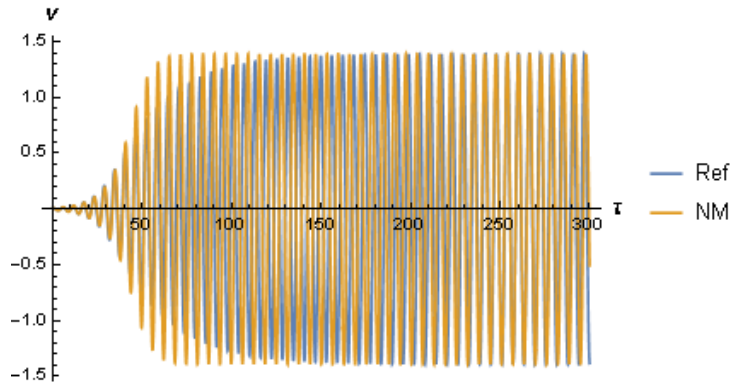

Source: The author.

Figure 115 – Time series of the coordinate q. Reference (Ref) and nonlinear mode solution (NM).

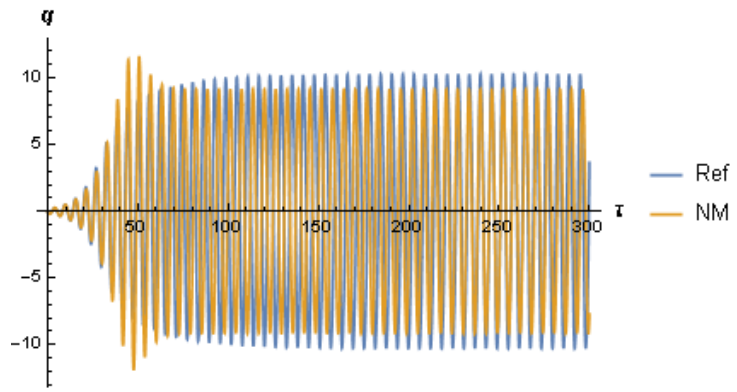

Source: The author.

Figure 116 – Time series of the coordinate w. Reference (Ref) and nonlinear mode solution (NM).

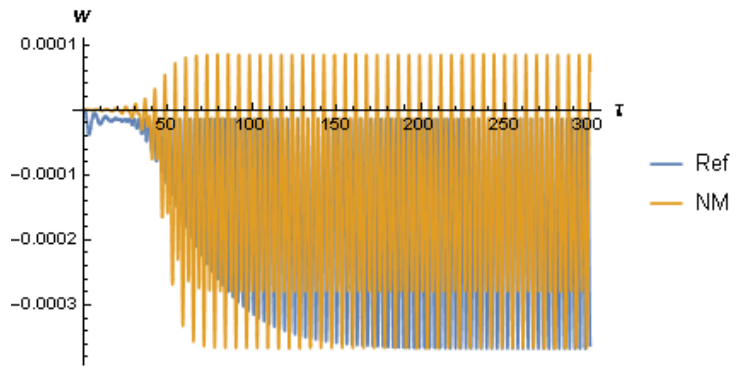

Source: The author.

It is possible to see that there is an extra frequency in the response furnished by the nonlinear modes in the axial and cross-wise motions. One of the possibilities for

Figure 117 – Time series of the coordinate u. Reference (Ref) and nonlinear mode solution (NM).

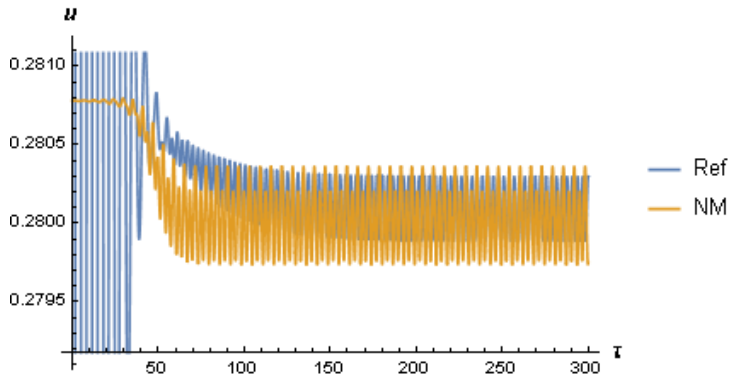

Source: The author.

that is the use of the nonlinear modes of free vibrations as an approximation for these variables. The complexity of mathematically solving these nonlinear modes together with the manifold for the wake variable, rather than separated as it was done, is significantly higher. This is then left as suggestion for further works. Finally, the geometrical adherence of the nonlinear modes to the simulation of the full ROM can be seen in Figs. 118 to 120. It is possible to see that the results of the full ROM are neighbouring the obtained nonlinear modes, showing that only some refinement of these modes is needed for even better results.

Figure 118 – Reference solution (red dots) over the defined manifold for the variable q.

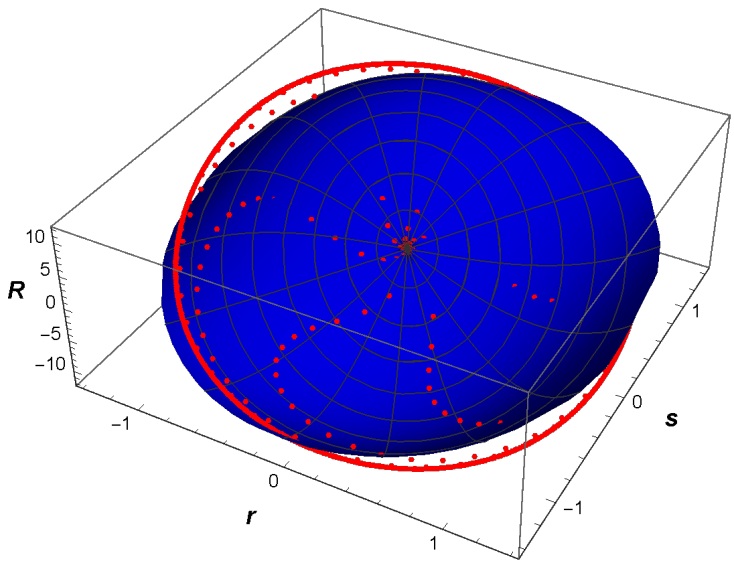

Source: The author.

Figure 119 – Reference solution (red dots) over the defined manifold for the variable w.

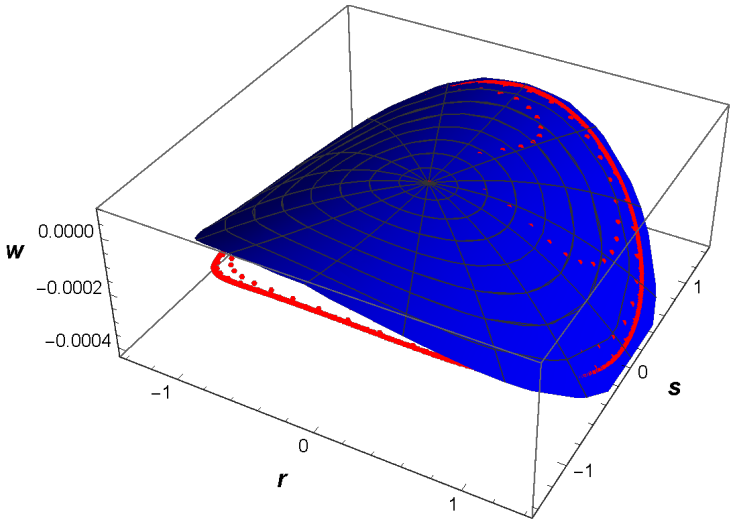

Source: The author.

Figure 120 – Reference solution (red dots) over the defined manifold for the variable u.

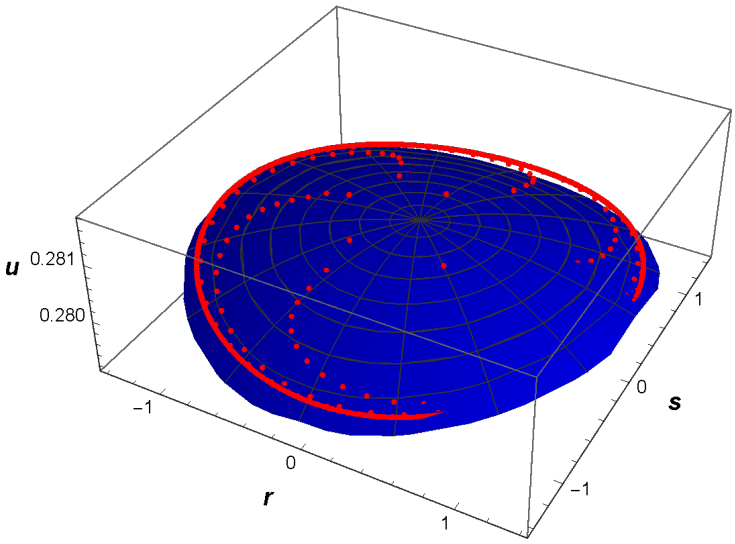

Source: The author.

7 Conclusions and suggestions for further works

The focus of the thesis is on the investigation of qualitative aspects regarding the construction of reduced-order models (ROM). Another aspect is the evaluation of the advantages in using this type of model for analysis and engineering practice. To do so, different scenarios, common to the offshore engineering field, were chosen as background for motivation. The first scenario is that of flexible rods, immersed in fluid and under parametric excitation. The second one is that of elastic and curved cables, immersed in fluid and under the action of imposed boundary motion. Finally, the last case is that of vortex-induced vibrations (VIV) of a flexible rod.

Some procedures for the investigation are the same for all three cases. Initially, a model described by partial differential equations (PDE) is obtained for each case, being then discretized with a Galerkin projection. This step is what turns the PDE model into a ROM. In order to evaluate qualitative aspects on the constructions of such ROMs, different projection basis are used for the Galerkin projection in each scenario.

For the problem of parametric excitation of straight and flexible rods, it is shown that a more detailed projection function, in this case a “Bessel-like” function, can furnish accurate results using only a single degree of freedom (DOF) in the projection. In turn, when simpler functions are used, like trigonometric functions, the number of DOFs for accurate representation is larger. It is interesting that, in the investigated case, the difference in shape between the “Bessel-like” function and a sine function is very small. However, the difference in the mathematical structure of both functions led significantly different results between a ROM with a single “Bessel-like” function and one with a single sine function in the projection basis. For the trigonometric case, three DOFs were needed for an accurate representation. This is a novel work in the literature in the sense that it investigate qualitative advantages in using different projection functions containing differences in their mathematical structures.

The use of a single DOF by means of adopting the “Bessel-like” function leads to the straightforward advantage of a smaller computational effort needed to simulate the model. This, however, is not the only advantage. Since only one DOF is involved, it is possible to deal with the nonlinear Morison damping with ease in order to obtain an analytical solution for the response of the structure, which is not readily feasible with a larger model. The solution obtained with the method of multiple time scales (MMTS) is much more efficient in terms of computational effort than any other type of solution, since it requires a simple algebraic procedure to obtain the response of the structure.

Still in the problem of a straight rod under parametric excitation, an innovative analytical solution obtained by applying MMTS directly on the PDEs is also presented. This procedure has the advantage of not involving any assumption over the displacement field, and is not affected by discretization steps. The analytical solution is then used to perform some parametric studies about the phenomenon, revealing, amongst other aspects, that the nonlinear Morison damping is able to magnify the effects of a small structural damping when both are combined, in the sense that the effective amplitude reducing provided by the presence of the structural damping is more pronounced if the Morison damping is present. This analytical solution is also converted into a simplified version using polynomial terms to evaluate the structural response. This allows the implementation of such rich solution into an electronic spreadsheet for usage as a design aiding tool. Such tool can be used in real time, since all evaluations are purely algebraic, in order to furnish results for conditions of interest.

Giving sequence to the investigations, the scenario of a statically curved and immersed elastic cable under support motion is investigated. In the thesis, only the case of planar motion is considered, showing that there is still plenty of room for future works in the field. It is important to highlight that there is a significant amount of works in the literature for this type of excitation but restricted to vibrations in air. The analysis carried-out considering the fluid-structure interaction by means of the Morison model for this particular scenario is novel. Following what is made for the straight structure case, different ROMs are obtained and compared. A key factor revealed in this analysis is that an interpolating function to distribute the top motion along the structural length is required, and it plays a major role on the quality of the obtained models. It is shown that, a poorly detailed function for this interpolation leads to a ROM that is not accurate, and it cannot be improved by the mere addition of more DOFs to the model. This shows that the quality of the functions to represent the displacement field is responsible to define if the solution of the ROM will converge to the actually right response.

It is also developed an iterative procedure to evaluate the steady-state response in this case by analytical means using the MMTS. This is made in order to deal with a sum of terms that appears inside the Morison damping expression, which involves the absolute value function and thus any summations are not easily treatable. This procedure is also an innovative contribution of the thesis. An important aspect is that the computational effort for such procedure quickly grows with the number of DOFs of the model, becoming more computationally costly than integrating the ROM. This highlights another advantage of searching for projection functions with good quality, in order to reduce the number of DOFs, allowing for a better application of analytical techniques. Closing the matter, the solution proposed in the thesis involves a quasi-static hypothesis over the displacement field, in which the top motion is instantaneously transferred to the entire cable by means of the adopted interpolating function. The results shows that the creation of ROM may be

further enhanced if a dynamical approach is developed for this portion of the displacements.

Moving on to the case of VIV, a phenomenological approach is used to model the problem. This approach enlarges the number of DOFs involved in order to obtain a solution. Again, different ROMs are obtained, and it is made an hypothesis that the wake-variable follows the same spatial distribution as the transversal displacement. The results show that this approach leads to satisfactory quantitative evaluations compared to a numerical solution of the PDE model. However, this usage hinders the ability of the ROM to obtain multifrequency responses, working as an imposed filter. The ROMs, when built with more detailed projection functions, are able to furnish suitable results in the region of interest, around the lock-in condition.

In the case of VIV, since the wake-variable must be present in the ROM and the axial dynamics is kept as well, the smallest possible number of DOFs for the ROM is 3 considering its construction with the Galerkin method. In order to further reduce such number, the nonlinear modes of vibration for this particular problem are sought. To the best of the author's knowledge, this is one of the first works in the literature to obtain the nonlinear modes considering the wake oscillator in the equations of motion. The approach that can be found in the literature is that in which the nonlinear modes of the structure are obtained without considering the wake oscillator, which is later added to the model in an *ad-hoc* manner. During the development, it is shown that the classical approach of using polynomials to describe the manifolds representing the nonlinear modes is inadequate for this problem. Instead, a coordinate transformation is proposed. This allows writing the system in polar coordinates. In the new system, the nonlinear modes can be defined with the aid of further Galerkin projections, now over the manifold equations. The results show that this procedure leads to qualitatively good ROMs with a single DOF. This means that, with the right choice of projection functions and with the effort of obtaining the nonlinear modes, an analyst may represent the phenomena of interest and perform the necessary analysis in a very small system, saving significant computation effort.

For a fast systematic visualization of the conclusions, Tab. 27 brings a summary of the main conclusions regarding the reduced-order modelling of the three different problems investigated along the thesis.

With that, it is considered that the thesis is able to answer questions about the influence of simplifying or not the projection functions used in the construction of ROMs. It also clarifies the advantages of pursuing and obtaining the smallest possible ROM that furnishes accurate results. In addition, analytical considerations are made aiming at obtaining analytical solutions, of great value for assessing the main aspects of the dynamic behaviour and for obtaining closed-form solutions for important quantities such as the steady-state amplitude of responses. Pathways on how obtaining ROMs are also addressed and discussed, showing the corresponding strengths and drawbacks. The thesis also brings

the application of advanced techniques over the models obtained after the application of the Galerkin procedure, rather than simply numerically integrating such models. This allows for faster computations and to obtain all the possible stable and unstable branches within the capabilities of each model. Such applications, together with further algebraic work, also allow for the development of simple formulations and tools to be used in design practice, without the need of advanced computational resources. Still, some refinements can be done in the investigations, and further uses of the ROMs and procedures herein developed can be made. That said, a list of possible future works is:

- Obtain analytical solutions directly from the PDEs for straight structures under parametric excitation considering the existence of internal resonances;
- Investigation of the range of applicability of different ROMs for straight structures under parametric excitation with multiple simultaneous frequencies;
- Use wave analysis techniques to develop better proposals of displacement fields for the problem of elastic cables under imposed boundary motion;
- Analysis of the quality of different ROMs for the three-dimensional dynamics of elastic cables under imposed boundary motion;
- Create and investigate better representations for the spatial distribution of the wake-variable for the analysis of flexible structures under VIV.
- Develop a continuation technique over the procedure to obtain the nonlinear modes for flexible structures under VIV in order to verify the evolution of such modes with the variation of the reduced velocity;
- Combine the results for VIV and for elastic cables to investigate the case of curved structures under VIV;
- Perform correlations with experimental data and proceed to modelling enhancement;
- Investigation of the dynamics of statically curved cables under VIV and/or parametric excitation considering unilateral contact;
- Extend the results, analysis and conclusions concerning the creation of ROMs to other problems (for example, vortex-self-induced vibrations, VSIV), using the similarity between the mathematical structure of the continuous models to generate insights on how to proceed in different scenarios.

Table 27 – Shortened exposition of the main conclusions obtained with the investigation of different ROMs in the problems worked in the thesis.

	Straight rod under parametric excitation	Statically curved cable under support motion	Straight rod under VIV
Number of functions	Can be reduced to a single one if the proper choice of function is made.	Two functions are the minimum needed, one for a single degree of freedom and one for interpolating the effect of the imposed boundary motion	Can be reduced to a single one if the proper choice of function is made, however it limits the range of reduced velocities that can be investigated
Quality of projection functions	Functions of lesser quality with respect to the vibration modes may be used, with the drawback of requiring a larger number of functions for better results	The quality of the functions that interpolate the effects of the imposed motion are of paramount importance, with the use of functions with less quality leading to incorrect results which can not be enhanced with the use of additional functions. Regarding the degrees of freedom of the cable, less rich functions lead to the need of a greater amount of them to be used	Functions with worse quality may be used at the expense of requiring a larger amount of projection functions for the quality of the model
Main outcomes	The possibility of the reduction to a single DOF by means of using richer projection functions allows for fast numerical integrations and the obtaining of an analytical solution	The interpolation of the effects of the top motion must be carefully addressed for a good representation. Also, due to the need of a minimum of two functions for the displacement field composition and the presence of the Morison damping, a purely analytical solution is not feasible, requiring the aid of numerical iterations to be obtained	It is possible to obtain a ROM with good results using a single DOF for the structural part, given a suitable projection function is used. Obtaining then the NNMs for the problem, it is possible to reduce the system even further by writing the wake DOF as function of the structural DOF

Bibliography

ALFOSAIL, F. K.; YOUNIS, M. I. Two-to-one internal resonance of an inclined marine riser under harmonic excitations. Springer Nature, v. 95, n. 2, p. 1301–1321, 2018. 66

ALFOSAIL, F. K.; YOUNIS, M. I. Three-to-one internal resonance of inclined marine riser. *International Journal of Non-Linear Mechanics*, Elsevier BV, v. 109, p. 107–117, mar 2019. 66

ALFOSAIL, F. K.; YOUNIS, M. I. Multifrequency excitation of an inclined marine riser under internal resonances. Springer Science and Business Media LLC, v. 99, p. 149–171, 2020. 66

ARANHA, J. A. P. Weak three dimensionality of a flow around a slender cylinder: the ginzburg-landau equation. *Journal of the Brazilian Society of Mechanical Sciences and Engineering*, FapUNIFESP (SciELO), v. 26, n. 4, p. 355–367, dec 2004. 49

BARACHO NETO, O. G. P.; MAZZILLI, C. E. N. Evaluation of multi-modes for finite-element models: systems tuned into 1:2 internal resonance. Elsevier BV, v. 42, n. 21-22, p. 5795–5820, 2005. 69

BEARMAN, P. W. Vortex shedding from oscillating bluff bodies. *Annual Review of Fluid Mechanics*, v. 16, p. 195–222, Jan 1984. 44

BENDER, C. M.; ORSZAG, S. A. *Advanced Mathematical Methods for Scientists and Engineers*. [S.l.]: McGraw-Hill, 1978. 42, 43, 60, 263

BENEDETTINI, F.; REGA, G. Planar non-linear oscillations of elastic cables under superharmonic resonance conditions. *Journal of Sound and Vibration*, Elsevier BV, v. 132, n. 3, p. 353–366, aug 1989. 62

BENEDETTINI, F.; REGA, G.; ALAGGIO, R. Non-linear oscillations of a four-degree-of-freedom model of a suspended cable under multiple internal resonance conditions. Elsevier BV, v. 182, n. 5, p. 775–798, 1995. 64

BENEDETTINI, F.; REGA, G.; VESTRONI, F. Modal coupling in the free nonplanar finite motion of an elastic cable. *Meccanica*, Springer Nature, v. 21, n. 1, p. 38–46, mar 1986. 61, 62

BLEVINS, R. D.; COUGHRAN, C. S. Experimental investigation of vortex-induced vibration in one and two dimensions with variable mass, damping, and reynolds number. v. 131, p. 101202–1 – 101202–7, 2009. 47

CHANDRASEKARAN, S.; CHANDAK, N. R.; ANUPAM, G. Stability analysis of TLP tethers. Elsevier BV, v. 33, n. 3-4, p. 471–482, 2006. 136

CHAPLIN, J. R.; BEARMAN, P. W.; CHENG, Y.; FONTAINE, E.; GRAHAM, J. M. R.; HERFJORD, K.; HUARTE, F. J. H.; ISHERWOOD, M.; LAMBRACOS, K.; LARSEN, C. M.; MENEGHINI, J. R.; MOE, G.; PATTENDEN, R.; TRIANTAFYLLOU, M. S.; WILLDEN, R. H. J. Blind predictions of laboratory measurements of Vortex-Induced Vibrations of a tension riser. *Jounal of Fluids and Structures*, v. 21, p. 25–40, 2005. 55

CHAPLIN, J. R.; BEARMAN, P. W.; HUARTE, F. J. H.; PATTENDEN, R. J. Laboratory measurements of Vortex-Induced Vibrations of a vertical tension riser in a stepped current. *Jounal of Fluids and Structures*, v. 21, p. 3–24, 2005. 55

CHATJIGEORGIOU, I. On the parametric excitation of vertical elastic slender structures and the effect of damping in marine applications. *Applied Ocean Research*, Elsevier BV, v. 26, n. 1-2, p. 23–33, feb 2004. 51, 71

CHEN, H.; ZUO, D.; ZHANG, Z.; XU, Q. Bifurcations and chaotic dynamics in suspended cables under simultaneous parametric and external excitations. Springer Science and Business Media LLC, v. 62, n. 3, p. 623–646, 2010. 64

CHUCHEEPSAKUL, S.; MONPRAPUSSORN, T.; HUANG, T. Large strain formulations of extensible flexible marine pipes transporting fluid. Elsevier BV, v. 17, n. 2, p. 185–224, 2003. 87, 91

DA SILVA, M. R. M. C. Non-linear flexural-flexural-torsional-extensional dynamics of beams-I. Formulation. *International Journal of Solids and Structures*, v. 24, n. 12, p. 1225–1234, 1988. ISSN 00207683. 74, 75, 79, 80, 82

DA SILVEIRA, L. M. Y.; MARTINS, C. de A.; CUNHA, L. D.; PESCE, C. P. An investigation on the effect of tension variation on VIV of risers. In: *Volume 1: Offshore Technology Special Symposium on Ocean Measurements and Their Influence on Design*. [S.l.]: ASMEDC, 2007. 53

DAHL, J. M.; HOVER, F. S.; TRIANTAFYLLOU, M. S.; DONG, S.; KARNIADAKIS, G. E. Resonant vibrations of bluff bodies cause multivortex shedding and high frequency forces. *Physical Review Letters*, American Physical Society (APS), v. 99, n. 14, oct 2007. 47, 48, 49

DEFENSOR FILHO, W. A.; FRANZINI, G. R.; PESCE, C. P. An experimental investigation on the dual-resonance revealed in the VIV of flexible cantilevers with orthotropic bending stiffness. Elsevier BV, v. 126, p. 103263, 2022. 55

EL-ATTAR, M.; GHOBARAH, A.; AZIZ, T. Non-linear cable response to multiple support periodic excitation. Elsevier BV, v. 22, n. 10, p. 1301–1312, 2000. 64

FACCHINETTI, M. L.; de LANGRE, E.; BIOLLEY, F. Coupling of structure and wake oscillators in vortex-induced vibrations. *Journal of Fluids and Structures*, v. 19, p. 123–140, 2004. 48, 49, 181

FLORY, J. F.; BANFIELD, S. J.; RIDGE, I. M.; YEATS, B.; MACKAY, T.; WANG, P.; HUNTER, T.; JOHANNING, L.; HERDUIN, M.; FOXTON, P. Mooring systems for marine energy converters. In: *OCEANS 2016 MTS/IEEE Monterey*. [S.l.]: IEEE, 2016. 39

FRANZINI, G.; PESCE, C.; GONÇALVES, R.; FUJARRA, A.; MENDES, P. An experimental investigation on concomitant vortex-induced vibration and axial top-motion excitation with a long flexible cylinder in vertical configuration. *Ocean Engineering*, Elsevier BV, v. 156, p. 596–612, may 2018. 56

FRANZINI, G. R.; BUNZEL, L. O. A numerical investigation on piezoelectric energy harvesting from vortex-induced vibrations with one and two degrees of freedom. *Journal of Fluids and Structures*, Elsevier BV, v. 77, p. 196–212, feb 2018. 24, 49, 186, 190

FRANZINI, G. R.; DIAS, T.; MAZZILLI, C.; PESCE, C. P. Parametric excitation of an offshore riser using reduced-order models based on bessel-type modes: assessment on hydrodynamic coefficients effects. In: *Proceedings of the 6th International Conference on Nonlinear Science and Complexity*. [S.l.]: INPE Instituto Nacional de Pesquisas Espaciais, 2016a. 53, 54, 132

FRANZINI, G. R.; GONÇALVES, R. T.; MENEGHINI, J. R.; FUJARRA, A. L. C. Comparison between force measurements of one and two degrees-of-freedom VIV on cylinder with small and large mass ratio. In: *Proceedings of the 10th FIV 2012 - International Conference on Flow-Induced Vibrations Conference (& Flow-Induced Noise)*. [S.l.: s.n.], 2012. 47

FRANZINI, G. R.; GONÇALVES, R. T.; MENEGHINI, J. R.; FUJARRA, A. L. C. One and two degrees-of-freedom vortex-induced vibration experiments with yawed cylinders. *Journal of Fluids and Structures*, v. 42, p. 401–420, 2013. 47

FRANZINI, G. R.; MAZZILLI, C. E. N. Non-linear reduced-order model for parametric excitation of vertical and immersed slender rod. *International Journal of Non-linear Mechanics*, v. 80, p. 29–39, 2016. 54, 100, 104, 148

FRANZINI, G. R.; PESCE, C. P.; GONÇALVES, R. T.; FUJARRA, A. L. C.; MENDES, P. Experimental investigations on Vortex-Induced Vibrations with a long flexible cylinder. Part I: modal-amplitude analysis with a vertical configuration. In: *Proceedings of the 11th International Conference on Flow-Induced Vibration - FIV2016*. [S.l.: s.n.], 2016. 56

FRANZINI, G. R.; PESCE, C. P.; SALLES, R.; GONÇALVES, R. T.; FUJARRA, A. L. C.; MENDES, P. Experimental investigation with a vertical and flexible cylinder in water: response to top motion excitation and parametric resonance. *Journal of Vibration and Acoustics*, v. 137 (3), p. 031010–1 – 031010–12, 2015. 54

FRANZINI, G. R.; SANTOS, C. C. P.; MAZZILLI, C. E. N.; PESCE, C. P. Parametric excitation of an immersed, vertical and slender beam using reduced-order models: influence of hydrodynamic coefficients. *Marine Systems & Ocean Technology*, Springer Nature, v. 11, n. 1-2, p. 10–18, 2016b. 53, 54, 132

FUJARRA, A.; PESCE, C.; FLEMMING, F.; WILLIAMSON, C. Vortex-induced vibration of a flexible cantilever. *Journal of Fluids and Structures*, v. 15, p. 651–658, 2001. 55

GAMBHIR, M.; BATCHELOR, B. deV. Parametric study of free vibration of sagged cables. *Computers & Structures*, Elsevier BV, v. 8, n. 5, p. 641–648, may 1978. 59

GAY NETO, A. Dynamics of offshore risers using a geometrically-exact beam model with hydrodynamic loads and contact with the seabed. *Engineering Structures*, Elsevier BV, v. 125, p. 438–454, oct 2016. 120

GAY NETO, A. *Giraffe user's manual - generic interface readily accessible for finite elements*. 2021. Disponível em: <http://sites.poli.usp.br/p/alfredo.gay/giraffe/GIRAFFE_Manual.pdf>. 120

GAY NETO, A.; MARTINS, C. A.; PIMENTA, P. M. Static analysis of offshore risers with a geometrically-exact 3d beam model subjected to unilateral contact. *Computational Mechanics*, Springer Nature, v. 53, n. 1, p. 125–145, jul 2013. 120

GERRARD, J. H. The mechanics of the formation region of vortices behind bluff bodies. *Journal of Fluid Mechanics*, v. 25, p. 401–413, 1966. 44, 45

GONZALEZ-BUELGA, A.; NEILD, S.; WAGG, D.; MACDONALD, J. Modal stability of inclined cables subjected to vertical support excitation. Elsevier BV, v. 318, n. 3, p. 565–579, 2008. 65

GUO, T.; KANG, H.; WANG, L.; ZHAO, Y. A boundary modulation formulation for cable's non-planar coupled dynamics under out-of-plane support motion. Springer Science and Business Media LLC, v. 86, n. 4, p. 729–741, 2015. 64

GUO, T.; KANG, H.; WANG, L.; ZHAO, Y. Cable's mode interactions under vertical support motions: boundary resonant modulation. Springer Science and Business Media LLC, v. 84, n. 3, p. 1259–1279, 2015. 64

GUO, T.; KANG, H.; WANG, L.; ZHAO, Y. Cable dynamics under non-ideal support excitations: Nonlinear dynamic interactions and asymptotic modelling. Elsevier BV, v. 384, p. 253–272, 2016. 64

GUO, T.; KANG, H.; WANG, L.; ZHAO, Y. Cable's non-planar coupled vibrations under asynchronous out-of-plane support motions: travelling wave effect. Springer Science and Business Media LLC, v. 86, n. 9, p. 1647–1663, 2016. 64

GUO, T.; KANG, H.; WANG, L.; ZHAO, Y. An investigation into cables' in-plane dynamics under multiple support motions using a boundary modulation approach. Springer Science and Business Media LLC, v. 87, n. 6, p. 989–1006, 2017. 64

GUO, T.; REGA, G.; KANG, H.; WANG, L. Two perturbation formulations of the nonlinear dynamics of a cable excited by a boundary motion. Elsevier BV, v. 79, p. 434–450, 2020. 70

HAGEDORN, P.; SCHäFER, B. On non-linear free vibrations of an elastic cable. Elsevier BV, v. 15, n. 4-5, p. 333–340, 1980. 60

HARTLEN, R. T.; CURRIE, I. G. Lift-oscillator model of vortex-induced vibration. *Journal of the Engineering Mechanics Division*, American Physical Society (APS), v. 99, n. 14, oct 1970. 48

HSU, C. The response of a parametrically excited hanging string in fluid. *Journal of Sound and Vibration*, Elsevier BV, v. 39, n. 3, p. 305–316, apr 1975. 50

HUERA-HUARTE, F. J.; BEARMAN, P. W. Wake structures and vortex-induced vibrations of a long flexible cylinder - part 1:dynamic response. *Journal of Fluids and Structures*, v. 25, p. 969–990, 2009. 55

IBRAHIM, R. A. *Parametric Random Vibration*. [S.l.]: DOVER PUBN INC, 2008. ISBN 0486462625. 44

IRVINE, H. M.; CAUGHEY, T. K. The linear theory of free vibrations of a suspended cable. *Proceedings of the Royal Society*, v. 341, p. 299–315, 1974. 57, 58, 59, 62, 63, 244

IRVINE, M. *Cable Structures*. [S.l.: s.n.], 1981. 57

IWAN, W. D.; BLEVINS, R. D. A model for vortex induced oscillation of structures. ASME International, v. 41, n. 3, p. 581–586, 1974. 48

JAUVTIS, N.; WILLIAMSON, C. H. K. The effect of two degrees of freedom on vortex-induced vibration at low mass and damping. *Journal of Fluid Mechanics*, v. 509, p. 23–62, 2004. 47

JIANG, D.; PIERRE, C.; SHAW, S. W. The construction of non-linear normal modes for systems with internal resonance. Elsevier BV, v. 40, n. 5, p. 729–746, 2005. 68

KEBER, M.; WIERCIGROCH, M. Comparison of dynamical responses of an offshore riser with linear and nonlinear structural characteristics through nonlinear normal modes. In: *OCEANS 2007 - Europe*. [S.l.]: IEEE, 2007. 69

KEBER, M.; WIERCIGROCH, M. Dynamics of a vertical riser with weak structural nonlinearity excited by wakes. *Journal of Sound and Vibration*, Elsevier BV, v. 315, n. 3, p. 685–699, aug 2008. 69

KERSCHEN, G.; PEETERS, M.; GOLINVAL, J. C.; VAKAKIS, A. F. Nonlinear normal modes, part i: A useful framework for the structural dynamicist. Elsevier BV, v. 23, n. 1, p. 170–194, 2009. 69

KHALAK, A.; WILLIAMSON, C. H. K. Motions, forces and modes transitions in vortex-induced vibration at low reynolds number. *Journal of Fluids and Structures*, v. 13, p. 813–851, 1999. 46

KING, M. E.; VAKAKIS, A. F. An energy-based approach to computing resonant nonlinear normal modes. ASME International, v. 63, n. 3, p. 810–819, 1996. 68

KLODA, L.; LENCI, S.; WARMINSKI, J. Nonlinear dynamics of a planar beam–spring system: analytical and numerical approaches. Springer Science and Business Media LLC, v. 94, n. 3, p. 1721–1738, 2018. 110

KRENK, S.; NIELSEN, S. R. K. Energy balanced double oscillator model for vortex-induced vibrations. *Journal of Engineering Mechanics*, American Society of Civil Engineers (ASCE), v. 125, n. 3, p. 263–271, mar 1999. 48

LACARBONARA, W.; PAOLONE, A.; VESTRONI, F. Elastodynamics of nonshallow suspended cables: Linear modal properties. *Journal of Vibration and Acoustics*, ASME International, v. 129, n. 4, p. 425, 2007. 62, 63

LACARBONARA, W.; REGA, G. Resonant non-linear normal modes. part II: activation/orthogonality conditions for shallow structural systems. Elsevier BV, v. 38, n. 6, p. 873–887, 2003. 69

LACARBONARA, W.; REGA, G.; NAYFEH, A. H. Resonant non-linear normal modes. part i: analytical treatment for structural one-dimensional systems. Elsevier BV, v. 38, n. 6, p. 851–872, 2003. 69

LEI, S.; ZHANG, W.-S.; LIN, J.-H.; YUE, Q.-J.; KENNEDY, D.; WILLIAMS, F. W. Frequency domain response of a parametrically excited riser under random wave forces. Elsevier BV, v. 333, n. 2, p. 485–498, 2014. 136

LENCI, S.; REGA, G. Dimension reduction of homoclinic orbits of buckled beams via the non-linear normal modes technique. Elsevier BV, v. 42, n. 3, p. 515–528, 2007. 69

LENCI, S.; REGA, G. Detecting stable–unstable nonlinear invariant manifold and homoclinic orbits in mechanical systems. Springer Science and Business Media LLC, v. 63, n. 1-2, p. 83–94, 2010. 69

LIFE-MO. *Laboratório de Interação Fluido-Estrutura e Mecânica Offshore. Hydroelastic Experiments with vertical flexible cylinders in the IPT towing tank (in Portuguese). Technical Report RT-3; Part 4, Project "Nonlinear Dynamics of Risers" (sponsored by PETROBRAS)*. 2013. 86 p. 53

LUONGO, A.; REGA, G.; VESTRONI, F. Monofrequent oscillations of a non-linear model of a suspended cable. Elsevier BV, v. 82, n. 2, p. 247–259, 1982. 60

LUONGO, A.; ZULLI, D. Dynamic instability of inclined cables under combined wind flow and support motion. Springer Science and Business Media LLC, v. 67, n. 1, p. 71–87, 2011. 65, 147

MACDONALD, J. Multi-modal vibration amplitudes of taut inclined cables due to direct and/or parametric excitation. Elsevier BV, v. 363, p. 473–494, 2016. 65

MACDONALD, J.; DIETZ, M.; NEILD, S.; GONZALEZ-BUELGA, A.; CREWE, A.; WAGG, D. Generalised modal stability of inclined cables subjected to support excitations. Elsevier BV, v. 329, n. 21, p. 4515–4533, 2010. 65

MANSOUR, A.; MEKKI, O. B.; MONTASSAR, S.; REGA, G. Catenary-induced geometric nonlinearity effects on cable linear vibrations. *Journal of Sound and Vibration*, Elsevier BV, v. 413, p. 332–353, jan 2018. 63

MAZZILLI, C. E.; RIZZA, F.; DIAS, T. Heave-imposed motion in vertical risers: A reduced-order modelling based on bessel-like modes. *Procedia IUTAM*, Elsevier BV, v. 19, p. 136–143, 2016. 53, 54

MAZZILLI, C. E. N.; BARACHO NETO, O. G. P. Evaluation of non-linear normal modes for finite-element models. Elsevier BV, v. 80, n. 11, p. 957–965, 2002. 69

MAZZILLI, C. E. N.; DIAS, T. Non-linear reduced-order modelling of heave-imposed motion in vertical risers. In: *Proceedings of the 15th Pan-American Congress of Applied Mechanics - PACAM XV*. [S.l.: s.n.], 2015. 53, 54

MAZZILLI, C. E. N.; GONÇALVES, P. B.; FRANZINI, G. R. Reduced-order modelling based on non-linear modes. Elsevier BV, v. 214, p. 106915, 2022. 69

MAZZILLI, C. E. N.; LENCI, S.; DEMEIO, L. Non-linear free vibrations of tensioned vertical risers. In: *Proceedings of the 8th European Nonlinear Dynamics Conference - ENOC2014*. [S.l.: s.n.], 2014. 53, 54, 98, 110, 115, 187, 241, 242, 243, 245, 246

MAZZILLI, C. E. N.; SANCHES, C. T. Active control of vortex-induced vibrations in offshore catenary risers: A nonlinear normal mode approach. Mathematical Sciences Publishers, v. 6, n. 7-8, p. 1079–1088, 2011. 70

MAZZILLI, C. E. N.; SANCHES, C. T.; Baracho Neto, O. G. P.; WIERCIGROCH, M.; KEBER, M. Non-linear modal analysis for beams subjected to axial loads: Analytical and finite-element solutions. *International Journal of Non-linear Mechanics*, v. 43, p. 551–561, 2008. 83, 96, 241, 244

MEIROVITCH, L. *Analytical Methods in Vibrations*. [S.l.]: Macmillan, 1967. 42

MENEGHINI, J. R. *Tópicos de Pesquisa em Geração e Desprendimento de Vórtices*. 2002. Tese de Livre Docência apresentada à Escola Politécnica de Universidade de São Paulo. 44

NAYFEH, A. H. *Perturbation Methods*. [S.l.]: John Wiley & Sons, 1973. 263

NAYFEH, A. H.; BALACHANDRAN, B. *Applied Nonlinear Dynamics: Analytical, Computational and Experimental Methods*. [S.l.]: John Wiley & Sons, Inc., 1995. ISBN 0-471-59348-6. 40, 42, 263

NAYFEH, A. H.; CHIN, C.; NAYFEH, S. A. On nonlinear normal modes of systems with internal resonance. *Journal of Vibration and Acoustics*, ASME International, v. 118, n. 3, p. 340, 1996. 68

NAYFEH, A. H.; LACARBONARA, W.; CHIN, C.-M. Nonlinear normal modes of buckled beams: Three-to-one and one-to-one internal resonances. Springer Science and Business Media LLC, v. 18, n. 3, p. 253–273, 1999. 69

NAYFEH, A. H.; MOOK, D. T. *Nonlinear oscillations*. [S.l.]: John Wiley & Sons, 1979. 42, 50, 104, 105, 134, 153, 263

NAYFEH, A. H.; NAYFEH, S. A. On nonlinear modes of continuous systems. ASME International, v. 116, n. 1, p. 129–136, 1994. 69

NAYFEH, S. A.; NAYFEH, A. H.; MOOK, D. T. Nonlinear response of a taut string to longitudinal and transverse end excitation. SAGE Publications, v. 1, n. 3, p. 307–334, 1995. 65

OGINK, R. H. M.; METRIKINE, A. V. A wake oscillator with frequency dependent coupling for the modeling of vortex-induced vibration. *Journal of Sound and Vibration*, v. 329, p. 5452–5473, 2010. 48, 49

PATEL, M.; PARK, H. Dynamics of tension leg platform tethers at low tension. part i - mathieu stability at large parameters. *Marine Structures*, Elsevier BV, v. 4, n. 3, p. 257–273, jan 1991. 50, 51

PATEL, M.; PARK, H. Combined axial and lateral responses of tensioned buoyant platform tethers. *Engineering Structures*, Elsevier BV, v. 17, n. 10, p. 687–695, dec 1995. 50

PEETERS, M.; VIGUIÉ, R.; SÉRANDOUR, G.; KERSCHEN, G.; GOLINVAL, J.-C. Nonlinear normal modes, part II: Toward a practical computation using numerical continuation techniques. Elsevier BV, v. 23, n. 1, p. 195–216, 2009. 69

PERKINS, N. Modal interactions in the non-linear response of elastic cables under parametric/external excitation. Elsevier BV, v. 27, n. 2, p. 233–250, 1992. 63

PESCE, C. P. *Mecânica de cabos e tubos submersos lançados em "catenária": Uma abordagem analítica e experimental.* 1997. Tese de Livre Docência apresentada à Escola Politécnica de Universidade de São Paulo. 65, 86, 89

PESCE, C. P.; FUJARRA, A. L. C. Vortex-induced vibrations and jump phenomenon: Experiments with a clamped flexible cylinder in water. *International Journal of Offshore and Polar Engineering*, v. 10, p. 26–33, 2000. 55

PESCE, C. P.; FUJARRA, A. L. C.; SIMOS, A. N.; TANNURI, E. A. Analytical and closed form solutions for deep water riser-like eigenvalue problem. In: *Proceedings of the Ninth (9th) International Offshore and Polar Engineering Conference*. [S.l.: s.n.], 1999. 60, 65, 244, 245

PESCE, C. P.; MARTINS, C. d. A.; SILVEIRA, L. M. Y. da. Riser-Soil Interaction: Local Dynamics at TDP and a Discussion on the Eigenvalue and the VIV Problems. *Journal of Offshore Mechanics and Arctic Engineering*, v. 128, n. 1, p. 39, 2006. ISSN 08927219. Disponível em: <http://offshoremechanics.asmedigitalcollection.asme.org/article.aspx?articleid=1456013>. 23, 66, 154

PESHECK, E.; PIERRE, C.; SHAW, S. A new galerkin-based approach for accurate non-linear normal modes through invariant manifolds. Elsevier BV, v. 249, n. 5, p. 971–993, 2002. 68, 207, 209

REGA, G.; ALAGGIO, R.; BENEDETTINI, F. Experimental investigation of the nonlinear response of a hanging cable. part i. local analysis. Springer Science and Business Media LLC, v. 14, n. 2, p. 89–117, 1997. 64

REGA, G.; BENEDETTINI, F. Planar non-linear oscillations of elastic cables under subharmonic resonance conditions. Elsevier BV, v. 132, n. 3, p. 367–381, 1989. 62

REGA, G.; LACARBONARA, W.; NAYFEH, A.; CHIN, C. Multiple resonances in suspended cables: direct versus reduced-order models. Elsevier BV, v. 34, n. 5, p. 901–924, 1999. 70

REGA, G.; LUONGO, A. Natural vibrations of suspended cables with flexible supports. Elsevier BV, v. 12, n. 1, p. 65–75, 1980. 63

REGA, G.; VESTRONI, F.; BENEDETTINI, F. Parametric analysis of large amplitude free vibrations of a suspended cable. Elsevier BV, v. 20, n. 2, p. 95–105, 1984. 61

ROSENBERG, R. M. On nonlinear vibrations of systems with many degrees of freedom. In: *Advances in Applied Mechanics*. [S.l.]: Elsevier, 1966. p. 155–242. 66

RUSSELL, J. C.; LARDNER, T. J. Experimental determination of frequencies and tension for elastic cables. *Journal of Engineering Mechanics*, American Society of Civil Engineers (ASCE), v. 124, n. 10, p. 1067–1072, oct 1998. 60

SARPKAYA, T. A critical review of the intrinsic nature of vortex-induced vibrations. *Journal of Fluids and Structures*, v. 19, p. 389–447, 2004. 47

SHAW, S. W.; PIERRE, C. Normal modes for non-linear vibratory systems. *Journal of Sound and Vibration*, v. 164, p. 85–124, 1993. 66, 67, 68, 197

SIMOS, A. N.; PESCE, C. P. Mathieu stability in the dynamics of tlp's tethers considering variable tension along the length. In: *Transactions on the Built Environment, vol. 29*. [S.l.: s.n.], 1997. 50

SOARES, M. E. S.; MAZZILLI, C. E. N. Nonlinear normal modes of planar frames discretised by the finite element method. Elsevier BV, v. 77, n. 5, p. 485–493, 2000. 68

SPARKS, C. Transverse modal vibrations of vertical tensioned risers. a simplified analytical approach. *Oil & Gas Science and Technology*, EDP Sciences, v. 57, n. 1, p. 71–86, jan 2002. 189

SPARKS, C. P. The influence of tension, pressure and weight on pipe and riser deformations and stresses. ASME International, v. 106, n. 1, p. 46–54, 1984. 90

SRINIL, N.; REGA, G. Two-to-one resonant multi-modal dynamics of horizontal/inclined cables. part II: Internal resonance activation, reduced-order models and nonlinear normal modes. Springer Science and Business Media LLC, v. 48, n. 3, p. 253–274, 2006. 62

SRINIL, N.; REGA, G.; CHUCHEEPSAKUL, S. Large amplitude three-dimensional free vibrations of inclined sagged elastic cables. Springer Science and Business Media LLC, v. 33, n. 2, p. 129–154, 2003. 62

SRINIL, N.; REGA, G.; CHUCHEEPSAKUL, S. Three-dimensional non-linear coupling and dynamic tension in the large-amplitude free vibrations of arbitrarily sagged cables. *Journal of Sound and Vibration*, Elsevier BV, v. 269, n. 3-5, p. 823–852, jan 2004. 62

SRINIL, N.; REGA, G.; CHUCHEEPSAKUL, S. Two-to-one resonant multi-modal dynamics of horizontal/inclined cables. part i: Theoretical formulation and model validation. Springer Science and Business Media LLC, v. 48, n. 3, p. 231–252, 2006. 62

STAPPENBELT, B.; LALJI, F. Vortex-induced vibration super-upper branch boundaries. v. 18, p. 99–105, 2008. 47

TRIANTAFYLLOU, M. S. The dynamics of taut inclined cables. *The Quarterly Journal of Mechanics and Applied Mathematics*, Oxford University Press (OUP), v. 37, n. 3, p. 421–440, 1984. 59, 60, 61, 244

TRIANTAFYLLOU, M. S.; GRINFOGEL, L. Natural frequencies and modes of inclined cables. *Journal of Structural Engineering*, American Society of Civil Engineers (ASCE), v. 112, n. 1, p. 139–148, jan 1986. 60, 63

VERNIZZI, G. J.; FRANZINI, G. R.; LENCI, S. Reduced-order models for the analysis of a vertical rod under parametric excitation. Elsevier BV, v. 163, p. 105122, 2019. 93, 122, 123, 124, 125, 126, 127, 147, 148

VERNIZZI, G. J.; FRANZINI, G. R.; PESCE, C. P. Non-linear free vibrations of a hanging cable with small sag. In: *IUTAM Symposium on Exploiting Nonlinear Dynamics for Engineering Systems*. [S.l.]: Springer International Publishing, 2019. p. 261–270. 243, 247, 248, 249

VERNIZZI, G. J.; LENCI, S.; FRANZINI, G. R. A detailed study of the parametric excitation of a vertical heavy rod using the method of multiple scales. Springer Science and Business Media LLC, v. 55, n. 12, p. 2423–2437, 2020. 93, 128, 129, 130, 131, 132, 133, 134, 135

VERNIZZI, G. J.; LENCI, S.; FRANZINI, G. R. A discussion regarding reduced-order modelling of inclined elastic and immersed cables under support excitation. Elsevier BV, p. 104078, 2022. 143, 144, 155, 156, 157, 158, 160, 161, 162, 163, 164, 165, 166, 167, 168, 169, 170, 171, 172, 173, 174, 175, 176, 177

WANG, L.; ZHAO, Y. Large amplitude motion mechanism and non-planar vibration character of stay cables subject to the support motions. Elsevier BV, v. 327, n. 1-2, p. 121–133, 2009. 65

WARMINSKI, J.; ZULLI, D.; REGA, G.; LATALSKI, J. Revisited modelling and multimodal nonlinear oscillations of a sagged cable under support motion. Springer Science and Business Media LLC, v. 51, n. 11, p. 2541–2575, 2016. 64

WILLIAMSON, C. H. K.; GOVARDHAN, R. A brief review of recent results in vortex-induced vibrations. Elsevier BV, v. 96, n. 6-7, p. 713–735, 2008. 46

WILLIAMSON, C. H. K.; GOVARDHAN, R. N. Vortex-induced vibrations. *Annual Review of Fluids Mechanics*, v. 36, p. 413–455, 2004. 47

WU, X.; GE, F.; HONG, Y. A review of recent studies on vortex-induced vibrations of long slender cylinders. *Journal of Fluids and Structures*, v. 28, p. 292–308, 2012. 55

YANG, H.; XIAO, F. Instability analyses of a top-tensioned riser under combined vortex and multi-frequency parametric excitations. *Ocean Engineering*, Elsevier BV, v. 81, p. 12–28, may 2014. 52

YANG, H.; XIAO, F.; XU, P. Parametric instability prediction in a top-tensioned riser in irregular waves. *Ocean Engineering*, Elsevier BV, v. 70, p. 39–50, sep 2013. 52, 53

ZENG, X.; XU, W.; LI, X.; WU, Y. Nonlinear dynamic responses of the tensioned tether under parametric excitations. *in: Proceedings of the 18th International Offshore and Polar Engineering Conference, ISOPE2008*, 2008. 51

ZHOU, X.; YAN, S.; CHU, F. In-plane free vibrations of an inclined taut cable. *Journal of Vibration and Acoustics*, ASME International, v. 133, n. 3, p. 031001, 2011. 63

Appendices

APPENDIX A – Algebraic steps for the formulation of the equations of motion of straight flexible rods

In this appendix some algebraic steps used in the derivation of the equations of motion for straight beam are shown. More precisely, the steps herein presented are necessary to expand Eq. (3.20). First of all, the unit vectors of the Cartesian frame, $\widehat{i}$, $\widehat{j}$ and $\widehat{k}$, are written in the local frame as

$$\begin{aligned}
\widehat{i} &= \Big(\cos\theta_z\cos\theta_y + \sin\theta_z\sin\theta_x\sin\theta_y\Big)\,\widehat{\eta} + \Big(-\sin\theta_z\cos\theta_y + \cos\theta_z\sin\theta_x\sin\theta_y\Big)\,\widehat{\zeta} \\
&+ \cos\theta_x\sin\theta_y\widehat{\xi} = i_\eta\widehat{\eta} + i_\zeta\widehat{\zeta} + i_\xi\widehat{\xi}, \qquad \text{(A.1)}\\
\widehat{j} &= \sin\theta_z\cos\theta_x\widehat{\eta} + \cos\theta_z\cos\theta_x\widehat{\zeta} + \cos\theta_x\cos\theta_y\widehat{\xi} = j_\eta\widehat{\eta} + j_\zeta\widehat{\zeta} + j_\xi\widehat{\xi}, \qquad \text{(A.2)}\\
\widehat{k} &= \Big(-\cos\theta_z\sin\theta_y + \sin\theta_z\sin\theta_x\cos\theta_y\Big)\,\widehat{\eta} + \Big(\sin\theta_z\sin\theta_y + \cos\theta_z\sin\theta_x\cos\theta_y\Big)\,\widehat{\zeta} \\
&+ \cos\theta_x\cos\theta_y\widehat{\xi} = k_\eta\widehat{\eta} + k_\zeta\widehat{\zeta} + k_\xi\widehat{\xi}. \qquad \text{(A.3)}
\end{aligned}$$

The expression for $\mathrm{d}\vec{r}_{\mathrm{P}^*}$ becomes then

$$\begin{aligned}
\mathrm{d}\vec{r}_{\mathrm{P}^*} &= \mathrm{d}s\,\Big((1+W')k_\eta + U'i_\eta + V'j_\eta + \mathrm{d}\eta\Big)\,\widehat{\eta} \\
&+ \mathrm{d}s\,\Big((1+W')k_\zeta + U'i_\zeta + V'j_\zeta + \mathrm{d}\zeta\Big)\,\widehat{\zeta} + \mathrm{d}s\,\Big((1+W')k_\xi + U'i_\xi + V'j_\xi + \mathrm{d}\xi\Big)\,\widehat{\xi} \\
&+ \mathrm{d}s\,\Big(-C_\xi\zeta\widehat{\eta} + C_\xi\eta\widehat{\zeta} + \Big(C_\eta\zeta - C_\zeta\eta\Big)\,\widehat{\xi}\Big)\,. \qquad \text{(A.4)}
\end{aligned}$$

Now, keeping in mind that

$$i_\eta^2 + i_\zeta^2 + i_\xi^2 = j_\eta^2 + j_\zeta^2 + j_\xi^2 = k_\eta^2 + k_\zeta^2 + k_\xi^2 = 1, \qquad \text{(A.5)}$$

it follows that

$$
\begin{aligned}
&\mathrm{d}\vec{r}_{\mathrm{P}*}\cdot\mathrm{d}\vec{r}_{\mathrm{P}*} = \mathrm{d}s^2\left((1+W')^2+U'^2+V'^2+C_\xi^2\zeta^2+C_\xi^2\eta^2+C_\eta^2\zeta^2+C_\zeta^2\eta^2\right)\\
&+2\mathrm{d}s\mathrm{d}\zeta\left((1+W')\,k_\zeta+U'i_\zeta+V'j_\zeta+C_\xi\eta\right)\\
&+2\mathrm{d}s\mathrm{d}\eta\left((1+W')\,k_\eta+U'i_\eta+V'j_\eta-C_\xi\zeta\right)+\mathrm{d}\eta^2+\mathrm{d}\zeta^2\\
&+\mathrm{d}s^2\left(2\,(1+W')\,U'\left(i_\eta k_\eta+i_\zeta k_\zeta+i_\xi k_\xi\right)+2\,(1+W')\,V'\left(j_\eta k_\eta+j_\zeta k_\zeta+j_\xi k_\xi\right)\right.\\
&\left.+2U'V'\left(i_\eta j_\eta+i_\zeta j_\zeta+i_\xi j_\xi\right)\right)\\
&+\mathrm{d}s^2\left(-2C_\xi\zeta\left((1+W')\,k_\eta+U'i_\eta+V'j_\eta\right)+2C_\xi\eta\left((1+W')\,k_\zeta+U'i_\zeta+V'j_\zeta\right)\right.\\
&\left.+2\left(C_\eta\zeta-C_\zeta\eta\right)\left((1+W')\,k_\xi+U'i_\xi+V'j_\xi\right)\right).
\end{aligned}
\tag{A.6}
$$

The first aspect to be noticed is that $i_\eta j_\eta + i_\zeta j_\zeta + i_\xi j_\xi$, $i_\eta k_\eta + i_\zeta k_\zeta + i_\xi k_\xi$ and $j_\eta k_\eta + j_\zeta k_\zeta + j_\xi k_\xi$ are all zero since they are the evaluation of inner products between the unit vectors of the Cartesian frame, happening to be written in the local frame. In the sequence, it is possible to write the components of the vectors in terms of the displacements rather than in terms of the Euler angles θ_x and θ_y, leading to, for i

$$
i_\eta = \cos\theta_z\frac{(1+W')}{\sqrt{(1+W')^2+U'^2}} - \sin\theta_z\frac{U'V'}{\sqrt{(1+W')^2+U'^2+V'^2}}\frac{1}{\sqrt{(1+W')^2+U'^2}},
\tag{A.7}
$$

$$
i_\zeta = -\sin\theta_z\frac{(1+W')}{\sqrt{(1+W')^2+U'^2}} - \cos\theta_z\frac{U'V'}{\sqrt{(1+W')^2+U'^2+V'^2}}\frac{1}{\sqrt{(1+W')^2+U'^2}},
\tag{A.8}
$$

$$
i_\xi = \frac{U'}{\sqrt{(1+W')^2+U'^2+V'^2}},
\tag{A.9}
$$

then for j

$$
j_\eta = \sin\theta_z\frac{\sqrt{(1+W')^2+U'^2}}{\sqrt{(1+W')^2+U'^2+V'^2}},
\tag{A.10}
$$

$$
j_\zeta = \cos\theta_z\frac{\sqrt{(1+W')^2+U'^2}}{\sqrt{(1+W')^2+U'^2+V'^2}},
\tag{A.11}
$$

$$
j_\xi = \frac{V'}{\sqrt{(1+W')^2+U'^2+V'^2}},
\tag{A.12}
$$

and finally for k

$$k_\eta = -\cos\theta_z \frac{U'}{\sqrt{(1+W')^2 + U'^2}} - \sin\theta_z \frac{V'(1+W')}{\sqrt{(1+W')^2 + U'^2 + V'^2}} \frac{1}{\sqrt{(1+W')^2 + U'^2}}, \tag{A.13}$$

$$k_\zeta = \sin\theta_z \frac{U'}{\sqrt{(1+W')^2 + U'^2}} - \cos\theta_z \frac{V'(1+W')}{\sqrt{(1+W')^2 + U'^2 + V'^2}} \frac{1}{\sqrt{(1+W')^2 + U'^2}}, \tag{A.14}$$

$$k_\xi = \frac{1+W'}{\sqrt{(1+W')^2 + U'^2 + V'^2}}. \tag{A.15}$$

With such definitions, it is possible to evaluate some additional terms in the equations, being them

$$(1+W')\,k_\xi + U' i_\xi + V' j_\xi = \sqrt{(1+W')^2 + U'^2 + V'^2} = 1 + \varepsilon_\ell, \tag{A.16}$$

$$(1+W')\,k_\eta + U' i_\eta + V' j_\eta = 0, \tag{A.17}$$

$$(1+W')\,k_\zeta + U' i_\zeta + V' j_\zeta = 0. \tag{A.18}$$

This lets clear that a significant amount of terms in $\mathrm{d}\vec{r}_{\mathrm{P}*} \cdot \mathrm{d}\vec{r}_{\mathrm{P}*}$ are actually null. This leads to

$$\begin{aligned}\mathrm{d}\vec{r}_{\mathrm{P}*} \cdot \mathrm{d}\vec{r}_{\mathrm{P}*} &= \mathrm{d}\eta^2 + \mathrm{d}\zeta^2 + 2\mathrm{d}s\mathrm{d}\zeta C_\xi \eta - 2\mathrm{d}s\mathrm{d}\eta C_\xi \zeta \\ &+ \mathrm{d}s^2 \left((1+\varepsilon_\ell)^2 - 1 + \left(\eta^2 + \zeta^2\right) C_\xi^2 + \left(\zeta C_\eta - \eta C_\zeta\right)^2 + 2\,(1+\varepsilon_\ell)\left(\zeta C_\eta - \eta C_\zeta\right)\right).\end{aligned} \tag{A.19}$$

With this last expression, the algebraic steps are completed.

APPENDIX B – Vibration modes of rods under varying traction

In this appendix, the mathematical procedure presented in Mazzilli, Lenci & Demeio (2014) is detailed, with some observations made when considered valuable to do so. This is made considering the extensive use of the formulation presented in the paper along this thesis.

The work starts with the equation of motion for transversal vibrations of a vertical beam under varying tension, already considering the static condensation procedure shown in Mazzilli et al. (2008). The resulting equation can be obtained from Eq. (4.12) by removing the damping terms and the top-motion excitation, leading to

$$\mu\ddot{V} + EIV'''' - \gamma_s V' - (\gamma_s Z + T_b)\, V'' - \frac{EA}{2\ell} V'' \int_0^\ell (V')^2 \, \mathrm{d}Z = 0. \tag{B.1}$$

The potential added mass μ_a is also not indicated since it is merely a change in the value of the inertial term for the case at hand. The authors proceed with an application of the Galerkin method in the temporal domain rather than the spatial one, which is not commonly found in the literature for this type of analysis. Let then the solution to be sought as

$$V(Z,t) = v(Z) \sin \omega t, \tag{B.2}$$

with ω being a natural frequency of the structure. The Galerkin projection in this case can be defined as an integral over one period of vibration, resulting in the equation for the modal shapes given by

$$EIv'''' - \gamma_s v' - (\gamma_s Z + T_b)\, v'' - \frac{3EA}{8\ell} v'' \int_0^\ell (v')^2 \, \mathrm{d}Z - \mu\omega^2 \ddot{v} = 0. \tag{B.3}$$

Now, considering the typical scenario of the offshore engineering, the geometrical stiffness is usually dominant over the flexural stiffness in the global behaviour. This motivates for an adaptation of Eq. (B.3) into a cable-like equation. To that end, consider the function $N(Z)$, named fictitious additional 'normal' force given as

$$EIv'''' - \frac{3EA}{8\ell} v'' \int_0^\ell (v')^2 \, \mathrm{d}Z = -Nv''. \tag{B.4}$$

With that, the equation for the modal shapes becomes

$$\left(N + (\gamma_s Z + T_b)\right) v'' + \gamma_s v' + \mu\omega^2 \ddot{v} = 0, \tag{B.5}$$

which is the equation of transverse motions of a cable under varying traction. In order to compute N, an approximation is introduced in Mazzilli, Lenci & Demeio (2014), namely, it is given as $N = N_{0n}$, where N_{0n} is the solution of Eq. (B.4) when the linear modes of a beam under constant normal force are used, that is,

$$v = v_{0n} \sin\left(\frac{n\pi Z}{\ell}\right). \tag{B.6}$$

The constant n is the number of the sought mode of vibration. Due to the nonlinear term present in Eq. (B.4), the value of the fictitious normal force is dependent on the amplitude of vibration v_{0n}, leading to a dependence of both the modal shape and the natural frequency on the amplitude of response. It is important to highlight that the nonlinearity at hand always introduces a hardening effect for the case of imposed boundary motion. Following, for a given amplitude v_{0n}, Eq. (B.5) becomes the Bessel equation, whose solution is given in terms of the Bessel functions of first and second kind with order zero. Finally, considering the typical range of values of the structural parameters involved, it is possible to obtain an analytical expression for the solutions of Eq. (B.5) by means of an asymptotic approach as detailed in Mazzilli, Lenci & Demeio (2014). Considering the linear modes, that is, setting $v_{0n} = 0$ in the evaluation of N_{0n}, this procedure leads to the solution

$$v = \sqrt[4]{\frac{T_b + EI\left(n\pi/\ell\right)^2}{T_b + EI\left(n\pi/\ell\right)^2 + \gamma_s Z}} \sin\left(n\pi \frac{\sqrt{T_b + EI\left(n\pi/\ell\right)^2 + \gamma_s Z} - \sqrt{T_b + EI\left(n\pi/\ell\right)^2}}{\sqrt{T_b + EI\left(n\pi/\ell\right)^2 + \gamma_s \ell} - \sqrt{T_b + EI\left(n\pi/\ell\right)^2}}\right), \tag{B.7}$$

which is the modal shape used for vertical structures along this thesis. For further details, specially regarding the nonlinear extension of the vibration modes, the reader is refered to Mazzilli, Lenci & Demeio (2014).

APPENDIX C – Non-linear modes of statically curved flexible cables

In this appendix the results regarding nonlinear modes of free vibrations of cables with curved static configuration are shown. The results were presented at the "IUTAM Symposium on Exploiting Nonlinear Dynamics for Engineering Systems" (ENOLIDES2018) and at the "10th European Nonlinear Dynamics Conference" (ENOC2022), and also resulted in a publication in Vernizzi, Franzini & Pesce (2019).

Two different cases are found within this appendix. In the first one, the nonlinear vibrations of a cable with small sag are considered. The small sag hypothesis allows for some simplifications that result in the possibility of closed-form expressions to be obtained for the problem. In the second case, the problem of arbitrarily sagged cables in considered, with the investigation being made with the direct application of the MMTS over the PDEs of motion of the structure. The latter approach for the problem at hand does not allow for closed-form expression to be obtained due to the complexity of the involved expressions. It is however possible to automatize the process of obtaining the nonlinear modes with the aid of symbolic computation.

C.1 Nonlinear free vibrations of a cable with small sag

In this first part of the present appendix, the problem of a cable with small sag is considered, which has been presented at ENOLIDES2018 and is also published in Vernizzi, Franzini & Pesce (2019). The simplification adopted are mentioned along the text when appropriate, and allow for a similar use of the techniques presented in Mazzilli, Lenci & Demeio (2014). A closed-form solution is obtained, and at the end of this section it is shown that the nonlinear effect over inclined cable with small sag is that of hardening.

C.1.1 Mathematical modelling and solution

The basic model is that of Eqs. (3.59) and (3.59) with the same inertia in both directions (vibrations in air). Considering that the dynamic variation of the angle with the horizontal γ is small, the trigonometric terms may be linearized, resulting in

$$[T_s' - \gamma_s \sin\theta] + T_d' - (T_s + T_d)(\theta' + \gamma')\gamma = m\ddot{u}, \tag{C.1}$$

$$[T_s\theta' - \gamma_s \cos\theta] + (T_s\gamma)' + (T_d\gamma)' + T_d\theta' = m\ddot{v}. \tag{C.2}$$

The brackets in Eqs. (C.1) and (C.2) separate the portion of the equations of motion referent to the static equilibrium. In the sequence, a static condensation procedure is applied. Following Mazzilli et al. (2008) and Pesce et al. (1999), the inertial term in the tangential direction is disregarded. This eliminates the dynamical coupling between the two directions of motion. This procedure greatly simplifies the algebraic steps to obtain a closed-form solution, with the drawback of limiting the phenomena that can be explored with this model. In particular, the cross-over and the veering occurrences as shown in Irvine & Caughey (1974) and Triantafyllou (1984) cannot be investigated.

In addition, a scaling is proposed to simplify Eq. (C.1). Such scaling considers v of unity order, implying that v' is of order ϵ, which is a small parameter. The static curvature, θ', and the additional one, $\gamma' \approx v''$, are of order ϵ^2. This hypothesis limits the number of wavelengths that can be considered in the investigated modes, since a large number of them implies in larger additional dynamic curvature. Finally, considering the scaling between tangential and transversal displacements presented in Irvine & Caughey (1974), T_d is of order ϵ. Collecting terms only on the smallest power of ϵ in Eq. (C.1) leads to

$$EA\varepsilon_d' - T_s v'\theta' - T_s v' v'' = 0 \tag{C.3}$$

where the relations $T_d = EA\varepsilon_d$[1] and $\gamma = v'$ were used. Using a dummy variable ξ, the integration of Eq. (C.3) leads to

$$EA\varepsilon_d = C_1 + \int_0^s T_s v'\theta' \,\mathrm{d}\xi + \int_0^s T_s v' v'' \,\mathrm{d}\xi. \tag{C.4}$$

At this point it is useful to express the strain measure in terms of u and v. Considering the ordering hypothesis already presented, it is given as

$$\varepsilon_d = u' - v\theta' + \frac{(v')^2}{2}. \tag{C.5}$$

Following Mazzilli et al. (2008), the constant C_1 is obtained by means of a spatial averaging of Eq. (C.4), leading to

$$C_1 = \frac{EA}{2\ell}\int_0^\ell (v')^2 \,\mathrm{d}s - \frac{EA}{\ell}\int_0^\ell v\theta' \,\mathrm{d}s - \frac{1}{\ell}\int_0^\ell\int_0^s T_s v'\theta' \,\mathrm{d}\xi \,\mathrm{d}s - \frac{1}{\ell}\int_0^\ell\int_0^s T_s v' v'' \,\mathrm{d}\xi \,\mathrm{d}s. \tag{C.6}$$

[1] Since the problem at hand is of a cable vibrating in air, no terms of surrounding fluid pressure appear contributing to the effective traction.

The decoupled transversal equation of motion becomes

$$\theta'\left(C_1+\int_0^s T_s v'\theta'\,\mathrm{d}\xi+\int_0^s T_s v'v''\,\mathrm{d}\xi\right)+\left(T_s v'\right)'+T_s v'^2\left(\theta'+v''\right)$$
$$+v''\left(C_1+\int_0^s T_s v'\theta'\,\mathrm{d}\xi+\int_0^s T_s v'v''\,\mathrm{d}\xi\right)=\mu\ddot{v}. \tag{C.7}$$

As made in Mazzilli, Lenci & Demeio (2014), it is considered that the case of a dynamical response governed by a single mode, with the use of a temporal Galerkin scheme, adopting a solution of the form

$$v=\psi\left(s\right)\sin\left(\omega t\right). \tag{C.8}$$

The equation that defines the shape of the vibration modes is then

$$-\frac{EA\theta'}{\ell}\int_0^\ell \psi\theta'\,\mathrm{d}s-\frac{\theta'}{\ell}\int_0^\ell\left(\int_0^s T_s\psi'\theta'\,\mathrm{d}\xi\right)\mathrm{d}s+\theta'\int_0^s T_s\psi'\theta'\,\mathrm{d}\xi+T_s'\psi'+T_s\psi''+\frac{3}{4}T_s\psi'^2\psi''$$
$$+\frac{3EA}{8\ell}\psi''\int_0^\ell\left(\psi'\right)^2\,\mathrm{d}s-\frac{3}{4\ell}\psi''\int_0^\ell\int_0^s T_s\psi'\psi''\,\mathrm{d}\xi\,\mathrm{d}s+\frac{3}{4}\psi''\int_0^s T_s\psi'\psi''\,\mathrm{d}\xi+\mu\omega^2\psi=0. \tag{C.9}$$

Now, a fictitious 'normal force' N is defined as

$$-\frac{EA\theta'}{\ell}\int_0^\ell \psi\theta'\,\mathrm{d}s-\frac{\theta'}{\ell}\int_0^\ell\left(\int_0^s T_s\psi'\theta'\,\mathrm{d}\xi\right)\mathrm{d}s+\theta'\int_0^s T_s\psi'\theta'\,\mathrm{d}\xi+\frac{3}{4}T_s\psi'^2\psi''$$
$$+\frac{3EA}{8\ell}\psi''\int_0^\ell\left(\psi'\right)^2\,\mathrm{d}s-\frac{3}{4\ell}\psi''\int_0^\ell\int_0^s T_s\psi'\psi''\,\mathrm{d}\xi\,\mathrm{d}s+\frac{3}{4}\psi''\int_0^s T_s\psi'\psi''\,\mathrm{d}\xi=N\psi''. \tag{C.10}$$

This fictitious normal force can be numerically evaluated by means of a Galerkin projection, adopting for example a set of sinusoidal functions for ψ in such evaluation. Keeping in mind that the case at hand is that of a catenary with small sag, it is possible to approximate the static traction by a linear function with small error (see Pesce et al. (1999)). Letting then $T_s\approx\overline{T}=\alpha+\beta s$, the equation that rules the modal shape ψ_n, containing n half-waves along the cable span, associated with the fictitious normal force N_n is written as

$$\left(\overline{T} + N_n\right)\psi_n'' + \overline{T}'\psi_n' + \mu\omega_n^2\psi_n = 0, \tag{C.11}$$

with ω_n being the natural frequency of the desired mode. Defining now $a = \beta/\mu\omega_n^2$, $T_{bn} = \alpha + N_n$ and $T_{tn} = \alpha + \ell\beta + N_n$, it is possible to write a variable transformation given by

$$z = \frac{2\omega_n}{\beta}\sqrt{\mu\left(T_{bn} + \beta s\right)}, \tag{C.12}$$

$$s = \frac{az^2}{4} - \frac{T_{bn}}{\beta}. \tag{C.13}$$

Now, Eq (C.11) becomes

$$\frac{\mathrm{d}^2\psi_n}{\mathrm{d}z^2} + \frac{1}{z}\frac{\mathrm{d}\psi_n}{\mathrm{d}z} + \psi_n = 0. \tag{C.14}$$

The solution of this equations by means of an asymptotic approach can be found in Mazzilli, Lenci & Demeio (2014), which leads to the natural frequency

$$\omega_n = \frac{n\pi}{2\ell\sqrt{\mu}}\left(\sqrt{T_{tn}} + \sqrt{T_{bn}}\right), \tag{C.15}$$

and the modal shape

$$\psi_n = \sqrt[4]{\frac{T_{bn}}{T_{bn} + \beta s}}\sin\left(z - z_0\right). \tag{C.16}$$

The expression may be written in the original coordinate s by means of the transformation

$$z = \frac{\sqrt{T_{bn} + \beta s}}{\sqrt{T_{tn}} - \sqrt{T_{bn}}}n\pi. \tag{C.17}$$

C.1.2 Numerical example

In order to illustrate the behaviour of the nonlinear modes, consider a cable with $EA = 22970$ kN, $D = 1.57$ cm and $\mu = 1.29$ kg/m. The cable is hanged between two supports with a vertical distance given by $h = 200$ m and a horizontal distance given by

$d = 100$ m, with a static equilibrium length of $\ell = 223.73$ m. In Fig. 121, the linear and nonlinear modes with $n = 20$ are presented, considering a response amplitude equal to $A_n = 3D$. As it can be seen, there is no noticeable difference in the modal shapes, which is expected since the modal amplitude in this case is small.

Figure 121 – Mode n =20, linear solution in red and non-linear in blue with $A_n = 3D$.

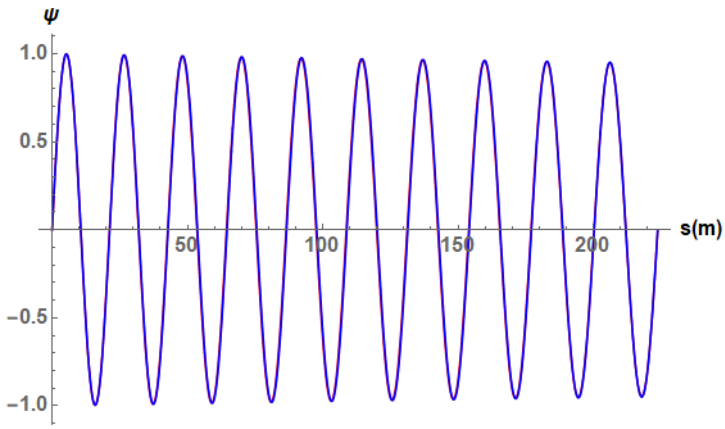

Source: Vernizzi, Franzini & Pesce (2019).

In the sequence, in Figs. 122 and 123 the linear and nonlinear modes with $n = 10$ and $n = 20$ are presented, considering now a modal amplitude of $A_n = 20D$[2]. The difference in the modal shapes is now highlighted, including alterations in the position of nodal points and in the rate of change of the vibration amplitude along the cable length. It is also possible to notice that higher modes are more affected by nonlinearities when compared to lower ones.

Figure 122 – Mode $n = 10$, linear solution in red and non-linear in blue with $A_n = 20D$.

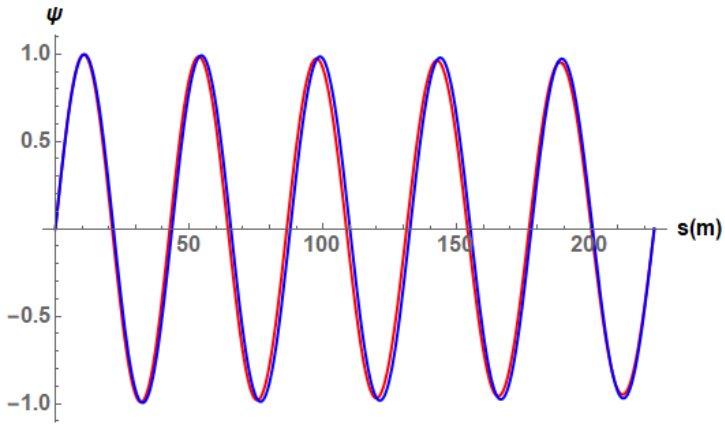

Source: Vernizzi, Franzini & Pesce (2019).

[2] Usually, the physical phenomena involved in cable applications hardly achieve such magnitude. This however is used in this work for a better illustration of the nonlinear effects over both the modal shapes and frequencies.

Figure 123 – Mode $n = 20$, linear solution in red and non-linear in blue with $A_n = 20D$.

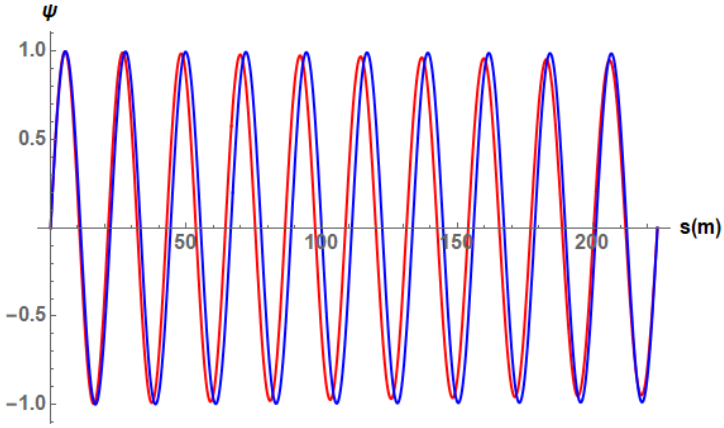

Source: Vernizzi, Franzini & Pesce (2019).

Finally, the effects of the nonlinearities over the natural frequencies are shown in Tab. 28. The modes are identified using the number of half-waves n present in the modal shape. It is possible to conclude that for this type of configurations the nonlinearities lead to a hardening behaviour of the cable, increasing the natural frequencies with the vibration amplitude. Such effect is clearly more significant for higher modes. The results in Tab. 28 are shown in graphical form by means of the backbone curves presented in Fig. 124.

Table 28 – Frequencies comparison (rad/s).

n	Linear	$A_n = 1D$	$A_n = 3D$	$A_n = 5D$	$A_n = 10D$	$A_n = 20D$
2	2.617	2.626	2.627	2.628	2.635	2.665
3	3.926	3.980	3.983	3.988	4.013	4.109
5	6.543	6.556	6.568	6.593	6.706	7.141
10	13.086	13.098	13.196	13.389	14.260	17.310
15	19.629	19.670	19.998	20.639	23.406	32.169
20	26.171	26.269	27.041	28.521	34.619	52.317
30	39.257	39.587	42.135	46.812	64.338	109.205

Figure 124 – Backbone curves for the cable in study, being ω_{n0} the natural frequency of the linear problem.

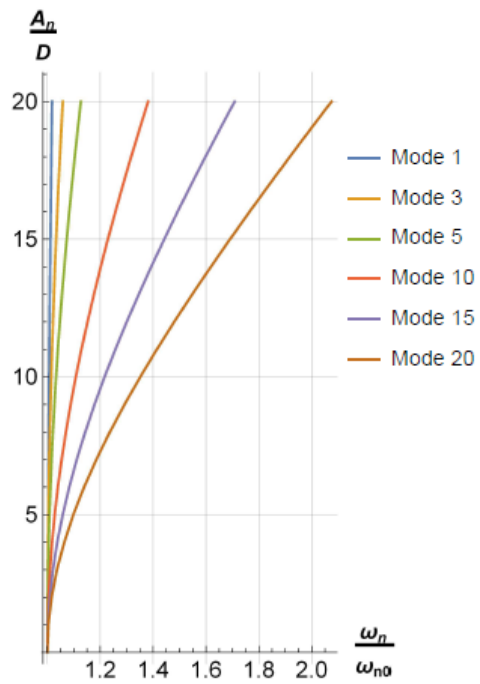

Source: Vernizzi, Franzini & Pesce (2019).

C.2 Nonlinear free vibrations of generic hanging cables

Now, the problem of an inclined cable with generic sag is considered, which has been presented at ENOC2022. The analysis is mainly made using the aid of symbolic computation in the software Mathematica®.

C.2.1 Multiple scale solution

The mathematical model under consideration is composed of the PDEs given in Eqs. (3.75) and (3.76), reproduced in the sequence for clearness.

$$
\begin{aligned}
m\ddot{u} &= T_s'\left(\frac{u'-v\theta'-\varepsilon_d}{1+\varepsilon_d}\right) - T_s\left(\frac{(u\theta'+v')\,\theta'}{(1+\varepsilon_d)} + \frac{(u\theta'+v')}{(1+u'-v\theta')}\left(\frac{(u\theta'+v')}{(1+\varepsilon_d)}\right)'\right) \\
&- \rho g A\left((u'-v\theta')\sin\theta + (v'+u\theta')\cos\theta\right)\frac{(1+u'-v\theta')}{(1+\varepsilon_d)} + EA\varepsilon_d'\frac{(1+u'-v\theta')}{(1+\varepsilon_d)} \\
&+ \left[\left(\frac{(u\theta'+v')\,\theta'}{(1+\varepsilon_d)} + \frac{(u\theta'+v')}{(1+u'-v\theta')}\left(\frac{(u\theta'+v')}{(1+\varepsilon_d)}\right)'\right)\left(-EA\varepsilon_d + \rho g A u\sin\theta + \rho g A v\cos\theta\right)\right],
\end{aligned}
\tag{C.18}
$$

$$
\begin{aligned}
m_t\ddot{v} &= T_s'\frac{(u\theta'+v')}{(1+\varepsilon_d)} + T_s\left(\frac{(1+u'-v\theta')\,\theta'}{(1+\varepsilon_d)} + \left(\frac{(u\theta'+v')}{(1+\varepsilon_d)}\right)'\right) \\
&- \rho g A\left((u'-v\theta')\sin\theta + (v'+u\theta')\cos\theta\right)\frac{(u\theta'+v')}{(1+\varepsilon_d)} - T_s\theta' + EA\varepsilon_d'\frac{(u\theta'+v')}{(1+\varepsilon_d)} \\
&+ \left[\left(\frac{(1+u'-v\theta')\,\theta'}{(1+\varepsilon_d)} + \left(\frac{(u\theta'+v')}{(1+\varepsilon_d)}\right)'\right)\left(EA\varepsilon_d - \rho g A u\sin\theta - \rho g A v\cos\theta\right)\right].
\end{aligned}
\tag{C.19}
$$

Considering only terms that are correct up to the cubic order, it is possible to write the equations of motion as

$$
m\ddot{u} + \mathcal{L}_{1,u}(u,v) + \mathcal{L}_{2,u}(u,v) + \mathcal{L}_{3,u}(u,v) = 0, \tag{C.20}
$$

$$
m_t\ddot{v} + \mathcal{L}_{1,v}(u,v) + \mathcal{L}_{2,v}(u,v) + \mathcal{L}_{3,v}(u,v) = 0, \tag{C.21}
$$

where the indexes of the differential operators $\mathcal{L}$ indicate the order of each operator and from which equation it originates from. To exemplify, $\mathcal{L}_{2,v}$ is the differential operator that contains only quadratic order terms and is originated from the transversal equation of motion. It is also important to remind that the nonlinear operators are, in general, not commutative, that is, $\mathcal{L}(u,v) \neq \mathcal{L}(v,u)$ for the nonlinear operators. In order to apply the MMTS, three time scales are created, and the displacement fields are written as

$$u = \epsilon u_1 + \epsilon^2 u_2 + \epsilon^3 u_3, \tag{C.22}$$
$$v = \epsilon v_1 + \epsilon^2 v_2 + \epsilon^3 v_3, \tag{C.23}$$
$$t_0 = t, \tag{C.24}$$
$$t_1 = \epsilon t, \tag{C.25}$$
$$t_2 = \epsilon^2 t. \tag{C.26}$$

As usual, ϵ is a small bookkeeping parameter. The time scales proposed lead to the definition of the operators

$$D_0 = \frac{\partial}{\partial t_0}, \tag{C.27}$$
$$D_1 = \frac{\partial}{\partial t_1}, \tag{C.28}$$
$$D_2 = \frac{\partial}{\partial t_2}, \tag{C.29}$$
$$\frac{\partial^2}{\partial t^2} = D_0^2 + \epsilon(2D_0D_1) + \epsilon^2(D_1^2 + 2D_0D_2). \tag{C.30}$$

Expanding the equations of motion, applying the different time scales and collecting terms of equal order of ϵ leads to three sequential problems. The problem of order ϵ^1 is given as

$$mD_0^2 u_1 + \mathcal{L}_{1,u}(u_1, v_1) = 0, \tag{C.31}$$
$$m_t D_0^2 v_1 + \mathcal{L}_{1,v}(u_1, v_1) = 0, \tag{C.32}$$

with the associated boundary conditions of that order being $u_1(t, 0) = 0$, $v_1(t, 0) = 0$, $u_1(t, \ell) = 0$ and $v_1(t, \ell) = 0$. For order ϵ^2, the problem is written as

$$mD_0^2 u_2 + \mathcal{L}_{1,u}(u_2, v_2) = -2D_0D_1u_1 - \mathcal{L}_{2,u}(u_1, v_1), \tag{C.33}$$
$$m_t D_0^2 v_2 + \mathcal{L}_{1,v}(u_2, v_2) = -2D_0D_1v_1 - \mathcal{L}_{2,v}(u_1, v_1), \tag{C.34}$$

with its boundary conditions being $u_2(t, 0) = 0$, $v_2(t, 0) = 0$, $u_2(t, \ell) = 0$ and $v_2(t, \ell) = 0$. Finally, the problem or order ϵ^3 reads

$$mD_0^2u_3 + \mathcal{L}_{1,u}(u_3, v_3) = -2D_0D_1u_2 - 2D_0D_2u_1 - \left(\mathcal{L}_{2,u}(u_1, v_2) + \mathcal{L}_{2,u}(u_2, v_1) + \mathcal{L}_{3,u}(u_1, v_1)\right), \tag{C.35}$$

$$m_tD_0^2v_3 + \mathcal{L}_{1,v}(u_3, v_3) = -2D_0D_1v_2 - 2D_0D_2v_1 - \left(\mathcal{L}_{2,v}(u_1, v_2) + \mathcal{L}_{2,v}(u_2, v_1) + \mathcal{L}_{3,v}(u_1, v_1)\right), \tag{C.36}$$

subjected to the boundary conditions $u_3(t, 0) = 0$, $v_3(t, 0) = 0$, $u_3(t, \ell) = 0$ and $v_3(t, \ell) = 0$. The solution to the problem of order ϵ^1 given in Eqs. (C.31) and (C.32) are the linear modes of vibration of the structure. Such solution can be put in the vectorial form

$$\vec{U}_1 = \{u_1, v_1\} = B(t_1, t_2)\{\phi_n, \psi_n\}e^{(i\omega_n t_0)} + \text{c.c.}. \tag{C.37}$$

The choice for a vectorial representation will be justified in the application on the subsequent problems. In Eq. (C.37), ϕ_n and ψ_n are the axial and transversal shapes of the nth mode of vibration of the structure, with associated linear natural frequency ω_n and B is its modulated amplitude. The natural modes and frequencies are obtained numerically by Mathematica®. Applying the solution of first order to Eqs. (C.33) and (C.34) leads to

$$mD_0^2u_2 + \mathcal{L}_{1,u}(u_2, v_2) = -2i\omega_n(D_1B)e^{(i\omega_n t_0)}\phi_n - \left(B^2e^{(2i\omega_n t_0)} + BB^*\right)\mathcal{L}_{2,u}(\phi_n, \psi_n) + \text{c.c.}, \tag{C.38}$$

$$m_tD_0^2v_2 + \mathcal{L}_{1,v}(u_2, v_2) = -2i\omega_n(D_1B)e^{(i\omega_n t_0)}\psi_n - \left(B^2e^{(2i\omega_n t_0)} + BB^*\right)\mathcal{L}_{2,v}(\phi_n, \psi_n) + \text{c.c..}, \tag{C.39}$$

Now, in order to proceed, a solvability condition must be applied to Eqs. (C.38) and (C.39). This is done by applying the Fredholm Alternative Theorem (See Appendix D) to ensure a solution exists for those equations. For that, consider the adjoint problem that is given by

$$mD_0^2\overline{u} + \overline{\mathcal{L}}_{1,u}(\overline{u}, \overline{v}) = 0, \tag{C.40}$$

$$m_tD_0^2\overline{v} + \overline{\mathcal{L}}_{1,v}(\overline{u}, \overline{v}) = 0, \tag{C.41}$$

where the overbar is used to denote the adjoint quantities. Notice that inertial terms are self-adjoint. For the particular case of cables hanging of fixed supports, the boundary conditions are also self-adjoint. From the latter system of equations, the correspondent modes of vibration of the adjoint problem are obtained, being labelled $\overline{\phi}_n$ and $\overline{\psi}_n$. Since all

involved boundary terms evaluate to zero, the condition of Fredholm Alternative Theorem in this case reduces to ensure that the forcing vector composed of the forcing terms in Eqs. (C.38) and (C.39) is orthogonal to the adjoint modes. This conditions leads to

$$-2i\omega_n(D_1B)\int_0^\ell \overline{\phi}_n\phi_n + \overline{\psi}_n\psi_n \,\mathrm{d}s = 0, \tag{C.42}$$

with i denoting the imaginary constant. In this application, it is used the hypothesis that no internal resonances are activated, resuming the evaluation to the only single mode of vibration considered in Eq. (C.37). This solvability condition implies in $B = B(t_2)$, that is, no modulation occurs at the time scale t_1. Returning this condition to Eqs. (C.38) and (C.39) and solving the remaining terms leads to the solution of order ϵ^2 being

$$u_2 = B^2e^{(2i\omega_n t_0)}\phi_{2,a} + BB^*\phi_{2,b} + \text{c.c.}, \tag{C.43}$$
$$v_2 = B^2e^{(2i\omega_n t_0)}\psi_{2,a} + BB^*\psi_{2,b} + \text{c.c.}. \tag{C.44}$$

The new spatial functions $\phi_{2,a}$, $\phi_{2,b}$, $\psi_{2,a}$ and $\psi_{2,b}$ are obtained from

$$-4m\omega_n^2\phi_{2,a} + \mathcal{L}_{1,u}(\phi_{2,a},\psi_{2,a}) = -\mathcal{L}_{2,u}(\phi_n,\psi_n), \tag{C.45}$$
$$-4m_t\omega_n^2\psi_{2,a} + \mathcal{L}_{1,v}(\phi_{2,a},\psi_{2,a}) = -\mathcal{L}_{2,v}(\phi_n,\psi_n), \tag{C.46}$$
$$\mathcal{L}_{1,u}(\phi_{2,b},\psi_{2,b}) = -\mathcal{L}_{2,u}(\phi_n,\psi_n), \tag{C.47}$$
$$\mathcal{L}_{1,v}(\phi_{2,b},\psi_{2,b}) = -\mathcal{L}_{2,u}(\phi_n,\psi_n), \tag{C.48}$$

subjected to the same boundary conditions of the main problem. With the solution of order ϵ^2 defined, it is now possible to move on to the order ϵ^3 problem, which is now written as

$$\begin{aligned} &mD_0^2u_3 + \mathcal{L}_{1,u}(u_3,v_3) = (-2i\omega_n(D_2B)e^{(i\omega_n t_0)}\phi_n + \text{c.c.}) \\ &-\left(\mathcal{L}_{2,u}(u_1,v_2) + \mathcal{L}_{2,u}(u_2,v_1) + \mathcal{L}_{3,u}(u_1,v_1)\right), \end{aligned} \tag{C.49}$$
$$\begin{aligned} &m_tD_0^2v_3 + \mathcal{L}_{1,v}(u_3,v_3) = (-2i\omega_n(D_2B)e^{(i\omega_n t_0)}\psi_n + \text{c.c.}) \\ &-\left(\mathcal{L}_{2,v}(u_1,v_2) + \mathcal{L}_{2,v}(u_2,v_1) + \mathcal{L}_{3,v}(u_1,v_1)\right). \end{aligned} \tag{C.50}$$

For a better evaluation of the solvability condition, the operators are expanded in terms according to each of its resulting frequencies. Such terms are in relations of 1:1, 2:1, 3:1 and 4:1 with the natural frequency ω_n, and, in this work, it is considered that

no internal resonances of the types 2:1, 3:1 and 4:1 exist. The collection of terms and operations are made with symbolic computation, being written as

$$
\begin{aligned}
&mD_0^2u_3 + \mathcal{L}_{1,u}(u_3, v_3) = -2i\omega_n(D_2B)e^{(i\omega_n t_0)}\phi_n + (\Gamma_{0,ua}BB^* + \Gamma_{0,ub}(BB^*)^2) \\
&+ \Gamma_{1,u}B^2B^*e^{(i\omega_n t_0)} + (\Gamma_{2,ua}B^2 + \Gamma_{2,ub}B^3B^*)e^{(2i\omega_n t_0)} + \Gamma_{3,u}B^3e^{(3i\omega_n t_0)} \\
&+ \Gamma_{4,u}B^4e^{(4i\omega_n t_0)} + \text{c.c.}, \qquad \text{(C.51)} \\
&m_tD_0^2v_3 + \mathcal{L}_{1,v}(u_3, v_3) = -2i\omega_n(D_2B)e^{(i\omega_n t_0)}\psi_n + (\Gamma_{0,va}BB^* + \Gamma_{0,vb}(BB^*)^2) \\
&+ \Gamma_{1,v}B^2B^*e^{(i\omega_n t_0)} + (\Gamma_{2,va}B^2 + \Gamma_{2,vb}B^3B^*)e^{(2i\omega_n t_0)} + \Gamma_{3,v}B^3e^{(3i\omega_n t_0)} \\
&+ \Gamma_{4,v}B^4e^{(4i\omega_n t_0)} + \text{c.c.}. \qquad \text{(C.52)}
\end{aligned}
$$

The terms Γ are not reported since they can be excessively lengthy and not directly treatable, making the use of symbolic computation mandatory in this procedure. Using orthogonality conditions, and recalling that no internal resonances are being considered, the solvability condition for this order reads

$$
-2i\omega_n(D_2B)\int_0^\ell \overline{\phi}_n\phi_n + \overline{\psi}_n\psi_n \,\mathrm{d}s + B^2B^*\int_0^\ell \overline{\phi}_n\Gamma_{1,u} + \overline{\psi}_n\Gamma_{1,v}\,\mathrm{d}s = 0. \qquad \text{(C.53)}
$$

Let now $B = \frac{R}{2}e^{i\beta}$, with R and β being real-valued functions. By separating the imaginary and real parts of the solvability condition leads to

$$
D_2R = 0, \qquad \text{(C.54)}
$$

$$
D_2\beta = R^2\Lambda \Rightarrow \beta = \beta_0 + R^2\Lambda t_2, \qquad \text{(C.55)}
$$

where

$$
\Lambda = \frac{-\int_0^\ell \overline{\phi}_n\Gamma_{1,u} + \overline{\psi}_n\Gamma_{1,v}\,\mathrm{d}s}{8\omega_n\int_0^\ell \overline{\phi}_n\phi_n + \overline{\psi}_n\psi_n\,\mathrm{d}s}. \qquad \text{(C.56)}
$$

With the use of the solvability condition, Eqs. (C.51) and (C.52) can be numerically solved to obtain u_3 and v_3. The final solution may then be written as

$$
u = A_m\cos\left(\left(\omega_n + A_m^2\Lambda\right)t + \beta_0\right)\phi_n + \epsilon^2u_2 + \epsilon^3u_3, \qquad \text{(C.57)}
$$

$$
v = A_m\cos\left(\left(\omega_n + A_m^2\Lambda\right)t + \beta_0\right)\psi_n + \epsilon^2v_2 + \epsilon^3v_3, \qquad \text{(C.58)}
$$

where the amplitude A_m is related to R by $a_m = \epsilon R$. In the final solution, the relation between the amplitude of vibration and the natural frequency is also shown, being given as

$$\omega = \omega_n \left(1 + \frac{A_m^2 \Lambda}{\omega_n}\right), \tag{C.59}$$

where it is clear that the sign of Λ defines if the behaviour of the structure will be of hardening or softening. Recall also that the solutions of order ϵ^2 and ϵ^3 contain terms that do not oscillate, meaning that the average configuration of the nonlinear modes is not the static one.

C.2.2 Numerical examples

In order to illustrate the type of results that can be obtained with the developed solution, some examples are presented. To that end, consider the data presented in Tab. 29, and a chord distance between supports of 2350 m.

Table 29 – Common data for the worked examples.

Property	Value
m	108.0 kg/m
m_t	141.0 kg/m
γ_s	727.0 N/m
EA	2314.0×10^6 N
ρ	1025 kg/m^3
D	0.5588 m
H	680.5×10^3 N

The parameter H is the horizontal component of the traction of the cable at the bottom support. Consider now four different scenarios for evaluation. Scenario (i) is defined by an inclination angle of 30 degrees between supports. Following, scenario (ii) is defined also with an inclination of 30 degrees between support, but the horizontal traction at the bottom support is reduced to 475×10^3 N. In scenario (iii), an inclination of 60 degrees is considered. Finally, in scenario (iv) an inclination of 60 degrees is repeated with an increment on the transversal inertia to $m_t = 207.0$ kg/m. For scenario (i) the static configuration, the modal shape and the backbone curve of the first mode of vibration are shown in Figs. 125 to 127. In all scenarios, the amplitude considered to evaluate the modal shapes is of $100D$. Notice that this level of amplitude is quite large for a series of phenomena, being herein used for illustrative purposes.

In this first example, asides the influence over the natural frequency, the changes are small. It is possible to see a slight difference in the modal shape when the nonlinear mode is considered, as well as a small average deviation from the static configuration. One

Figure 125 – Static configuration of the cable for scenario (i).

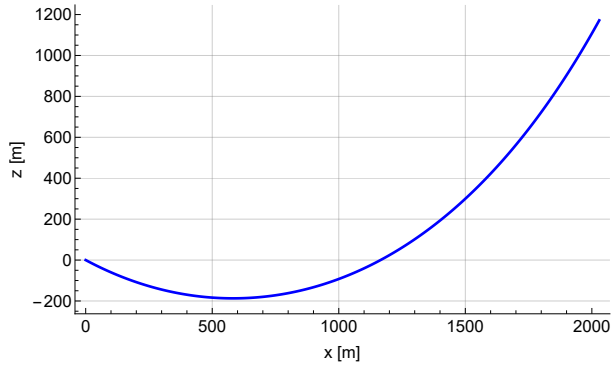

Source: The author.

Figure 126 – Linear, nonlinear and average configuration of the first mode of vibration for scenario (i).

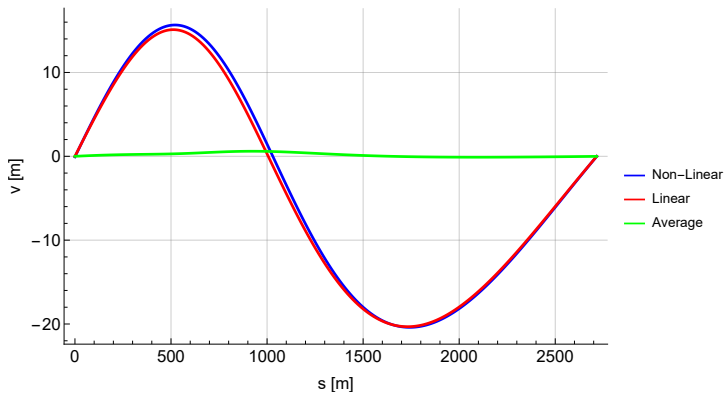

Source: The author.

condition that leads to more noticeable nonlinear effects is the reduction of the linear stiffness of a structure. That said, consider now the results in Figs. 128 to 130, relative to scenario (ii).

As expected, the nonlinear effects indeed produced more visible effects in this case. There is a significant difference between the linear and nonlinear modes, as well as a noticeable shift in the position of the nodal point. The average configuration of the nonlinear mode is also more pronounced. One interesting aspect is that the greater effects over the modal shapes occur with the counterpart of a less significant influence over the natural frequency, as it can be seen by the values achieved in the backbone curve. Moving further into the examples, the influence of the inclination is shown in scenario (iii), with the correspondent results being presented in Figs. 131 to 133.

Comparing the results of scenario (iii) with scenario (i) it is possible to notice that the influence of the nonlinear terms over the modal shapes and frequencies is significantly larger when the inclination is risen. It is interesting to notice that the influence over the modal shape is more visible in the second half-wave in the modal shape, while in scenario

Figure 127 – Backbone curve of the first mode of vibration for scenario (i).

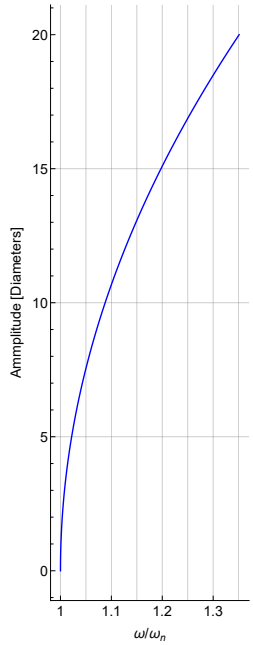

Source: The author.

Figure 128 – Static configuration of the cable for scenario (ii).

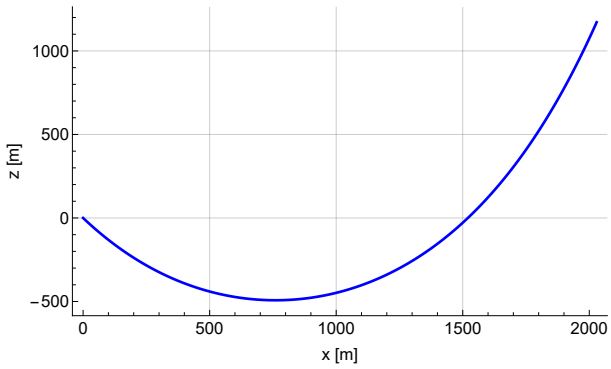

Source: The author.

(ii) the reducing of the linear stiffness lead to significant changes over the entire span of the cable. Regarding the average configuration of the nonlinear mode, notice that while for the small inclination case there were both negative and positive values, in scenario (iii) the average configuration has the same sign in all the cable length. Finally, the effects of different inertia between the directions of motion is shown in scenario (iv) by means of the results shown in Figs. 131 to 133. Recall that in problems involving immersed structures, the added mass coefficients in the transversal and tangential directions are not the same.

As it can be seen, the effects of the variation of inertial terms is restricted to the amplitude-frequency relation, as it can be seen by the values of the backbone curve. In what concerns the modal shapes, no difference can be noticed.

Figure 129 – Linear, nonlinear and average configuration of the first mode of vibration for scenario (ii).

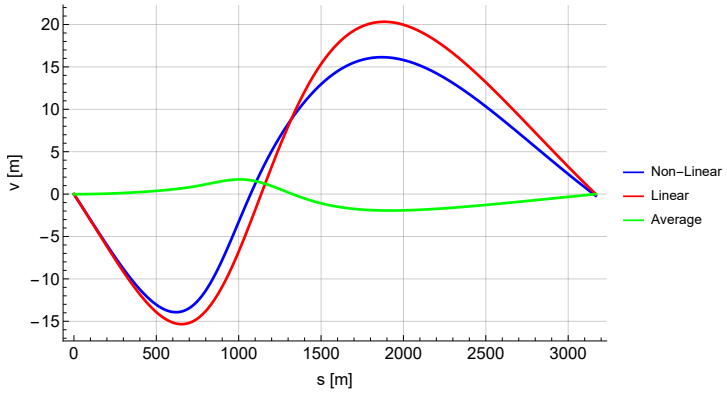

Source: The author.

Figure 130 – Backbone curve of the first mode of vibration for scenario (ii).

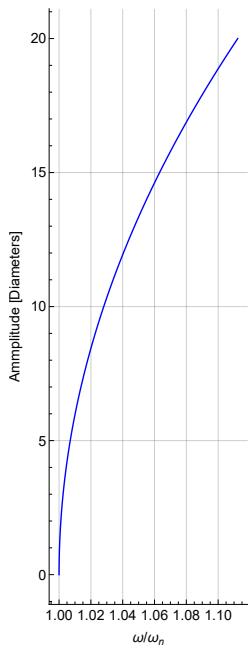

Source: The author.

C.3 Final remarks

This appendix presented two different approaches for obtaining nonlinear modes of vibration for elastic cables. In one of them, the condition of small sag is adopted, while in the second this requirement is dropped. It is expected that the techniques and explanations herein provided can be useful for future researches and analysts as tools for more complex analysis and for order reducing purposes.

Figure 131 – Static configuration of the cable for scenario (iii).

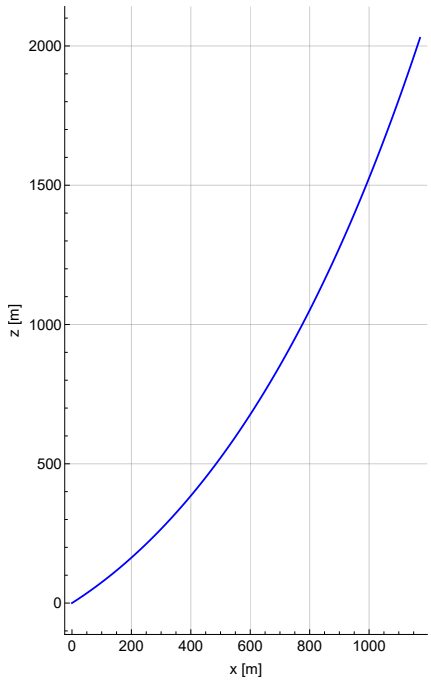

Source: The author.

Figure 132 – Linear, nonlinear and average configuration of the first mode of vibration for scenario (iii).

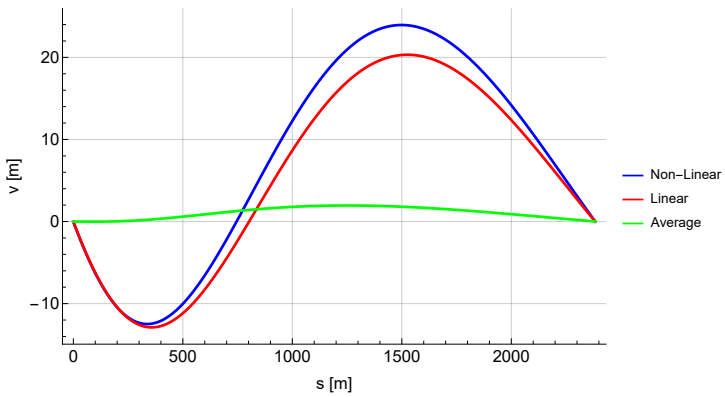

Source: The author.

Figure 133 – Backbone curve of the first mode of vibration for scenario (iii).

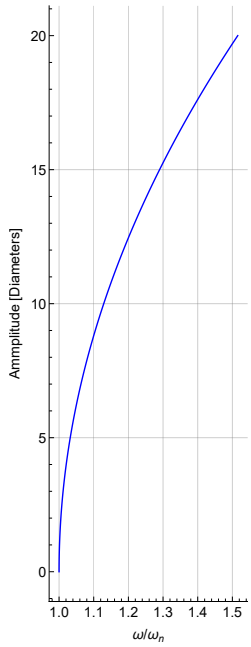

Source: The author.

Figure 134 – Static configuration of the cable for scenario (iv).

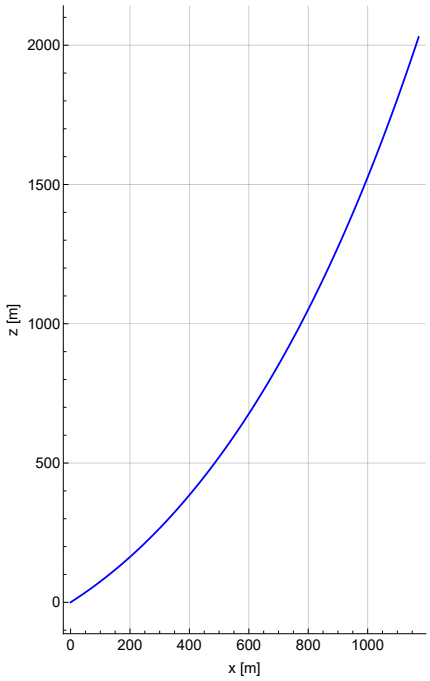

Source: The author.

Figure 135 – Linear, nonlinear and average configuration of the first mode of vibration for scenario (iv).

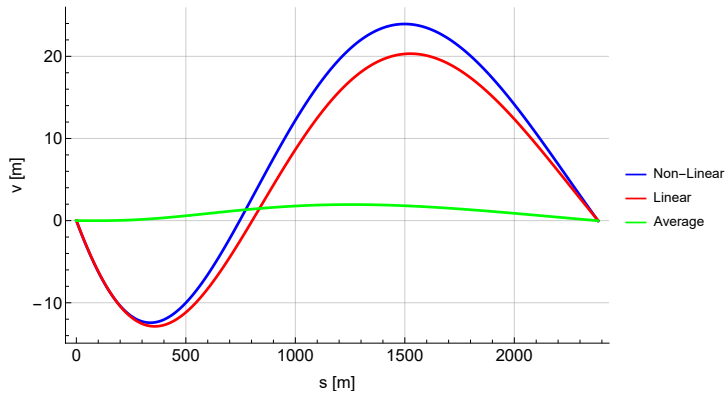

Source: The author.

Figure 136 – Backbone curve of the first mode of vibration for scenario (iv).

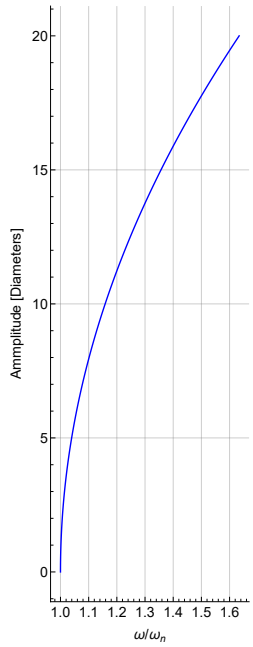

Source: The author.

APPENDIX D – A mathematical justification for the solvability condition of the MMTS

In this appendix, some mathematical background is presented in order to justify some steps on the application of MMTS. This is made since the method is largely used along the present thesis, and also because, although there is plenty of materials showing the procedures for the application of the method, it is hard to find, if even possible, texts with a detailed description of the mathematical reason behind some steps.

This appendix starts then with the classical application, which involves the solution of dynamical systems governed by an ODE of second order. Following, the justification is made for general systems of ODEs. Finally, the case of PDEs is evaluated, with a clear mathematical statement on how to obtain the solvability condition.

D.1 Justification for an ODE of second order

The case of a single ODE of second order is the most common example of application of MMTS. Many textbooks have examples regarding this particular problem, for instance, Nayfeh (1973), Bender & Orszag (1978), Nayfeh & Mook (1979), Nayfeh & Balachandran (1995), and certainly many others. To clarify this exposition, consider the general second order ODE given by

$$\ddot{x} + \omega^2 x = f(x, \dot{x}, t), \tag{D.1}$$

where f is a generic function, commonly nonlinear. The general procedure of any solution using MMTS involves solving a sequence of oscillators obtained from a proper scaling of the original one in Eq. (D.1), which can be put on the general format

$$D_0^2 x_i + \omega^2 x_i = f_{i-1}. \tag{D.2}$$

In Eq. (D.2), D_0 is the partial derivative operator with respect to the base time-scale t_0, x_i is the solution of order i and f_{i-1} is a function, usually nonlinear, composed of all the solutions up to order $i-1$. This is simply the problem of a linear oscillator, without damping, presentiong a natural frequency ω under the action of known forcing terms. Since the main hypothesis on the scaling used on the method is that the solutions

occur in different orders, it is then expected that the solution of each individual problem given in Eq. (D.2) exists and it is bounded. From basic results for linear oscillators it is easy to see that, for this case, such conditions are satisfied when there are no terms in f_{i-1} with frequency ω. Hence the common explanation found in classical textbooks that the solvability is ensured by eliminating resonant terms.

D.2 Justification for a generic system of ODEs

Suppose now that one is interested in applying MMTS to a system of ODEs. Consider also that this system is not necessarily of an oscillator, and not necessarily being a system of second order. In general form, the system of ODEs is given as

$$\mathcal{A}\vec{x} = \mathcal{F}(\vec{x}, \dot{\vec{x}}, t). \tag{D.3}$$

This time, $\mathcal{A}$ is a known linear differential operator applied to the vector $\vec{x}$, while $\mathcal{F}$ is a generic vectorial function. Holding to the main aspect of the MMTS that is, a sequence of simpler problems that can be solved and then used as input for the subsequent problem, the general form at order i is given as

$$\mathcal{A}_0\vec{x}_i = \mathcal{F}_{i-1}(\vec{x}, \dot{\vec{x}}). \tag{D.4}$$

The operator $\mathcal{A}_0$ is identical in form to $\mathcal{A}$, the difference being only in the fact that it operates with derivatives on the first time scale rather than on the original time coordinate. Analogous to the case of a single equation, $\mathcal{F}_{i-1}$ contains only terms involving solutions of order $i-1$ or smaller. The first idea that comes to mind is to look into the mathematical meaning of the natural frequencies and modes of vibration, leading to the use of the eigenvectors of the homogeneous problem $\mathcal{A}_0\vec{x}_i = 0$. It would be then an initial attempt to define the solvability condition as requiring the forcing terms $\mathcal{F}_{i-1}$ to be orthogonal to the eigenvectors of the homogeneous problem, thus ensuring the existence of a particular solution for Eq. (D.4). This however is only true for self-adjoint systems. The actual solvability conditions must be obtained with the use of the Fredholm Alternative Theorem. This theorem states that Eq. (D.4) has a solution if and only if $\left\langle \mathcal{F}_{i-1},\ \vec{v} \right\rangle = 0$ for all $\vec{v}$ satisfying $\mathcal{A}_0^*\vec{v} = 0$, that is, the eigenvectors of the homogeneous adjoint problem, with the angles indicating the operation of a suitable inner product. This ensures that, for self-adjoint systems, the adoption of the eigenvectors of $\mathcal{A}_0\vec{x}_i = 0$ is indeed correct. The adjoint operator is defined as

$$\langle \mathcal{A}_0\vec{x}_i,\ \vec{v} \rangle = \langle \vec{x}_i,\ \mathcal{A}_0^*\vec{v} \rangle\,. \tag{D.5}$$

From the definition of the adjoint operator it is easy to verify that the condition actually holds when $\vec{v}$ are eigenvectors of the adjoint homogeneous problem, by doing

$$\left\langle \mathcal{F}_{i-1},\ \vec{v} \right\rangle = \langle \mathcal{A}_0 \vec{x}_i,\ \vec{v} \rangle = \langle \vec{x}_i,\ \mathcal{A}_0^* \vec{v} \rangle = \left\langle \vec{x}_i,\ \vec{0} \right\rangle = 0. \tag{D.6}$$

A final remark is now made on a possible approximation and simplifying procedure, that is, to consider only one of the eigenvectors of the homogeneous problem to be significant in the response, and then performing the evaluation of the solvability condition only for the corresponding eigenvector of the adjoint problem. This is feasible when internal resonances in the original problem are not under consideration. Otherwise, the adequate span of eigenvectors and their adjoint counterparts must be considered.

With the exposed, it is possible to conclude that the intermediary steps for the solution with MMTS is simply a consequence of a mathematical condition for the existence of such solutions. Note however that nothing ensures that the adopted scaling will lead to the actual correct solution for the problem. Alongside it, no guarantees are made regarding if the expansion in the different scales is actually capable of obtaining the correct solution for a given problem.

D.3 Justification for a generic system of PDEs

Finally, focus is placed on the case of systems governed by PDEs. The use of MMTS on such systems can be found in the literature, however, the actual derivation and reasoning behind the definition of the solvability conditions are often obscure, without a proper didactic exposure on how to obtain such condition and where do they come from. This is particularly troublesome for the PDE case since boundary conditions may play a significant role on the solvability, even in cases where the operator is self-adjoint, since the self-adjointness of the operator does not ensure that the corresponding boundary conditions are also self-adjoint. Let then a system of PDEs to be defined as

$$\mathcal{A}\vec{x} = \mathcal{F}(\vec{x}, \dot{\vec{x}}, t). \tag{D.7}$$

Notice that the generic expression is the same as for the case of the system of ODEs. The only difference is that now the operator $\mathcal{A}$ involves partial derivatives accordingly to all the involved coordinates, including time, and the vector of variables $\vec{x}$ is a function of multiple coordinates as well. Yet again, the general problem to be solved at each step of MMTS is given by

$$\mathcal{A}_0 \vec{x}_i = \mathcal{F}_{i-1}(\vec{x}, \dot{\vec{x}}). \tag{D.8}$$

Let now the inner product between two vectorial functions $\vec{u}$ and $\vec{v}$ to be defined as

$$\langle \vec{u},\ \vec{v} \rangle = \int_{\Omega} \vec{u} \cdot \vec{v}\, \mathrm{d}\Omega, \tag{D.9}$$

where the centralized dot indicates the classical scalar product between vectors and Ω is the domain of the problem with exception to the time coordinate. Since the operator $\mathcal{A}_0$ in this case comprises derivatives applied to the functions over which it operates, the process to obtain the adjoint operator $\mathcal{A}_0^*$ involves the use of integration by parts. In this case, the definition of the adjoint leads to

$$\langle \mathcal{A}_0 \vec{x}_i,\ \vec{v} \rangle = \langle \vec{x}_i,\ \mathcal{A}_0^* \vec{v} \rangle + \mathcal{B}(\Omega). \tag{D.10}$$

The new term $\mathcal{B}$ represents the resulting boundary conditions that appear from the process of integrating by parts the left-hand side in order to obtain the adjoint operator. The Fredholm Alternative now becomes given by

$$\left\langle \mathcal{F}_{i-1},\ \vec{v} \right\rangle = \mathcal{B}. \tag{D.11}$$

Here the importance of the boundary conditions is evident. It must be remarked that there are cases in which $\mathcal{B}$ is identically null, but this is not true for any problems. Common scenarios in the dynamics of slender structures that are significantly affected by the existence of such terms are those of applied forces at the boundaries or springs positioned at the ends of the structure.

For the particular cases where the method is applied in this thesis, it results that $\mathcal{B} = 0$.

APPENDIX E – Coefficients for the polynomial solution of vertical rods under parametric excitation

In this appendix the coefficients for the polynomial solution obtained in Chapter 4 are presented.

Table 30 – Coefficients for the polynomials considering the first mode of vibration.

	C_0	C_1	C_2	C_3	C_4	C_5	C_6	C_7	C_8	C_9	C_{10}
p_1	0.49989	-0.12323	0.054993	-0.023955	0.008206	-0.002023	0.00034469	-3.928×10^{-5}	2.8454×10^{-6}	-1.1817×10^{-7}	2.1387×10^{-9}
p_2	0.42424	-0.15628	0.078268	-0.035781	0.012538	-0.0031278	0.00053662	-6.1416×10^{-5}	4.4621×10^{-6}	-1.857×10^{-7}	3.366×10^{-9}
p_3	2.4497	-4.0105	3.3631	-1.9955	0.80227	-0.21641	0.038959	-0.0046032	0.00034197	-1.4466×10^{-5}	2.6548×10^{-7}
p_4	-1.3848	1.9605	-1.7669	1.0785	-0.43948	0.11941	-0.021592	0.0025585	-0.00019045	8.0682×10^{-6}	-1.4824×10^{-7}
p_5	0.019397	7.0665	-4.027	2.2974	-0.90994	0.24367	-0.043686	0.0051482	-0.00038178	1.613×10^{-5}	-2.9574×10^{-7}
p_6	2.451	-3.3542	2.9548	-1.7846	0.72329	-0.19594	0.035365	-0.0041854	0.00031129	-1.3179×10^{-5}	2.4202×10^{-7}
p_7	-9.8644	2.3792	-1.5255	0.79554	-0.29911	0.077663	-0.013655	0.0015883	-0.0001167	4.8966×10^{-6}	-8.9311×10^{-8}
p_8	7.5695	-4.4388	2.9176	-1.5376	0.58093	-0.15122	0.026629	-0.0031002	0.00022793	-9.568×10^{-6}	1.7457×10^{-7}
p_9	-1.13	0.48886	-0.26885	0.12837	-0.045939	0.011588	-0.002001	0.00022995	-1.6753×10^{-5}	6.9856×10^{-7}	-1.2681×10^{-8}
p_{10}	-6.0468	2.3146	-5.3489	3.636	-1.5505	0.43155	-0.07917	0.0094703	-0.00070964	3.0208×10^{-5}	-5.5708×10^{-7}
p_{11}	-12.137	5.4048	-6.34	3.956	-1.6274	0.44456	-0.080658	0.0095794	-0.00071425	3.0295×10^{-5}	-5.5715×10^{-7}
p_{12}	18.282	8.8237	-3.1694	1.8248	-0.73566	0.19953	-0.036085	0.0042785	-0.00031868	1.3508×10^{-5}	-2.483×10^{-7}
p_{13}	-8.7382	-2.8894	1.2873	-0.62515	0.22933	-0.058888	0.010292	-0.0011928	8.7424×10^{-5}	-3.6618×10^{-6}	6.6701×10^{-8}
p_{14}	0.5939	-0.035275	0.81189	-0.66744	0.30641	-0.08853	0.016601	-0.002014	0.00015239	-6.5331×10^{-6}	1.2112×10^{-7}
p_{15}	-0.55872	1.081	-1.2084	0.82457	-0.357	0.10054	-0.018601	0.0022386	-0.0001685	7.1979×10^{-6}	-1.331×10^{-7}
p_{16}	0.9999	-0.12337	0.050955	-0.02186	0.0074646	-0.0018393	0.00031343	-3.5727×10^{-5}	2.5887×10^{-6}	-1.0753×10^{-7}	1.9465×10^{-9}

Table 31 – Coefficients for the polynomials considering the second mode of vibration.

	C_0	C_1	C_2	C_3	C_4	C_5	C_6	C_7	C_8	C_9	C_{10}
p_1	0.49989	-0.12323	0.054992	-0.023954	0.0082058	-0.0020229	0.00034468	-3.9278×10^{-5}	2.8453×10^{-6}	-1.1816×10^{-7}	2.1386×10^{-9}
p_2	0.42423	-0.15612	0.07931	-0.036635	0.012917	-0.003234	0.00055611	-6.3744×10^{-5}	4.6361×10^{-6}	-1.9309×10^{-7}	3.5021×10^{-9}
p_3	9.7985	-16.038	13.483	-8.0046	3.2187	-0.86828	0.15632	-0.01847	0.0013721	-5.8043×10^{-5}	1.0653×10^{-6}
p_4	-6.2885	8.2037	-7.2982	4.4344	-1.8031	0.48939	-0.088435	0.010474	-0.00077946	3.3013×10^{-5}	-6.0645×10^{-7}
p_5	0.077586	28.266	-16.108	9.1895	-3.6398	0.97467	-0.17474	0.020593	-0.0015271	6.4518×10^{-5}	-1.183×10^{-6}
p_6	9.8036	-13.594	11.962	-7.2189	2.9245	-0.79203	0.14293	-0.016913	0.0012578	-5.3249×10^{-5}	9.7783×10^{-7}
p_7	-39.458	9.5315	-5.9804	3.092	-1.158	0.30009	-0.052704	0.0061258	-0.00044987	1.8869×10^{-5}	-3.4408×10^{-7}
p_8	27.281	-16.308	10.749	-5.6694	2.1428	-0.5579	0.098252	-0.01144	0.0008411	-3.531×10^{-5}	6.4427×10^{-7}
p_9	-1.2821	0.48968	-0.25934	0.12194	-0.043326	0.010889	-0.0018762	0.00021532	-1.5672×10^{-5}	6.531×10^{-7}	-1.185×10^{-8}
p_{10}	-96.928	40.186	-68.131	44.011	-18.453	5.0991	-0.93203	0.11126	-0.0083257	0.00035411	-6.526×10^{-6}
p_{11}	-194.32	88.698	-89.134	53.299	-21.552	5.8381	-1.0542	0.12484	-0.0092901	0.0003935	-7.2292×10^{-6}
p_{12}	292.45	142.22	-46.109	24.95	-9.8006	2.6248	-0.47141	0.055652	-0.0041334	0.00017485	-3.2092×10^{-6}
p_{13}	-132.4	-35.256	16.25	-8.1258	3.0302	-0.78547	0.13808	-0.016064	0.0011805	-4.9544×10^{-5}	9.038×10^{-7}
p_{14}	-13.982	2.9048	6.01	-5.7789	2.7917	-0.82659	0.15719	-0.019242	0.0014649	-6.3084×10^{-5}	1.1735×10^{-6}
p_{15}	8.7321	-3.9953	-0.77432	2.0017	-1.1769	0.38	-0.075824	0.0095669	-0.00074353	3.2498×10^{-5}	-6.1134×10^{-7}
p_{16}	0.99997	-0.062002	0.020188	-0.0078443	0.0025591	-0.00061593	0.00010356	-1.1706×10^{-5}	8.4341×10^{-7}	-3.4895×10^{-8}	6.2979×10^{-10}

Table 32 – Coefficients for the polynomials considering the third mode of vibration.

	C_0	C_1	C_2	C_3	C_4	C_5	C_6	C_7	C_8	C_9	C_{10}
p_1	0.49989	-0.12323	0.054993	-0.023955	0.0082061	-0.002023	0.00034469	-3.928×10^{-5}	2.8455×10^{-6}	-1.1817×10^{-7}	2.1387×10^{-9}
p_2	0.42423	-0.15609	0.079502	-0.036786	0.012983	-0.0032526	0.00055952	-6.415×10^{-5}	4.6665×10^{-6}	-1.9438×10^{-7}	3.5258×10^{-9}
p_3	22.047	-36.085	30.349	-18.019	7.2459	-1.9547	0.35191	-0.04158	0.003089	-0.00013067	2.3982×10^{-6}
p_4	-14.461	18.608	-16.519	10.03	-4.0773	1.1065	-0.19992	0.023678	-0.0017619	7.4623×10^{-5}	-1.3708×10^{-6}
p_5	0.17458	63.598	-36.243	20.676	-8.1894	2.193	-0.39317	0.046333	-0.003436	0.00014516	-2.6616×10^{-6}
p_6	22.058	-30.661	26.973	-16.276	6.5932	-1.7856	0.32222	-0.03813	0.0028357	-0.00012004	2.2044×10^{-6}
p_7	-88.782	21.452	-13.406	6.923	-2.5914	0.67132	-0.11788	0.013699	-0.0010059	4.2191×10^{-5}	-7.6929×10^{-7}
p_8	60.134	-36.095	23.792	-12.546	4.7406	-1.2341	0.21732	-0.025301	0.0018601	-7.8085×10^{-5}	1.4247×10^{-6}
p_9	-1.3102	0.48981	-0.2579	0.121	-0.042953	0.01079	-0.0018587	0.00021329	-1.5523×10^{-5}	6.4683×10^{-7}	-1.1736×10^{-8}
p_{10}	-490.85	206.19	-328.5	212.51	-89.096	24.601	-4.4933	0.53601	-0.04009	0.0017043	-3.1399×10^{-5}
p_{11}	-983.85	450.99	-439.68	262.49	-106.01	28.687	-5.1759	0.61252	-0.045558	0.0019289	-3.5426×10^{-5}
p_{12}	1480.5	720.91	-229.06	123.22	-48.284	12.911	-2.316	0.27319	-0.020277	0.00085733	-1.5729×10^{-5}
p_{13}	-663.32	-168.39	77.096	-38.438	14.316	-3.7085	0.65172	-0.075801	0.00557	-0.00023374	4.2637×10^{-6}
p_{14}	-103.33	26.26	13.045	-17.221	8.9372	-2.7273	0.52706	-0.065156	0.0049931	-0.00021602	4.0325×10^{-6}
p_{15}	85.447	-69.744	40.512	-17.228	5.2764	-1.1454	0.17322	-0.017759	0.0011732	-4.4964×10^{-5}	7.5871×10^{-7}
p_{16}	0.99781	-0.030551	-0.0068995	0.012121	-0.0069182	0.0022492	-0.00045498	5.8201×10^{-5}	-4.579×10^{-6}	2.0225×10^{-7}	-3.839×10^{-9}

Table 33 – Coefficients for the polynomials considering the fourth mode of vibration.

	C_0	C_1	C_2	C_3	C_4	C_5	C_6	C_7	C_8	C_9	C_{10}
p_1	0.49989	-0.12323	0.054992	-0.023955	0.008206	-0.002023	0.00034469	-3.9279×10^{-5}	2.8454×10^{-6}	-1.1817×10^{-7}	2.1387×10^{-9}
p_2	0.42423	-0.15608	0.079567	-0.036837	0.013005	-0.0032588	0.00056064	-6.4284×10^{-5}	4.6764×10^{-6}	-1.948×10^{-7}	3.5336×10^{-9}
p_3	39.194	-64.147	53.957	-32.035	12.881	-3.4748	0.62557	-0.073913	0.005491	-0.00023227	4.2628×10^{-6}
p_4	-25.903	33.173	-29.427	17.863	-7.2605	1.9702	-0.35596	0.042157	-0.003137	0.00013286	-2.4405×10^{-6}
p_5	0.311	113.06	-64.425	36.751	-14.555	3.8975	-0.69873	0.08234	-0.0061061	0.00025796	-4.7298×10^{-6}
p_6	39.214	-54.552	47.984	-28.952	11.728	-3.1761	0.57313	-0.067819	0.0050435	-0.00021351	3.9207×10^{-6}
p_7	-157.83	38.14	-23.801	12.287	-4.5983	1.1911	-0.20913	0.024302	-0.0017845	7.4841×10^{-5}	-1.3646×10^{-6}
p_8	106.13	-63.796	42.05	-22.171	8.3767	-2.1805	0.38395	-0.044699	0.0032862	-0.00013795	2.5169×10^{-6}
p_9	-1.3201	0.48983	-0.2574	0.12066	-0.042817	0.010753	-0.0018522	0.00021251	-1.5466×10^{-5}	6.444×10^{-7}	-1.1691×10^{-8}
p_{10}	-1551.5	654.73	-1020.3	661.11	-277.06	76.458	-13.958	1.6644	-0.12445	0.0052898	-9.7436×10^{-5}
p_{11}	-3109.6	1427.5	-1376.9	822.03	-331.81	89.736	-16.184	1.9146	-0.14237	0.0060269	-0.00011067
p_{12}	4679	2279.4	-719.16	386.31	-151.22	40.404	-7.2441	0.85415	-0.063381	0.0026792	-4.9146×10^{-5}
p_{13}	-2088.7	-521.07	237.68	-118.31	44.032	-11.402	2.0033	-0.23297	0.017117	-0.00071827	1.3101×10^{-5}
p_{14}	-365.98	103.23	8.5273	-29.096	16.333	-5.0607	0.97782	-0.12029	0.0091619	-0.00039389	7.3087×10^{-6}
p_{15}	322.43	-283.9	185.74	-90.303	31.479	-7.6785	1.2859	-0.14402	0.010272	-0.00042089	7.5301×10^{-6}
p_{16}	0.98696	-0.044908	0.10843	-0.13129	0.079155	-0.027517	0.0058808	-0.00078566	6.3989×10^{-5}	-2.9066×10^{-6}	5.6458×10^{-8}

Table 34 – Coefficients for the polynomials considering the fifth mode of vibration.

	C_0	C_1	C_2	C_3	C_4	C_5	C_6	C_7	C_8	C_9	C_{10}
p_1	0.49989	-0.12323	0.054992	-0.023954	0.0082058	-0.0020229	0.00034468	-3.9278×10^{-5}	2.8453×10^{-6}	-1.1816×10^{-7}	2.1386×10^{-9}
p_2	0.42423	-0.15608	0.0796	-0.036863	0.013017	-0.0032621	0.00056125	-6.4357×10^{-5}	4.682×10^{-6}	-1.9504×10^{-7}	3.5379×10^{-9}
p_3	61.24	-100.23	84.317	-50.061	20.13	-5.4303	0.97764	-0.11551	0.0085814	-0.000363	6.6621×10^{-6}
p_4	-40.614	51.901	-46.025	27.935	-11.354	3.0809	-0.55664	0.065923	-0.0049054	0.00020775	-3.8163×10^{-6}
p_5	0.48508	176.66	-100.67	57.433	-22.748	6.0914	-1.0921	0.1287	-0.009544	0.00040321	-7.393×10^{-6}
p_6	61.271	-85.271	75.001	-45.253	18.331	-4.9643	0.89582	-0.106	0.0078833	-0.00033373	6.1283×10^{-6}
p_7	-246.62	59.597	-37.167	19.183	-7.1786	1.8593	-0.32644	0.037934	-0.0027854	0.00011682	-2.13×10^{-6}
p_8	165.26	-99.413	65.526	-34.546	13.052	-3.3974	0.59821	-0.069642	0.00512	-0.00021492	3.9213×10^{-6}
p_9	-1.3246	0.48983	-0.25714	0.12048	-0.04274	0.010732	-0.0018482	0.00021203	-1.5429×10^{-5}	6.4285×10^{-7}	-1.1662×10^{-8}
p_{10}	-3788	1602	-2470.7	1602.6	-671.45	185.23	-33.807	4.0307	-0.30135	0.012807	-0.00023589
p_{11}	-7591.9	3487.6	-3347.4	1998.7	-806.52	218.06	-39.32	4.651	-0.34582	0.014638	-0.00026878
p_{12}	11423	5566.2	-1750.4	939.7	-367.66	98.198	-17.601	2.075	-0.15395	0.0065069	-0.00011935
p_{13}	-5090.7	-1259.6	573.42	-285.2	106.1	-27.468	4.8254	-0.56112	0.041225	-0.0017298	3.1551×10^{-5}
p_{14}	-901.42	49.662	423.7	-453.34	242.31	-77.466	15.609	-1.9979	0.15754	-0.0069788	0.00013287
p_{15}	849.37	-768.74	522.57	-263.55	94.68	-23.641	4.0309	-0.45778	0.033012	-0.0013646	2.4592×10^{-5}
p_{16}	0.99999	-0.024851	0.0066885	-0.0024718	0.00079208	-0.00018913	3.1667×10^{-5}	-3.5707×10^{-6}	2.5687×10^{-7}	-1.0616×10^{-8}	1.9145×10^{-10}

APPENDIX F – List of publications originated from this research up to its finalization date

In the present appendix the resulting publications and participation in international events originated from the research done during the PhD program are listed.

F.1 Works presented in international events

Vernizzi, G. J.; Franzini, G. R.; Pesce, C. P. "Non-linear free vibrations of a catenary cable with small sag", IUTAM Symposium on Exploiting Nonlinear Dynamics for Engineering Systems – ENOLIDES, 2018.

Vernizzi, G. J.; Franzini, G. R. "Vortex-induced vibration analysis through invariant manifolds", International Symposium on Dynamic Problems of Mechanics – DINAME, 2019.

Vernizzi, G. J.; Franzini, G. R.; Lenci, S. "A comparison between reduced-order models for a vertical riser undergoing parametric excitation", Fourth International Conference on Recent Advances in Nonlinear Mechanics – RANM, 2019.

Vernizzi, G. J.; Franzini, G. R.; Lenci, S. "Comparison between some reduced-order models for the analysis of a vertical rod undergoing vortex-induced vibrations", International Conference on Nonlinear Solid Mechanics – ICoNSoM, 2019.

Vernizzi, G. J.; Lenci, S.; Franzini, G. R. "Invariant manifold for the analysis of flexible cylinders under vortex-induced vibrations", International Conference on Engineering Vibration – ICoEV, 2020.

Vernizzi, G. J.; Franzini, G. R.; Lenci, S. "Reduced-order models for inclined elastic cables with arbitrary sag under support excitation", 25th International Congress of Theoretical and Applied Mechanics – ICTAM 2021.

Vernizzi, G. J.; Lenci, S.; Franzini, G. R. "Revisiting the nonlinear free vibrations of hanging cables – The use of a direct approach on the partial differential equations of motion", 10th European Nonlinear Dynamics Conference – ENOC 2022.

F.2 Articles published in international journals or as book chapters

Vernizzi, G. J.; Franzini, G. R.; Pesce, C. P. "Non-linear free vibrations of a hanging cable with small sag". In: Kovacic, I., Lenci, S. (eds) IUTAM Symposium on Exploiting Nonlinear Dynamics for Engineering Systems. ENOLIDES 2018. IUTAM Bookseries, vol 37. Springer, Cham (2020). https://doi.org/10.1007/978-3-030-23692-2_ 23.

Vernizzi, G. J.; Franzini, G. R.; Lenci, S. "Reduced-order models for the analysis of a vertical rod under parametric excitation". International Journal of Mechanical Sciences, 2019, 163, 105-122.

Vernizzi, G. J.; Lenci, S.; Franzini, G. R. "A detailed study of the parametric excitation of a vertical heavy rod using the method of multiple scales". Meccanica, 2020, 55, 2423-2437.

Vernizzi, G. J.; Lenci, S.; Franzini, G. R. "A discussion regarding reduced-order modelling of inclined elastic and immersed cables under support excitation". International Journal of Non-Linear Mechanics, 2022, 145, 104078.